

Aus der Fachrichtung Biophysik  
Theoretische Medizin und Biowissenschaften  
der Medizinischen Fakultät  
der Universität des Saarlandes, Homburg /Saar

**Maturation of activity-dependent endocytosis in inner hair cells of  
the mouse cochlea**

Dissertation  
Zur Erlangung des Grades eines Doktors der Naturwissenschaften  
der Medizinischen Fakultät  
der Universität des Saarlandes

2023

vorgelegt von  
Guobin Huang  
geb. am 29.10.1990 in Guangdong, China

Die Dissertation „Maturation of activity-dependent endocytosis in inner hair cells of the mouse cochlea“ wurde in der Arbeitsgruppe von Frau Prof. Dr. Jutta Engel am Centrum für Integrative Physiologie und Molekulare Medizin (CIPMM) angefertigt.

Tag der Promotion: 16.04.2024  
Dekan: Univ.-Prof. Dr. med. Michael D. Menger  
Berichterstatter: Prof. Dr. Jutta Engel  
Prof. Dr. Gabriela Krasteva-Christ

## Table of content

<b>List of Figures</b>	<b>4</b>
<b>List of tables</b>	<b>7</b>
<b>Abbreviations</b>	<b>9</b>
<b>Abstract</b>	<b>11</b>
<b>Zusammenfassung</b>	<b>13</b>
<b>1 Introduction</b>	<b>15</b>
1.1 Mammalian peripheral auditory system	15
1.2 The organ of Corti	17
1.3 Exo- and endocytosis of inner hair cells	18
1.4 Development of the organ of Corti in rodents	20
1.5 Objectives of the study	21
<b>2 Materials and Methods</b>	<b>23</b>
2.1 Ethical statement	23
2.2 Animals	23
2.3 Solutions	23
2.4 General tissue preparation	26
2.5 RNAscope™ fluorescent <i>in situ</i> hybridization	26
2.6 Immunohistochemistry	30
2.7 Image acquisition	32
2.8 Quantification of RNAscope™ fluorescent <i>in situ</i> hybridization data	32
2.9 Electrophysiology	32
2.9.1 Patch clamp setup	33
2.9.2 Pipettes	37
2.9.3 Patch clamp workflow	37
2.9.4 Patch clamp protocols and data analysis	38
2.10 Statistical analysis	42
<b>3 Results</b>	<b>43</b>
3.1 Fluorescence <i>in situ</i> hybridization in the whole-mount organ of Corti	43
3.2 Age-dependent changes of <i>dnm1</i> , <i>dnm3</i> , and <i>sh3gl2</i> mRNA transcription in inner and outer hair cells	50
3.3 Developmental changes in protein expression of dynamin-1 and dynamin-3 in the organ of Corti	57
3.4 The choice of fixative affects the appearance of dynamin-3 labeling	68
3.5 Electrophysiology	70
3.5.1 Maturation of endocytosis in inner hair cells	70
<i>Endocytosis is enhanced after maturation of inner hair cells</i>	70

	<i>Maturation of inner hair cells affects sustained release in response to moderate stimulation</i>	74
	<i>Maturation of inner hair cells affects sustained release in response to excessive stimulation</i>	77
3.5.2	Temperature-dependence of endocytosis of inner hair cells	80
	<i>Body temperature accelerates endocytosis of mature but not pre-mature IHCs</i>	80
	<i>Temperature-dependence of sustained release in response to moderate stimulation of inner hair cells</i>	83
	<i>Temperature-dependence of sustained release in response to excessive stimulation of inner hair cells</i>	86
3.5.3	Effect of blocking dynamin on endocytosis of inner hair cells	89
	<i>Blocking dynamin decelerates endocytosis of mature but not pre-mature inner hair cells</i>	89
	<i>Blocking of dynamin affects moderate sustained release in mature but not pre-mature inner hair cells</i>	92
	<i>Sustained release upon excessive repetitive stimulation is altered in inner hair cells in presence of dyngo-4a</i>	95
3.5.4	Low concentrated DMSO in inner hair cells does not affect the calcium current	98
<b>4</b>	<b>Discussion</b>	<b>99</b>
4.1	Endocytosis is enhanced after inner hair cell maturation	99
4.2	Endocytosis in inner hair cells at different ages is differently affected by temperature	102
4.3	Expression of endocytic proteins is developmentally regulated in inner hair cells	105
4.4	Blocking dynamin differentially affects endocytosis of pre-mature and mature inner hair cells	106
4.5	Endocytic proteins in outer hair cells	108
<b>5</b>	<b>References</b>	<b>110</b>
<b>6</b>	<b>Supplement</b>	<b>124</b>
	<b>Acknowledgments</b>	<b>144</b>
	<b>Publications and conferences</b>	<b>145</b>
	<b>Curriculum Vitae</b>	<b>146</b>

## List of Figures

Figure 1	Structure of the human peripheral auditory system.	15
Figure 2	Cross section of one cochlear turn.	16
Figure 3	Schematic of the readily releasable pool and the secondary releasable pool.	19
Figure 4	Simplified principle of RNAscope™ showing bindings among involved molecules.	27
Figure 5	Container for RNAscope™ experiment.	29
Figure 6	Bath chamber with an immobilizing grid for patch clamp.	34
Figure 7	Part of the patch clamp setup.	35
Figure 8	Close-up of patch clamp set-up components in vicinity of the bath chamber.	36
Figure 9	Pre-recording of calcium currents.	38
Figure 10	Seal test protocol.	38
Figure 11	Single pulse protocol and reference recording.	39
Figure 12	50-ms short-term and 1-s long-term repetitive protocol.	40
Figure 13	50-ms, 100-ms and 1-s reference protocol.	41
Figure 14	RNAscope™ fluorescent <i>in situ</i> hybridization on whole-mount pre-mature organs of Corti using positive and negative control probes.	44
Figure 15	X-projection of positive controls of RNAscope™ fluorescent <i>in situ</i> hybridization on the whole-mount pre-mature organ of Corti.	45
Figure 16	RNAscope™ fluorescent <i>in situ</i> hybridization on whole-mount mature organs of Corti using positive and negative control probes.	46
Figure 17	X-projection of the positive control of RNAscope™ fluorescent <i>in situ</i> hybridization on the whole-mount mature organ of Corti.	47
Figure 18	Quantification of puncta in RNAscope™ fluorescent <i>in situ</i> hybridization controls.	48
Figure 19	Differential mRNA transcription of the endocytic genes <i>dnm1</i> , <i>dnm3</i> and <i>sh3gl2</i> in the pre-mature organ of Corti.	51
Figure 20	X-projection of the signals of <i>dnm1</i> , <i>dnm3</i> and <i>sh3gl2</i> in the pre-mature organ of Corti.	52
Figure 21	Mature inner hair cells express more <i>dnm1</i> and <i>sh3gl2</i> mRNA but less <i>dnm3</i> than mature outer hair cells.	53
Figure 22	X-projection of the signals of <i>dnm1</i> , <i>dnm3</i> and <i>sh3gl2</i> in the mature organ of Corti.	54

Figure 23	Quantification of <i>dnm1</i> , <i>dnm3</i> and <i>sh3gl2</i> puncta in RNAscope™ fluorescent <i>in situ</i> hybridization.	55
Figure 24	Protein expression of dynamin-1 and ap-180 in whole-mount organs of Corti.	58
Figure 25	Dynamin-1 and ap-180 are mainly expressed in nerve fibers of the pre-mature organ of Corti.	60
Figure 26	Hair cells in the mature organ of Corti express high levels of dynamin-1 and ap-180.	61
Figure 27	Protein expression of dynamin-1 and ap-180 in spiral ganglion neurons of the mature organ of Corti.	62
Figure 28	Protein expression of dynamin-3 and myosin-7a in whole-mount organs of Corti.	63
Figure 29	Strong expression of dynamin-3 in outer hair cells but not in inner hair cells of the pre-mature organ of Corti.	65
Figure 30	Outer hair cells show higher dynamin-3 expression than inner hair cells in the mature organ of Corti.	66
Figure 31	Protein expression of dynamin-3 and myosin-7a in spiral ganglion neurons of the mature organ of Corti.	67
Figure 32	Dynamin-3 staining in organs of Corti fixed with Zamboni's fixative.	69
Figure 33	Endocytosis of pre-mature and mature inner hair cells.	72
Figure 34	Stimulus-independent decline of membrane capacitance in inner hair cells.	73
Figure 35	Maturity level affects release upon moderate repetitive stimulation of inner hair cells.	76
Figure 36	Maturity level affects release upon excessive repetitive stimulation of inner hair cells.	79
Figure 37	Effect of temperature on endocytosis of inner hair cells.	82
Figure 38	Effect of temperature on release upon repetitive moderate stimulation of inner hair cells.	85
Figure 39	Effect of temperature on release upon excessive stimulation of inner hair cells.	88
Figure 40	Effect of dyngo-4a on endocytosis of inner hair cells.	91
Figure 41	Effect of dyngo-4a on sustained moderate release of inner hair cells.	94
Figure 42	Effect of dyngo-4a on sustained excessive release of inner hair cells.	97
Figure 43	Effect of DMSO on inner hair cells.	98

Supplement Figure 1	Transcription of <i>dnm1</i> , <i>dnm3</i> and <i>sh3gl2</i> in spiral ganglion neurons of the mature organ of Corti.	124
Supplement Figure 2	Negative controls of immunolabeling.	125
Supplement Figure 3	Negative controls of immunolabeling in organs of Corti fixed with Zamboni's fixative.	126

## List of tables

Table 1	Composition of extracellular and application solutions.	25
Table 2	Composition of intracellular solutions.	26
Table 3	RNAscope™ fluorescence <i>in situ</i> hybridization workflow.	28
Supplement Table 1	Slope of the linear function fitted to the change of membrane capacitance ( $\Delta C_m$ ) of the reference recordings and to the last 8 s of the $\Delta C_m$ following a 100-ms stimulus.	127
Supplement Table 2	Peak $\Delta C_m$ reflecting exocytosis induced by a 100-ms depolarization.	127
Supplement Table 3	Time required for $\Delta C_m$ to return to the baseline at 0 fF (time to 0) following exocytosis induced by a 100-ms depolarization.	128
Supplement Table 4	Endocytosis (decline) rate of $\Delta C_m$ (calculated as peak $\Delta C_m$ divided by time to 0) following exocytosis induced by a 100-ms depolarization.	128
Supplement Table 5	Ca <sup>2+</sup> charge ( $Q_{Ca}$ ) calculated from the Ca <sup>2+</sup> current ( $I_{Ca}$ ) elicited by a 100-ms depolarization.	129
Supplement Table 6	Exponential amplitude (A) of the exponential-linear function fitted to cumulative $\Delta C_m$ traces following repetitive 50-ms depolarizations.	129
Supplement Table 7	Exponential time constant ( $\tau$ ) of the exponential-linear function fitted to cumulative $\Delta C_m$ traces following repetitive 50-ms depolarizations.	130
Supplement Table 8	Slope of the linear function and the linear part of the exponential-linear function fitted to cumulative $\Delta C_m$ traces following repetitive 50-ms depolarizations.	130
Supplement Table 9	Total $Q_{Ca}$ summarized from all stimuli during repetitive 50-ms depolarizations.	131
Supplement Table 10	Difference between $Q_{Ca}$ at the first and last, 50 <sup>th</sup> stimulus ( $\Delta Q_{(1-50)}$ ) during repetitive 50-ms depolarizations.	131
Supplement Table 11	Total efficiency ( $\Delta C_m/Q_{Ca}$ , calculated from interstep $\Delta C_m$ normalized to $Q_{Ca}$ ) summarized from all stimuli during repetitive 50-ms depolarizations.	132
Supplement Table 12	Exponential A of the exponential-linear function fitted to cumulative $\Delta C_m$ traces following repetitive 1-s depolarizations.	132
Supplement Table 13	Exponential $\tau$ of the exponential-linear function fitted to cumulative $\Delta C_m$ traces following repetitive 1-s depolarizations.	133

Supplement Table 14	Slope of the linear function and the linear part of the exponential-linear function fitted to cumulative $\Delta C_m$ traces following repetitive 1-s depolarizations.	133
Supplement Table 15	Total $Q_{Ca}$ summarized from all stimuli during repetitive 1-s depolarizations.	134
Supplement Table 16	$\Delta Q_{(1-50)}$ during repetitive 1-s depolarizations.	134
Supplement Table 17	Total efficiency summarized from all stimuli during repetitive 1-s depolarizations.	135
Supplement Table 18	List of equipment.	136
Supplement Table 19	List of software.	136
Supplement Table 20	List of chemicals.	137
Supplement Table 21	List of primary antibodies.	138
Supplement Table 22	List of secondary antibodies.	138
Supplement Table 23	List of tested immunohistochemistry experiment conditions.	139

## Abbreviations

4-AP	4-aminopyridine
A	amplitude
amp	amplifier
AP	action potential
BSA	bovine serum albumin
BT	body temperature
$C_m$	membrane capacitance
$\Delta C_m$	change in membrane capacitance
$\Delta C_{(max-50)}$	difference between the maximum $\Delta C_m$ and $\Delta C_m$ at the last, 50th stimulus
DAM	donkey anti-mouse
DAPI	4',6-diamidino-2-phenylindole
DAR	donkey anti-rabbit
DMSO	dimethylsulfoxide
ECS	extracellular solution
ECS-Lactobionic	extracellular solution containing lactobionic acid
EGTA	ethylene glycol-bis( $\beta$ -aminoethyl ether)-N,N,N',N'-tetraacetic acid
EtOH	ethanol
Fig.	figure
<i>FISH</i>	fluorescence <i>in situ</i> hybridization
GAM	goat anti-mouse
GAR	goat anti-rabbit
GTP	guanosine-5'-triphosphate
HC	hair cell
HEPES	N-2-hydroxyethylpiperazine-N-2-ethane sulfonic acid
$I_{Ca}$	calcium current
IHC	inner hair cell
K-W test	Kruskal-Wallis test
KO	knock-out
m	mouse
mat	mature
MeOH	methanol
MET	mechanoelectrical transduction
MIXP	maximum intensity X-axis projection
MIZP	maximum intensity Z-axis projection
mRNA	messenger ribonucleic acid
$Na_2ATP$	adenosin-5'-triphosphat dinatriumsalz hydrat
NF	nerve fiber
NGS	normal goat serum
No.	number
OC	organ of Corti
OHC	outer hair cell
P	postnatal day
pre	pre-mature
PAB	primary antibody

PBS	phosphate-buffered saline
PBT	0.1% Tween 20 in phosphate-buffered saline
PFA	paraformaldehyde
$Q_{Ca}$	calcium charge
$\Delta Q_{(1-50)}$	difference between $Q_{Ca}$ at the first and last, 50th stimulus
r	rabbit
$R_{leak}$	leak resistance
$R_s$	series resistance
RRP	readily releasable pool
RT	room temperature
SAB	secondary antibody
S.D.	standard deviation
SGN	spiral ganglion neuron
SL	spiral limbus
SRP	secondary releasable pool
Suppl.	supplement
$\tau$	time constant
TEA-chloride	tetraethylammonium chloride
TX-100	Triton X-100; 2-[4-(2,4,4-trimethylpentan-2-yl)phenoxy]ethanol

## Abstract

The organ of Corti contains inner hair cells (IHCs), named for their hair-shaped structures called stereocilia, as the primary sensory cells of the auditory system. IHCs transmit acoustic information to the auditory pathway by constantly releasing synaptic vesicles without exhaustion. For stable sound encoding, it is crucial that the active zone is cleared by retrieval of the vesicle membrane via endocytosis and that the synaptic vesicle pool is efficiently replenished. Before the onset of hearing (at postnatal day 12 in mice), IHCs and their synaptic release machinery undergo terminal differentiation, which involves the up- and downregulation of several proteins and fundamental changes in their physiology. Whether endocytosis experiences a similar maturation process is so far poorly understood. Here, I aimed to investigate potential developmental changes in the molecular composition and kinetics of the endocytic machinery of IHCs.

Using quantitative fluorescence *in situ* hybridization, I compared the transcription profiles of three endocytic proteins – dynamin1, dynamin-3, and endophilin-A1 – in pre-mature and mature mouse organs of Corti. The results revealed that IHCs expressed low levels of *dnm1* (encoding dynamin-1), *dnm3* (encoding dynamin-3) and *sh3gl2* (encoding endophilin-A1) mRNA transcripts. After the onset of hearing, *dnm1* transcription was upregulated. Immunolabeling corroborated robust expression of dynamin-1 and another endocytic protein, adapter protein 180, in the soma of mature IHCs, while both were weakly expressed before the onset of hearing. Dynamin-3 was largely absent from IHCs but was abundant on mRNA and protein levels in outer hair cells, the sound amplifiers of the auditory system with low synaptic activity. It was localized in the soma and at the periphery of the cuticular plates of both pre-mature and mature outer hair cells, suggesting an activity-independent function, such as for recycling of proteins from the stereocilia.

Through whole-cell patch clamp recordings at near-physiological temperature, I furthermore evaluated activity-dependent exocytosis and endocytosis in IHCs before and after the onset of hearing by analyzing the change in their membrane capacitance. Following depolarization-induced exocytosis, the decline in membrane capacitance – indicating endocytosis – was faster in mature IHCs compared to pre-mature IHCs. Moderate repetitive stimulation was used to elicit sustained release of the readily releasable pool of synaptic vesicles. In mature IHCs, it caused an initially steep rise in membrane capacitance that subsequently slowed down to a linear course, suggesting the intervention of efficient endocytosis, which contrasts the saturating increase in pre-mature IHCs that might indicate the onset of pool depletion upon repetitive moderate stimulation. Similarly, following excessive repetitive stimulation that presumably challenged the secondary releasable pool, membrane capacitance increased less

in mature than pre-mature IHCs. These data suggest that increased endocytosis in mature IHCs efficiently compensates for exocytosis, which might result in faster replenishment of the vesicle pools than in pre-mature IHCs. In addition, the temperature-sensitivity of endocytosis was increased in mature IHCs as revealed by recordings at ambient temperature, further supporting that the endocytic machinery changes during terminal differentiation. When blocking dynamin activity, endocytosis was largely unaffected in pre-mature IHCs, whereas it was significantly hampered in mature IHCs. This implies that dynamin, presumably dynamin-1 due to its developmentally increased expression, is more important in endocytosis of IHCs after terminal differentiation.

In summary, this thesis reveals *i)* developmentally regulated expression of endocytic proteins in hair cells and *ii)* enhanced endocytosis in mature IHCs, both supporting that the endocytic machinery of IHCs indeed undergoes terminal differentiation. Moreover, in pre-mature IHCs the low expression of dynamin-1 and insensitivity to dynamin inhibition suggests a pivotal role of a so far unknown process of dynamin-independent endocytosis, whereas endocytosis of mature IHCs might be reinforced by mechanisms requiring dynamin-1 along with adapter protein 180.

## Zusammenfassung

Das Corti-Organ enthält als primäre Sinneszellen des Hörsystems die inneren Haarsinneszellen (IHZ), die nach ihren haarförmigen Strukturen, den sogenannten Stereozilien, benannt sind. Die IHZ übermitteln akustische Informationen an die Hörbahn, indem sie unermüdlich synaptische Vesikel freisetzen. Für eine zuverlässige Schallkodierung ist von entscheidender Bedeutung, dass die Vesikelmembran mittels Endozytose von den aktiven Zonen entfernt und der synaptische Vesikelpool effizient wiederaufgefüllt wird. Vor Hörbeginn (am postnatalen Tag 12 in Mäusen) durchlaufen die IHZ und ihre Synapsen eine Phase terminaler Differenzierung, welche die Hoch- und Herunterregulierung mehrerer Proteine, sowie umfassende physiologische Veränderungen beinhaltet. Bisher ist weitgehend unbekannt, ob die Endozytose einen ähnlichen Reifungsprozess durchläuft. Die vorliegende Arbeit hatte das Ziel, die molekulare Zusammensetzung und Kinetik der endozytischen Maschinerie auf mögliche Veränderungen während der Reifung der IHZ zu untersuchen.

Mittels quantitativer Fluoreszenz-*in-situ*-Hybridisierung verglich ich die Transkriptionsprofile von drei endozytischen Proteinen – Dynamin-1, Dynamin-3 und Endophilin-A1 – vor und nach Hörbeginn in Corti-Organen von Mäusen. Die Ergebnisse zeigten, dass unreife IHZ nur geringe mRNA-Kopien von *dnm1* (kodiert Dynamin-1), *dnm3* (kodiert Dynamin-3) und *sh3gl2* (kodiert Endophilin-A1) enthielten. Nach Hörbeginn war die Transkription von *dnm1* hochreguliert. Immunhistochemische Färbungen bestätigten die robuste Expression von Dynamin-1 und Adapterprotein-180, einem weiteren endozytischen Protein, im Soma reifer IHZ, während beide Proteine vor der Reifung nur schwach exprimiert waren. Dynamin-3 war in den IHZ kaum vorhanden, jedoch in äußeren Haarzellen, den Schallverstärkern des auditorischen Systems mit geringer eigener synaptischer Aktivität, auf mRNA- sowie Proteinebene stark exprimiert. Dynamin-3 war im Soma und am Rand der Kutikularplatten sowohl unreifer als auch reifer äußerer Haarzelle lokalisiert, und könnte dort eine aktivitätsunabhängige Funktion erfüllen, z.B. beim Recycling von Proteinen aus den Stereozilien.

Mit Hilfe von Patch-Clamp-Ableitungen bei annähernd physiologischer Temperatur untersuchte ich die Exozytose und Endozytose in Abhängigkeit des Reifegrades, indem ich die aktivitätsabhängige Änderung der Membrankapazität der IHZ vor und nach Hörbeginn analysierte. Nach depolarisierungsabhängiger Exozytose war die Abnahme der Membrankapazität, ein Maß für Endozytose, in reifen IHZ schneller als in unreifen. Moderate repetitive Stimulation wurde verwendet, um eine anhaltende Vesikelausschüttung aus dem schnell freisetzbaren Vesikelpool auszulösen. Diese Stimulation verursachte in reifen IHZ einen anfänglich steilen Anstieg der Membrankapazität, der sich zu einem linearen Verlauf

verlangsamte, was Kompensation durch effiziente Endozytose hindeutet, wohingegen der sättigende Anstieg in unreifen IHCs auf eine beginnende Erschöpfung des Pools hinweisen könnte. Auch nach exzessiver repetitiver Stimulation, die eine übermäßige Freisetzung des langsam freisetzbaren Pools auslösen sollte, stieg die Membrankapazität bei reifen IHZ weniger stark an als bei unreifen. Diese Daten deuten darauf hin, dass in reifen IHZ eine erhöhte Endozytoserate die Exozytose effizienter kompensiert, was mit einem schnelleren Wiederauffüllen der Vesikelpools als in unreifen IHZ verbunden sein könnte. Darüber hinaus zeigten Ableitungen bei Raumtemperatur eine erhöhte Temperatursensitivität der Endozytose in reifen IHZ, was ein weiterer Hinweis auf eine Veränderung der endozytischen Maschinerie während der terminalen Differenzierung ist. Die Blockierung der Dynamin-Funktion durch Dyngo-4a beeinflusste die Endozytose unreifer IHZ kaum, während die Endozytose reifer IHZ erheblich beeinträchtigt wurde. Dies deutet darauf hin, dass Dynamin, vermutlich Dynamin-1 (aufgrund seiner erhöhten Expression nach Reifung der IHZ), erst nach der terminalen Differenzierung eine wichtige Funktion in der Endozytose der IHZ erfüllt.

Zusammenfassend zeigte diese Arbeit *i)* eine entwicklungsabhängige Regulierung endozytischer Proteine, verbunden mit *ii)* einer erhöhten Endozytoserate in reifen IHZ. Beides spricht dafür, dass die endozytische Maschinerie der IHZ tatsächlich eine terminale Differenzierung erfährt. Darüber hinaus deutet die geringe Expression von Dynamin-1 und die Unempfindlichkeit gegenüber Dynamin-Inhibition auf eine bisher unbekannte, dynamin-unabhängige Form der Endozytose in unreifen IHZ hin, während die Hochregulierung von Dynamin-1 sowie Adapterprotein-180 zur effizienteren Endozytose reifer IHZ beitragen könnte.

## 1 Introduction

Many animals rely on their auditory system, which perceives sounds of varying frequencies and amplitudes, to identify and locate sounds in the environment for different tasks including communication, navigation, and predation (Chen and Wiens, 2020; Moss and Surlykke, 2010; Brown and Santos-Sacchi, 2013). For instance, with the ability to process sounds in the range spanning from 20 Hz to 20 kHz, humans are most sensitive to sounds within the 1 to 4 kHz range, where the majority of speech frequencies are found (Brown and Santos-Sacchi, 2013).

### 1.1 Mammalian peripheral auditory system

The mammalian peripheral auditory system (**Fig. 1**) is composed of three major parts: the external, middle and inner ear (Lindsay and Norman, 1977).

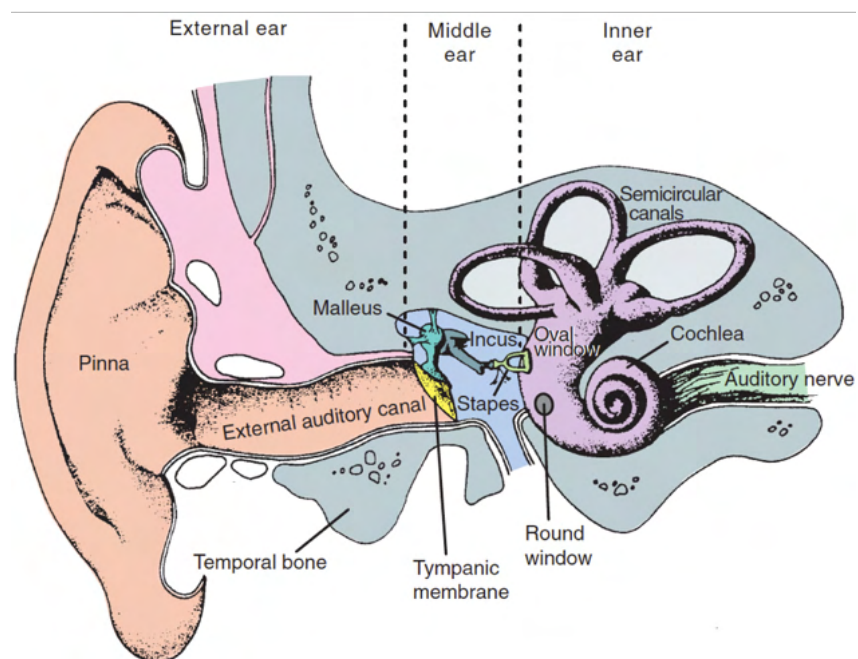


**Figure 1 Structure of the human peripheral auditory system.** The external, middle and inner ear with respective structures are shown. From Lindsay and Norman (1977).

The pinna and external auditory canal make up the external ear, through which sound waves are collected and conveyed to the middle ear (Brown and Santos-Sacchi, 2013). The middle ear is an air-filled cavity containing three ossicles (malleus, incus and stapes) separated from the external ear by the tympanic membrane (Anthwal and Thompson, 2016; Brown and Santos-Sacchi, 2013). Sound causes vibration of the tympanic membrane that in turn induces vibration of the ossicles. Impedance matching, including lever action of the ossicles, pressure increase due to the area difference between the tympanic membrane and the stapes footplate, and bulking motion of the tympanic membrane, ensures efficient energy transmission of sound

(Brown and Santos-Sacchi, 2013; Neuweiler and Heldmaier, 2003). Eventually, the stapes passes the sound wave to the inner ear fluid at the oval window.

The inner ear has two parts: the semicircular canals as the sensory end-organ of the vestibular system and the cochlea as the sensory end-organ of the auditory system (Brown and Santos-Sacchi, 2013). The cochlea is a coiled structure resembling a snail shell, whose number of turns varies from 0.5 to 5 in mammals (Solntseva, 2007). The central axis of the cochlea, called the modiolus, is present in almost all mammals, within which the spiral ganglion neurons (SGNs) are located (Brown and Santos-Sacchi, 2013). The cochlea contains three fluid compartments (**Fig. 2**): the scala vestibuli, scala media, and scala tympani (Brown and Santos-Sacchi, 2013). The extracellular fluid of the scala vestibuli and the scala tympani, called perilymph, is generated by the lymphatic system and is rich in  $\text{Na}^+$  but poor in  $\text{K}^+$ , whereas the scala media is filled with endolymph containing low  $[\text{Na}^+]$  but high  $[\text{K}^+]$  generated by the stria vascularis (Ekdale, 2016; Wangemann, 2006).  $\text{K}^+$  in the endolymph serves as the main charge carrier for sensory transduction (Wangemann, 2006). The scala media is separated from the other two scalae by the Reissner's membrane and the basilar membrane, respectively. The basilar membrane houses the sensory epithelium called the organ of Corti (OC), which is covered by the tectorial membrane, a ribbon-like strip of extracellular matrix made up of various collagens and other proteins (Richardson et al., 2008).

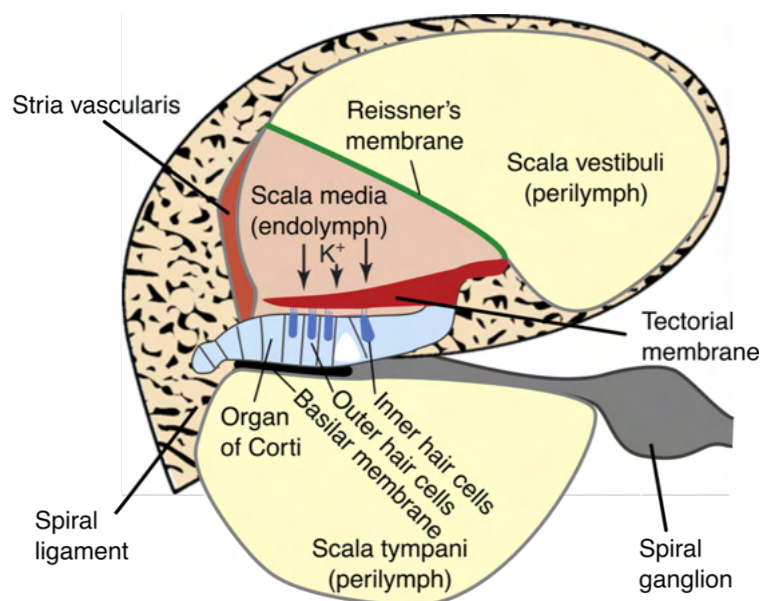


**Figure 2** Cross section of one cochlear turn. Fluid compartments and major cell groups are shown. From Brown & Santos-Sacchi (2013).

## 1.2 The organ of Corti

The OC is a sensory organ containing supporting cells and the auditory receptor cells called hair cells (HCs). There are at least five different types of supporting cells that play roles in various tasks including cell patterning, synaptogenesis, preservation of the structural integrity of the OC, and modulation of ion and small molecule homeostasis (Wan et al., 2013). HCs comprise three to four rows of outer hair cells (OHCs) and one row of inner hair cells (IHCs). HCs are polarized: their apical pole is required for mechanotransduction and their basal pole for the release of neurotransmitter, which occurs mainly in IHCs (Ashmore, 2008; Brown and Santos-Sacchi, 2013). For the apical pole, three rows of actin-based microvilli called stereocilia originate at the apex of HCs and protrude into the extracellular environment (Ekdale, 2016). For the basal pole, OHCs are mostly innervated by efferent nerve fibers and few type II SGNs as afferent fibers (Dannhof and Bruns, 1993; Huang et al., 2007). In contrast, IHCs are innervated by afferent type I SGNs and only these afferents, instead of IHCs per se, are innervated by few efferent fibers, which modulate signals from IHCs (Dannhof and Bruns, 1993; Huang et al., 2007). Notably, only 5-10% of the neuronal population is formed by the unmyelinated type II SGNs, while the myelinated type I SGNs represent 90-95% of the population (Delacroix and Malgrange, 2015). Vibrations induced by sounds of specific frequencies reach their maximum amplitude at specific positions in the cochlea and stimulate only specific HCs, of which HCs at the basal cochlear turn encode high-frequency sounds and HCs at the apical turn encode low-frequency sounds (Safieddine et al., 2012). Apart from the prerequisite that sounds of different frequencies have different wavelengths, this tonotopy is achieved by the gradual changes in the width and thickness of the basilar and tectorial membranes (Dallos, 1996; Mann and Kelley, 2011), and several other factors differing between the cochlear base and apex, including the height of the stereocilia (Kaltenbach et al., 1994; Wright, 1984) and the length of the OHCs' somata (Fettiplace, 2017).

In terms of function, OHCs change their length in response to stimulation, which is referred to as "electromotility" and crucial for sensitivity enhancement and frequency tuning, whereas IHCs are the primary sensors of sound perception that transmit the acoustic signal to the afferent SGNs (Ashmore, 2008; Dallos, 1992; Johnson et al., 2019). Both types of HCs are activated by the shear motion between basilar membrane and tectorial membrane resulting from sound-induced vibrations. Consequently, stereocilia are deflected and tip-links, which interconnect stereocilia, are stretched leading to the opening of mechano-electrical transduction (MET) channels located at the tip of stereocilia (Fettiplace and Kim, 2014; Hudspeth, 1989). Ions, most of which are  $K^+$  (Wangemann, 2006), flow into the HCs through the MET channels. This leads to a graded receptor potential (Kros et al., 1998), causing the opening of L-type ( $Ca_v1.3$ ) voltage-gated  $Ca^{2+}$  channels in the basolateral membrane of IHCs,

which subsequently induce the  $\text{Ca}^{2+}$  influx (Platzner et al., 2000). The increase in intracellular  $\text{Ca}^{2+}$  concentration triggers exocytosis of synaptic vesicles. As a result, glutamate, the neurotransmitter of IHCs, is released. It activates afferent SGNs that eventually relay the signal to the cochlear nucleus in the brainstem (Brown and Santos-Sacchi, 2013; Fuchs et al., 2003). Interplay of BK, KCNQ4 and various rectifier  $\text{K}_v$  channels repolarizes the IHCs by mediating the  $\text{K}^+$  efflux (Dierich et al., 2020; Kros et al., 1998; Marcotti et al., 2003a; Oliver et al., 2003).

### 1.3 Exo- and endocytosis of inner hair cells

IHCs can initiate firing of afferent SGNs at rates of hundreds of Hz, which requires rapid, temporally precise and untiring exocytosis (Neef et al., 2014). Such exocytosis is supported by presynaptic electron-dense structures called synaptic ribbons, which are mainly composed of RIBEYE, a structural cytomatrix protein (Schmitz et al., 2000). Ribbons are clustered with presynaptic  $\text{Ca}_v1.3$  channels and can tether up to 100 synaptic vesicles containing glutamate (Frank et al., 2010; Liberman et al., 1990; Sheets et al., 2011; Smith and Sjöstrand, 1961). Two pools of vesicles have been defined based on their functional differences (**Fig. 3**): The readily releasable pool (RRP) is considered to be formed by the vesicles near the base of ribbons and attached to the presynaptic membrane, which are released upon moderate stimuli, while the secondary releasable pool (SRP) is thought to be formed by vesicles remote from their release site that are triggered by excessive stimuli (Duncker et al., 2013; Johnson et al., 2005). Intriguingly, some exocytic proteins essential for neurons are either absent or their blocking does not affect exocytosis in IHCs, for instance synaptotagmins-1 to -3, major  $\text{Ca}^{2+}$  sensors for fast exocytosis in synapses of the central nervous system (Safieddine and Wenthold, 1999); synaptophysins and synapsins (Eybalin et al., 2002); complexins-I to -IV, which regulate a late step in synaptic vesicle release (Strenzke et al., 2009); and soluble N-ethylmaleimide-sensitive factor attachment receptor proteins (SNAREs; namely SNAP-25, syntaxin-1, and synaptobrevin-1/2), which are crucial for membrane fusion in conventional synapses (Nouvian et al., 2011). Instead, a multifunctional protein called otoferlin, which plays a critical role in human and rodent hearing, is thought to serve as a  $\text{Ca}^{2+}$  sensor for priming and fusion of synaptic vesicles (Pangrsic et al., 2010; Roux et al., 2006; Vogl et al., 2015). Furthermore, synaptic transmission in IHCs is only fulfilled by L-type  $\text{Ca}^{2+}$  channels, whereas it is mediated in other cells by the combined activity of different voltage gated  $\text{Ca}^{2+}$  channels like R-, P/Q- and N-type  $\text{Ca}^{2+}$  channels (Brandt et al., 2005, 2003; Dunlap et al., 1995; Midorikawa et al., 2014; Mintz et al., 1995; Reid et al., 2003; Wong et al., 2014).

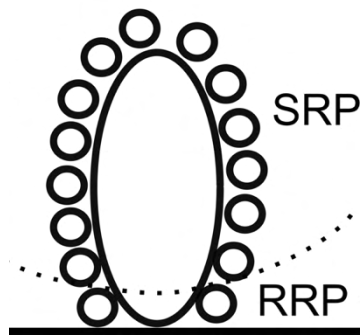


**Figure 3 Schematic of the readily releasable pool and the secondary releasable pool.** Ellipse: synaptic ribbon. Circles: synaptic vesicles. Solid line: cell membrane. Dotted line: a putative boundary between RRP and SRP.

Compensating for the high rates of exocytosis and replenishing vesicle pools require efficient endocytosis. Endocytosis in IHCs can be functionally divided into at least two phases: A slow linear phase is recruited upon moderate activation of IHCs; a fast-exponential phase appears upon intense stimulation of IHCs (Jung et al., 2015; Michalski et al., 2017; Neef et al., 2014). These two phases might represent clathrin-mediated endocytosis (CME), in which individual synaptic vesicles are retrieved from the membrane by the formation of a clathrin coat, and bulk endocytosis, in which large membrane pieces are retrieved upon high-intensity stimulation, respectively (Clayton and Cousin, 2009; Neef et al., 2014). In addition to clathrin, several endocytic proteins are expressed and presumably involved in endocytosis of IHCs, such as, dynamin (Neef et al., 2014), amphiphysin (McMahon and Boucrot, 2011), synaptojanin (Trapani et al., 2009), ap-180 (Kroll et al., 2020), and endophilin-A (Kroll et al., 2019). Specifically, dynamin mediates membrane fission for vesicle formation and possibly regulates endocytosis indirectly by regulating the actin cytoskeleton (Boumil et al., 2010; Gu et al., 2010; Neef et al., 2014), ap-180 takes part in clathrin recruitment and clearance of exocytosed material (Kroll et al., 2020), and endophilin-A recruits dynamin and facilitates membrane bending for pit formation (Kroll et al., 2019; Sundborger and Hinshaw, 2014; Zhang et al., 2022). As a crucial component of the exocytosis machinery in IHCs, otoferlin also interacts with ap-2, a part of the clathrin coat, and is involved in vesicle priming, control of the topographical development of active zones and vesicle pool replenishment (Heidrych et al., 2009; Jung et al., 2015; Pangrsic et al., 2010). Exocytosis and endocytosis are closely coupled in IHCs. This coupling is presumably mediated by the presynaptic  $Ca^{2+}$  signal, which is required for both exocytosis and endocytosis possibly via otoferlin (Beutner et al., 2001; Duncker et al., 2013). Unlike IHCs, mature OHCs seem to have barely synaptic release but possess activity-independent endocytosis at the apex, presumably required for protein degradation and indirect protein sorting (Griesinger et al., 2004; Kaneko et al., 2006).

Exocytosis and endocytosis can be indirectly studied by recording changes in their membrane capacitance ( $C_m$ ): The cell membrane is a lipid bilayer that has the characteristics of a capacitor, with an estimated specific  $C_m$  value of  $0.9 \mu\text{F}/\text{cm}^2$  for neurons (Gentet et al., 2000). Fusion of vesicles to the membrane causes an increase in membrane area and hence a corresponding increase in  $C_m$  by a factor of around 37 aF per vesicle (Lenzi et al., 1999), or of 48 aF and 45 aF specifically for immature and mature IHCs (Neef et al., 2007), respectively; conversely, the retrieval of a fraction from the membrane causes a decline in membrane area and in  $C_m$ . Using the patch clamp technique, a voltage sinusoid, which is small enough causing no opening of ion channels, is applied to the cell, whose resulting sinusoidal current is analyzed to gain the cell resistance ( $R$ ) and  $C_m$  (Gillis, 1995). An Optopatch patch clamp amplifier (Cairn Research Ltd., UK), which employs a so-called 'track-in' mode by integrating a self-balancing lock-in amplifier into the circuit, allows measurement of real-time changes in  $R$  and  $C_m$  (Johnson et al., 2002).

#### **1.4 Development of the organ of Corti in rodents**

Differentiation of HCs begins at around E13 at the mid-basal cochlear turn and propagates towards the apex and base in approximately four days (Basch et al., 2016; Chen et al., 2002). At E19, the pattern of one row of IHCs and three rows of OHCs emerges throughout the entire cochlea (Basch et al., 2016). Afferents of both SGN types extend to HCs and are pruned between E18 and around P6, after which only type I SGN afferents innervate IHCs and only type II SGN afferents innervate OHCs (Huang et al., 2007). Each type I SGN contacts only one IHC, whereas each type II SGN contacts up to 100 OHCs (Liberman and Liberman, 2016; Simmons and Liberman, 1988). Specifically, each IHC is innervated by 10 to 20 type I SGNs (Eybalin, 1993).

HCs undergo terminal differentiation prior to the onset of hearing (P12 in most rodents) (Ehret, 1983), which involves many morphological and physiological changes such as up- and down-regulation of various ion channels.

In OHCs, the  $\text{Ca}^{2+}$  current ( $I_{\text{Ca}}$ ) that appears before birth, spontaneous  $\text{Ca}^{2+}$ -dependent action potentials (APs) and corresponding synaptic exocytosis that appear after birth obtain their peaks during the first week of postnatal development (Beurg et al., 2008; Jeng et al., 2020). After the first postnatal week,  $I_{\text{Ca}}$  and the number of synaptic ribbons are downregulated along with little remaining exocytosis, whose function is still under debate (Ceriani et al., 2019; Huang et al., 2012; Michna et al., 2003). Eventually, a motor protein called prestin began to be expressed in the lateral membrane of OHCs, leading to their electromotile activity, and this

activity becomes functionally mature at around P8 (Abe et al., 2007; Liberman et al., 2002). Expression of the negatively activated  $K^+$  channel KCNQ4, which is crucial for keeping the resting membrane potential of OHCs for optimal activation of prestin (Johnson et al., 2011), starts at P8 (Marcotti and Kros, 1999).

Maturation of IHCs differs from that of OHCs. Synaptic ribbon precursors and membrane-anchored ribbons fuse to generate single ribbons starting at around P7 in the IHCs (Michanski et al., 2019). As they fuse, ribbons enlarge from their original small, round shape to a large, elongated form in mature IHCs, to which more but smaller synaptic vesicles are attached (Michanski et al., 2019; Sobkowicz et al., 1982; Wong et al., 2014). As result of the interplay between depolarizing  $Ca_v1.3$  channels and repolarizing  $K^+$  channels, spontaneous APs of pre-mature IHCs drive maturation of IHCs themselves and the auditory pathway (Johnson et al., 2013; Shrestha et al., 2018), starting at E16.5 (Brandt et al., 2003; Marcotti et al., 2003a, 2003b). At the onset of hearing around P12, a time when IHCs reach functional maturity, ribbons gain the mature status and spontaneous APs are switched to the graded receptor potentials by upregulation of KCNQ4 and BK channels, a rapid-activated large conductance  $Ca^{2+}$ - and voltage-dependent  $K^+$  channel (Kros et al., 1998; Marcotti et al., 2003a, 2004a; Michanski et al., 2019; Oliver et al., 2003). The number of  $Ca_v1.3$  channels and the corresponding  $I_{Ca}$  amplitude peak at around P6 and decline thereafter until P12, when only the presynaptic  $Ca_v1.3$  channels remain and the  $I_{Ca}$  amplitude reaches a steady state with much faster kinetics and weaker inactivation (Beutner and Moser, 2001; Johnson et al., 2005; Johnson and Marcotti, 2008; Oliver et al., 2003; Wong et al., 2014). Moreover, the  $Ca_v1.3$  channel clusters located under ribbons change from a dot-like during development to a stripe-like shape after maturation, leading to tighter coupling between  $Ca^{2+}$  channels and synaptic vesicles (Wong et al., 2014; Zampini et al., 2010). Owing to this coupling in mature IHCs, despite the smaller  $Ca^{2+}$  influx, exocytosis retains its amount compared to that in the pre-mature cells, implying an increased release efficiency of synaptic vesicles (Beutner et al., 2001; Johnson et al., 2005). Together with the higher efficiency, exocytosis displays a linear  $Ca^{2+}$  dependence upon maturation, whereas it is non-linear in the pre-mature IHCs (Johnson et al., 2005).

### **1.5 Objectives of the study**

Exocytosis in IHCs undergoes developmental changes, e.g. in its  $Ca^{2+}$  dependence and the expression profile of synaptic proteins. In contrast, little is known about the endocytic machinery and its developmental changes in IHCs. So far, several endocytic proteins are found to be developmentally regulated in IHCs: e.g. more ap-2 is present in mature IHCs (Duncker et al., 2013); and otoferlin in IHCs is upregulated until P6 and stays unchanged thereafter

(Roux et al., 2006). In light of these findings, I assumed that during terminal differentiation of IHCs, endocytosis also undergoes changes in kinetics and molecular composition.

In this thesis, I aimed to gain a deeper understanding of the endocytic machinery in IHCs in order to answer the following questions:

- 1) Which endocytic proteins are present in pre-mature and mature IHCs?
- 2) Are there developmental changes in the transcription, translation and localization of endocytic proteins in IHCs?
- 3) What are the functions of endocytic proteins in IHCs?
- 4) Are there developmental changes in the kinetics of endocytosis of IHCs?

The transcription profile of endocytic proteins was investigated using quantitative fluorescence *in situ* hybridization (*FISH*). This is the first study, in which the transcripts of multiple mRNA species were simultaneously visualized and subsequently quantified at the single-cell level in whole-mount OCs. Their translation profile was accessed using whole-mount immunolabeling. Considering the temperature sensitivity of endocytosis (Delvendahl et al., 2016), endocytosis was studied not only at room temperature but also at near-physiological temperature in IHCs in acutely dissected OCs via electrophysiological membrane capacitance recordings, despite the increased fragility of the tissue and the accompanying difficulty of recording at higher temperatures.

## 2 Materials and Methods

### 2.1 Ethical statement

All procedures of experiments with animals were in accordance with the European Communities Council Directive (86/609/EEC) and approved by the regional board for scientific animal experiments of Saarland, Germany.

### 2.2 Animals

NMRI mice at postnatal day (P) 2–6 (hereafter referred to as pre-mature for tissues and cells from mice at these ages) or at P13–23 (hereafter referred to as mature for tissues and cells from mice at these ages) of either sex were utilized. Animals were housed at 22°C with free access to water and food, and with a 12-h light/dark cycle. For all experiments, animals younger than P7 were sacrificed by decapitation without anesthesia, while animals older than P12 were anesthetized by inhalation of isoflurane prior to decapitation.

### 2.3 Solutions

The extracellular (**Table 1**) and intracellular (**Table 2**) solutions used in this study were prepared with purified water. Their pH was measured using a pH meter (HI 221, Hanna Instruments Deutschland GmbH, Germany) calibrated with standard solutions of pH 7.01 and 10.01 (HI70007 & HI70010, Hanna Instruments Deutschland GmbH, Germany) before each measurement. Depending on the solution, pH was adjusted with HCl (1.09057.1000, Merck KGaA, Germany) or NaOH (either 1N solution 71463-1L, Honeywell, USA, or prepared from pellets 28244.295, VWR, USA). Osmolarity was measured using an OSMOMAT 030 (Gonotec Meß- und Regeltechnik GmbH, Germany) calibrated with 300 mOsmol/kg NaCl/H<sub>2</sub>O solution (30.9.0020, Gonotec Meß- und Regeltechnik GmbH, Germany).

A perilymph-like extracellular solution (ECS) was used in immunohistochemical and fluorescent *in situ* hybridization (*FISH*) experiments of both age groups, and in electrophysiological experiments of pre-mature OCs. Another ECS containing lactobionic acid called ECS-Lactobionic, which kept the cell more viable and allowed longer recordings (Siegel et al., 2001), was used in electrophysiological experiments of mature OCs. Extracellular solutions were filtered with a sterile filter (83.1827, Sarstedt AG & Co. KG, Germany) connected to the efflux tube of a peristaltic pump (PLP 330, behr Labor-Technik GmbH, Germany) and irradiated with a UV lamp for 1h before storage at 4°C.

During electrophysiological experiments, an application solution containing TEA chloride, a non-selective K<sup>+</sup> channel blocker, and 4-AP that blocks voltage-gated potassium channels,

was locally superfused (Dietrich et al., 2021; Khodakhah et al., 1997; Smith et al., 2009). The application solution was stored at -20°C. Depending on the age group, different ion channel blockers were freshly added to the application solution: the SK2 channel blocker apamin for pre-mature OCs, and the KCNQ4 channel blocker linopirdine for mature OCs (Marcotti et al., 2004b, 2003a). 50 µM apamin stock solution and 10 mM linopirdine stock solution were prepared in DMSO, stored at -20°C, and added to the application solution on the day of the experiment.

The intracellular solution used in the patch pipette replaced the cytosol and further blocked K<sup>+</sup> influx. It was stored at -20°C after preparation. On the day of the experiment, the intracellular solution was filtered using a Minisart RC4 syringe filter (17821, Sartorius AG, Germany). Depending on the experiment, the dynamin-1/2 blocker dyngo-4a was added to the intracellular solution (McCluskey et al., 2013): 100 mM dyngo-4a stock solution was prepared in DMSO and stored in 1 µl aliquots at -80°C; on the day of the experiment, 2.3 µl DMSO was added to this stock solution and 1 µl of the resulting solution was transferred to the intracellular solution, which was then treated in an ultrasonic bath for 10 min before filtration.

**Table 1 Composition of extracellular and application solutions.**

Chemical (in mM if not specified otherwise)	ECS	ECS- Lactobionic	Application (pre-mature)	Application (mature)
CaCl <sub>2</sub>	1.3	1.3	5.0	5.0
BaCl <sub>2</sub>	-	-	-	-
Glucose•H <sub>2</sub> O	5.6	5.3	5.6	5.6
HEPES	10.0	10.0	10.0	10.0
KCl	5.8	5.8	5.8	5.8
Lactobionic acid	-	70	-	-
MgCl <sub>2</sub>	0.9	0.95	1.0	1.0
NaCl	143.0	83.0	110.0	110.0
NaH <sub>2</sub> PO <sub>4</sub> •H <sub>2</sub> O	0.9	0.7	-	-
TEA chloride	-	-	35.0	35.0
4-AP	-	-	15.0	15.0
Apamin (nM, freshly added)	-	-	~500.0	-
Linopirdine (μM, freshly added)	-	-	-	~100.0
pH	7.35	7.35	7.35	7.35
Osmolarity (mOsmol/kg)	308	320	320	320

**Table 2 Composition of intracellular solutions.**

Chemical (in mM if not specified otherwise)	Intracellular solution	Intracellular solution with dyngo-4a
L-glutamic acid	106.0	106.0
CsCl	20.0	20.0
Na <sub>2</sub> Phosphocreatine	10.0	10.0
HEPES acid	5.0	5.0
Na <sub>2</sub> ATP	5.0	5.0
MgCl <sub>2</sub>	3.0	3.0
EGTA-CsOH	1.0	1.0
GTP	0.3	0.3
Dyngo-4a ( $\mu$ M, freshly added)	-	~30.0
pH	7.28	7.28
Osmolarity (mOsmol/kg)	295	295

## 2.4 General tissue preparation

The mouse skull was divided into two parts along the sagittal axis and the brain was removed. Skull segments containing the temporal bones of neonatal animals were transferred to ice-cold ECS, where tissues and structures other than the inner ear were removed, while inner ears of adult animals were dissected directly from the temporal bone after decapitation. The inner ear was stored in ice-cold ECS (for immunohistochemistry of both pre-mature and mature OCs, and electrophysiology of pre-mature OCs) or ECS-Lactobionic (for electrophysiology of mature OCs) before further use.

## 2.5 RNAscope™ fluorescent *in situ* hybridization

Although real-time PCR is widely used to analyze gene expression because of its high sensitivity and wide dynamic range, it requires RNA extraction thereby providing no spatial information about RNA transcripts within cells (Wang et al., 2012; Wong and Medrano, 2005). In contrast, RNAscope™ *FISH* allowed us to detect single molecules of three different mRNA species at a time with high signal-to-noise ratio (Wang et al., 2012). In addition, it can be used on whole-mount OCs and allows quantification of all target mRNA content within individual HCs (Kersigo et al., 2018). RNAscope™ uses target probes containing an 18 to 25-base region complementary to the target RNA. A pair of target probes, which hybridize contiguously to the target, induces an amplification cascade. Fluorescence labeled probes eventually bind to the amplifiers, making the RNA molecule visible under a fluorescence microscope (**Fig. 4**).

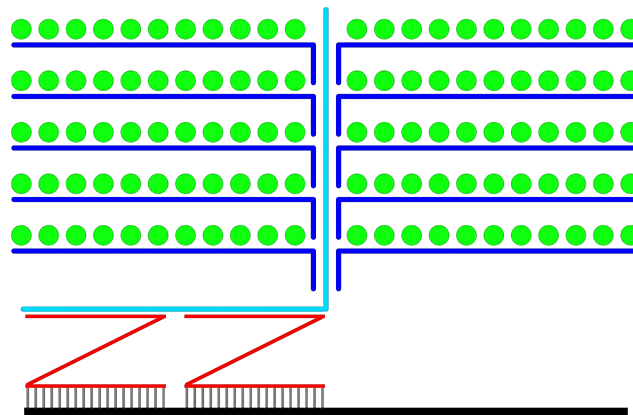


**Figure 4 Simplified principle of RNAscope™ showing bindings among involved molecules.** Black: target RNA. Red: target probe. Cyan: pre-amplifier. Blue: amplifier. Green: fluorescent labeled probe.

Experiments in this study were performed according to the guidelines from Advanced Cell Diagnostics (USA) with procedures modified from a previous study (Kersigo et al., 2018) (**Table 3**). Note that the following experimental procedure for RNAscope™ *FISH* has been published previously (Huang and Eckrich, 2021).

After dissection of the inner ear, a portion of the cochlear bone at the helicotrema was removed to allow thorough immersion of the tissue in fixative. Exclusively for mature cochlea, 1 ml 4% paraformaldehyde (PFA) in phosphate-buffered saline (PBS; 10.0 mM Na<sub>2</sub>HPO<sub>4</sub>, 2.68 mM KCl, 140.0 NaCl) was injected into the round and the oval window. Incubation steps were carried out on a shaker at room temperature (RT) unless otherwise stated. The inner ear was fixed in 4% PFA in PBS for 1 h (pre-mature) or 2 h (mature). It was washed in 0.1% Tween 20 in PBS (PBT) for 3 × 10 min and dehydrated in a 50%-75%-100%-gradient methanol (MeOH) series (in PBT, 10 min for each grade). The inner ear was stored in 100% MeOH at -20°C for up to two weeks.

On the day of the experiment the inner ear was rehydrated in a 100%-75%-50%-gradient MeOH series (in PBT, 10 min for each grade). It was washed 2 × 6 min in PBT and transferred to a petri dish containing PBT. The cartilage shell (pre-mature) or bony shell (mature) of the cochlea was carefully removed stepwise until the apical cochlear turn of the basilar membrane with the OC was exposed, and then the apical turn was disconnected from the rest part. The spiral ligament containing the stria vascularis was removed from the pre-mature basilar membrane, which was not necessary in the mature cochlea, where it was usually tightly attached to the bone and automatically separated from the basilar membrane during the process. The tectorial membrane was subsequently removed. The apical OC was transferred

to a container with a mesh at the bottom (one OC per container; modified from a cell strainer; pluriStrainer Mini 40  $\mu\text{m}$ , 43-10040, pluriSelect Life Science, Germany; **Fig. 5**). The container was placed on a 48-well plate. Up to four OCs were processed per experiment.

**Table 3 RNAscope™ fluorescence *in situ* hybridization workflow.** pre: pre-mature. mat: mature.

	Operation	Chemical	Time	Temperature
Day 1	Fixation	4% PFA in 1x PBS	2 h	RT
	Wash	PBT	3 × 10 min	RT
	Dehydration	50% MeOH in PBT	10 min	RT
	Dehydration	75% MeOH in PBT	10 min	RT
	Dehydration	100% MeOH	10 min	RT
Tissue was stored in 100% MeOH up to 3 weeks at -20 °C				
Day 2	Rehydration	100% MeOH	10 min	RT
	Rehydration	75% MeOH in PBT	10 min	RT
	Rehydration	50% MeOH in PBT	10 min	RT
	Wash	PBT	5 × 6 min	RT
	Permeabilization	Protease III	pre: 25 min mat: 12 min	RT
	Wash	PBT	5 × 3 min	RT
	Hybridization	Target probes	2 h	40 °C
	Wash	Wash buffer	8 × 5.5 min	RT
	Re-fixation	4% PFA in 1x PBS	10 min	RT
	Wash	Wash buffer	5 × 3 min	RT
	Pre-amplifier hybridization	Amp1	35 min	40 °C
	Wash	Wash buffer	8 × 5.5 min	RT
	Signal enhancement	Amp2	20 min	40 °C
	Wash	Wash buffer	8 × 5.5 min	RT
	Amplifier hybridization	Amp3	35 min	40 °C
	Wash	Wash buffer	8 × 5.5 min	RT
	Label probe hybridization	Amp4	20 min	40 °C
	Wash	Wash buffer	5 × 3 min	RT
	Nuclear staining	DAPI 1:333 in 1x PBS	1 min	RT
	Wash	PBT	3 × 1 min	RT
Mounting	FluorSave	-	RT	

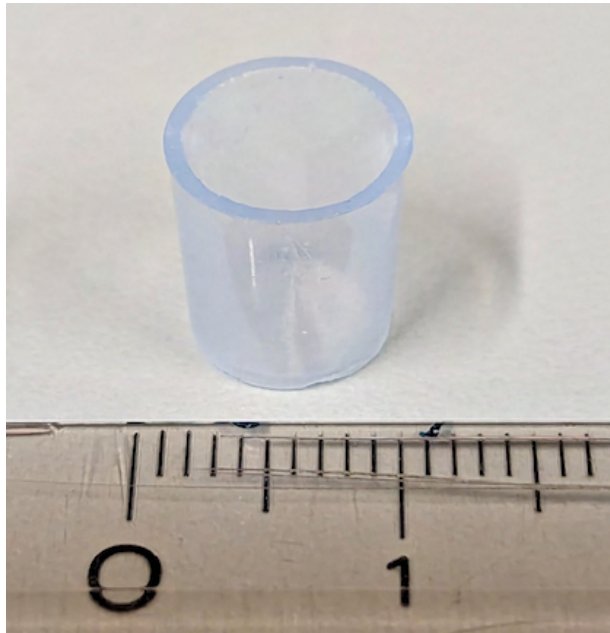


**Figure 5 Container for RNAscope™ experiment.** A ruler showing 0 to 1 cm was placed here for comparison.

Each step onward was performed by transferring these containers between wells of the well plate. Probes, amplifiers, protease and wash buffer were supplied by Advanced Cell Diagnostics (USA). Washing, protease treatment, PFA fixation and incubation with DAPI were carried out on a shaker at RT using 500  $\mu$ l solution per well unless otherwise stated. Probe hybridization and amplification steps were performed in an incubator at 40°C. For incubation at 40°C, each container was wrapped in Parafilm (Bemis Company, Inc, USA) in order to reduce the required volume of solution to 80  $\mu$ l for probes and 60  $\mu$ l for amplifiers, and the well plate was sealed by plate sealing film to avoid evaporation of solution.

Target probes for *dnm1* (detection channel-1; 446931), *dnm3* (detection channel-2; 451841-C2), and *sh3gl2* (detection channel-3; 49264-C3); positive control probes (detection channel-1 for *polr2a*, detection channel-2 for *ppib*, and detection channel-3 for *ubc*; 320881); and negative control probes (detection channel 1-3 for *dapB*; 320871) were pre-warmed to 40°C for 10 min and cooled down to RT for 10 min. The OC was washed 3  $\times$  6 min with PBT, and treated with 60  $\mu$ l Protease III (322337) for 25 min (pre-mature) or 12 min (mature) at RT. The OC was washed 5  $\times$  3 min in PBT at RT and subsequently incubated with 80  $\mu$ l probe mixture for 2 h. The OC was then washed with RNAscope™ wash buffer (310091) for 8  $\times$  5.5 min, re-fixed with 500  $\mu$ l 4 % PFA in PBS for 10 min and washed again with RNAscope™ wash buffer for 5  $\times$  3 min.

The OC was incubated with 60  $\mu$ l of amplifier 1 (Amp1; 320852) for 35 min, Amp2 (320853) for 20 min, Amp3 (320854) for 35 min and Amp4 (combination Alt-B; fluorophore: Atto550 for

detection channel-1, Alexa488 for detection channel-2 and Alexa647 for detection channel-3; 320856) for 20 min and washed between each incubation with RNAscope™ buffer for 8 × 5.5 min. After the final wash step with RNAscope™ buffer for 5 × 3 min, nuclei were stained with DAPI (1:333 in PBS) for 5 min (pre-mature) or 3 min (mature), then washed with PBT for 3 × 1 min. The OC was embedded with FluorSave (345789, Millipore, USA).

## **2.6 Immunohistochemistry**

Immunohistochemistry enables the detection and localization of proteins in tissues by binding of specific antibodies (Polak and Van Noorden, 2003; Ramos-Vara and Miller, 2014). Antigen-antibody reactions can be visualized using reporter molecules, such as fluorophores, which are either directly conjugated to the primary antibodies (PABs) or conjugated to PAB-targeting secondary antibodies (SABs) (Coons and Kaplan, 1950; Polak and Van Noorden, 2003). I used SABs, as they have higher sensitivity owing to the stronger antigen binding of unconjugated PABs, and higher signal amplification due to the binding of multiple SABs to a single PAB (Polak and Van Noorden, 2003). Like *FISH*, fluorophores were visualized with fluorescence microscopy to investigate potential changes in the cellular distribution and expression levels of endocytic proteins during terminal differentiation of the inner ear.

Tissue fixation is a crucial step in immunohistochemistry. It immobilizes the antigen, preserves tissue morphology and the antigen immunoreactivity, and facilitates staining (Berod et al., 1981; Ramos-Vara, 2005). Fixatives can be categorized into two types: Cross-linking fixatives, such as PFA, cause cross-linking of proteins with other proteins and nucleic acids, which reliably preserves the tissue integrity and morphology but may cause masking of epitopes and loss of antigenicity (Ramos-Vara, 2005; Werner et al., 2000); Coagulating (denaturing) fixatives, such as ethanol (EtOH), break the hydrogen bonds of proteins, leading to their precipitation (Howat and Wilson, 2014; Ramos-Vara, 2005; Werner et al., 2000). While coagulating fixatives preserve the antigenicity better, the tissue morphology is more fragile than that treated with cross-linking fixatives (Matsuda et al., 2011). After fixation, cells must be permeabilized with organic solvents, such as MeOH, or detergents, such as Triton X-100 (TX-100) to make intracellular antigens accessible to antibodies (Jamur and Oliver, 2010). Furthermore, the background signal can be optimized using protein blocking reagents such as serum or synthetic peptides, thereby reducing nonspecific binding of antibodies (Kim et al., 2016). Depending on antigens and antibodies, different combinations of fixatives, permeabilizing and blocking reagents were used. Note that the following experimental procedure for immunohistochemistry has been published previously (Huang and Eckrich, 2021).

To better fix the OC, a portion of the cochlear bone at the helicotrema was removed prior to fixation. For pre-mature cochleae, the inner ear was directly immersed in the fixative. For mature cochleae, 1 ml fixative was injected into the round and the oval window, before the inner ear was immersed in the fixative. For each antibody, the same type of fixative was used in both age groups with the same conditions and immersion time: either in EtOH at -20°C for 20 min, in Zamboni's fixative on ice for 5, 8 or 15 min, or in 4% PFA in PBS on ice for 8 min. After fixation, the pre-mature inner ear was washed in ice-cold PBS, while 1 ml PBS was additionally injected into the mature inner ear. The OC was dissected as described in the *FISH* section.

Procedures onwards were carried out at RT unless otherwise stated. Basilar membrane was placed individually on a microscope slide with the OC facing upward. A circular hydrophobic barrier surrounding the OC was generated using an ImmunoPen (402176, Merck KGaA, Germany). The OC was washed in PBS for 10 min, permeabilized in 0.5% Triton in PBS for 10 min. The blocking solution was prepared in PBS. Depending on the experiment, the OC was blocked either in 1% bovine serum albumin (BSA) for 30, 40 or 60 min, in 4% BSA for 30 or 60 min, in 4% BSA with 0.3% TX-100 for 60 min, in 10% BSA for 60 min, in 30% BSA for 60 min, in 10% normal goat serum (NGS) for 60 min, or in 5% NGS with 0.2% TX-100 for 2 h. PABs against target proteins were prepared in reaction buffer (0.5% BSA with 0.2% TX-100 in PBS). The OC was incubated with the PABs (**Suppl. Table 21**) overnight at 4°C or 90 min at RT before being washed with washing buffer (0.1% TX-100 in PBS) for 2 × 15 min. Fluorophore-conjugating SABs (**Suppl. Table 22**) directed against the PAB were prepared in reaction buffer and the OC was incubated with SABs for either 90 min at RT, 2 h at RT or overnight at 4°C, and subsequently washed in wash buffer for 2 × 15 min. For nuclear staining, the tissue was washed in PBS for 5 min, incubated with DAPI (1:333 in PBS) for 5 min and washed again in PBS for 3 × 1 min. Solution was removed, and the hydrophobic barrier was wiped off using cotton swabs before embedding the OC in FluorSave (345789, Millipore, USA), Vectashield (H-1000, Vector Laboratories, Inc., USA) or Prolong (P36982, Thermo Fisher (Kandel) GmbH, Germany). At least three repeats were performed for all immunohistochemical experiments (for details of all tested PAB/SAB combinations, fixation, blocking and incubation conditions, see **Suppl. Table 23**).

Negative controls for antibodies were tested in all immunohistochemistry experiments, but are shown only for dynamin-1 and dynamin-3. Antibody specificity was validated in negative controls in absence of the dynamin-1 and dynamin-3 antibodies, respectively. **Suppl. Fig. 2** shows the results of OCs fixed with EtOH (dynamin-1: pre-mature OC in **A-A2** and mature OC

in **B-B2**; dynamin-3: pre-mature OC in **C-C2** and mature OC in **D-D2**), while **Suppl. Fig. 3** shows the results of OCs fixed with Zamboni's fixative (pre-mature: **A-A2**; mature: **B-B2**).

## 2.7 Image acquisition

16-bit single plane overview and z-stack images of fluorescence signals from the OC were acquired with a confocal laser-scanning microscope (LSM 710, Zeiss, Germany) using a 20x objective (Plan-Apochromat 20x /0.8, Zeiss, Germany; only for immunohistochemistry) and a 63x objective (Plan-Apochromat 63x /1.4 Oil DIC, Zeiss, Germany; for RNAscope™ *FISH* and immunohistochemistry), respectively. Z-stack images had a pixel size of 0.07 μm and the interslice interval was 0.32 μm. The resulting images were analyzed in Fiji (Schindelin et al., 2012), where maximum intensity Z-axis projections (MIZP) were created using the “Z Project” function, and maximum intensity X-axis projections (MIXP) were created using the “Reslice” function followed by a Z-Projection. For RNAscope™ *FISH*, areas containing whole cell bodies of ten IHCs and the adjacent three rows of OHCs were captured in z-stack images, and at least five images were made for each animal.

## 2.8 Quantification of RNAscope™ fluorescent *in situ* hybridization data

Quantification of fluorescence-labeled mRNA molecules was conducted separately for IHCs and OHCs using Fiji. Maximum intensity projections were generated from the z-stack images and split into separate images. Each of them containing signals of one single detection channel, which were analyzed individually. The background was treated using the rolling ball background subtraction with a radius between 2 and 9 pixels. Based on the intensity of images, the lower threshold was set between 6000 and 10000, while the upper threshold was set at 65535. Images were converted to 8-bit images and underwent watershed segmentation, followed by “Analyze Particles” with minimum and maximum sizes set to 0.02-0.03 μm<sup>2</sup> and 0.3 μm<sup>2</sup>, respectively. The number of particles contained in each image was divided by the number of cells (ten for IHCs and ~30 for OHCs) to obtain the average number per cell. Data of the target mRNAs were normalized by subtracting the median number of the negative controls for the respective detection channels and respective experiment from the number of the target mRNA particles.

## 2.9 Electrophysiology

The processing and transmission of information in cells rely on electrical signals mediated by ion channels that can be recorded by electrophysiological methods, such as patch clamp. In patch clamp, an electrical seal, whose resistance can reach > 1 GΩ, is generated between a pipette filled with electrolyte solution and the cell membrane. The seal isolates the patch from the environment thereby ensuring high fidelity of the recorded current and reduction of noise

(Sakmann and Neher, 1984). In this study, the whole-cell patch configuration with the voltage clamp mode was utilized to measure  $\text{Ca}^{2+}$  currents ( $I_{\text{Ca}}$ ) and membrane capacitance ( $C_m$ ). In the whole-cell configuration, the membrane patch is ruptured so that the cytoplasm is electrically connected with the pipette (intracellular) solution, and the intracellular composition is considered controlled by the solution in the pipette due to the small cell volume compared to the pipette (Molleman, 2003). In the voltage clamp mode, the membrane potential is controlled by the amplifier. Upon changes in the potential, a compensatory current representing the ionic current across the membrane in the opposite direction is injected into the cell through the pipette and recorded by the amplifier (Molleman, 2003).

### 2.9.1 Patch clamp setup

The acutely dissected OC was transferred to a homemade bath chamber and immobilized with nylon threads supported by a piece of metal (**Fig. 6**). The experiment chamber was placed on the stage of an upright microscope (Axioscope, Carl Zeiss AG, Germany) and observed using a 63x objective (Achromplan 63x/0.90 W, Carl Zeiss AG, Germany). A camera (B FWCAM X M, The Imaging Source Europe GmbH, Germany) was connected to the microscope, allowing the display of the image on a monitor. To reduce the effect of mechanical vibrations on the recording, the microscope and micromanipulators were fixed on an anti-vibration table (VH-3036-OPT, Newport Spectra-Physics GmbH, USA), which was equipped with a Faraday cage surrounding the setup to shield the interior from ambient electrical noise. The OC was superfused with ECS or ECS-Lactobionic through a tube connected to the bath chamber throughout the experiment. Influx and efflux of the solution were driven by a tubing pump (ISM940E, Cole-Parmer GmbH, Germany). The solution was filtered with a Minisart RC15 syringe filter (17761, Sartorius AG, Germany) connected to the influx tube. For experiments performed near body temperature (BT), the superfused solution was preheated to 40°C by a heater surrounding the influx tube before entering the experimental chamber. The bath chamber was kept at approximately 37°C via its indium-tin-oxide (ITO)-coated glass bottom, which generates heat when voltage is applied. Both heating components were controlled by a temperature controller (TC-20, npi electronic GmbH, Germany). The pipette holder (640825, Warner Instruments, LLC, USA) for the cleaning pipette was mounted on a manual micromanipulator (MP85-1120, Sutter Instrument Co., USA). The cleaning pipette was connected to a syringe filled with ECS or ECS-Lactobionic, with which negative and positive pressure were generated to remove cells surrounding the target cells. During the recording, the OC was superfused locally by a gravity-fed application system that enabled fast exchange of superfusion solution. This perfusion system was composed of two 10-ml syringes, one containing ECS or ECS-Lactobionic and another containing the application solution (see section **Solutions**). Both syringes were controlled by three-way valves and connected by

tubing to the application pipette, which was mounted on an electronic micromanipulator (MCL-3, Bachofer GmbH & Co. KG Laboratoriumsgeräte, Germany) and placed in close vicinity of the OC. The patch pipette was inserted into a pipette holder (640825, Warner Instruments, LLC, USA) connected to the head stage of the patch-clamp amplifier, and the pipette holder was mounted on an electronic micromanipulator (PatchStar Micromanipulator, Scientifica Ltd., UK; see **Fig. 7-8** for more details on the patch clamp setup). All recordings were performed using an Optopatch patch clamp amplifier (Cairn Research Ltd., UK), whose track-in mode allows measurement of real-time changes in membrane capacitance ( $\Delta C_m$ ) as a measure of exocytosis and endocytosis, under the control of the PatchMaster software (HEKA Elektronik GmbH, Germany).

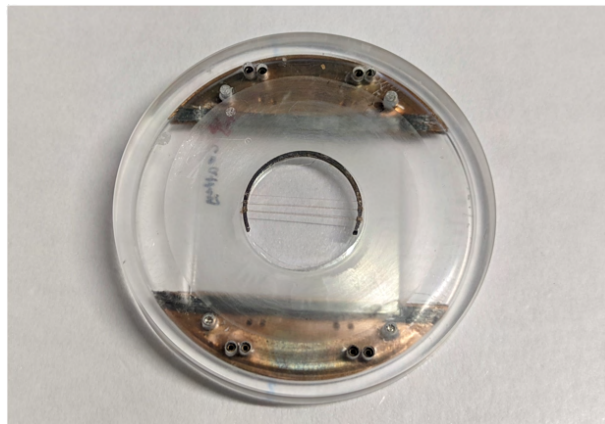


**Figure 6 Bath chamber with an immobilizing grid for patch clamp.** Nylon threads were fixed on a piece of metal using superglue to form the immobilizing tool.

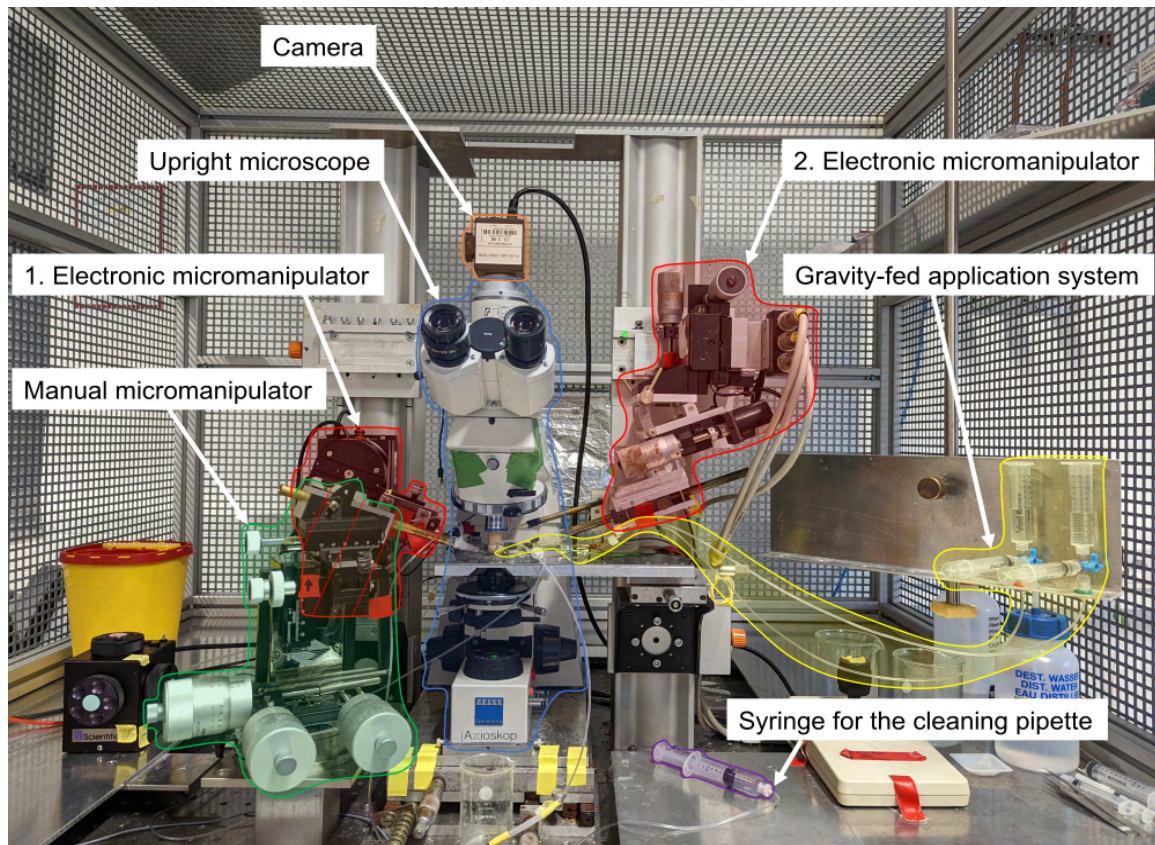


**Figure 7 Part of the patch clamp setup.** The microscope and micromanipulators with pipette holders were placed on an anti-vibration table covered by a Faraday cage. Important components were labeled. Areas of different colors indicate the corresponding components, respectively. The patch pipette, application pipette and cleaning pipette were attached to the 1st electronic micromanipulator, 2nd electronic micromanipulator and manual micromanipulator, respectively.

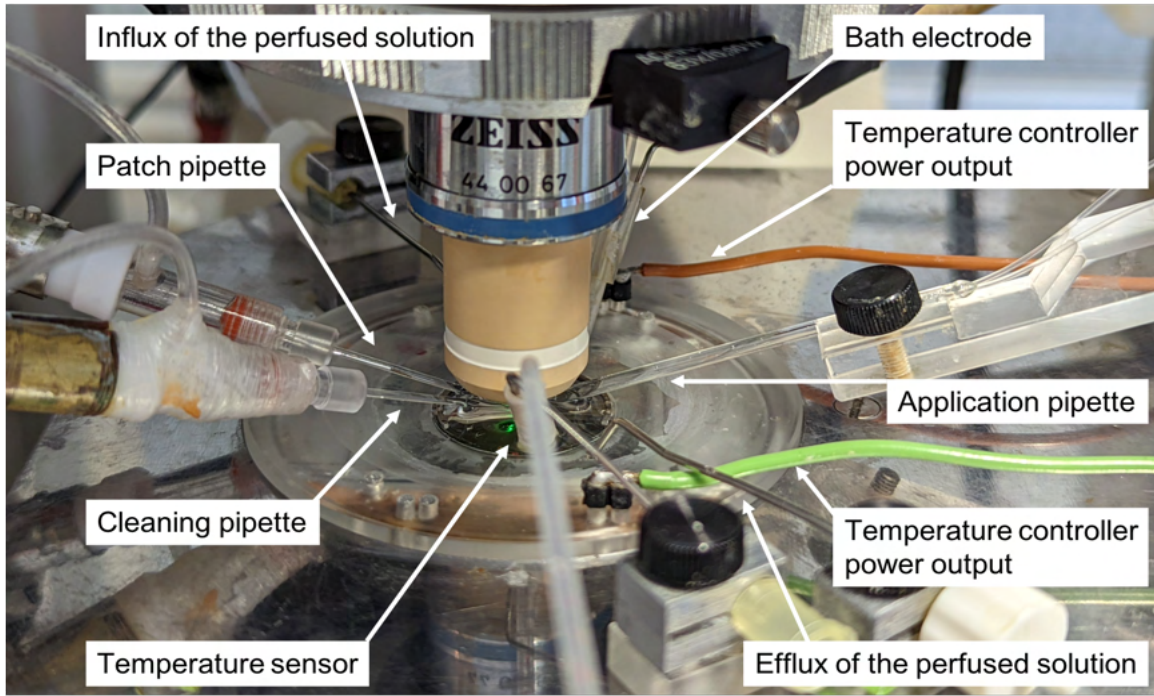


Figure 8 Close-up of patch clamp set-up components in vicinity of the bath chamber.

## 2.9.2 Pipettes

Patch pipettes and cleaning pipettes were prepared on the day of the experiment. Quartz glass capillaries (Q100-50-7.5, Sutter Instrument, USA) were used to produce patch pipettes on a laser-based micropipette puller (P-2000, Sutter Instrument, USA). Borosilicate glass capillaries (GB100T-8P, Science Products, Germany) and theta borosilicate glass capillaries with an internal septum (1401021, Hilgenberg GmbH, Germany) were used to produce cleaning and application pipettes on a DMZ-universal puller (Zeitz-Instrumente Vertriebs GmbH, Germany), respectively.

## 2.9.3 Patch clamp workflow

The OC was acutely dissected in ice-cold ECS as described above in the *FISH* section and placed in the recording chamber. To gain access to the target cell, adjacent supporting cells were partially removed using the cleaning pipette. Bath solution (ECS or ECS-Lactobionic) was applied through the application pipette when the patch pipette was near the target cell. Once the seal between the cell and the patch pipette was established, the bath superfusion via the application pipette was turned off and the local application was turned on simultaneously, which reduced mechanical interference, when changing the flowing solution of the application pipette.

For  $C_m$  recordings, IHCs were held at a holding potential of -80 mV and a sine wave with a frequency of 4 kHz and an amplitude of 13 mV was applied. This very negative holding potential was chosen to avoid opening of  $Ca^{2+}$  channels due to the sine wave (**Fig. 9**). To trigger maximum exocytosis and compensatory endocytosis, cells were depolarized to the voltage of maximum  $I_{Ca}$ , which was determined to be approximately 0 mV in pre-recordings (**Fig. 9**). This allowed us to neglect the liquid junction potential in the present study. In some cases, only  $I_{Ca}$  was recorded (see below): the seal test protocol, pre-recording, and 50-ms, 100-ms and 1-s reference protocols. For endocytosis-relevant protocols,  $\Delta C_m$ ,  $I_{Ca}$ , and the series resistance ( $R_s$ ) were recorded. The recorded capacitance signal was amplified 10 – 50× depending on the protocol, filtered at 500 Hz, and sampled at 1 kHz. The current signal was filtered at 10 kHz and sampled at 100 kHz, unless otherwise specified.

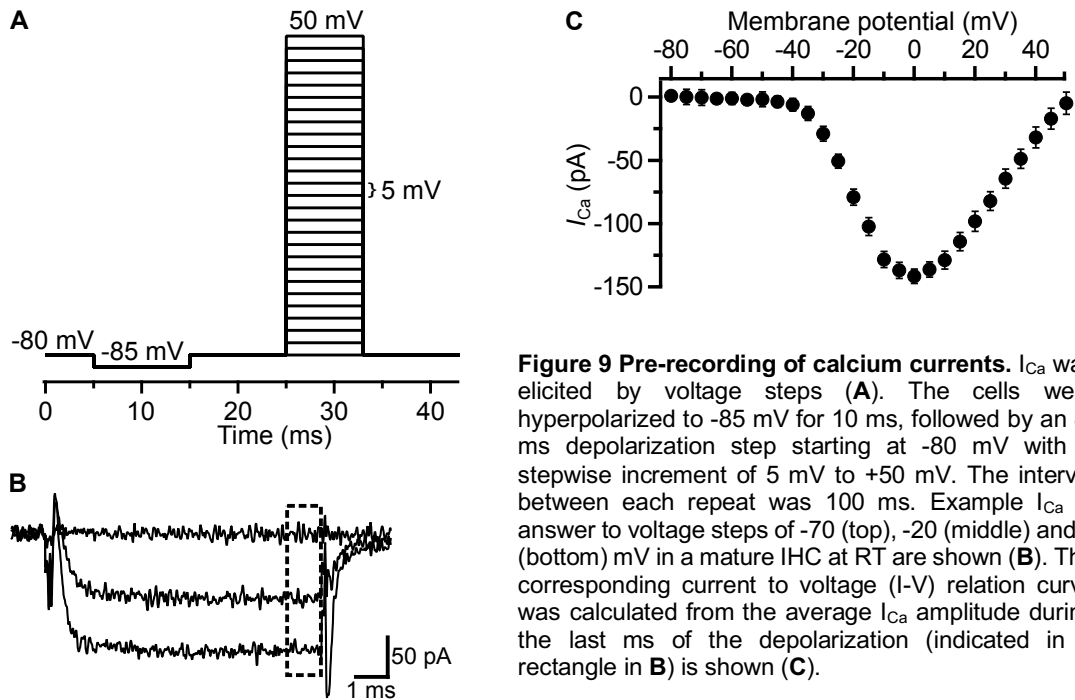


**Figure 9 Pre-recording of calcium currents.**  $I_{Ca}$  was elicited by voltage steps (A). The cells were hyperpolarized to -85 mV for 10 ms, followed by an 8-ms depolarization step starting at -80 mV with a stepwise increment of 5 mV to +50 mV. The interval between each repeat was 100 ms. Example  $I_{Ca}$  in answer to voltage steps of -70 (top), -20 (middle) and 0 (bottom) mV in a mature IHC at RT are shown (B). The corresponding current to voltage (I-V) relation curve was calculated from the average  $I_{Ca}$  amplitude during the last ms of the depolarization (indicated in a rectangle in B) is shown (C).

#### 2.9.4 Patch clamp protocols and data analysis

Data recorded by PatchMaster were processed using Igor Pro (WaveMetrics, Inc., USA). Cells were excluded if  $R_s$  was greater than 15 M $\Omega$  or changed more than 1.5 M $\Omega$  during recording, or if the leak resistance ( $R_{leak}$ ) was below 500 M $\Omega$ . Average  $R_s$  in all experiments ranged from 6.2 to 7.1 M $\Omega$ , and average  $R_{leak}$  ranged from 920 to 1132 M $\Omega$ . Average  $C_m$  of pre-mature IHCs was  $7.2 \pm 0.7$  pF ( $n = 117$ ), and that of mature IHCs was  $8.8 \pm 0.8$  pF ( $n = 79$ ).

1) Seal test protocol. This protocol elicited a capacitive transient, which allowed determination of  $R_{leak}$ ,  $R_s$  and  $C_m$  of each cell.  $R_s$  and  $C_m$  were not compensated in this protocol. The cell was repeatedly (20 times) stimulated by a 5-ms hyperpolarization to -90 mV (Fig. 10), and  $I_{Ca}$  was recorded.  $C_m$ ,  $R_s$ , and the time constant  $\tau$  were determined according to previous studies (Huang and Santos-Sacchi, 1993; Oliver and Fakler, 1999).

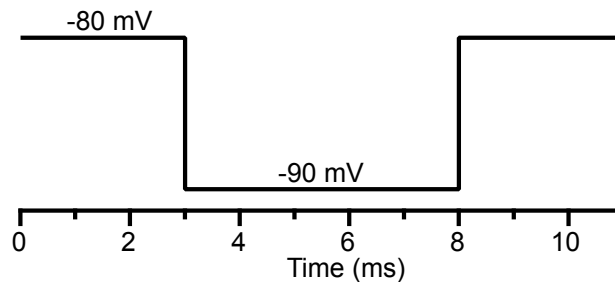


**Figure 10 Seal test protocol.** The cell was hyperpolarized for 5 ms from a holding potential of -80 mV to -90 mV. The command was repeated 20 times with no interval.

The seal test protocol was run before and after each single pulse protocol, reference recording, 50-ms short-term repetitive protocol, and 1-s long-term repetitive protocol (see below) to obtain two  $R_{leak}$  values, the average of which was used as the  $R_{leak}$  for the respective protocol and corrected in the analysis of  $I_{Ca}$ .

2) Single pulse protocol and reference recording: The single pulse protocol was used to measure compensatory endocytosis of IHCs for 20 s, following exocytosis evoked by a 100-ms depolarization to 0 mV. The reference recording was used to monitor the stimulus-independent decline of  $\Delta C_m$  as previously described (Neef et al., 2014) and was identical to the single pulse protocol, but no depolarizing stimulus was applied (**Fig. 11**).

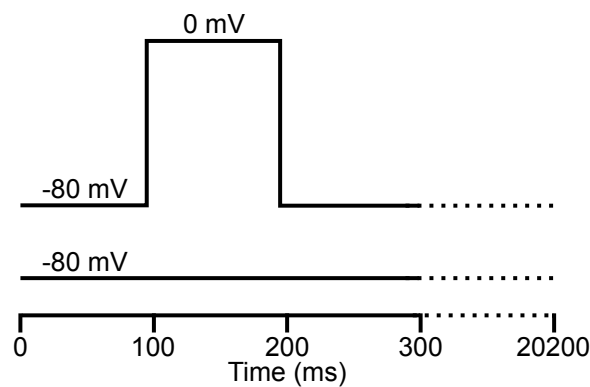


**Figure 11 Single pulse protocol and reference recording.** Single pulse protocol (top): The cell was kept at a holding potential of -80 for 95 ms, depolarized to 0 mV for 100 ms, and again kept at -80 mV for 20 s. Reference recording (bottom): The cell was constantly held at -80 mV for the duration of the single pulse protocol.

For the single pulse protocol,  $\Delta C_m$  was recorded before and after the stimulus, while  $I_{Ca}$  was recorded during the stimulus. The average  $\Delta C_m$  before the stimulus (from 0 to 50 ms) was subtracted from the  $\Delta C_m$  averaged between 25 – 75 ms after the end of the stimulus to obtain the amplitude of the stimulus-induced increase in  $\Delta C_m$ , reflecting exocytosis. The  $\Delta C_m$  trace underwent smoothing (algorithm: box; points: 50; end effects: bounce). Subsequently, “time to 0”, i.e. the time between the end of the stimulus and the time point when  $\Delta C_m$  returned to the baseline at 0 fF (the endpoint of stimulus-dependent endocytosis), was determined as the duration of compensatory endocytosis. The decline rate of  $\Delta C_m$  was calculated by dividing the amplitude of exocytosis by the time to 0. Calcium charge ( $Q_{Ca}$ ) was calculated by integrating the  $I_{Ca}$  elicited during the depolarizing stimulus.

For both the single pulse protocol and the reference recording, the stimulus-independent decline of  $\Delta C_m$  was calculated by fitting the following linear function to the last 8 s of the single pulse recording protocol and to the entire reference recording (**Equation 1**):

$$y = bx + y_0$$

where  $b$  is the slope and  $y_0$  is the trace offset.

3) 50-ms short-term and 1-s long-term repetitive protocol: The 50-ms short-term repetitive protocol (**Fig. 12A**), as an indirect measure of endocytosis, tested the responses of IHCs to moderate stimulation, which has been previously suggested to trigger sustained release and replenishment of the RRP (Duncker et al., 2013; Johnson et al., 2008). The cell was depolarized to 0 mV with repetitive 50-ms voltage steps and  $\Delta C_m$  was recorded during the 100-ms interstimulus intervals. The 1-s long-term repetitive protocol (**Fig. 12B**) tested the response of IHCs to excessive stimulation, which presumably triggers sustained release and replenishment of the SRP (Duncker et al., 2013; Johnson et al., 2008). The cell was depolarized to 0 mV with repetitive 1-s voltage steps and  $\Delta C_m$  was recorded during the 200-ms interstimulus intervals.

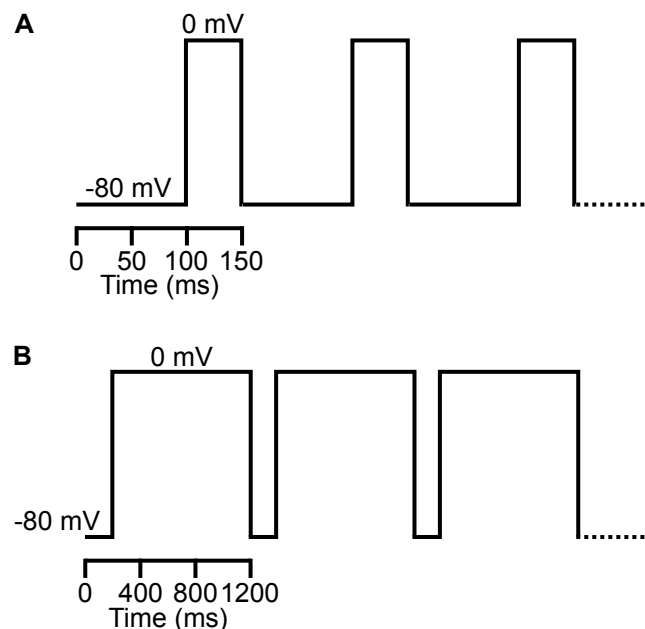


**Figure 12 50-ms short-term and 1-s long-term repetitive protocol.** 50-ms short-term repetitive protocol (**A**): The cell was kept at -80 mV for 100 ms, depolarized to 0 mV for 50 ms. 1-s long-term repetitive protocol (**B**): The cell was kept at -80 mV for 200 ms, depolarized to 0 mV for 1 s. The depolarization steps of both protocols were repeated 50 times.

The mean  $C_m$  during the 99 ms (short-term repetitive protocol) and 199 ms (long-term repetitive protocol) before each stimulus was used to calculate the cumulative  $\Delta C_m$  (i.e. the absolute increase in  $\Delta C_m$ ) and the interstep  $\Delta C_m$  (i.e. the difference of  $\Delta C_m$  between each stimulus). Depending on the traces, the cumulative  $\Delta C_m$  was fitted with either a linear function (**Equation 1**) or an exponential-linear function (**Equation 2**):

$$y = -A \cdot e^{\frac{-x}{\tau}} + bx + y_0$$

where  $A$  is the exponential amplitude,  $\tau$  is the time constant,  $b$  is the linear slope and  $y_0$  is the trace offset.

$I_{Ca}$  was recorded during depolarizations and  $Q_{Ca}$  was calculated for each stimulus by integrating  $I_{Ca}$ . Subsequently,  $Ca^{2+}$ -efficiency was determined by dividing the interstep  $\Delta C_m$  by the corresponding  $Q_{Ca}$  ( $\Delta C_m/Q_{Ca}$ ).

4) 50-ms, 100-ms and 1-s reference recording. This protocol was used to determine whether 0.1% intracellular DMSO affects  $I_{Ca}$  of IHCs (**Fig. 13**). Cells were depolarized to 0 mV for 50 ms, 100 ms and 1 s, respectively.  $R_{leak}$  was computed based on  $I_{Ca}$  during the hyperpolarization phase and corrected in the analysis of  $I_{Ca}$ . As described above,  $I_{Ca}$  was integrated to determine  $Q_{Ca}$ .

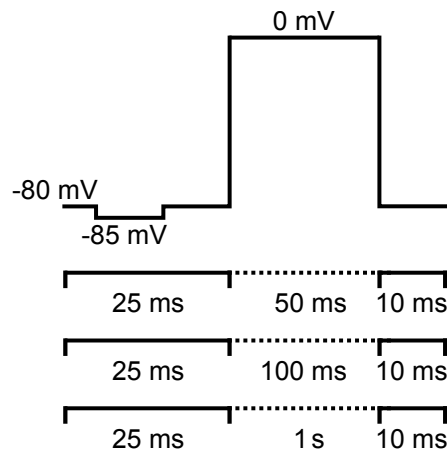


**Figure 13 50-ms, 100-ms and 1-s reference protocol.** The cell was hyperpolarized to -85 mV for 10 ms and depolarized to 0 mV for 50 ms/100 ms/1 s from a holding potential of -80mV.

## 2.10 Statistical analysis

SPSS (IBM Corp., USA) was used for all statistical analyses.

### FISH

Data containing two groups were compared using Mann–Whitney *U* test. Data containing multiple groups were compared using Friedman’s test followed by Dunn–Bonferroni *post hoc* test.

### Patch clamp

Data containing two groups were compared using Mann–Whitney *U* test. Comparisons of multiple groups were performed using Kruskal-Wallis (*K-W*) test followed by clustering of groups into homogeneous subsets according to Campbell and Skilling (1985), where groups belonging to different subsets are considered significantly different, whereas groups sharing a subset are considered not significantly different. *p*-value is given here for groups within one homogeneous subset. All groups (i.e. both age groups in all experimental conditions) were compared together unless otherwise stated.

### 3 Results

#### 3.1 Fluorescence *in situ* hybridization in the whole-mount organ of Corti

To answer the question of how the mRNA transcription profiles of endocytic proteins change during the development of HCs, I used RNAscope™ fluorescence *in situ* hybridization (*FISH*), which allows the detection and quantification of up to three different mRNA species in one tissue. An RNAscope™ *FISH* workflow suitable for the whole-mount OC was established in OCs from P4 and P20 mice by Stephanie Eckrich. Note that the following RNAscope™ *FISH* results have been published previously (Huang and Eckrich, 2021).

The quality of *FISH* was tested using positive and negative control probes. Positive probes targeted the mRNA of three housekeeping genes: weakly expressed *polr2a* (encoding RNA polymerase II subunit A), moderately expressed *ppib* (encoding peptidylprolyl isomerase B) and moderately-highly expressed *ubc* (encoding ubiquitin C), whose expression in pre-mature and mature HCs has been demonstrated in previous studies (Tiantian Cai et al., 2015; Li et al., 2018). They were assigned to detection channel-1 (visualized by Atto550), channel-2 (Alexa488), and channel-3 (Alexa647), respectively. Negative probes targeted the mRNA of a bacterial gene *dapb* (dihydrodipicolinate reductase) in all detection channels. Considering age-dependent differences in tissue morphology and structure, the duration of fixation and protease treatment varied between pre-mature and mature OCs, while the workflow was otherwise identical.

Z-projections of five IHCs and the adjacent three rows of OHCs show that in positive controls, mRNA puncta of all three housekeeping genes were evenly distributed across the OC in both age groups (**Fig. 14A-A3; Fig. 16A-A3**). X-projections of one IHC and adjacent OHCs confirm that none of the housekeeping genes was particularly enriched in pre-mature or mature HCs (**Fig. 15; Fig. 17**). In contrast, only few puncta were found in the negative controls in both age groups (**Fig. 14B-B3; Fig. 16B-B3**).

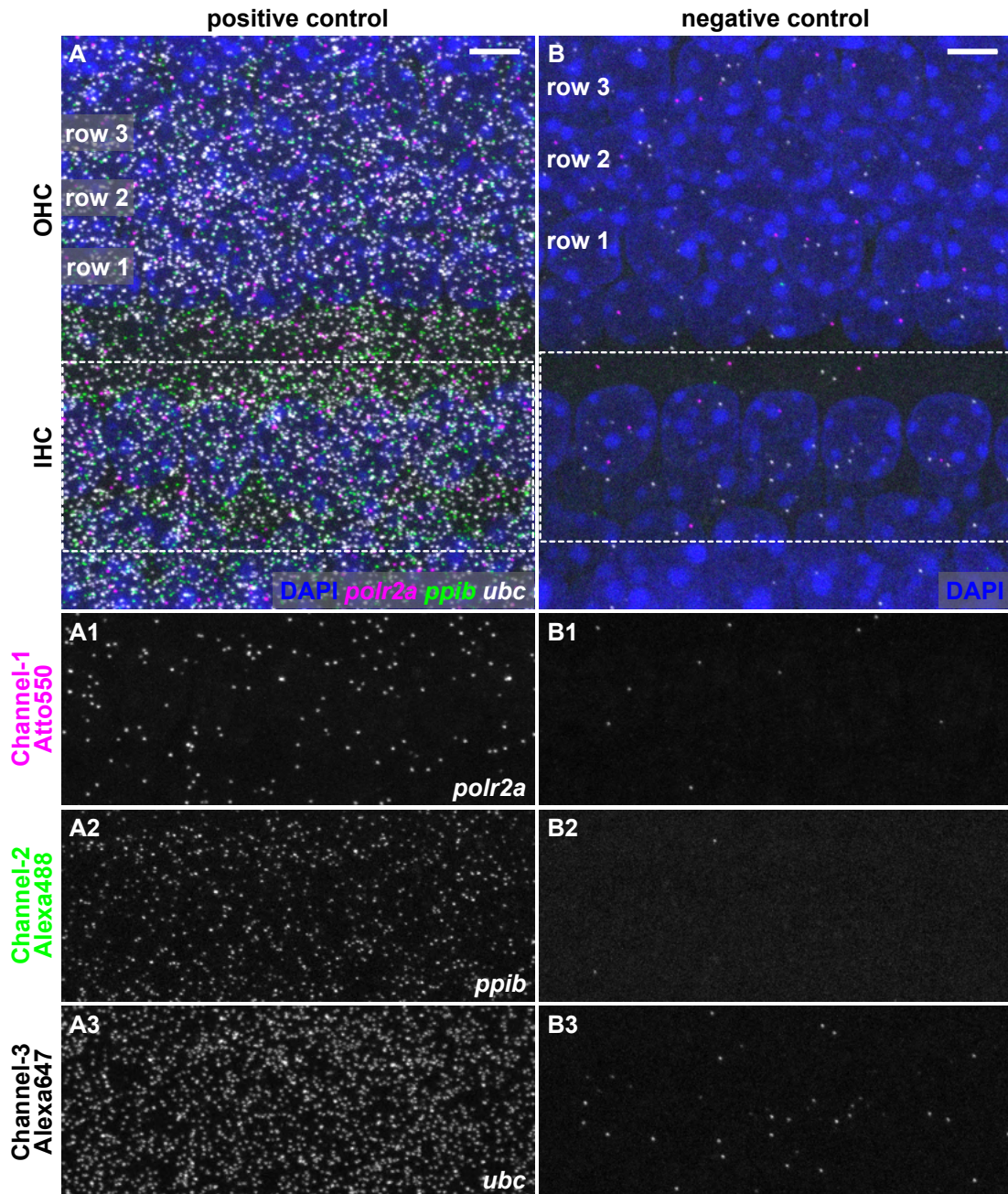


**Figure 14 RNAscope™ fluorescent *in situ* hybridization on whole-mount pre-mature organs of Corti using positive and negative control probes.** Maximum-intensity z-projections (MIZP) of *FISH* on the whole-mount apical cochlear turn of pre-mature OCs from P4 mice. Positive control probes targeting the housekeeping genes *polr2a*, *ppib*, and *ubc* were assigned to channel-1 (labeled by Atto550), channel-2 (Alexa488), and channel-3 (Atto647), respectively (**A-A3**). Negative control probes targeting the bacterial gene *dapB* were used in all detection channels (**B-B3**). Merged image of five IHCs with adjacent OHCs showing signals from channel-1, channel-2 and channel-3 in magenta, green and grayscale (**A, B**), respectively. Signals from the area of IHCs indicated by frames in **A** and **B** are shown separately according to the detection channel (**A1-3, B1-3**). Nuclei were labeled with DAPI (blue, **A, B**). Scale bars: 5  $\mu$ m.

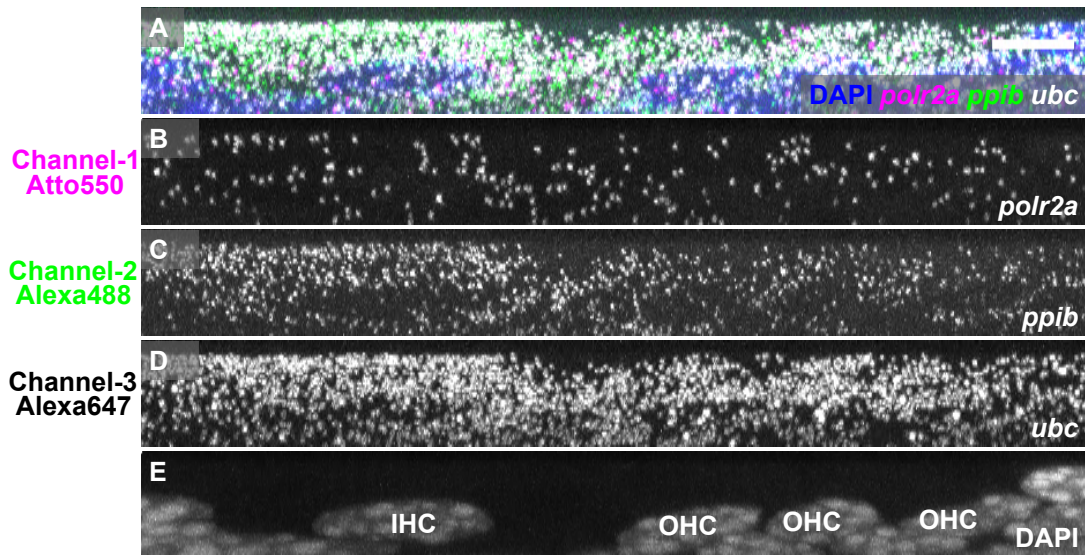


**Figure 15 X-projection of positive controls of RNAscope™ fluorescent *in situ* hybridization on the whole-mount pre-mature organ of Corti.** X-projection (MIXP) of one IHC and adjacent three OHCs (as indicated in **E**) re-sliced from positive controls shown in **Fig. 14A**. Signals from *polr2a*, *ppib*, and *ubc* are shown in the merged image as magenta, green and grayscale (**A**), respectively, or separated by detection channel (**B-D**). Nuclei were labeled with DAPI (blue in **A**; grayscale in **E**). HC types are indicated (**E**). Scale bars: 5  $\mu$ m.

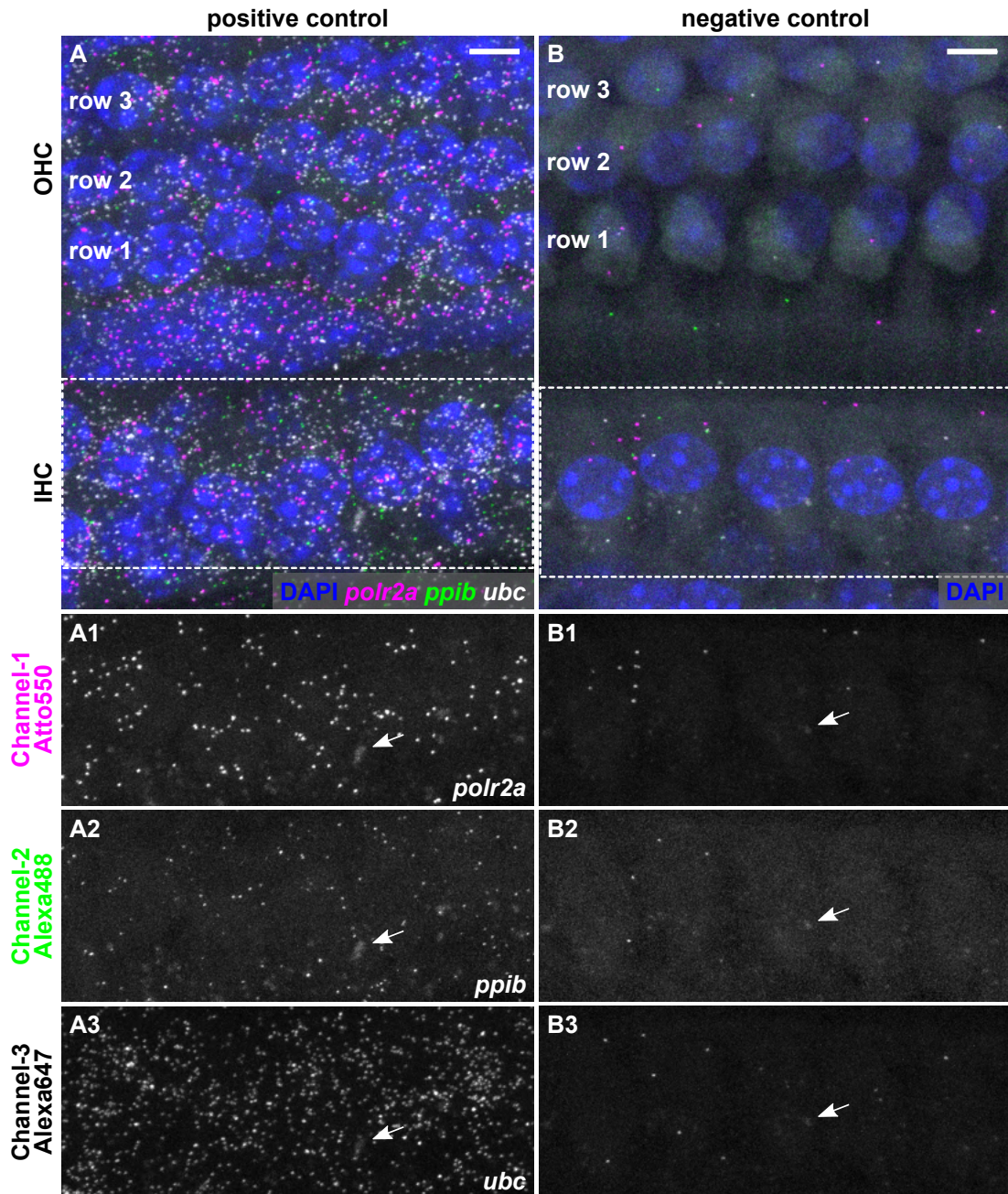


**Figure 16 RNAscope™ fluorescent *in situ* hybridization on whole-mount mature organs of Corti using positive and negative control probes.** MIZP of *FISH* on the whole-mount apical cochlear turn of mature OCs from P20 mice. Positive control probes targeted the housekeeping genes *polr2a*, *ppib*, and *ubc* (**A-A3**), and negative control probes targeted the bacterial gene *dapB* (**B-B3**). Signals in channel-1, channel-2 and channel-3 from five IHCs with the adjacent three rows of OHCs are shown in merged images as magenta, green and grayscale (**A, B**), respectively. Signals from the area of IHCs indicated by frames in **A** and **B** are shown separately according to their detection channel (**A1-3, B1-3**). Nuclei were labeled with DAPI (blue, **A, B**). Few large, uneven stains in the IHC region of mature OCs were indistinct between detection channels and groups and therefore considered non-specific (arrows). Scale bars: 5  $\mu$ m.

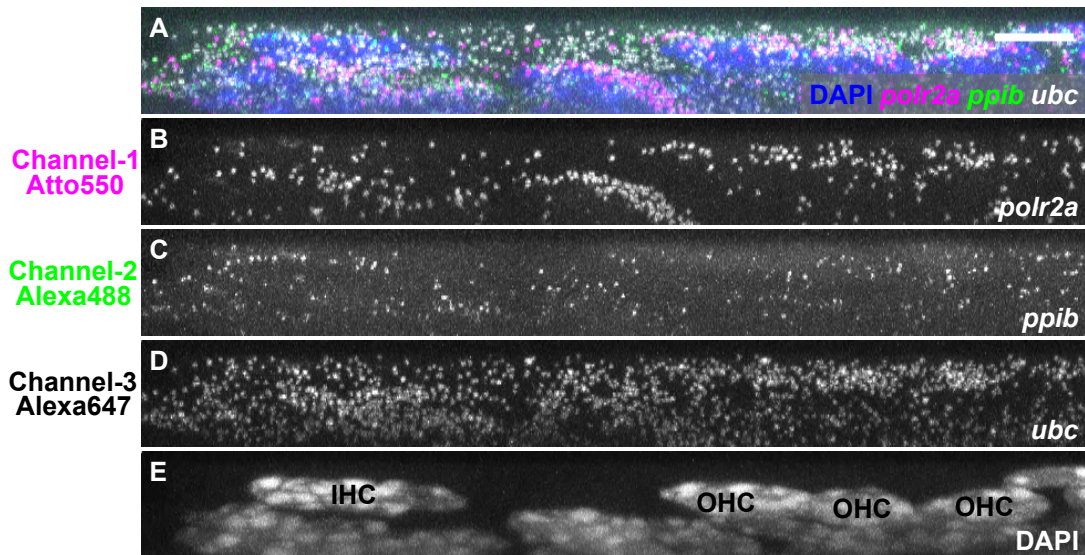


**Figure 17** X-projection of the positive control of RNAscope™ fluorescent *in situ* hybridization on the whole-mount mature organ of Corti. MIXP of one IHC and adjacent three OHCs (as indicated in **E**) re-sliced from the positive control shown in **Fig. 16A**. Signals from *polr2a*, *ppib*, and *ubc* are shown in the merged image as magenta, green and grayscale (**A**), respectively, or separated by detection channel (**B-D**). Nuclei were labeled with DAPI (blue in **A**; grayscale in **E**). HC types are indicated (**E**). Scale bar: 5  $\mu$ m.

Puncta in an area containing ten IHCs were counted and subsequently normalized to one cell (as described in **Materials and Methods**, section ‘**Quantification of fluorescence *in situ* hybridization data**’). In the positive control, the median count for *polr2a* was similar between both age groups (**Fig. 18A**; pre-mature:  $37.5 \pm 18.9$ ;  $n = 6$  images; mature:  $25.5 \pm 15.7$ ,  $n = 6$ ;  $p = 0.485$ , Mann-Whitney *U* test), whereas the number was developmentally reduced for both *ppib* (**Fig. 18B**; pre-mature:  $107.5 \pm 27.3$ ,  $n = 6$ ; mature:  $15.5 \pm 4.8$ ,  $n = 6$ ;  $p = 0.002$ , Mann-Whitney *U* test), and *ubc* (**Fig. 18C**; pre-mature:  $269.0 \pm 57.4$ ,  $n = 6$ ; mature:  $151.0 \pm 47.8$ ,  $n = 6$ ;  $p = 0.015$ , Mann-Whitney *U* test).

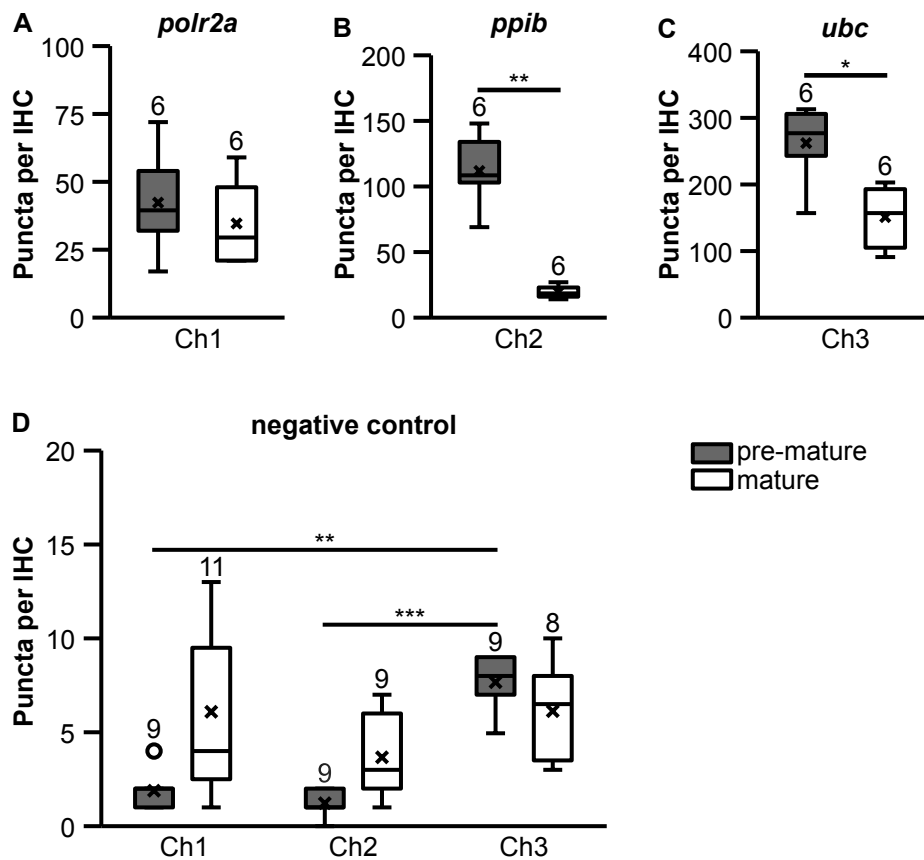


**Figure 18 Quantification of puncta in RNAscope™ fluorescent *in situ* hybridization controls.** Puncta from IHCs of both pre-mature and mature organs of Corti in RNAscope™ *FISH* controls were quantified and normalized to counts per one IHC. Transcripts of the housekeeping genes *polr2a*, *ppib*, and *ubc* were detected in both age groups (**A-C**; note the different y-axis scaling). The content of *polr2a* was similar between pre-mature and mature IHCs (**A**), whereas the content of *ppib* and *ubc* showed an age-dependent reduction (**B**, **C**). In negative controls, a low number of puncta was detected, which was comparable between age groups within the same detection channel but differed significantly between detection channels in pre-mature IHCs (**D**). Data were compared using Mann-Whitney *U* test (positive controls) or Friedman’s test with *post hoc* Dunn–Bonferroni test (negative controls). Numbers above boxes indicate the number of images analyzed with each image containing ten IHCs. \* $p < 0.05$ , \*\* $p < 0.01$ , \*\*\* $p < 0.001$ .

To assess the number of non-specific signals and to exclude possible age- or channel-dependent differences, all negative control groups (i.e. three channels and both age groups) were compared using Friedman's test with *post hoc* Dunn-Bonferroni test. The number of puncta was similar between pre-mature and mature IHCs of all detection channels (**Fig. 18D**): channel-1, pre-mature =  $2 \pm 0.9$  (n = 9); mature =  $4 \pm 4.2$  (n = 11,  $p = 0.167$ ); channel-2, pre-mature =  $1 \pm 0.7$  (n = 9), mature =  $3 \pm 2.4$  (n = 9,  $p = 0.242$ ); channel-3, pre-mature =  $8 \pm 1.3$  (n = 9), mature =  $6.5 \pm 2.6$  (n = 8,  $p = 1.000$ ). Within the pre-mature group, the number of puncta was similar between channel-1 and channel-2 ( $p = 1.000$ ), but significantly higher in channel-3 ( $p = 0.032$ , vs. channel-1;  $p < 0.001$ , vs. channel-2). Within the mature group, no difference was found among all channels ( $p = 1.000$  for channel-1 vs. channel-2, channel-1 vs. channel-3, and channel-2 vs. channel-3). Due to these differences of non-specific signals between detection channels in pre-mature IHCs, counts of the target mRNAs were hereafter never compared between different detection channels.

In summary, RNAscope™ *FISH* detected mRNA transcripts of three housekeeping genes (*polr2a*, *ppib* and *ubc*) and their developmental changes in pre-mature and mature OCs. In negative controls, the abundance of non-specific signals was generally low, but could still exaggerate the number of mRNA molecules detected – especially if only few copies of mRNA are present in a cell. Hence, the median count of negative controls was subtracted from the number of target mRNA of the corresponding detection channel in order to correct for non-specific signals.

### 3.2 Age-dependent changes of *dnm1*, *dnm3*, and *sh3gl2* mRNA transcription in inner and outer hair cells

Transcription profiles of three endocytic genes in HCs, namely dynamin1-encoding *dnm1* (Neef et al., 2014), dynamin3-encoding *dnm3* (Li et al., 2018), and endophilin-A1-encoding *sh3gl2* (Kroll et al., 2019), were studied before and after the onset of hearing using RNAscope™ *FISH*. Puncta representing mRNA molecules of all three genes were present in HCs but absent from supporting cells in both age groups (pre-mature: **Fig. 19-20**; mature: **Fig. 21-22**). This differs from positive controls, where mRNA of housekeeping genes was distributed evenly across all cell types of the OC. This enrichment allows the quantification of target mRNA in individual HCs. In the pre-mature OC, both types of HCs contained *dnm1* (**Fig. 19A-B**; **Fig. 20A-B**) and *sh3gl2* (**Fig. 19A, D**; **Fig. 20A, D**), whereas *dnm3* was mainly localized in OHCs (**Fig. 19A, C**; **Fig. 20A, D**). After maturation, *dnm1* (**Fig. 21A-B**; **Fig. 22A-B**) and *sh3gl2* (**Fig. 21A, D**; **Fig. 22A, D**) were more abundant in IHCs than OHCs, whereas *dnm3* retained its predominance in OHCs (**Fig. 21A, C**; **Fig. 22A, D**). Transcripts of all three endocytic genes were also detected in SGNs (**Suppl. Fig. 1**).

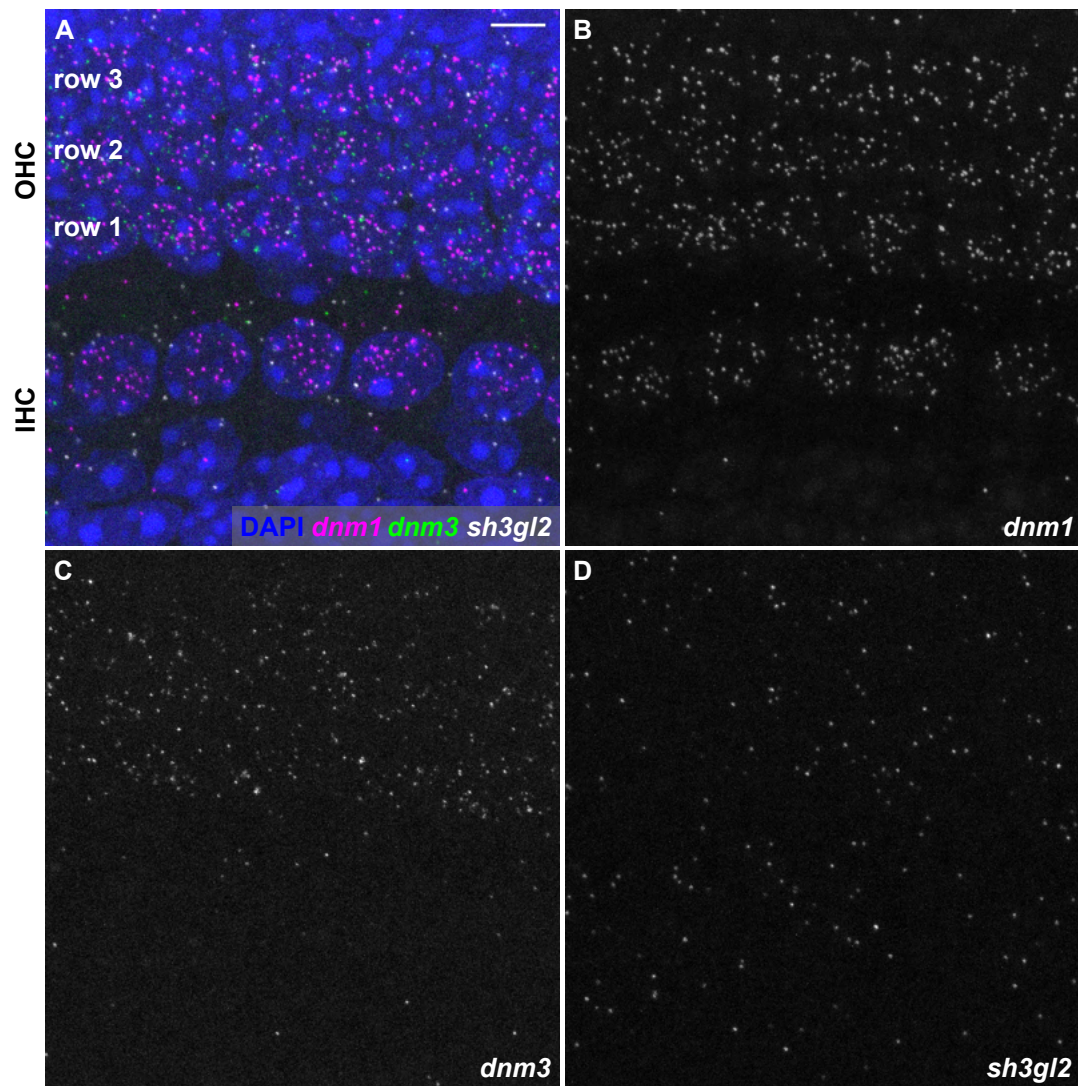


**Figure 19 Differential mRNA transcription of the endocytic genes *dnm1*, *dnm3* and *sh3gl2* in the pre-mature organ of Corti.** MIZP of FISH of the whole-mount apical turn of the pre-mature OC from a P4 mouse using probes targeting the endocytic genes *dnm1* (magenta), *dnm3* (green) and *sh3gl2* (greyscale). The resulting puncta were mostly restricted to HCs. Signals from five IHCs with the adjacent three rows of OHCs are shown in the merged image (A), or separated by target probe (B-D). *Dnm3* was mainly present in OHCs (C), whereas *dnm1* and *sh3gl2* were found in both HC types (B, D). Nuclei were labeled with DAPI (blue, A). Scale bar: 5 μm.

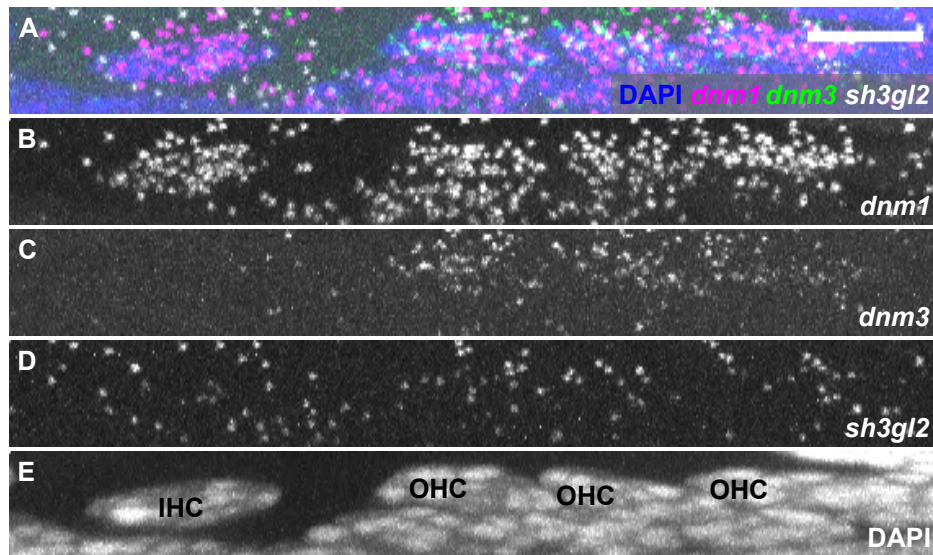


**Figure 20** X-projection of the signals of *dnm1*, *dnm3* and *sh3gl2* in the pre-mature organ of Corti. MIXP of one IHC and adjacent three OHCs (as indicated in **E**) re-sliced from the result shown in **Fig. 20A**. The signals from *dnm1*, *dnm3*, and *sh3gl2* are shown in the merged image as magenta, green and grayscale (**A**), respectively, or separated by target probe (**B-D**). Nuclei were labeled with DAPI (blue in **A**; grayscale in **E**). HC types are indicated in **E**. Scale bar: 5  $\mu\text{m}$ .

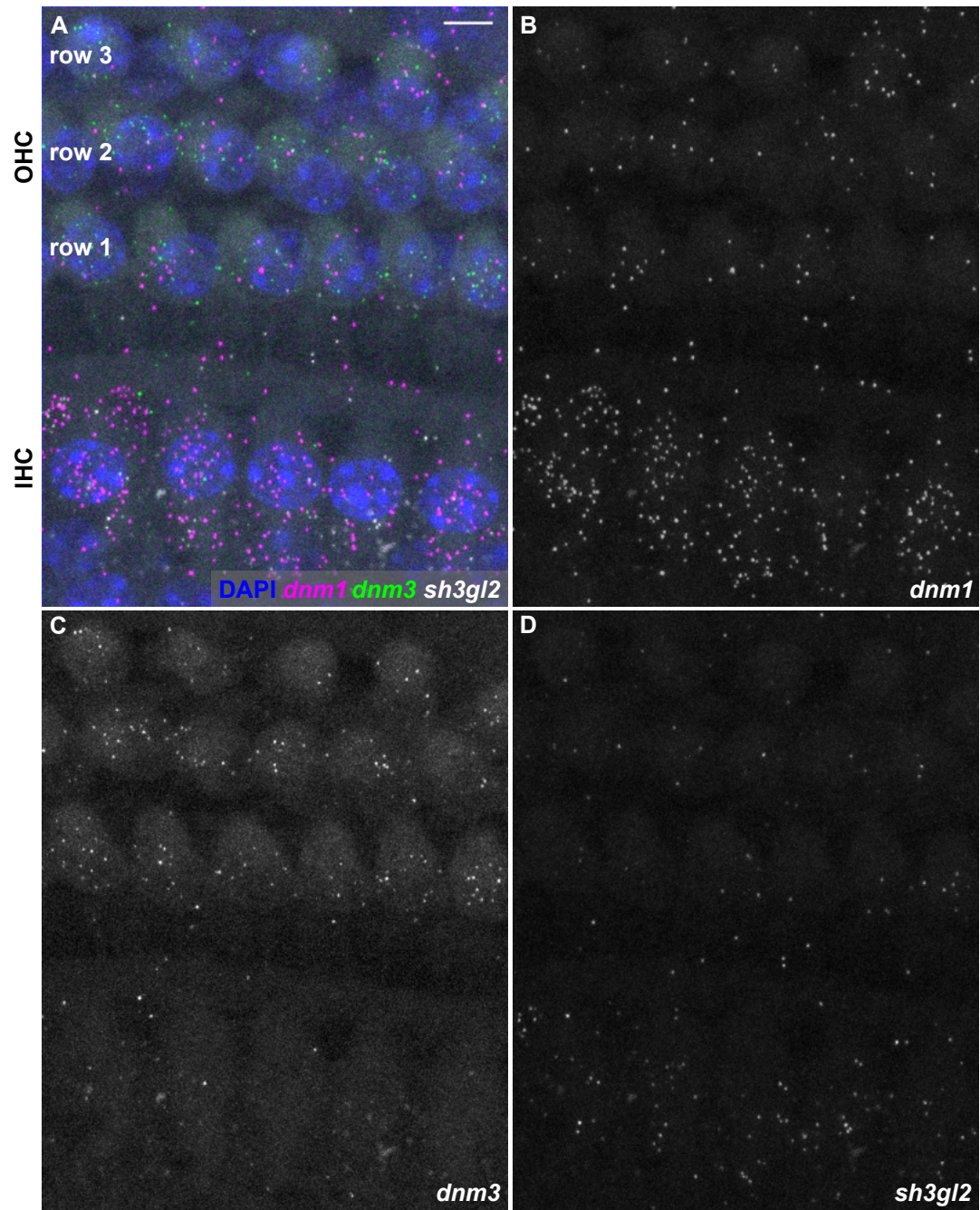


**Figure 21** Mature inner hair cells express more *dnm1* and *sh3gl2* mRNA but less *dnm3* than mature outer hair cells. MIZP of FISH of the whole-mount apical turn of the mature OC from a P20 mouse using probes targeting the endocytic genes *dnm1* (magenta), *dnm3* (green) and *sh3gl2* (greyscale). The puncta resulting from FISH were mostly restricted to HCs. The signals from five IHCs with adjacent three rows of OHCs are shown in the merged image (A) or separated by target probe (B-D). *Dnm1* and *sh3gl2* were detected in both HC types, albeit to a higher extent in IHCs (B, D). Most of *dnm3* was detected in OHCs, which is consistent with the result from the pre-mature OC. Nuclei were labeled with DAPI (blue, A). Scale bar: 5  $\mu$ m.

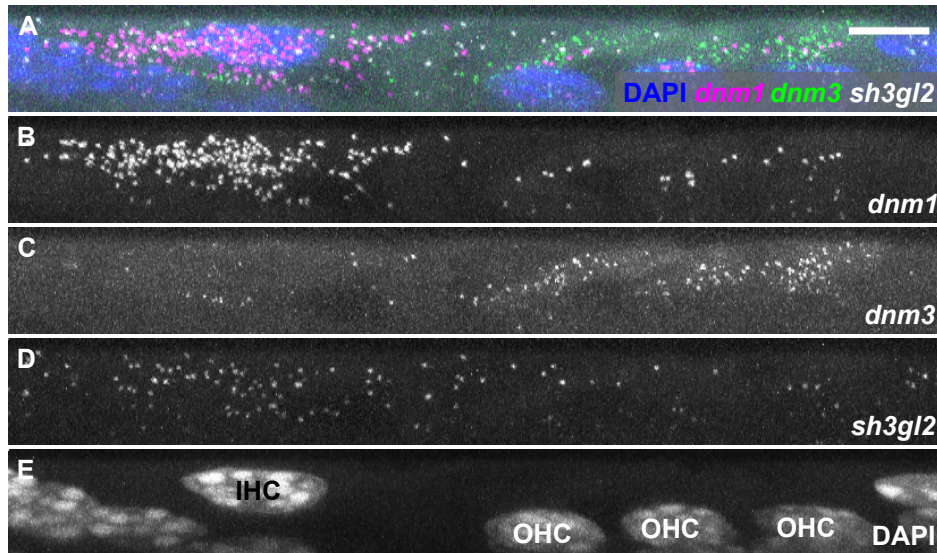


**Figure 22 X-projection of the signals of *dnm1*, *dnm3* and *sh3gl2* in the mature organ of Corti.** MIXP of one IHC and adjacent three OHCs (as indicated in **E**) re-sliced from the result shown in **Fig. 21A**. The signals from *dnm1*, *dnm3*, and *sh3gl2* are shown in the merged image as magenta, green and grayscale (**A**), respectively, or separated by target probe (**B-D**). Nuclei were labeled with DAPI (blue in **A**; grayscale in **E**). HC types are indicated in **E**. Scale bar: 5  $\mu$ m.

mRNA puncta of three target genes were quantified separately for each HC type in strips of 4–10 IHCs and the adjacent three rows of OHCs, averaged to puncta per IHC and OHC, and normalized to the accompanying negative control (**Fig. 23**). Results of different groups were compared using Friedman’s test with *post hoc* Dunn–Bonferroni test. Before maturation, OHCs contained less *dnm1* mRNA ( $20.3 \pm 6.7$ ,  $n = 34$ ) than IHCs ( $35.3 \pm 12.4$ ,  $n = 34$ ;  $p = 0.010$ ; **Fig. 23A**). After maturation, the amount of mRNA declined to 25% in OHCs ( $5.0 \pm 1.4$ ,  $n = 34$ ;  $p = 0.010$ , compared to pre-mature OHCs), but was doubled in IHCs ( $64.3 \pm 21.2$ ,  $n = 34$ ;  $p = 0.010$ , compared to pre-mature IHCs), thereby exacerbating the difference between HC types ( $p < 0.001$ ).

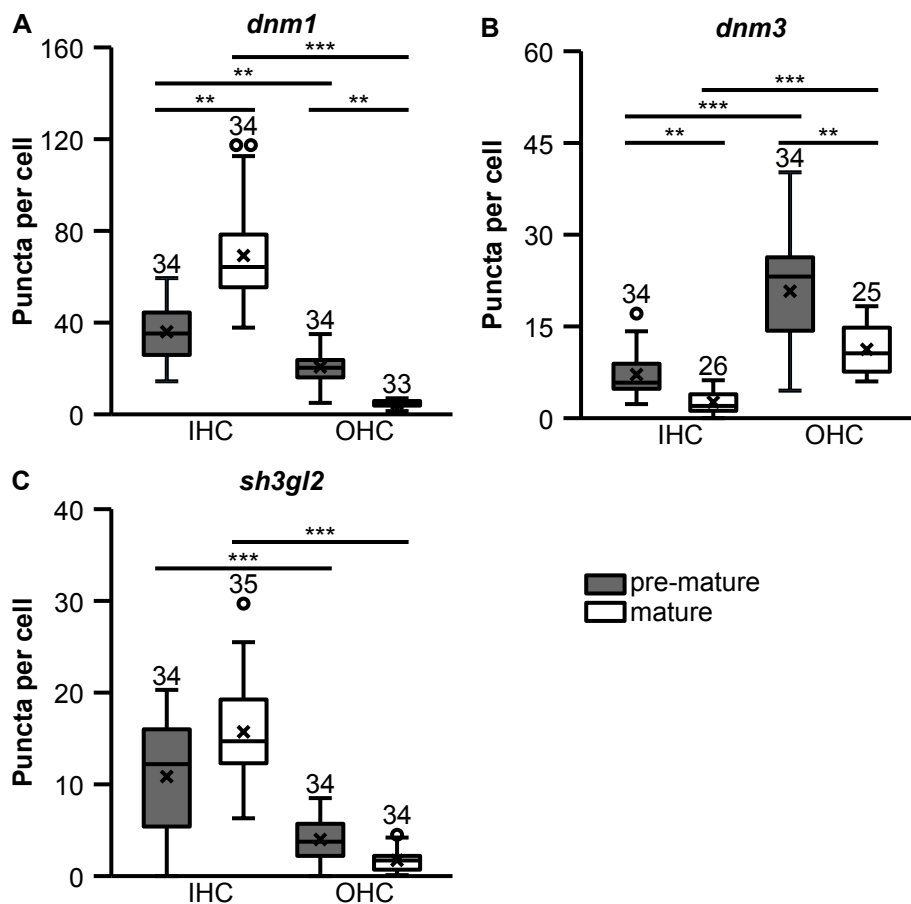


**Figure 23 Quantification of *dnm1*, *dnm3* and *sh3gl2* puncta in RNAscope™ fluorescent *in situ* hybridization.** Transcription levels of *dnm1* (A), *dnm3* (B) and *sh3gl2* (C) differed between HC types and age groups. Pre-mature IHCs contained more *dnm1* mRNA than OHCs. This difference was increased in mature IHCs (A). OHCs contained more *dnm3* mRNA than IHCs, even after age-dependent reduction of the transcript numbers in both HC types (B). The amount of *sh3gl2* mRNA was lower in IHCs than OHCs in the pre-mature OC and not affected by maturation (C). Numbers above the boxes indicate the number of images analyzed (each containing 4–10 IHCs and 12–30 OHCs). Data were compared using Friedman’s test with *post hoc* Dunn–Bonferroni test. \*\* $p < 0.01$ , \*\*\* $p < 0.001$ .

Transcript numbers of *dnm3* were higher in OHCs than in IHCs of both age groups (**Fig. 23B**): Pre-mature OHCs contained four times as much *dnm3* mRNA ( $23.2 \pm 8.6$ ,  $n = 34$ ) as age-matched IHCs ( $5.8 \pm 3.9$ ,  $n = 34$ ;  $p < 0.001$ ); after the onset of hearing, *dnm3* content was reduced in both IHCs ( $2.0 \pm 1.8$ ,  $n = 25$ ;  $p = 0.015$ , compared to pre-mature IHCs), and OHCs ( $10.6 \pm 3.8$ ,  $n = 25$ ;  $p = 0.015$ , compared to pre-mature OHCs), sharpening the difference between IHCs and OHCs ( $p < 0.001$ ).

*Sh3gl2* mRNA was generally more abundant in IHCs (**Fig. 23C**): In pre-mature IHC ( $12.2 \pm 6.7$ ;  $n = 34$ ) mRNA content was three times as much as in pre-mature OHC ( $3.8 \pm 2.4$ ,  $n = 34$ ;  $p < 0.001$ ). No age-dependent change was observed in either OHCs ( $1.7 \pm 1.1$ ,  $n = 34$ ;  $p = 1.000$ ) or IHCs ( $14.7 \pm 4.9$ ,  $n = 35$ ;  $p = 0.325$ ), and the difference between HC types remained significant ( $p < 0.001$ ).

In conclusion, IHCs contained more *dnm1* and *sh3gl2* mRNA than OHCs. Maturation of the OC increased this difference for *dnm1* but not *sh3gl2*. In contrast, *dnm3* was predominantly expressed in OHCs and showed an age-dependent reduction in both HC types.

### 3.3 Developmental changes in protein expression of dynamin-1 and dynamin-3 in the organ of Corti

The protein expression of dynamin-1 (encoded by *dnm1*) and dynamin-3 (encoded by *dnm3*) was analyzed with immunolabeling in pre-mature and mature OC to verify the findings from *FISH* and to study their localization in the cell, which is not possible with mRNA *FISH*. *Sh3gl2*-encoded endophilin-A1 could not be examined due to the lack of antibodies usable in the OC (own data, not shown; Kroll et al., 2019). Note that the following immunohistochemistry results have been published previously (Huang and Eckrich, 2021).

Dynamin-1 was labeled (overview: **Fig. 24**; section of pre-mature HCs: **Fig. 25**; section of mature HCs: **Fig. 26**) together with another endocytic protein, adaptor protein (ap)-180, which served as a marker for HCs and SGNs (Kroll et al., 2020). In apical-turn OCs, ap-180 and dynamin-1 were present in the HC region at both ages and in the soma of mature SGNs (**Fig. 24**; white color of IHCs indicating overlapping signals of ap-180 and dynamin-1). Data on SGNs of pre-mature OCs could not be obtained since pre-mature SGNs were often lost during tissue preparation. The staining in spiral limbus (SL) was non-specific because it was also present in the negative control (**Fig. 24**; overview of negative control not shown).

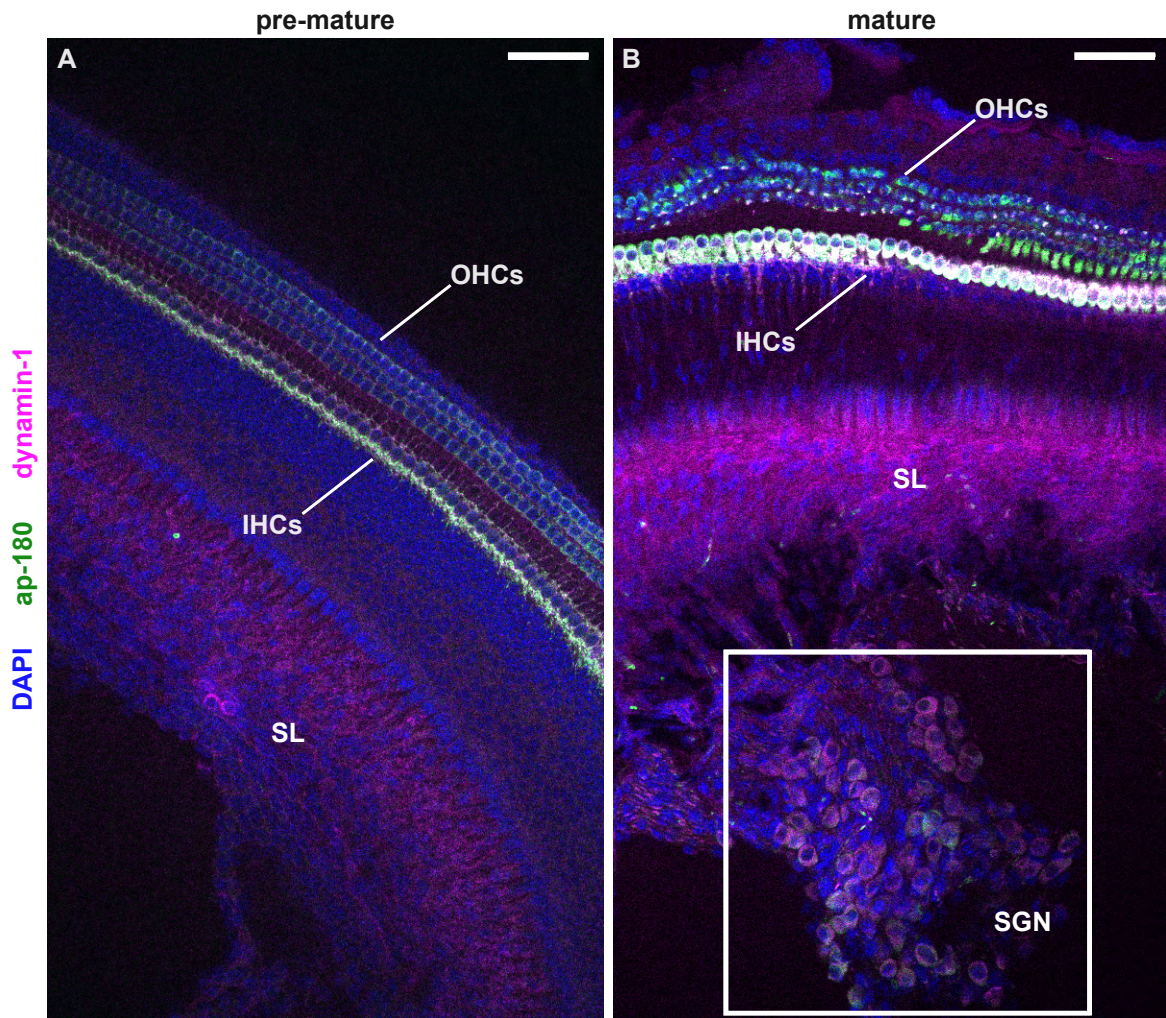


**Figure 24 Protein expression of dynamin-1 and ap-180 in whole-mount organs of Corti.** Overviews (single optical plane) of immunolabeling for dynamin-1 (magenta) and ap-180 (green) of the apical turn of whole-mount OCs from a pre-hearing (A) and a hearing mouse (B) showing one row of IHCs and three rows of OHCs. Mature SGNs are highlighted by a rectangle. Staining of the spiral limbus (SL) was non-specific since it was also present in the negative control (not shown). Note that the white color in IHCs was due to overlapping high intensity labeling for dynamin-1 and ap-180. Nuclei were labeled with DAPI (blue). Scale bars: 50  $\mu\text{m}$ .

Somata of pre-mature IHCs weakly expressed dynamin-1 and ap-180 (**Fig. 25A-C**), whereas both proteins were strongly labeled in nerve fibers (NFs) below IHCs (**Fig. 25A2-C2**). In pre-mature OHCs, weak labeling of dynamin-1 was found in the lateral membrane (**Fig. 25A1, C1**), whereas ap-180 was expressed in the soma (**Fig. 25B**) but was absent from the membrane (**Fig. 25B1**). In the mature OC, the expression pattern for both proteins changed: In IHCs, the dynamin-1 signal increased (**Fig. 26A, C**), now matching the intensity in NFs (**Fig. 26A1, C1**), while the increased ap-180 signal exceeded that in NFs (**Fig. 26B1**). Expression of both proteins in the somata of SGNs (**Fig. 27**) suggests that the labeled NFs below IHCs were afferent fiber terminals of SGNs. In mature OHCs, the weak expression of dynamin-1 was no longer found at the lateral membrane but in the soma (**Fig. 26C**), whereas the ap-180 signal increased and exceeded that of IHCs (**Fig. 26B**). Structures with intense labeling for both proteins were found near the base of mature OHCs (**Fig. 26A-C**), most likely representing terminals of medial olivocochlear efferent fibers (Spoendlin, 1985).

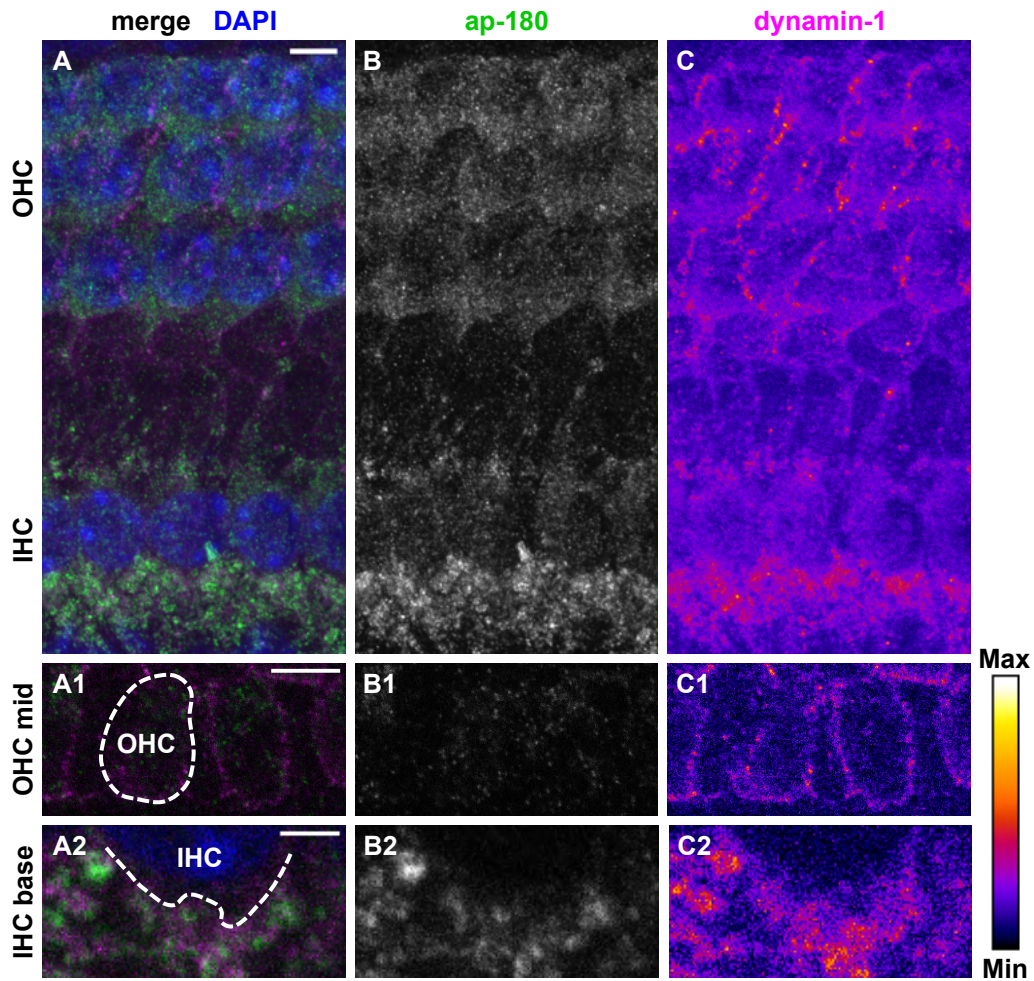


**Figure 25** Dynamin-1 and ap-180 are mainly expressed in nerve fibers of the pre-mature organ of Corti. MIZP of the apical-turn OC containing three IHCs and the adjacent three rows of OHCs from a P4 mouse shows that dynamin-1 (magenta in **A**, **A1-2**; intensity-coded in **C**, **C1-2**) and ap-180 (green in **A**, **A1-2**, grayscale in **B**, **B1-2**) were weakly expressed in HCs but strongly in NFs below IHCs (**A-C**). The mid region of OHCs showed dynamin-1 labeling in the lateral membrane, which was not the case for ap-180 (**A1-C1**). Dynamin-1 and ap-180 labeling in NFs did not overlap (**A2-C2**). Images in **A1-C1**, **A2-C2** show single optical planes. Nuclei were labeled with DAPI in the merged images (blue, **A**, **A1-2**). Dashed circle and dashed line in **A1** and **A2** indicate the shape of an OHC and the border between an IHC and NFs, respectively. Scale bars: 5  $\mu\text{m}$  (**A-C**, **A1-C1**) and 2  $\mu\text{m}$  (**A2-C2**).

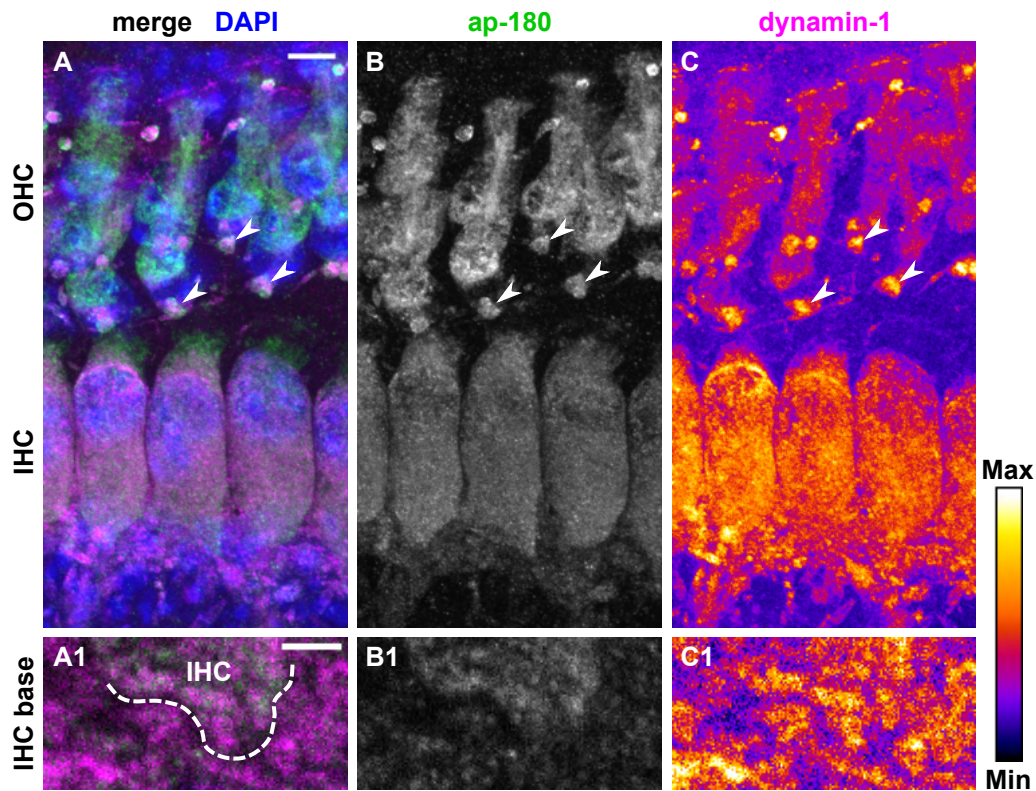


**Figure 26** Hair cells in the mature organ of Corti express high levels of dynamin-1 and ap-180. MIZP of the apical-turn OC containing three IHCs and the adjacent three rows of OHCs from a P20 mouse shows that expression of dynamin-1 (magenta in **A**, **A1**; intensity-coded in **C**, **C1**) was increased upon maturity in both HC types (**A**, **C**). The increase was stronger in IHCs, where the labeling intensity was comparable with that in NFs (**A**, **A1**, **C**, **C1**). Similarly, ap-180 expression (green in **A**, **A1**; grayscale in **B**, **B1**) was increased after maturation and the signal of IHCs now exceeded that of NFs (**A**, **A1**, **B**, **B1**). Arrowheads: putative efferent terminals close to the basolateral membrane of OHCs with strong labeling of both proteins. Images in **A1-C1** show single optical planes. Nuclei are labeled with DAPI in the merged images (blue, **A**, **A1**). Scale bars: 5  $\mu\text{m}$  (**A-C**) and 2  $\mu\text{m}$  (**A1-C1**).

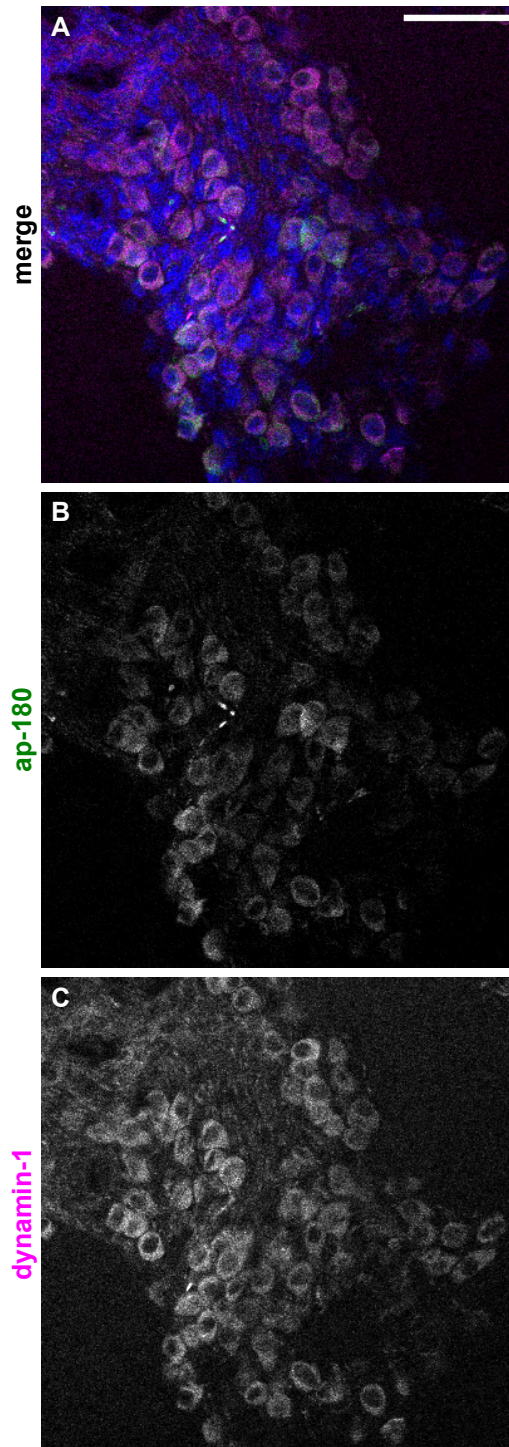


**Figure 27 Protein expression of dynamin-1 and ap-180 in spiral ganglion neurons of the mature organ of Corti.** MIZP of SGNs from a P20 mouse shows the co-expression of dynamin-1 (magenta in **A**; grayscale in **A2**) and ap-180 (green in **A**; grayscale in **A1**). Nuclei were labeled with DAPI (blue, **A**). Scale bar: 50  $\mu$ m.

Dynamin-3 and the HC marker myosin-7a (Li et al., 2020) were co-labeled in the OCs (overview: **Fig. 28**; section of pre-mature HCs: **Fig. 29**; section of mature HCs: **Fig. 30**). Dynamin-3 was detected in the HC region at both ages and in mature SGNs (**Fig. 28**). Again, signals in SGNs of pre-mature OCs were not available due to loss of SGNs during preparation and staining in SL was non-specific because it was also present in negative controls (**Fig. 28**; overview of negative control not shown).

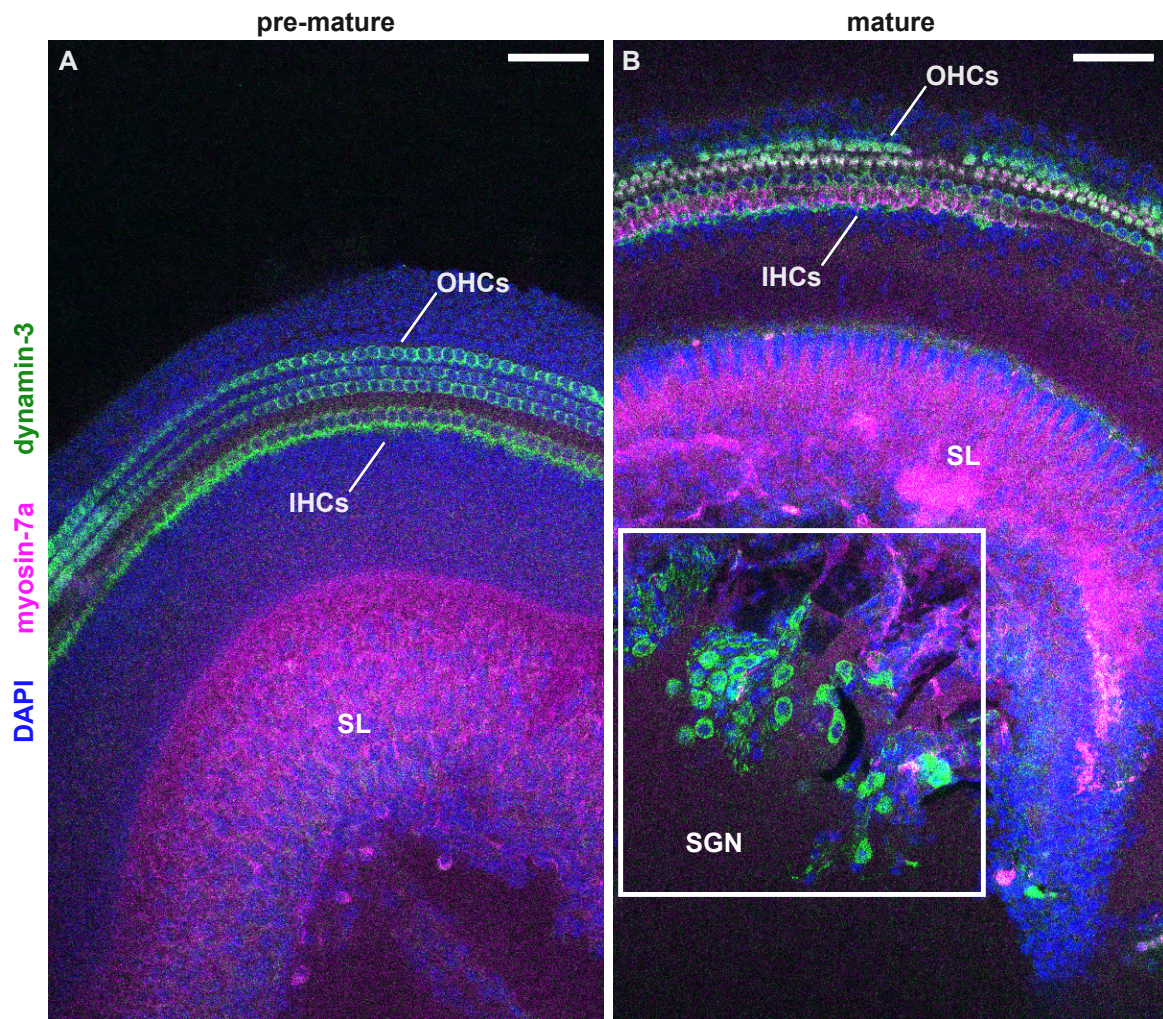


**Figure 28 Protein expression of dynamin-3 and myosin-7a in whole-mount organs of Corti.** Overview (single optical plane) of immunolabeling for dynamin-3 (green) and myosin-7a (magenta) of the apical turn of whole-mount OCs from a pre-hearing (**A**) and a hearing mouse (**B**) showing one row of IHCs and the adjacent three rows of OHCs. Mature SGNs are highlighted in a rectangle. Staining of the SL was non-specific since it was also present in the negative control (not shown). Nuclei were labeled with DAPI (blue). Scale bars: 50  $\mu$ m.

In the pre-mature OC, labeling of dynamin-3 was weaker in IHCs, when compared to the signal in OHCs (**Fig. 29A, C**) and NFs close to IHCs (**Fig. 29A3, C3**). In OHCs, dot-like labeling of dynamin-3 was concentrated surrounding the edge of their cuticular plates (**Fig. 29A1, C1**), which did not overlap with the stereocilia labeled by myosin-7a (**Fig. 29B1**). Such dot-like labeling was absent from the cuticular plates of IHCs (**Fig. 29A2, C2**). After maturation of the OC, dynamin-3 expression was increased in both OHCs (**Fig. 30A, C**) and NFs adjacent to IHCs (**Fig. 30A3, C3**), while remaining low in IHCs (**Fig. 30A, C**). The dot-like labeling persisted at the cuticular plate of OHCs (**Fig. 30A1, C1**), but was still absent from those of IHCs (**Fig. 30A2, C2**). Dynamin-3 was also found in the presumptive efferent terminals next to the base of OHCs (**Fig. 30A, C**, arrowheads) and in the soma of SGNs (**Fig. 31A, C**), both of which lacked myosin-7a (**Fig. 30B; Fig. 31B**).

In conclusion, the endocytic proteins dynamin-1 and ap-180 were enriched in mature IHCs, but only weakly expressed before the onset of hearing. In contrast, dynamin-3 was mainly present in OHCs regardless of age and was particularly enriched at the edge of their cuticular plates.

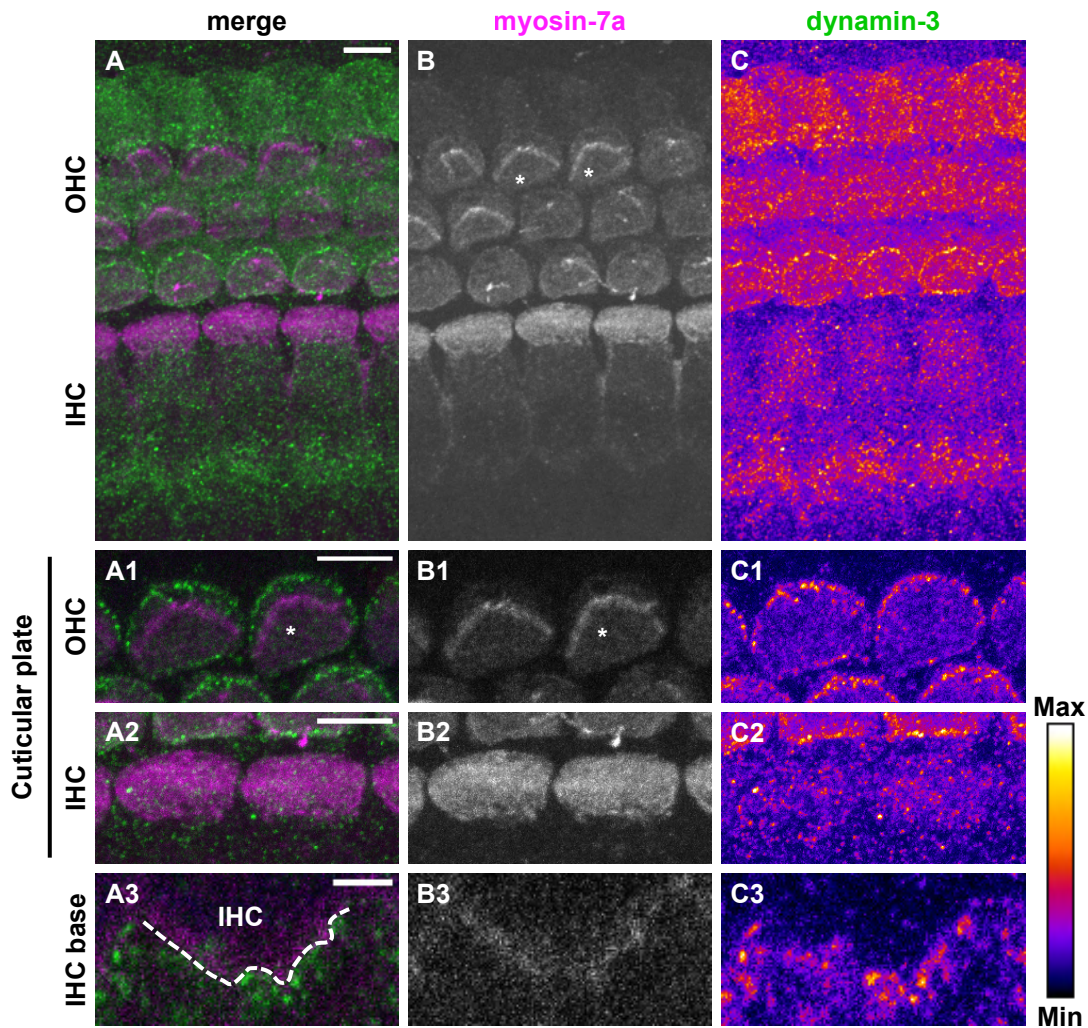


**Figure 29 Strong expression of dynamin-3 in outer hair cells but not in inner hair cells of the pre-mature organ of Corti.** MIZP of the apical-turn OC containing three IHCs and three adjacent rows of OHCs from a P4 mouse shows that dynamin-3 (green in **A**, **A1-A3**; intensity-coded in **C**, **C1-C3**) was strongly expressed in OHCs and NFs, but weakly in IHCs (**A**, **C**). Myosin-7a (magenta in **A**, **A1-A3**; grayscale in **B**, **B1-B3**) was found in both HCs (**A**, **B**). The edge of the cuticular plates of OHCs had intense dot-like dynamin-3 labeling (**A1**, **C1**), which did not overlap with the myosin-7a labeling of stereocilia (**B1**, indicated by asterisks). However, such labeling was absent from IHCs (**A2-C2**). Single optical plane images in **A3-C3** highlight the difference between myosin-7a-labeled IHCs (**B3**) and NFs enriched for dynamin-3 (**C3**). Dashed line in **A3** indicates the border between an IHC and NFs. Scale bars: 5  $\mu\text{m}$  (**A-C**, **A1-C1**, **A2-C2**) and 2  $\mu\text{m}$  (**A3-C3**).

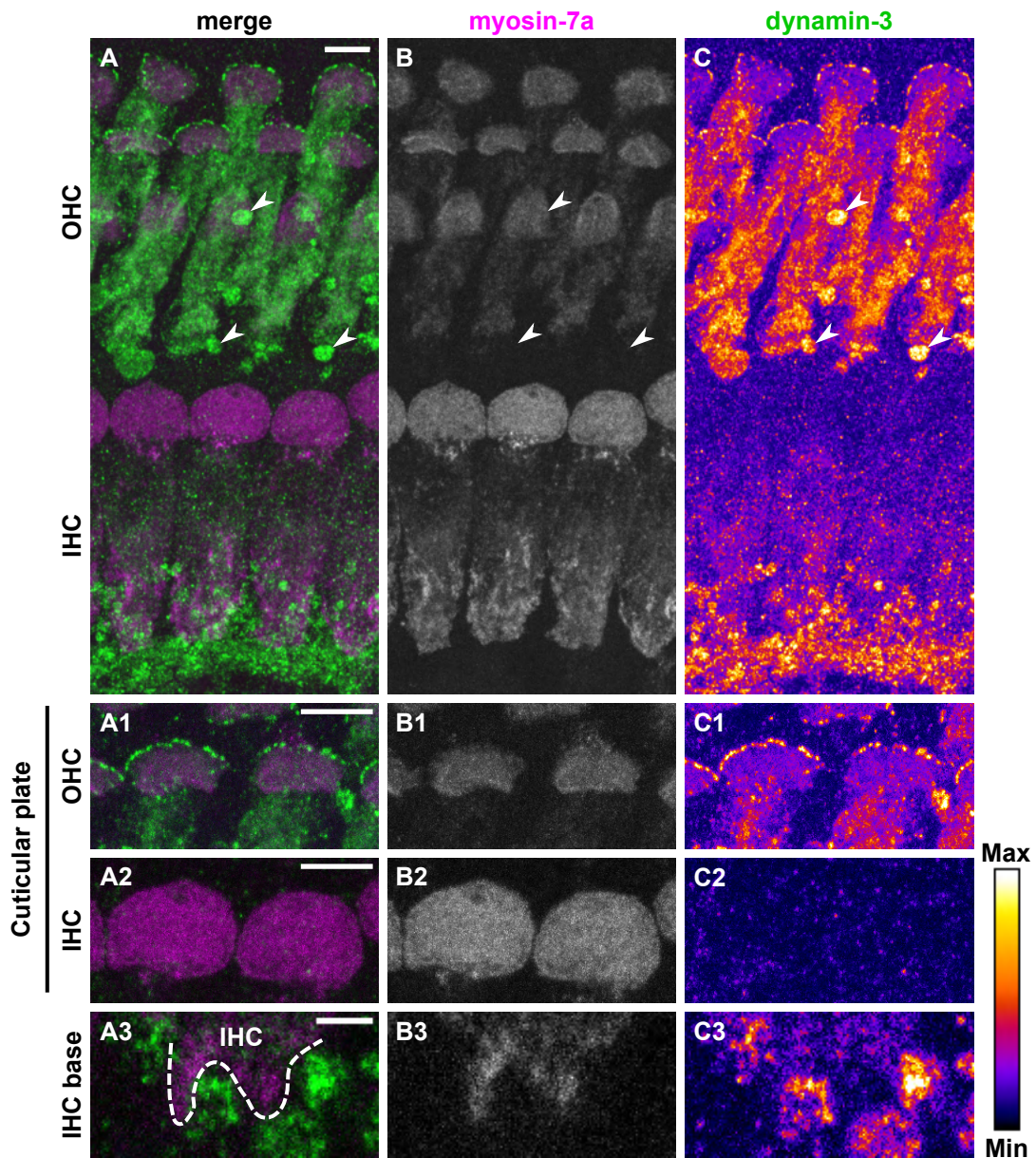


**Figure 30** Outer hair cells show higher dynamin-3 expression than inner hair cells in the mature organ of Corti. MIZP of the apical-turn OC containing three IHCs and the adjacent three rows of OHCs from a P20 mouse shows that dynamin-3 (green in **A**, **A1-A3**; intensity-coded in **C**, **C1-C3**) was mainly expressed in OHCs and NFs below IHCs (**A**, **C**). Myosin-7a (magenta in **A**, **A1-A3**; grayscale in **B**, **B1-B3**) was found in both HC types (**A**, **B**). The edge of the cuticular plate of OHCs showed intense dot-like dynamin-3 labeling (**A1**, **C1**, MIZP) that was absent in IHCs (**A2**, **C2**, MIZP). Single optical plane in **A3-C3** highlights the difference between myosin-7a-labeled IHCs (**B3**) and NFs enriched for dynamin-3 (**C3**). Dashed line in **A3** indicates the border between an IHC and NFs. Arrowheads: putative efferent terminals in vicinity of the basolateral membrane of OHCs showed strong labeling of dynamin-3, but not myosin-7a. Scale bars: 5  $\mu\text{m}$  (**A-C**, **A1-C1**, **A2-C2**) and 2  $\mu\text{m}$  (**A3-C3**).

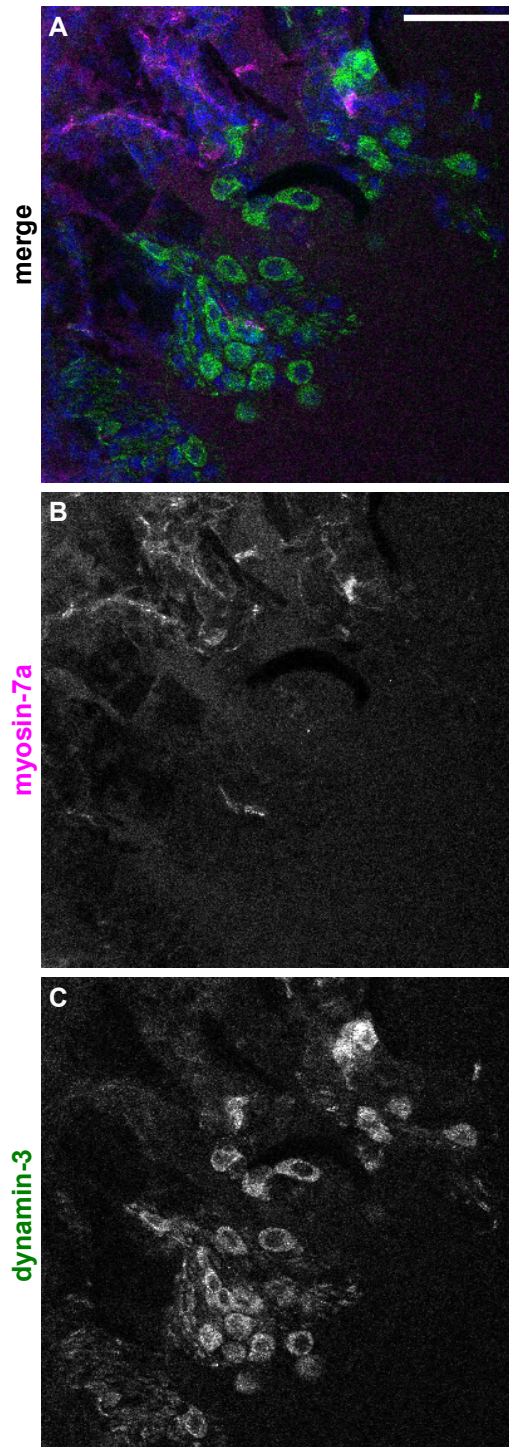


**Figure 31 Protein expression of dynamin-3 and myosin-7a in spiral ganglion neurons of the mature organ of Corti.** MIZP of SGNs from a P20 mouse shows expression of dynamin-3 (green in **A**; grayscale in **A2**) but not myosin-7a (magenta in **A**; grayscale in **A1**). Nuclei were labeled with DAPI (blue, **A**). Scale bar: 50  $\mu$ m.

### 3.4 The choice of fixative affects the appearance of dynamin-3 labeling

In contrast to the dynamin-1 antibody that exclusively worked when the OC was fixed with EtOH, the dynamin-3 antibody could be used with different fixatives, i.e. EtOH and Zamboni's fixative. Here, co-labeling of dynamin-3 and CtBP2/RIBEYE, a key component and marker of ribbon synapses, was performed in pre-mature (**Fig. 32A-A2**) and mature (**Fig. 32B-B2**) OCs fixed with Zamboni's fixative. In the pre-mature OC, dot-like CtBP2 labeling was present at the base of IHCs (**Fig. 32A-A1**). Dynamin-3 was abundant surrounding the CtBP2-labeled ribbon synapses and faintly labeled the nucleus of pre-mature IHCs (**Fig. 32A, A2**). Unlike the indistinct, cloudy appearance of dynamin-3 labeling in NFs below IHCs fixed with EtOH (**Fig. 32A3**), dynamin-3 labeling of Zamboni-fixed OCs was more condensed with relatively sharp edges. In the mature OC, CtBP2-labeled ribbons were reduced in their number but increased in their labeling intensity (**Fig. 32B-B1**) (Michanski et al., 2019). Dynamin-3 labeling was generally weak (presumably in NFs) with very intensive, sharp spots near the ribbons (presumably fiber terminals, **Fig. 32B, B2**), different from the pre-mature OC and contrasting the strong but cloudy dynamin-3 signal in the EtOH-fixed mature OC (**Fig. 32B3**). Moreover, the soma of mature IHCs was largely free from dynamin-3, and most CtBP2 signals partially overlapped with dynamin-3 in mature IHCs (**Fig. 32B**), which was less evident in pre-mature IHCs (**Fig. 32A**).

In brief, different fixatives affected the dynamin-3 labeling intensity, which was significantly different in pre-mature IHCs but comparable in mature IHCs. The choice of fixative also altered the appearance but confirmed the location of the labeling. Similarly, in a study using human tissue, different fixatives yielded varying staining patterns for identical antibodies (Paavilainen et al., 2010). This highlights the importance of considering the effect of fixatives employed when discussing immunohistochemistry findings.

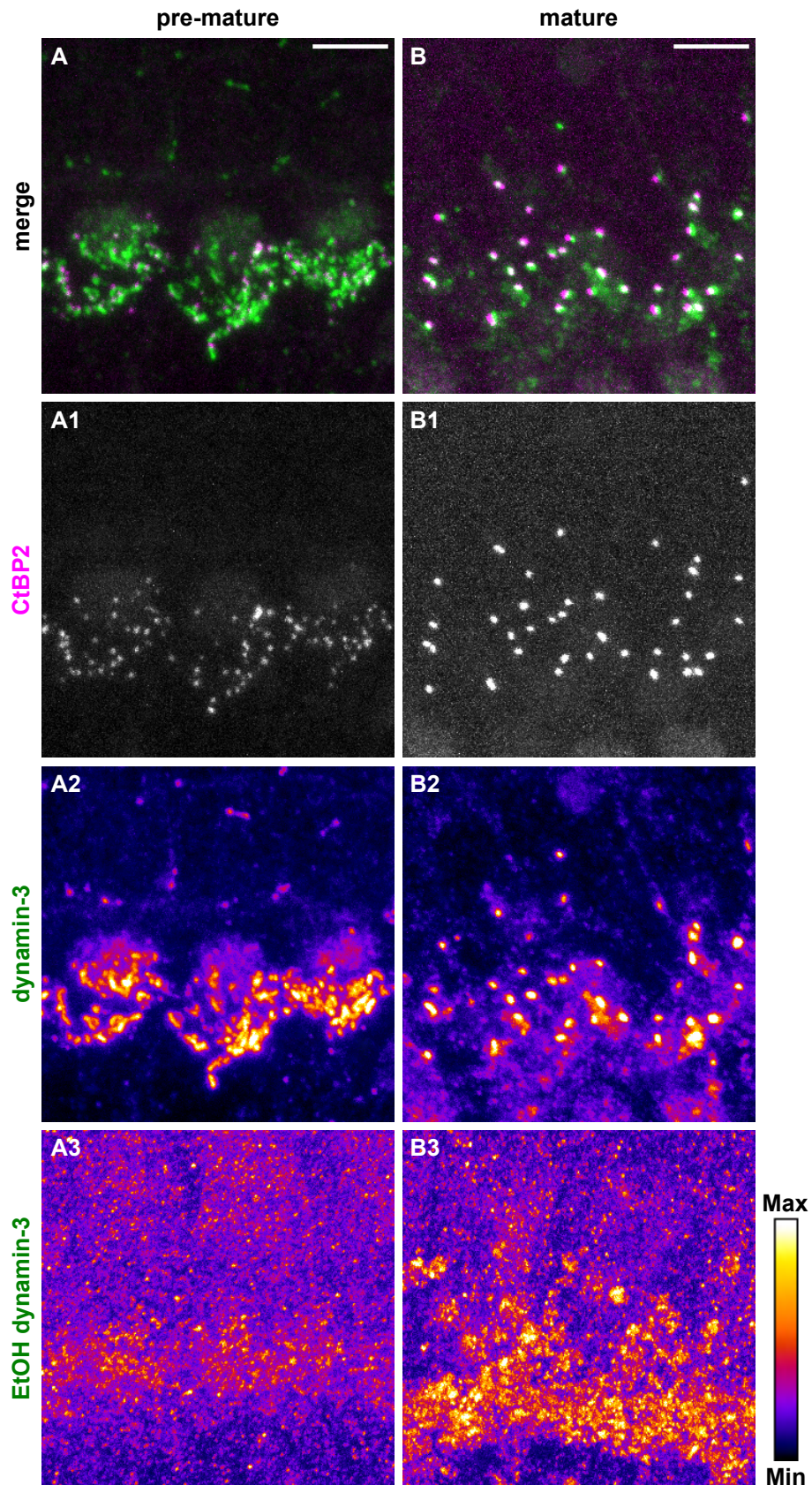


**Figure 32 Dynamin-3 staining in organs of Corti fixed with Zamboni's fixative.** Immunolabeling for dynamin-3 (green in **A, B**; intensity-coded in **A2, B2**) and the synaptic ribbon marker CtBP2 (magenta in **A, B**; grayscale in **A1, B1**) in apical-turn IHCs of whole-mount OCs from a pre-hearing (**A-A2**) and a hearing mouse (**B-B2**) using Zamboni's fixative. Dot-like dynamin-3 labeling was found near ribbon synapses (**A, B, A2, B2**). For comparison, dynamin-3 signals in the IHC region from EtOH-fixed OCs are shown (pre-mature: **A3**; mature: **B3**). Scale bar: 5  $\mu$ m.

### 3.5 Electrophysiology

The maturation process underlying endocytosis and the replenishment mechanisms governing the synaptic vesicle pools in IHCs remain largely unknown. In the present study, whole-cell patch clamp was used to investigate membrane capacitance changes ( $\Delta C_m$ ) of IHCs in response to depolarizing stimuli, whose increase reflects exocytosis and decline reflects endocytosis. Moreover, the effect of blocking dynamin-1/2 function was studied in both pre-mature and mature IHCs, since *FISH* and immunohistochemistry revealed the location and expression of endocytic proteins but did not provide information about their function.

Here, I measured endocytosis by recording the decline in  $\Delta C_m$  following exocytosis, i.e. the increase in  $\Delta C_m$  in response to a 100-ms depolarizing voltage step. In addition, I analyzed the ability of IHCs to maintain release from the synaptic vesicle pools (see **Introduction – Exocytosis and endocytosis of inner hair cells**) during sustained activity using repetitive stimulation that induced exocytosis and endocytosis, whose joint activity was measured and interpreted as follows: When  $\Delta C_m$  increased between stimuli, exocytosis exceeded endocytosis; when  $\Delta C_m$  decreased, endocytosis exceeded exocytosis; when  $\Delta C_m$  remained unchanged, exocytosis and endocytosis reached a state of equilibrium. I used *i*) 50-ms moderate repetitive stimuli to simulate constant activity, which has been suggested to trigger the readily releasable pool (RRP) – consisting of vesicles near or at the cell membrane (Duncker et al., 2013; Johnson et al., 2005), and *ii*) excessive stimulation with 1-s repetitive stimuli to challenge the secondary releasable pool (SRP) – comprising vesicles further away from the cell membrane as proposed previously (Duncker et al., 2013; Johnson et al., 2005).

#### 3.5.1 Maturation of endocytosis in inner hair cells

To address the hypothesis that terminal differentiation of IHCs includes changes in endocytosis, I conducted patch clamp experiments in IHCs before and after hearing onset near body temperature (BT;  $\sim 37^\circ\text{C}$ ), because endocytosis is highly temperature sensitive (Delvendahl et al., 2016).

##### *Endocytosis is enhanced after maturation of inner hair cells*

IHCs were depolarized to 0 mV by a single 100-ms voltage step. The resulting  $\Delta C_m$  was recorded for 20 s and the corresponding  $\text{Ca}^{2+}$  current ( $I_{\text{Ca}}$ ) elicited during the stimulus was measured (**Fig. 33**). The stimulus induced a rapid increase in  $\Delta C_m$  reflecting exocytosis, followed by a slower decline reflecting endocytosis, in both pre-mature and mature IHCs (**Fig. 33A**). In both groups, the decline of  $\Delta C_m$  was larger than its initial increase, i.e.  $\Delta C_m$  continued to decline throughout the recording period, falling below 0 fF after about 4–5 s. To investigate whether this substantial decline was due to the stimulus or an unrelated phenomenon, a

reference recording was conducted, where  $\Delta C_m$  was recorded for 20 s without applying any stimulus. **Fig. 34** shows all groups analyzed in this thesis (including those from other sections). Irrespective of age, temperature and application of endocytic blockers,  $\Delta C_m$  declined constantly in absence of any stimulation (**Fig. 34A**).  $\Delta C_m$  of the entire reference recording (**Fig. 34A**) and the last 8 s of each 20-s  $\Delta C_m$  recording following 100-ms depolarization (**Fig. 33A; 37A, G; 40A, G**) were fitted with a linear function (see **Materials and Methods – Patch clamp protocols and data analysis**). The resulting slope did not exceed -5 fF/s, revealing a decline that was similar in all groups irrespective of the presence of a depolarizing stimulus (**Fig. 34B;  $p = 0.113$ , K-W test; Suppl. Table 1**) and was therefore considered stimulus-independent. This phenomenon has been described before and might be caused by the capillary force generated by the patch pipette, which slowly pulls the cell membrane into the pipette, thereby reducing cell size and thus membrane capacitance (Kroll et al., 2019; Neef et al., 2014). Since the linear decline did not differ between all groups, it was not further considered in the analysis of endocytosis. Instead, only the return of  $\Delta C_m$  to the baseline of 0 fF was attributed to stimulus-induced endocytosis, which was completed within the first 6 s after stimulation in all groups (**Fig. 33A'; 37A', G'; 40A', G'**).

Several parameters were analyzed to assess endocytosis: *i*) stimulus-induced exocytosis (peak  $\Delta C_m$ ); *ii*) the time required for  $\Delta C_m$  to return to the baseline of 0 fF (time to 0), which was considered the endpoint of stimulus-induced endocytosis; and *iii*) the resulting decline rate, calculated by dividing the peak  $\Delta C_m$  by the time to 0.

Mature IHCs had a higher peak  $\Delta C_m$  ( $50.0 \pm 13.2$  fF,  $n = 15$ ) than pre-mature IHCs ( $35.8 \pm 18.9$  fF,  $n = 12$ ), indicating significantly stronger exocytosis in IHCs upon maturation (K-W Test, belonging to different homogeneous subsets; **Fig. 33C; Suppl. Table 2**). The time to 0 was indistinguishable at both ages (pre-mature,  $4.4 \pm 3.7$  s,  $n = 12$ ; mature,  $4.0 \pm 1.3$  s,  $n = 15$ ; K-W Test, belonging to the same homogeneous subset,  $p = 0.55$ ; **Fig. 33D; Suppl. Table 3**). However, due to their larger exocytosis, the endocytic decline rate was increased by 34% in mature IHCs ( $13.4 \pm 6.2$  fF/s,  $n = 15$ ) compared to pre-mature IHCs ( $10.0 \pm 3.9$  fF/s,  $n = 12$ ; K-W Test, belonging to different homogeneous subsets; **Fig. 33E; Suppl. Table 4**), demonstrating faster endocytosis in mature IHCs. Reflecting the smaller average  $I_{Ca}$  in mature IHCs (**Fig. 33B**; no statistical analysis), the  $Ca^{2+}$  charge ( $Q_{Ca}$ ), calculated by integrating  $I_{Ca}$ , was significantly reduced to 50% in mature IHCs ( $-15.0 \pm 3.3$  pC,  $n = 15$ ) compared to pre-mature IHCs (pre-mature,  $-29.7 \pm 6.0$  pC,  $n = 12$ ; K-W Test, belonging to different homogeneous subsets; **Fig. 33F; Suppl. Table 5**).

In summary, at near-physiological temperature, mature IHCs showed more exocytosis and faster endocytosis despite smaller  $\text{Ca}^{2+}$  influx than pre-mature IHCs.

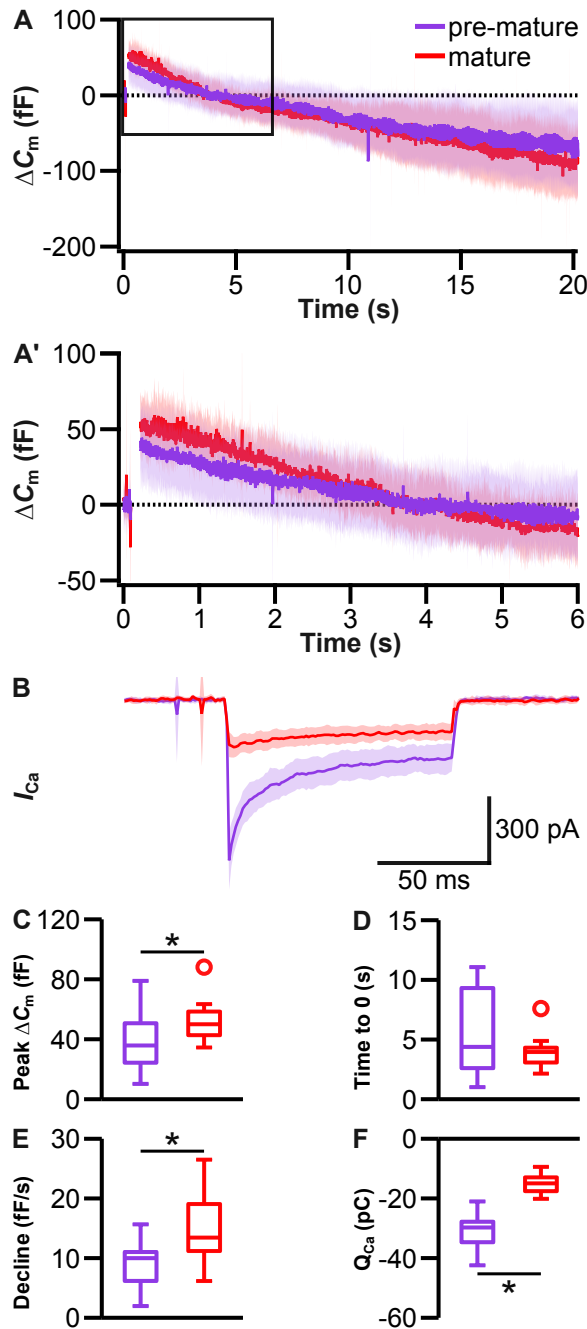


**Figure 33 Endocytosis of pre-mature and mature inner hair cells.** Average membrane capacitance changes ( $\Delta C_m$ ) and corresponding calcium current ( $I_{Ca}$ ) following a 100-ms depolarizing voltage step to 0 mV were recorded for 20 s in pre-mature and mature IHCs near body temperature (BT) (A-F).  $\Delta C_m$  traces of the entire recording (A), enlarged first 6 s of the  $\Delta C_m$  traces (A'; indicated by a rectangle in A) and  $I_{Ca}$  elicited during the stimulus (B) are shown. Maturation of IHCs increased the peak  $\Delta C_m$  averaged between 25 and 75 ms after the depolarization reflecting exocytosis (C). The time required for  $\Delta C_m$  to return to 0 fF (time to 0) remained unchanged (D), whereas the decline rate (fF/s) increased with age (E). The  $\text{Ca}^{2+}$  charge ( $Q_{Ca}$ ) integrated from  $I_{Ca}$  during the time of depolarization was reduced in mature IHCs (F). Traces are shown as mean  $\pm$  standard deviation (S.D.). Data were compared using Kruskal-Wallis (K-W) test followed by analysis of homogeneous subsets. \*: significantly different, i.e. belonging to different subsets. Circles: outliers. No. of cells (animals): pre-mature, BT = 12 (9); mature, BT = 15 (11).

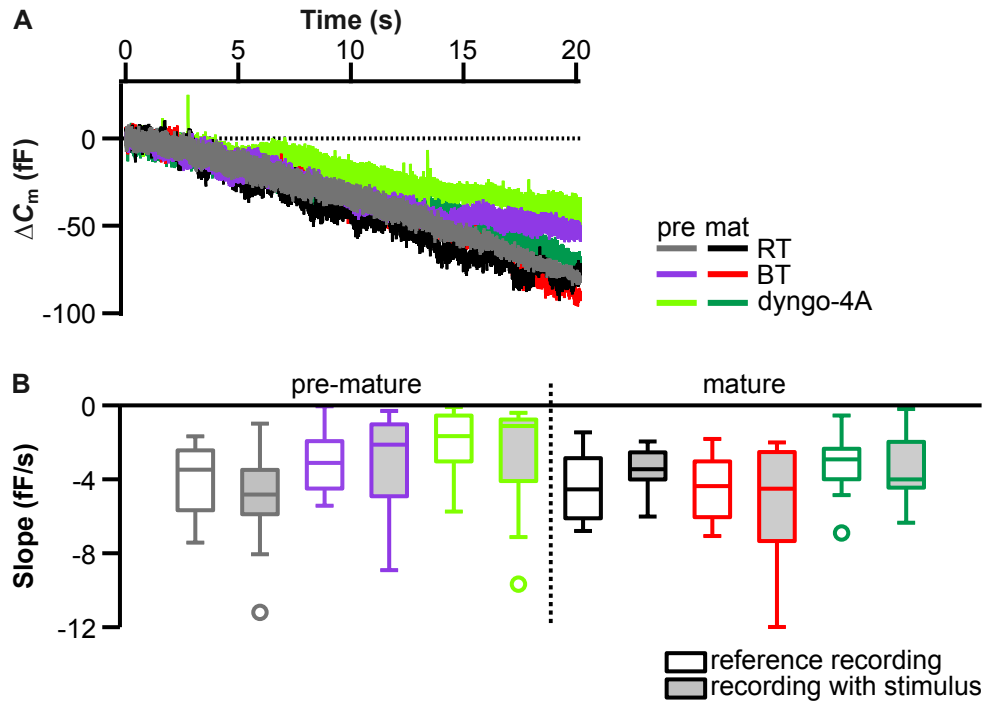


**Figure 34 Stimulus-independent decline of membrane capacitance in inner hair cells.** Averaged  $\Delta C_m$  of the reference recording in absence of stimulation in pre-mature (pre) and mature (mat) IHCs under different conditions, i.e. at room temperature (RT), BT, and using 30  $\mu\text{M}$  dyngo-4a at BT, declined during the entire recording in all groups (**A**).  $\Delta C_m$  traces of the reference groups and the last 8 s of the  $\Delta C_m$  traces of the groups following the 100-ms depolarization were fitted with a linear function (**Equation 1**; see **Materials and Methods – Patch clamp protocols and data analysis**), whose slopes showed no difference (**B**). Data were compared using K-W test ( $p = 0.113$ ). No. of cells (animals) of the reference groups: pre-mature, RT = 8 (5); BT = 9 (7); dyngo-4a = 10 (8); mature, RT = 7 (5); BT = 8 (6); dyngo-4a = 7 (6). No. of cells (animals) of the groups with stimulation: pre-mature, RT = 9 (8); BT = 12 (9); dyngo-4a = 12 (11); mature, RT = 10 (9); BT = 15 (11); dyngo-4a = 11 (10).

### *Maturation of inner hair cells affects sustained release in response to moderate stimulation*

The  $\Delta C_m$  induced by a single stimulus showed that IHCs had larger exocytosis and faster endocytosis after maturation. The following section addresses how this affected the kinetics of continuous vesicle release and retrieval upon moderate activation over a longer period. To this end, IHCs were stimulated by 50 short-term repetitive voltage steps (0 mV for 50 ms) as previously used to analyze RRP release and replenishment (Duncker et al., 2013; Johnson et al., 2009). The resulting  $\Delta C_m$  was measured during the 100-ms interstep-interval, and the corresponding  $I_{Ca}$  elicited during each stimulus was recorded (**Fig. 35**).

Typical traces of a pre-mature (P4) and a mature (P17) IHC demonstrate that the repetitive stimuli induced changes in  $\Delta C_m$ , reflecting the joint activity of exocytosis and endocytosis in IHCs at both ages (**Fig. 35A**). The average cumulative  $\Delta C_m$  of pre-mature IHCs increased non-linearly throughout the entire recording, approaching potential saturation. In contrast, the  $\Delta C_m$  increase of mature IHCs was steep during the first few stimuli, before approaching a slower, linear increase (**Fig. 35C**). This was also evident, when analyzing the change of  $\Delta C_m$  between each stimulus (interstep  $\Delta C_m$ , **Fig. 35D**). The courses of the cumulative  $\Delta C_m$  of all 14 mature and ten out of 15 pre-mature IHCs were fitted with an exponential-linear function (**Equation 2**; see **Materials and Methods – Patch clamp protocols and data analysis**); the remaining five pre-mature IHCs were better described by a linear function (**Equation 1**; see **Materials and Methods – Patch clamp protocols and data analysis**). While the resulting amplitude (A) of the fast initial increase of mature IHCs was significantly reduced by 80% ( $150.5 \pm 78.1$  fF,  $n = 14$ ) compared to pre-mature IHCs ( $825.1 \pm 232.9$  fF,  $n = 10$ ; K-W Test, belonging to different homogeneous subsets; **Suppl. Table 6**), the time constant ( $\tau$ ) in mature IHCs ( $0.9 \pm 1.3$  s,  $n = 14$ ) was six times as fast as in pre-mature IHCs ( $5.7 \pm 1.8$  s,  $n = 10$ ; K-W Test, belonging to different homogeneous subsets; **Suppl. Table 7**). The slope of the linear part was  $23.5 \pm 7.8$  fF/s in mature IHCs ( $n = 14$ ), and significantly differed from the negative slope of  $\Delta C_m$  from pre-mature IHCs ( $-6.9 \pm 40.4$  fF/s,  $n = 15$ ; K-W Test, belonging to different homogeneous subsets; **Suppl. Table 8**). Note that in pre-mature IHCs, considering the large amplitude and slow time constant, the non-linear increase dominated the overall course. Consequently, the  $\Delta C_m$  course was linear only during the last few stimuli in pre-mature IHCs, and therefore the slope was largely negligible in the analysis. Typical current traces of pre-mature IHCs revealed that  $I_{Ca}$  was larger and inactivated stronger (analysis of inactivation conducted by Stephanie Eckrich, not shown) than that of mature IHCs (**Fig. 35B**). The corresponding  $Q_{Ca}$  of pre-mature IHCs exceeded that of mature IHCs only during the first steps, then declined to values comparable to mature IHCs, whose  $Q_{Ca}$  remained nearly constant upon repetitive stimulation (**Fig. 35E**). As a result,  $\Delta Q_{(1-50)}$ , i.e. the difference between the first and the last, 50<sup>th</sup> stimulus, was significantly smaller in mature IHCs ( $1.2 \pm 0.5$  pC,  $n$

=14) compared to pre-mature IHCs (pre-mature,  $10.0 \pm 2.1$  pC,  $n = 15$ ; K-W Test, belonging to different homogeneous subsets; **Suppl. Table 10**), whereas the total  $Q_{Ca}$  (summarized from all stimuli) showed no difference between both groups (pre-mature,  $-461.1 \pm 196.7$  pC,  $n = 15$ ; mature,  $-348.4 \pm 74.5$  pC,  $n = 14$ ; K-W Test, belonging to the same homogeneous subset,  $p = 0.43$ ; **Suppl. Table 9**). The efficiency of  $Q_{Ca}$  to change  $\Delta C_m$  was calculated by normalizing the interstep  $\Delta C_m$  to  $Q_{Ca}$  ( $\Delta C_m/Q_{Ca}$ ). Mature IHCs showed an initially large efficiency that declined fast, while the efficiency of pre-mature IHCs was largely stable (**Fig. 35F**; no statistical analysis conducted), together resulting in a comparable total efficiency (summarized from all stimuli) between both age groups (pre-mature,  $54.3 \pm 18.1$  fF/pC,  $n = 15$ ; mature,  $41.6 \pm 12.7$  fF/pC,  $n = 14$ ; K-W Test, belonging to the same homogeneous subset,  $p = 0.08$ ; **Suppl. Table 11**).

In conclusion, in mature IHCs the initial steep rise and subsequent slower constant increase in  $\Delta C_m$  suggest that, after the first stimuli, fast endocytosis constantly counteracted exocytosis, which might reflect efficient replenishment of the RRP upon sustained moderate stimulation. By contrast, the overall non-linear increase in  $\Delta C_m$  approaching saturation in pre-mature IHCs might indicate the beginning of RRP depletion.

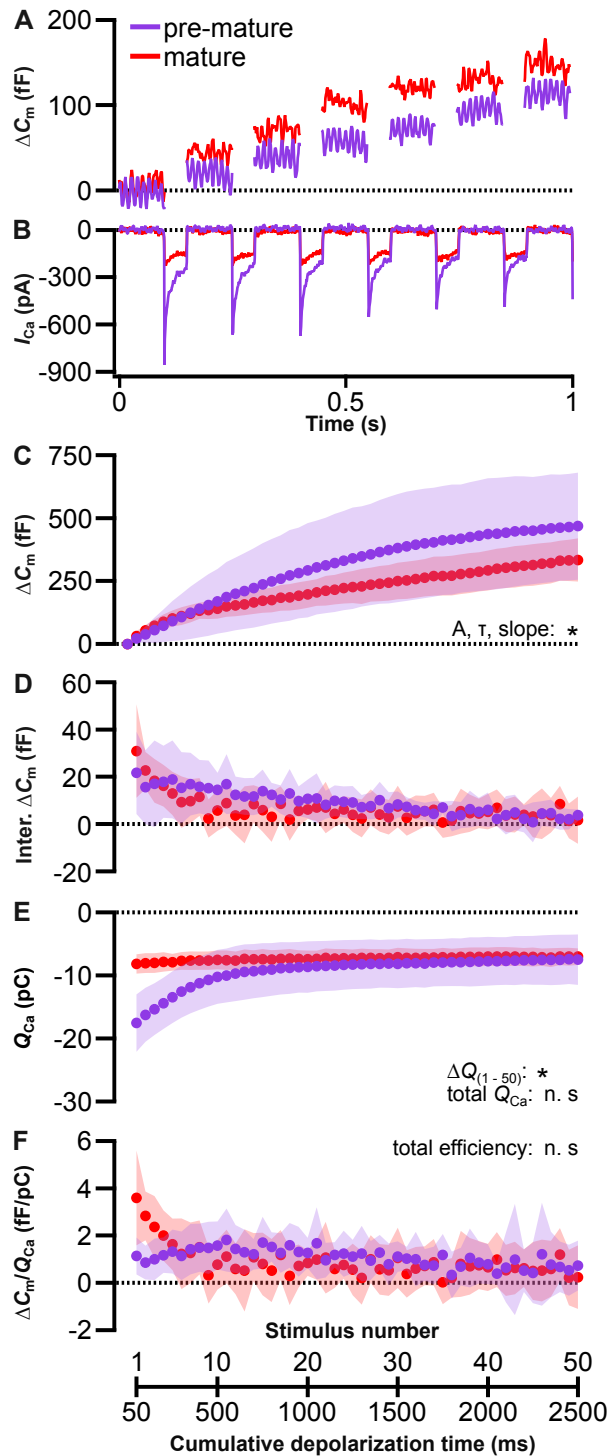


**Figure 35 Maturity level affects release upon moderate repetitive stimulation of inner hair cells.** Release of vesicles upon moderate stimulation over a longer period was studied in pre-mature and mature IHCs by repetitive depolarization to 0 mV using 50-ms voltage steps (100-ms interstimulus interval) at BT. Typical traces of the resulting  $\Delta C_m$  (A) and the corresponding  $I_{Ca}$  (B) in response to the first six stimuli are shown. Cumulative  $\Delta C_m$  averaged between voltage steps and fitted with a linear (five pre-mature IHCs) or an exponential-linear (ten pre-mature and 14 mature IHCs) function (Equation 1-2; see Materials and Methods – Patch clamp protocols and data analysis) differed in the exponential amplitude (A) and time constant ( $\tau$ ), and the linear slope (C). Interstep  $\Delta C_m$  was calculated as change of  $\Delta C_m$  between steps (D).  $Q_{Ca}$  was compared for the total  $Q_{Ca}$  of all steps and the difference of  $Q_{Ca}$  between the first and the last step ( $\Delta Q_{(1-50)}$ ; E).  $Ca^{2+}$  efficiency was calculated as interstep  $\Delta C_m$  normalized to  $Q_{Ca}$  ( $\Delta C_m/Q_{Ca}$ ), and compared for the total  $\Delta C_m/Q_{Ca}$  of all steps (F). Data in C-F, given as mean  $\pm$  S.D., were compared using K-W test followed by analysis of homogeneous subsets. \*: significantly different, i.e. belonging to different subsets; n.s.: not significant, i.e. same subset. No. of cells (animals): pre-mature, BT = 15 (10); mature, BT = 14 (12).

### *Maturation of inner hair cells affects sustained release in response to excessive stimulation*

The previous section showed that the developmental increase of the endocytic rate changed the release profile of IHCs in response to moderate continuous stimulation, which is thought to trigger RRP release and replenishment. To test the capability of IHCs to maintain release upon excessive stimulation, they were challenged by 50 long-lasting repetitive voltage steps (0 mV for 1 s), while measuring the resulting  $\Delta C_m$  during the 200-ms interstep-interval and the corresponding  $I_{Ca}$  during each stimulus (**Fig. 36**).

Typical  $\Delta C_m$  traces of a pre-mature (P3) and a mature (P17) IHC (**Fig. 36A**), and the averaged cumulative  $\Delta C_m$  exhibited a steep increase during the initial stimuli, which appeared larger in pre-mature IHCs (**Fig. 36C**). This increase was followed by a plateau phase that slowly declined at both ages (**Fig. 36C**), as also evident from the interstep  $\Delta C_m$  (**Fig. 36D**). Exponential-linear fits of the cumulative  $\Delta C_m$  confirmed that pre-mature IHCs had significantly larger exponential amplitudes ( $1639 \pm 738$  fF,  $n = 7$ ) than mature IHCs ( $1048 \pm 249$  fF,  $n = 9$ ; K-W Test, belonging to different homogeneous subsets; **Suppl. Table 12**), but comparable time constants (pre-mature,  $3.9 \pm 2.9$  s,  $n = 7$ ; mature,  $6.9 \pm 3.6$  s,  $n = 9$ ; K-W Test, belonging to the same homogeneous subset,  $p = 0.34$ ; **Suppl. Table 13**). The similar negative slopes, i.e. the decline of the linear  $\Delta C_m$  present during later steps in both age groups (pre-mature,  $-2.8 \pm 17.3$  fF/s,  $n = 7$ ; mature,  $-2.7 \pm 3.2$  fF/s,  $n = 9$ ; K-W Test, belonging to the same homogeneous subset,  $p = 0.32$ ; **Suppl. Table 14**), indicating that exocytosis no longer exceeded endocytosis. Both, typical  $I_{Ca}$  traces and  $Q_{Ca}$ , showed that  $I_{Ca}$  declined less upon repetitive stimulation in IHCs after maturation:  $\Delta Q_{(1-50)}$  of mature IHCs ( $32.0 \pm 9.5$  pC,  $n = 9$ ) was only 32% of that of pre-mature IHCs ( $100.2 \pm 45.1$  pC,  $n = 7$ ; K-W Test, belonging to different homogeneous subsets; **Fig. 36B, E**; **Suppl. Table 16**). However, comparable total  $Q_{Ca}$  was observed in both groups (pre-mature,  $-2838 \pm 1454$  pC,  $n = 7$ ; mature,  $-3911 \pm 775$  pC,  $n = 9$ ; K-W Test, belonging to the same homogeneous subset,  $p = 0.22$ ; **Suppl. Table 15**). Similar courses of efficiency were observed, and the total efficiency was indistinguishable between both ages (pre-mature,  $20.2 \pm 12.6$  fF/pC,  $n = 7$ ; mature,  $9.3 \pm 2.8$  fF/s,  $n = 9$ ; K-W Test, belonging to the same homogeneous subset,  $p = 0.12$ ; **Fig. 36F**; **Suppl. Table 17**), but pre-mature IHCs showed larger fluctuations (not further analyzed).

Taken together, these data show that, despite larger exocytosis (cf. **Fig. 33C**), the cumulative  $\Delta C_m$  in mature IHCs increased less upon excessive stimulation than in pre-mature IHCs. This might reflect fast endocytosis at the synaptic membrane (cf. **Fig. 33E**) and efficient SRP replenishment in mature IHCs. In both age groups, repetitive stimulation eventually led to a decline of  $\Delta C_m$ , which could be caused by *i*) depletion of the vesicle pool due to insufficient

replenishment, or alternatively, by *ii*) an increased rate of endocytosis activated upon excessive stimulation, such as bulk retrieval, thereby exceeding the rate of exocytosis.

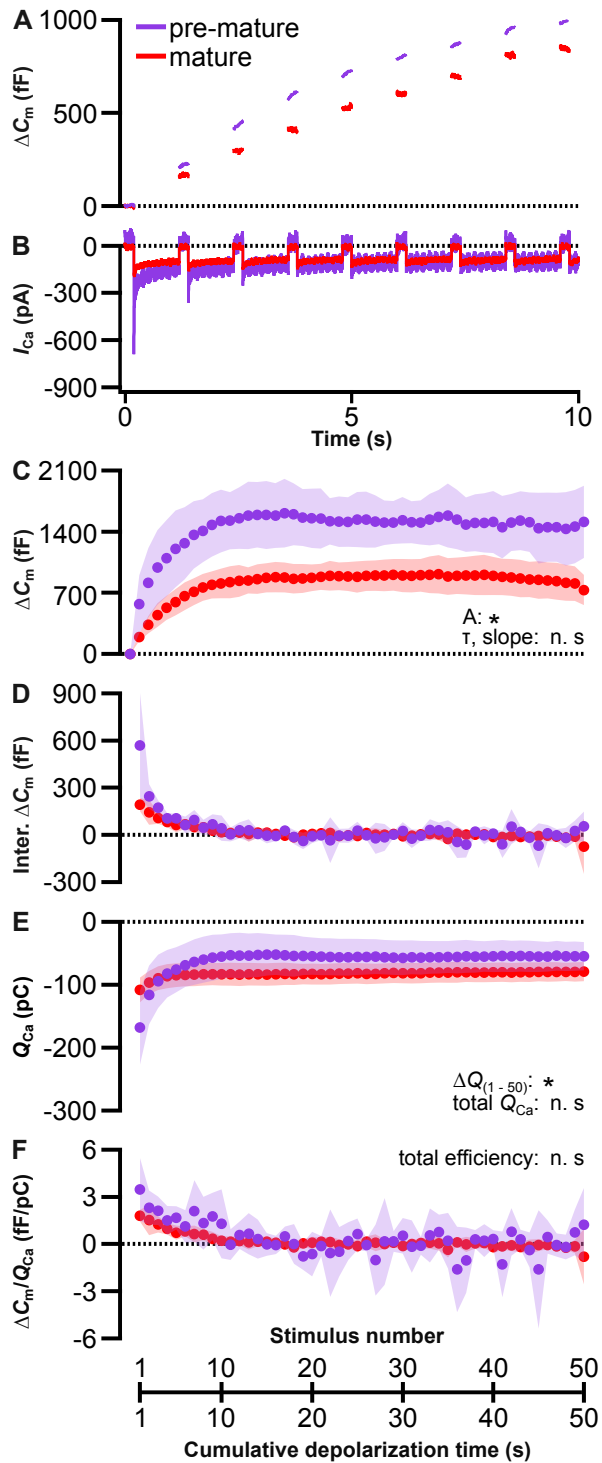


**Figure 36 Maturity level affects release upon excessive repetitive stimulation of inner hair cells.** The effect of cell maturation on sustained release upon excessive stimulation was studied in pre-mature and mature IHCs by application of 1-s repetitive voltage steps to 0 mV (200-ms interstimulus interval) at BT. Typical traces of the resulting  $\Delta C_m$  (A) and corresponding  $I_{Ca}$  (B) in response to the first eight stimuli are shown. Averaged cumulative  $\Delta C_m$  differed in the exponential A, while  $\tau$  and the linear slope resulting from fitting with an exponential-linear function were similar (C). Interstep  $\Delta C_m$  are shown (D).  $Q_{Ca}$  was compared for the total  $Q_{Ca}$  and  $\Delta Q_{(1-50)}$  (E).  $\Delta C_m/Q_{Ca}$  was compared for the total  $\Delta C_m/Q_{Ca}$  (F). Data in C-F, given as mean  $\pm$  S.D., were compared using K-W test followed by analysis of homogeneous subsets. \*: significantly different, i.e. belonging to different subsets; n.s: not significant, i.e. same subset. No. of cells (animals): pre-mature, BT = 7 (6); mature, BT = 9 (9).

### 3.5.2 Temperature-dependence of endocytosis of inner hair cells

Exocytosis and endocytosis are more efficient with increasing temperature (Delvendahl et al., 2016; Nouvian, 2007). At neuronal synapses of the calyx of Held, the temperature dependence of endocytosis changes upon cell maturation: Before maturation, the endocytosis rate increases up to threefold when the temperature is changed from room temperature (RT; ~22°C) to BT, whereas the increase is only twofold after maturation (Renden and von Gersdorff, 2007). Nevertheless, many previous studies on endocytosis in IHCs were performed at RT (Beutner and Moser, 2001; Jean et al., 2018; Neef et al., 2014), since tissue deterioration is accelerated at BT, making the technically challenging patch clamp recordings of IHCs even more difficult. Here, I performed whole-cell patch clamp recordings at RT and compared the result with that obtained at BT to study how temperature affects the rate of endocytosis in IHCs and whether maturation alters the temperature-dependence of endocytosis.

#### *Body temperature accelerates endocytosis of mature but not pre-mature IHCs*

Endocytosis of pre-mature and mature IHCs was analyzed at RT using a single 100-ms depolarizing voltage step to 0 mV (**Fig. 37**). The stimulus caused a rapid increase in  $\Delta C_m$  followed by a slow decline in both pre-mature (**Fig. 37A**) and mature IHCs (**Fig. 37G**) indicating functional exocytosis and endocytosis at RT.

In pre-mature IHCs, the peak  $\Delta C_m$ , reflecting exocytosis, significantly increased with temperature and the value at BT ( $35.8 \pm 18.9$  fF,  $n = 12$ ) was five times as high as at RT ( $6.7 \pm 5.6$  fF,  $n = 9$ ; K-W Test, belonging to different homogeneous subsets; **Fig. 37C**; **Suppl. Table 2**). The time to 0 was similarly increased and significantly longer at BT ( $4.4 \pm 3.7$  s,  $n = 12$ ) than RT ( $1.1 \pm 1.1$  s,  $n = 9$ ; K-W Test, belonging to different homogeneous subsets; **Fig. 37D**; **Suppl. Table 3**). The resulting endocytosis rate did not differ between both temperatures (RT,  $5.7 \pm 2.7$  fF/s,  $n = 9$ ; BT,  $10.0 \pm 3.9$  fF/s,  $n = 12$ ; K-W Test, belonging to the same homogeneous subset,  $p = 0.17$ ; **Fig. 37E**; **Suppl. Table 4**). The corresponding  $I_{Ca}$  measured during the depolarizing stimulus was larger at BT and showed stronger inactivation (**Fig. 37B**; no statistical analysis), and  $Q_{Ca}$  calculated by integrating  $I_{Ca}$  was doubled in pre-mature IHCs when switching from RT ( $-15.1 \pm 4.0$  pC,  $n = 9$ ) to BT ( $-29.7 \pm 6.0$  pC,  $n = 12$ ; K-W Test, belonging to different homogeneous subsets; **Fig. 37F**; **Suppl. Table 5**).

In mature IHCs, the peak  $\Delta C_m$  was also significantly higher at BT ( $50.0 \pm 13.2$ ,  $n = 15$ ) than RT ( $18.2 \pm 6.2$ ,  $n = 10$ ; in different homogeneous subsets; **Fig. 37I**; **Suppl. Table 2**), whereas at this age the time to 0 was not affected by temperature (RT,  $4.2 \pm 1.6$  s,  $n = 10$ ; BT,  $4.0 \pm 1.3$  s,  $n = 15$ ; K-W Test, belonging to the same homogeneous subset,  $p = 0.55$ ; **Fig. 37J**; **Suppl. Table 3**). As a result, the decline rate of  $\Delta C_m$  at BT ( $13.4 \pm 6.2$  fF/s,  $n = 15$ ) was tripled

compared to RT ( $4.3 \pm 2.3$  fF/s,  $n = 10$ ; K-W Test, belonging to different homogeneous subsets; **Fig. 37K; Suppl. Table 4**). Unlike pre-mature IHCs, increasing temperature had no significant effect on  $I_{Ca}$  (**Fig. 37H**) or  $Q_{Ca}$  of mature IHCs (RT,  $-11.7 \pm 1.7$  pC,  $n = 10$ ; BT,  $-15.0 \pm 3.3$  pC,  $n = 15$ ; K-W Test, belonging to the same homogeneous subset,  $p = 0.44$ ; **Fig. 37L; Suppl. Table 5**).

In conclusion, while exocytosis increased with temperature at both ages, the rate of endocytosis was accelerated with temperature only in mature IHCs.

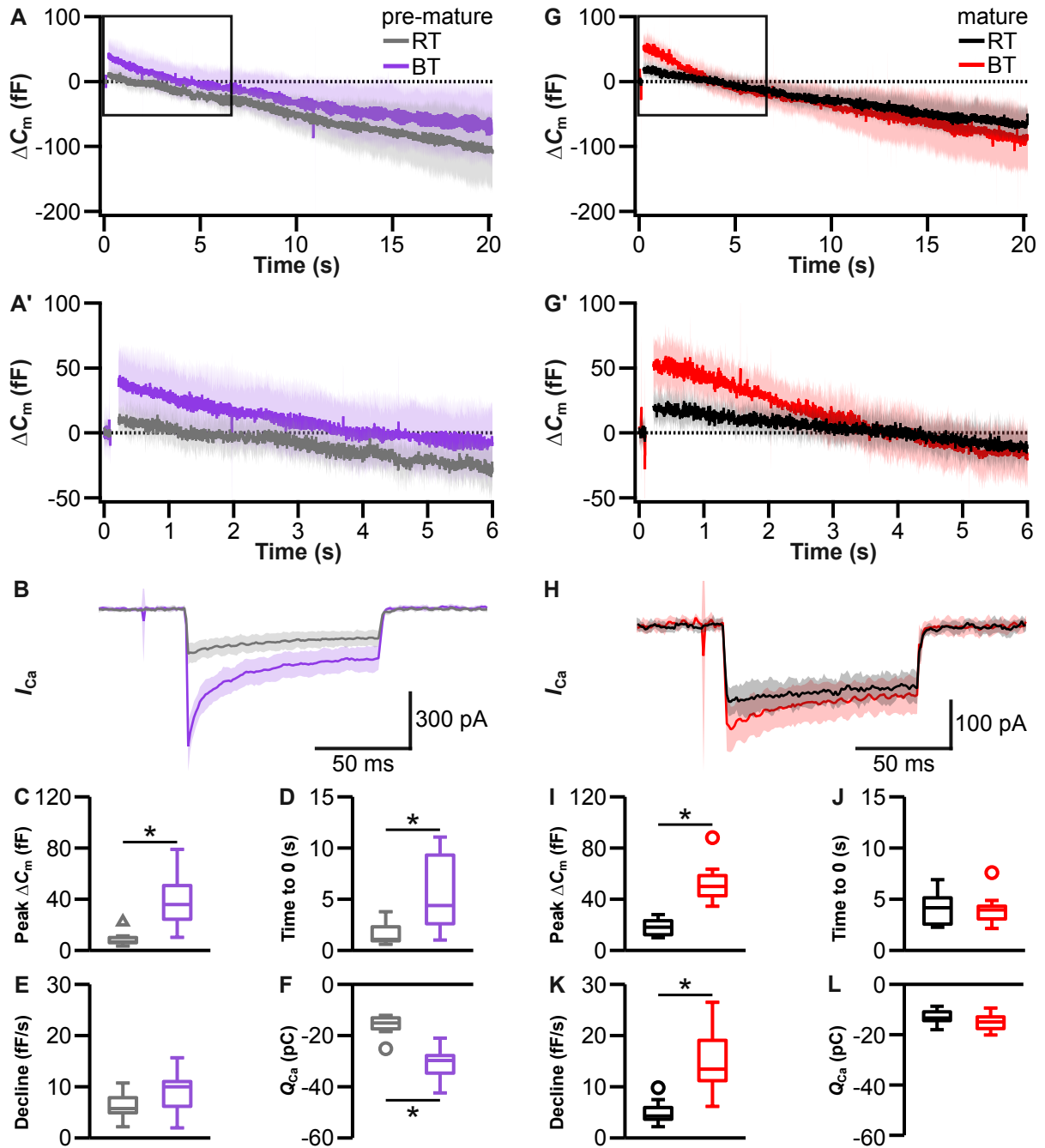


**Figure 37 Effect of temperature on endocytosis of inner hair cells.** To study the effect of temperature on endocytosis,  $\Delta C_m$  and corresponding  $I_{Ca}$  following a 100-ms depolarizing voltage step to 0 mV were recorded for 20 s in pre-mature (**A-F**) and mature IHCs (**G-L**) at RT and compared with BT controls.  $\Delta C_m$  traces of entire recording (**A**, **G**), enlarged first 6 s of the  $\Delta C_m$  traces (**A'**, **G'**; indicated by rectangles in **A** and **G**) and  $I_{Ca}$  elicited during the stimulus (**B**, **H**) are shown. Compared to RT, BT increased the peak  $\Delta C_m$  in both age groups (**C**, **I**), prolonged the time to 0 in pre-mature IHCs (**D**), and speeded up the decline in mature IHCs (**K**).  $Q_{Ca}$  was increased at BT in pre-mature IHCs (**F**), but not mature IHCs (**L**). Traces are shown as mean  $\pm$  S.D.. Data were compared using K-W test followed by analysis of homogeneous subsets. \*: significantly different, i.e. belonging to different subsets. Triangle: extreme value (not included in statistics). Circles: outliers. No. of cells (animals): pre-mature, RT = 9 (8); BT = 12 (9); mature, RT = 10 (9); BT = 15 (11).

### *Temperature-dependence of sustained release in response to moderate stimulation of inner hair cells*

Considering that, compared to RT, recordings at BT increased exocytosis in IHCs of both developmental states, but accelerated endocytosis only in mature IHCs, I next tested how the release upon moderate repetitive stimulation is affected by temperature at both ages.

For pre-mature IHCs, the typical  $\Delta C_m$  trace of a pre-mature (P5) IHC increased slower over time at RT than at BT (**Fig. 38A**). Accordingly, the average cumulative  $\Delta C_m$  increased linearly at RT, compared to the steeper non-linear increase observed at BT (**Fig. 38C**). This was also evident from the largely constant interstep  $\Delta C_m$  at RT compared to the declining course present at BT (**Fig. 38D**). At RT,  $\Delta C_m$  courses of 13 out of 17 pre-mature IHCs were best described with a linear function, and only the remaining four could be fitted with an exponential-linear function. While the resulting exponential amplitudes (RT,  $510.6 \pm 243.0$  fF,  $n = 4$ ; BT,  $825.1 \pm 232.9$  fF,  $n = 10$ ; K-W Test, belonging to the same homogeneous subset,  $p = 0.29$ ; **Suppl. Table 6**) and time constants (RT,  $5.1 \pm 1.0$  s,  $n = 4$ ; BT,  $5.7 \pm 1.8$ ,  $n = 10$ ; K-W Test, belonging to the same homogeneous subset,  $p = 1.00$ ; **Suppl. Table 7**) were similar between temperature groups, this is likely attributable to the very low sample number at RT. The slope of  $\Delta C_m$  at RT was  $24.0 \pm 23.1$  fF/s ( $n = 17$ ) and higher than the negative slope of the short linear section present at BT only during the last few stimuli ( $-6.9 \pm 40.4$  fF/s,  $n = 15$ ; K-W Test, belonging to different homogeneous subsets; **Suppl. Table 8**). The corresponding  $I_{Ca}$  (**Fig. 38B**) was smaller and less-inactivating at RT (preliminary analysis of inactivation conducted by Stephanie Eckrich, not shown). While  $Q_{Ca}$  declined upon repetitive stimulation at both temperatures, the difference between the first and last stimulus  $\Delta Q_{(1-50)}$  was almost tripled at BT ( $10.0 \pm 2.1$  pC,  $n = 15$ ) compared to RT ( $3.5 \pm 0.9$  pC,  $n = 17$ ; K-W Test, belonging to different homogeneous subsets; **Fig. 38E**; **Suppl. Table 10**). However, the total  $Q_{Ca}$  showed no significant increase with temperature (RT,  $-359.1 \pm 75.0$  pC;  $n = 17$ ; BT,  $-461.1 \pm 196.7$  pC,  $n = 15$ ; K-W Test, belonging to the same homogeneous subset,  $p = 0.43$ ; **Suppl. Table 9**). Since both, interstep  $\Delta C_m$  and  $Q_{Ca}$ , were larger at BT only during the first stimulations but not later on (**Fig. 38D, E**; no statistical analysis conducted), the resulting total efficiency was similar between both temperatures (RT,  $34.9 \pm 18.7$  fF/pC,  $n = 17$ ; BT,  $54.3 \pm 18.1$  fF/pC,  $n = 15$ ; K-W Test, belonging to the same homogeneous subset,  $p = 0.08$ ; **Fig. 38F**; **Suppl. Table 11**).

Like pre-mature IHCs,  $\Delta C_m$  of a typical mature (P21) IHC kept at RT increased less than that at BT during the first few stimuli (**Fig. 38A**). In contrast to the initial steep increase and subsequent slower linear  $\Delta C_m$  course observed in mature IHCs at BT, the increase of cumulative  $\Delta C_m$  was largely linear over the entire recording (**Fig. 38I**). The interstep  $\Delta C_m$ , revealed a short strong increase of  $\Delta C_m$  during the initial steps at RT, but it was negligible

when compared to BT (**Fig. 38J**): Ten out of 15 traces of the RT group could be fitted with an exponential-linear function, while the remaining five were fitted with a linear function. The resulting exponential amplitude at BT ( $150.5 \pm 78.1$  fF,  $n = 14$ ) was six times as high as at RT ( $25.0 \pm 24.1$ ,  $n = 10$ ; K-W Test, belonging to different homogeneous subsets; **Suppl. Table 6**), while the time constant was not affected (RT,  $0.8 \pm 0.7$  s,  $n = 10$ ; BT,  $0.9 \pm 1.3$  s; K-W Test, belonging to the same homogeneous subset,  $p = 0.91$ ; **Suppl. Table 7**). After the initial steep rise in  $\Delta C_m$  subsided at BT, the slope of the linear course showed no difference between temperatures (RT,  $35.8 \pm 13.9$  fF/s,  $n = 15$ ; BT,  $23.5 \pm 7.8$  fF/S,  $n = 14$ ; K-W Test, belonging to the same homogeneous subset,  $p = 0.49$ ; **Suppl. Table 8**). Although  $I_{Ca}$  inactivated stronger at BT (**Fig. 38H**; preliminary analysis of inactivation conducted by Stephanie Eckrich, not shown), the course of  $Q_{Ca}$  showed little decline in mature IHCs and was parallel at both temperatures (**Fig. 38K**), resulting in similar  $\Delta Q_{(1-50)}$  (RT,  $1.3 \pm 0.5$  pC,  $n = 15$ ; BT,  $1.2 \pm 0.5$  pC,  $n = 14$ ; K-W Test, belonging to the same homogeneous subset,  $p = 0.87$ ; **Suppl. Table 10**) and total  $Q_{Ca}$  (RT,  $-307.2 \pm 66.7$  pC,  $n = 15$ ; BT,  $-348.4 \pm 74.5$  pC,  $n = 14$ ; K-W Test, belonging to the same homogeneous subset,  $p = 0.09$ ; **Suppl. Table 9**). As a consequence, the decline in efficiency during the first few stimuli observed in mature IHCs at both temperatures (**Fig. 38L**) was attributed to the steep initial increase in cumulative  $\Delta C_m$ , rather than changes in  $I_{Ca}$ , and thus more pronounced at BT (no statistical analysis performed). The total efficiency was, however, similar at both temperatures (RT,  $48.1 \pm 14.4$  fF/pC,  $n = 15$ ; BT,  $41.6 \pm 12.7$ ,  $n = 14$ ; K-W Test, belonging to the same homogeneous subset,  $p = 0.08$ ; **Suppl. Table 11**).

To summarize, the constant linear increase in  $\Delta C_m$  upon moderate repetitive stimuli indicates that IHCs at both ages were capable of maintaining release at RT. This can likely be attributed, at least partially, to the strongly reduced exocytosis (cf. **Fig. 37C, I**), as evident from the lack of a prominent strong increase of  $\Delta C_m$  at RT.

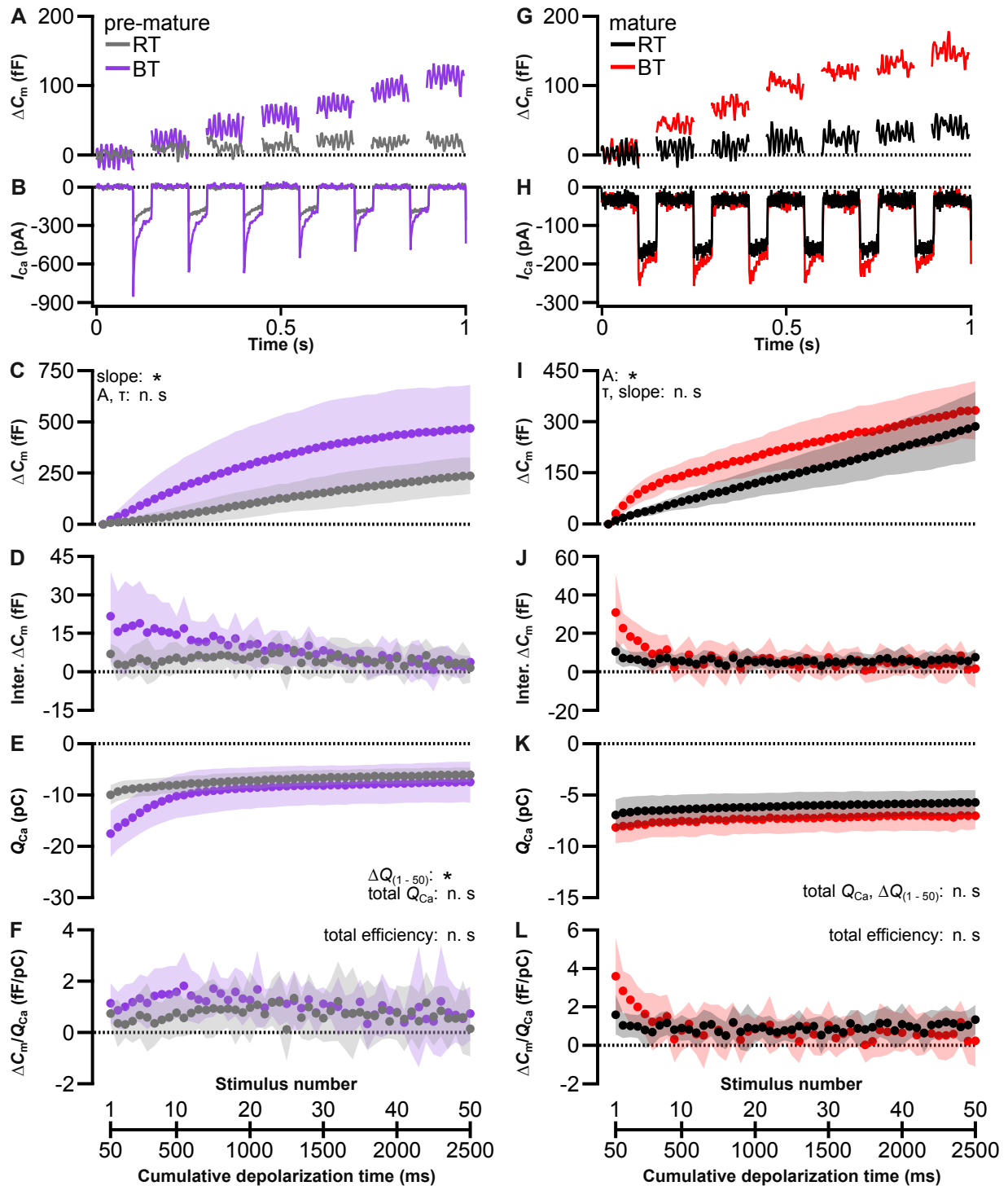


**Figure 38 Effect of temperature on release upon repetitive moderate stimulation of inner hair cells.** The effect of temperature on sustained release was studied in pre-mature and mature IHCs by application of repetitive 50-ms voltage steps to 0 mV (100-ms interstimulus interval) at RT compared with BT controls. Typical traces of the resulting  $\Delta C_m$  (**A**, **G**) and corresponding  $I_{Ca}$  (**B**, **H**) in response to the first six stimuli are shown. Averaged cumulative  $\Delta C_m$  were compared for the exponential A and  $\tau$ , and the linear slope resulting from fitting with an exponential-linear (four pre-mature and ten mature IHCs at RT; ten pre-mature and 14 mature IHCs at BT) or a linear (13 pre-mature and five mature IHCs at RT; five pre-mature IHCs at BT) function (**C**, **I**). Interstep  $\Delta C_m$  are shown (**D**, **J**).  $Q_{Ca}$  were compared for the total  $Q_{Ca}$  and  $\Delta Q_{(1-50)}$  (**E**, **K**).  $\Delta C_m/Q_{Ca}$  were compared for the total  $\Delta C_m/Q_{Ca}$  (**F**, **L**). Data in **C-F** and **I-L**, given as mean  $\pm$  S.D., were compared using K-W test followed by analysis of homogeneous subsets. \*: significantly different, i.e. belonging to different subsets; n.s.: not significant, i.e. same subset. No. of cells (animals): pre-mature, RT = 17 (13); pre-mature, BT = 15 (10); mature, RT = 15 (11); mature, BT = 14 (12).

### *Temperature-dependence of sustained release in response to excessive stimulation of inner hair cells*

The previous section demonstrated that temperature fundamentally affected the course of sustained release upon moderate repetitive stimulation. To investigate the effect of temperature on release following excessive stimulation, I stimulated IHCs kept at RT using 50 long-lasting repetitive voltage steps (0 mV for 1 s) and compared the result to that at BT.

In pre-mature IHCs at BT,  $\Delta C_m$  initially increased fast and subsequently slowed down until it remained constant or even decreased slightly, whereas at RT the brief initial increase was less pronounced, after which  $\Delta C_m$  continued to increase linearly as shown for a typical cell at P4 (**Fig. 39A**), for the average cumulative  $\Delta C_m$  (**Fig. 39C**), and for the interstep  $\Delta C_m$  (**Fig. 39D**). The course of the cumulative  $\Delta C_m$  of all IHCs from both temperature groups was fitted with an exponential-linear function. The resulting exponential amplitude of the initial rise at BT ( $1639 \pm 738$  fF,  $n = 7$ ) was 2.5 times as large as at RT ( $653 \pm 323$  fF,  $n = 11$ ; K-W Test, belonging to different homogeneous subsets; **Suppl. Table 12**), while the time constant was comparable at both temperatures (RT,  $6.2 \pm 2.3$  s,  $n = 11$ ; BT,  $3.9 \pm 2.9$  s,  $n = 7$ ; K-W Test, belonging to the same homogeneous subset,  $p = 0.34$ ; **Suppl. Table 13**). The slope of the following linear phase was slightly positive at RT ( $3.2 \pm 4.3$  fF/s,  $n = 11$ ), whereas a small decline was present at BT ( $-2.8 \pm 17.3$  fF/s,  $n = 7$ ), but was not significantly different between pre-mature IHCs of both temperature groups (K-W Test, belonging to the same homogeneous subset,  $p = 0.14$ ; **Suppl. Table 14**). Typical  $I_{Ca}$  and averaged  $Q_{Ca}$  were similar at both temperatures (**Fig. 39B, E**), with similar total  $Q_{Ca}$  (RT,  $-2384 \pm 716$  pC,  $n = 11$ ; BT,  $-2838 \pm 1454$  pC,  $n = 7$ ; K-W Test, belonging to the same homogeneous subset,  $p = 0.86$ ; **Suppl. Table 15**) and  $\Delta Q_{(1-50)}$  (RT,  $103.9 \pm 24.6$  pC,  $n = 11$ ; BT,  $100.2 \pm 45.1$  pC,  $n = 7$ ; K-W Test, belonging to the same homogeneous subset,  $p = 1.00$ ; **Suppl. Table 16**). Accordingly, while at BT the efficiency appeared to be larger and declined faster during the first stimuli than at RT (no statistical analysis conducted), the total efficiency was comparable between temperatures (RT,  $12.1 \pm 3.6$  fF/pC,  $n = 11$ ; BT,  $20.2 \pm 12.6$  fF/pC,  $n = 7$ ; K-W Test, belonging to the same homogeneous subset,  $p = 0.12$ ; **Fig. 42F**; **Suppl. Table 17**).

The  $\Delta C_m$  increase of a typical mature (P21) IHC was similar at RT and BT during the first few stimuli (**Fig. 39G**), as was the initial rapid increase of the cumulative  $\Delta C_m$  present at both temperatures (**Fig. 39I**). However, while the cumulative  $\Delta C_m$  then slowed down to a linear increase at RT, it saturated and eventually even slightly declined at BT (**Fig. 39I, J**). The exponential amplitude was similar between temperatures (RT,  $1626 \pm 995$  fF,  $n = 13$ ; BT,  $1048 \pm 249$ ,  $n = 9$ ; K-W Test, belonging to the same homogeneous subset,  $p = 0.16$ ; **Suppl. Table 12**), whereas the time constant was significantly faster at BT ( $6.9 \pm 3.6$  s,  $n = 9$ ) than at RT

( $10.3 \pm 11.2$  s,  $n = 13$ ; K-W Test, belonging to different homogeneous subsets; **Suppl. Table 13**). Reflecting the persistent increase in  $\Delta C_m$  at RT, the linear slope was positive ( $7.1 \pm 13.5$  fF/s,  $n = 13$ ), which significantly differed from the negative slope at BT ( $-2.7 \pm 3.2$  fF/s,  $n = 9$ ; K-W Test, belonging to different homogeneous subsets; **Suppl. Table 14**). While both typical  $I_{Ca}$  and averaged  $Q_{Ca}$  were similar during the first stimulus,  $Q_{Ca}$  showed a more pronounced decline at RT than at BT (**Fig. 39H, K**), as evident from  $\Delta Q_{(1-50)}$ , which was 47% smaller at BT compared to RT (RT,  $61.8 \pm 21.4$  pC,  $n = 13$ ; BT,  $32.0 \pm 9.5$  pC,  $n = 9$ ; K-W Test, belonging to different homogeneous subsets; **Suppl. Table 16**). Correspondingly, the total  $Q_{Ca}$  was 74% higher at BT ( $-3911 \pm 775$ ,  $n = 9$ ) than at RT ( $-2242 \pm 828$  pC,  $n = 13$ ; K-W Test, belonging to different homogeneous subsets; **Suppl. Table 15**). Efficiency showed a steeper initial decrease at BT (no statistical analysis conducted), and the total efficiency was significantly smaller at BT ( $9.3 \pm 2.8$  fF/pC,  $n = 9$ ) than at RT (RT,  $46.1 \pm 13.0$  fF/pC,  $n = 13$ ; in different homogeneous subsets; K-W Test, belonging to different homogeneous subsets; **Fig. 39L**; see Table **Suppl. Table 17**).

To conclude, the constant increase of  $\Delta C_m$  even after a total of 50 s of excessive stimulation suggests that at RT IHCs at both ages were capable of sustained release. In pre-mature IHCs, where exocytosis was temperature-sensitive, while endocytosis was not (cf. **Fig. 37C vs. E**), this might be due to the reduction of exocytosis at RT and thus slower depletion of the vesicle pool. However, contribution of possible additional endocytic processes switched on after long, intense stimulation cannot be excluded. In mature IHCs, the similar initial increase in  $\Delta C_m$  at both temperatures reflected the similar temperature-sensitivity of both exocytosis and endocytosis at this age (cf. **Fig. 37I vs. K**). An additional, highly temperature-sensitive, endocytosis process might be absent at RT and cause the further increase during later steps. Notably, the constant linear increase at RT added 2 pC to the total cell capacitance reflecting an enlargement of the IHC surface by ~23% (average  $C_m$  of mature IHCs: 8.8 pF; see **Materials and Methods – Patch clamp protocols and data analysis**).

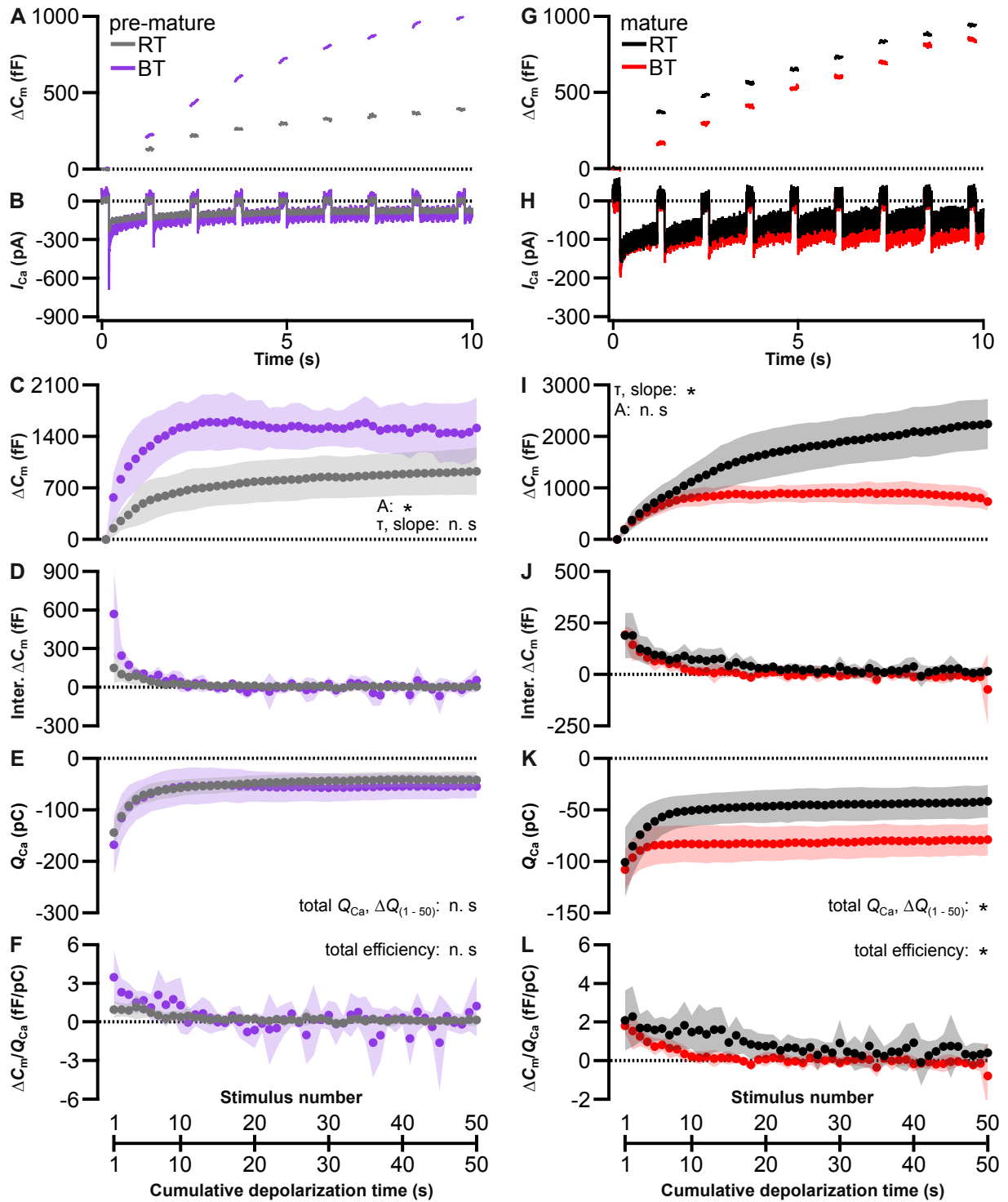


**Figure 39** Effect of temperature on release upon excessive stimulation of inner hair cells. The effect of temperature on sustained excessive release was studied in pre-mature and mature IHCs by application of 1-s repetitive voltage steps to 0 mV (200-ms interstimulus interval) compared with BT controls. Typical traces of the resulting  $\Delta C_m$  (**A**, **G**) and corresponding  $I_{Ca}$  (**B**, **H**) in response to the first eight stimuli are shown. Averaged cumulative  $\Delta C_m$  between voltage steps were compared for the exponential A and  $\tau$ , and linear slope resulting from fitting with an exponential-linear function (**C**, **I**). Interstep  $\Delta C_m$  are shown (**D**, **J**).  $Q_{Ca}$  was compared for the total  $Q_{Ca}$  and  $Q_{(1-50)}$  (**E**, **K**).  $\Delta C_m/Q_{Ca}$  was compared for the total  $\Delta C_m/Q_{Ca}$  (**F**, **L**). Data in **C-F** and **I-L**, given as mean  $\pm$  S.D., were compared using K-W test followed by analysis of homogeneous subsets. \*: significantly different, i.e. belonging to different subsets; n.s.: not significant, i.e. same subset. No. of cells (animals): pre-mature, RT = 11 (9); pre-mature, BT = 7 (6); mature, RT = 13 (9); mature, BT = 9 (9).

### 3.5.3 Effect of blocking dynamin on endocytosis of inner hair cells

Dynamin-1 plays a critical role in endocytosis of mature IHCs (Neef et al., 2014). In this study, I showed at mRNA and protein level that dynamin-1 was upregulated during maturation of IHCs, implying an increased importance of dynamin-1 for endocytosis after the onset of hearing (**Fig. 40, 41, 42**). To investigate the impact of dynamin-1 on endocytosis of pre-mature and mature IHCs, I recorded activity-dependent membrane capacitance, while using 30  $\mu\text{M}$  dyngo-4a in the pipette, blocking the GTPase function of dynamin-1/2 (McCluskey et al., 2013).

#### *Blocking dynamin decelerates endocytosis of mature but not pre-mature inner hair cells*

Endocytosis was recorded in IHCs kept at BT by measuring  $\Delta C_m$  and the corresponding  $I_{Ca}$  for 20 s following a single 100-ms depolarization to 0 mV (**Fig. 40**). The stimulus caused an instant increase in  $\Delta C_m$  reflecting exocytosis, followed by a slower decline reflecting endocytosis in presence of dyngo-4a in both pre-mature (**Fig. 40A, A'**) and mature IHCs (**Fig. 40G, G'**).

In pre-mature IHCs, dyngo-4a did not affect exocytosis, i.e. the peak  $\Delta C_m$  (control,  $35.8 \pm 18.9$  fF,  $n = 12$ ; dyngo-4a,  $24.6 \pm 14.8$  fF,  $n = 12$ ; K-W Test, belonging to the same homogeneous subset,  $p = 0.18$ ; **Fig. 40C; Suppl. Table 2**),  $I_{Ca}$ , or the resulting  $Q_{Ca}$  (control,  $-29.7 \pm 6.0$  pC,  $n = 12$ ; dyngo-4a,  $-28.4 \pm 7.6$  pC,  $n = 12$ ; K-W Test, belonging to the same homogeneous subset,  $p = 0.95$ ; **Fig. 40B, F; Suppl. Table 5**). Both the time to 0 (control,  $4.4 \pm 3.7$  s,  $n = 12$ ; dyngo-4a,  $4.0 \pm 3.6$  s,  $n = 12$ ; K-W Test, belonging to the same homogeneous subset,  $p = 0.55$ ; **Fig. 40D; Suppl. Table 3**) and the decline rate (control,  $10.0 \pm 3.9$  fF/s; dyngo-4a,  $4.8 \pm 4.7$  fF/s; K-W Test, belonging to the same homogeneous subset,  $p = 0.17$ ; **Fig. 40E; Suppl. Table 4**) were similar between dyngo-4a-treated and control IHCs, suggesting that in pre-mature IHCs the rate of endocytosis was not affected by the block of dynamin-1 function.

In mature IHCs, dyngo-4a reduced the peak  $\Delta C_m$  by 14% (control,  $50.0 \pm 13.2$  fF,  $n = 15$ ; dyngo-4a,  $42.8 \pm 9.7$  fF,  $n = 11$ ; K-W Test, belonging to different homogeneous subsets; **Fig. 40I; Suppl. Table 2**). The time to 0 was slightly but not significantly prolonged from  $4.0 \pm 1.3$  s in control IHCs ( $n = 15$ ) to  $6.2 \pm 1.9$  s in dyngo-4a-treated IHCs ( $n = 11$ ; K-W Test, belonging to the same homogeneous subset,  $p = 0.55$ ; **Fig. 40J; Suppl. Table 3**). These mild effects together resulted in a decline rate that was almost halved in presence of dyngo-4a (dyngo-4a,  $7.1 \pm 1.5$  fF/s,  $n = 11$ ) when compared to controls ( $13.4 \pm 6.2$  fF/s,  $n = 15$ ; K-W Test, belonging to different homogeneous subsets; **Fig. 40K; Suppl. Table 4**).  $I_{Ca}$  and averaged  $Q_{Ca}$  were both unaffected by dyngo-4a (control,  $-15.0 \pm 3.3$  pC,  $n = 15$ ; dyngo-4a,  $-15.1 \pm 3.4$  pC,  $n = 11$ ; K-W Test, belonging to the same homogeneous subset,  $p = 0.44$ ; **Fig. 40H, L; Suppl. Table 5**).

In summary, inhibition of dynamin using dyngo-4a slowed down endocytosis in mature IHCs, but did not affect pre-mature IHCs, which might be a result of the developmental increase of dynamin-1 expression in IHCs (cf. **Fig. 23A, 25, 26**).

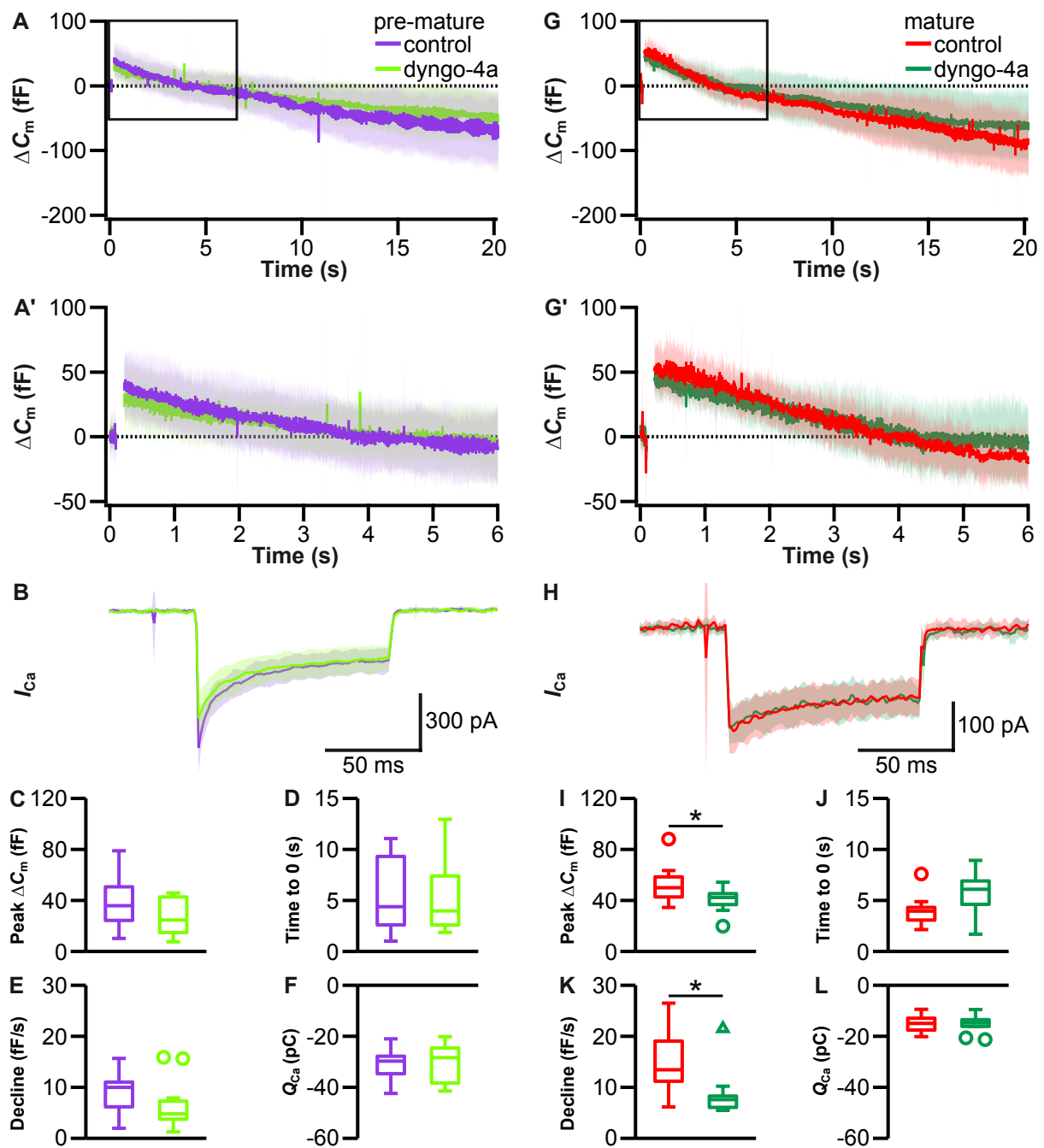


**Figure 40 Effect of dyngo-4a on endocytosis of inner hair cells.** To study the effect of dyngo-4a on endocytosis,  $\Delta C_m$  following a 100-ms depolarizing voltage step to 0 mV and the corresponding  $I_{Ca}$  were recorded for 20 s in pre-mature (**A-F**) and mature (**G-L**) IHCs at BT using 30  $\mu$ M dyngo-4a and compared with BT controls.  $\Delta C_m$  traces of the entire recording (**A**, **G**), enlarged first 6 s of the  $\Delta C_m$  traces (**A'**, **G'**; indicated by rectangles in **A** and **G**) and  $I_{Ca}$  elicited during the stimulus (**B**, **H**) are shown. In mature IHCs, application of dyngo-4a reduced the peak  $\Delta C_m$  (**I**) and the decline rate of  $\Delta C_m$  (**K**), but not the time to 0 (**J**) or the  $Q_{Ca}$  (**L**). In pre-mature IHCs, none of the tested parameters was affected by dyngo-4a (**C-F**). Traces are shown as mean  $\pm$  S.D.. Data were compared using K-W test followed by analysis of homogeneous subsets. \*: significantly different, i.e. belonging to different subsets. Triangle: extreme value (not included in statistics). Circles: outliers. No. of cells (animals): pre-mature, BT = 12 (9); pre-mature, dyngo-4a = 12 (11); mature, BT = 15 (11); mature, dyngo-4a = 11 (10).

*Blocking of dynamin affects moderate sustained release in mature but not pre-mature inner hair cells*

As shown above, endocytosis in response to a single depolarization was weakened by inhibition of dynamin in mature but not pre-mature IHCs. To determine whether the sustained release upon moderate stimulation is correspondingly affected by dyngo-4a, IHCs were stimulated by 50 repetitive 50-ms voltage steps to 0 mV (**Fig. 41**).

In pre-mature IHCs, the typical  $\Delta C_m$  trace of an IHC at P4 (**Fig. 41A**), and the average cumulative and interstep  $\Delta C_m$  were not affected by dyngo-4a (**Fig. 41C, D**). This was also evident from function fits, which were comparable between dyngo-4a-treated and control IHCs in their exponential amplitudes (control,  $825.1 \pm 232.9$  fF,  $n = 10$ ; dyngo-4a,  $627.5 \pm 428.3$  fF,  $n = 19$ ; K-W Test, belonging to the same homogeneous subset,  $p = 0.29$ ; **Suppl. Table 6**), time constants (control,  $5.7 \pm 1.8$  s,  $n = 10$ ; dyngo-4a,  $5.6 \pm 1.7$  s,  $n = 19$ ; K-W Test, belonging to the same homogeneous subset,  $p = 1.00$ ; **Suppl. Table 7**), and linear slopes (control,  $-6.9 \pm 40.4$  fF/s,  $n = 15$ ; dyngo-4a,  $-12.2 \pm 31.4$  fF/s,  $n = 19$ ; K-W Test, belonging to the same homogeneous subset,  $p = 0.76$ ; **Suppl. Table 8**). Notably,  $I_{Ca}$  inactivation of a typical pre-mature IHC was reduced in presence of dyngo-4a (**Fig. 41B**), which was confirmed by a preliminary analysis of  $I_{Ca}$  inactivation (conducted by Stephanie Eckrich, not shown). As a result, the total  $Q_{Ca}$  was 24% larger in presence of dyngo-4a ( $-573.9 \pm 190.9$  pC,  $n = 19$ ) than in controls ( $-461.1 \pm 196.7$  pC,  $n = 15$ ; K-W Test, belonging to different homogeneous subsets; **Fig. 41E**; **Suppl. Table 9**), whereas the decline  $\Delta Q_{(1-50)}$  was unaffected (control,  $10.0 \pm 2.1$  pC,  $n = 15$ ; dyngo-4a,  $7.4 \pm 4.9$  pC,  $n = 19$ ; K-W Test, belonging to the same homogeneous subset,  $p = 0.55$ ; **Suppl. Table 10**). The courses of efficiency were similar between control and dyngo-4a treated IHCs, while the total efficiency in the dyngo-4a group ( $29.1 \pm 11.0$  fF/pC,  $n = 19$ ) was reduced by 46% compared to the control group ( $54.3 \pm 18.1$  fF/pC,  $n = 15$ ; K-W Test, belonging to different homogeneous subsets; **Fig. 41F**; **Suppl. Table 11**), most likely resulting from the larger  $Q_{Ca}$ .

In mature IHCs, the  $\Delta C_m$  increase in presence of dyngo-4a was similar to controls during the initial few stimuli, as evident from typical  $\Delta C_m$  traces (dyngo-4a-treated IHC at P19; **Fig. 41G**) and the average cumulative  $\Delta C_m$  (**Fig. 41I**). However, while in controls the course of  $\Delta C_m$  slowed down to a linear increase after few stimuli, the dyngo-4a group showed an extended non-linear increase (**Fig. 41I**). Accordingly, in presence of dyngo-4a the exponential amplitude of the exponential-linear fit was increased by 60% (control,  $150.5 \pm 78.1$  fF,  $n = 14$ ; dyngo-4a,  $240.0 \pm 145.3$  fF,  $n = 14$ ; K-W Test, belonging to different homogeneous subsets; **Suppl. Table 6**) and its time constant was doubled (control,  $0.9 \pm 1.3$  s,  $n = 14$ ; dyngo-4a,  $2.1 \pm 1.6$  s,  $n = 14$ ; K-W Test, belonging to different homogeneous subsets; **Suppl. Table 7**). The slope of the

linear increase remained unchanged (control,  $23.5 \pm 7.8$  fF/s,  $n = 14$ ; dyngo-4a,  $27.8 \pm 20.5$  fF/s,  $n = 14$ ; K-W Test, belonging to the same homogeneous subset,  $p = 0.49$ ; **Suppl. Table 8**), but was only present during the last few stimuli in dyngo-4a-treated IHCs (**Fig. 41I**). The interstep  $\Delta C_m$  of the dyngo-4a group decreased slower than that of the control group (**Fig. 41J**; no statistical analysis), reflecting the course of cumulative  $\Delta C_m$ . In contrast to pre-mature IHCs,  $I_{Ca}$  (**Fig. 41H**) and the resulting total  $Q_{Ca}$  were not affected by dyngo-4a (control,  $-384.4 \pm 74.5$  pC,  $n = 14$ ; dyngo-4a,  $-345.3 \pm 69.4$  pC; K-W Test, belonging to the same homogeneous subset,  $p = 0.43$  or  $0.09$ ; **Fig. 41K**; **Suppl. Table 9**), so was  $\Delta Q_{(1-50)}$  (control,  $1.2 \pm 0.5$  pC,  $n = 14$ ; dyngo-4a,  $1.1 \pm 0.6$  pC,  $n = 14$ ; K-W Test, belonging to the same homogeneous subset,  $p = 0.87$ ; **Suppl. Table 10**). The total efficiency was increased by 58% in the dyngo-4a-treated group (control,  $41.6 \pm 12.7$  fF/pC,  $n = 14$ ; dyngo-4a,  $65.2 \pm 11.3$  fF/pC,  $n = 14$ ; K-W Test, belonging to different homogeneous subsets; **Fig. 41L**; **Suppl. Table 11**), most likely due to the slower decline of efficiency in presence of dyngo-4a (no statistical analysis conducted).

In summary, in pre-mature IHCs sustained release in response to moderate repetitive stimulation was not affected by inhibition of dynamin function, reflecting the low expression of dynamin-1 before the onset of hearing (cf. **Fig. 23A, 25**). In contrast, the extended non-linear increase of  $\Delta C_m$  in mature IHCs in presence of dyngo-4a suggests that suppression of dynamin activity weakened one or more endocytosis processes, potentially hampering replenishment of the RRP.

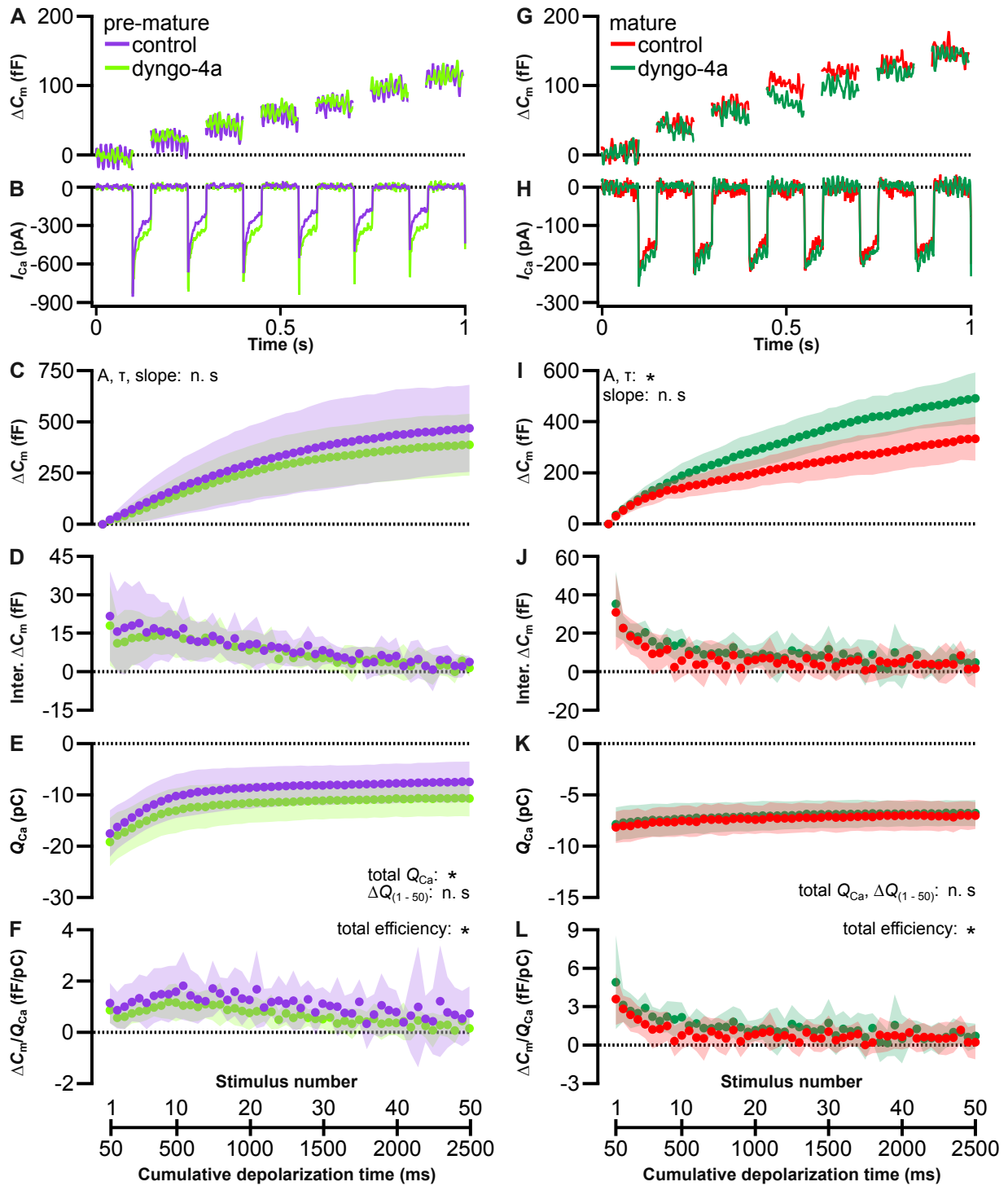


**Figure 41 Effect of dyngo-4a on sustained moderate release of inner hair cells.** The effect of dyngo-4a on sustained release upon moderate stimulation was studied in pre-mature and mature IHCs by application of repetitive 50-ms voltage steps to 0 mV (100-ms interstimulus interval) at BT in presence of 30  $\mu$ M dyngo-4a compared with BT controls. Typical traces of the resulting  $\Delta C_m$  (**A**, **G**) and corresponding  $I_{Ca}$  (**B**, **H**) in response to the first six stimuli are shown. Averaged cumulative  $\Delta C_m$  were compared for exponential A and  $\tau$ , and linear slope resulting from an exponential-linear (ten pre-mature and 14 mature control IHCs; 19 pre-mature and 14 mature IHCs treated with dyngo-4a) or a linear (five pre-mature control IHCs) fit (**C**, **I**). Interstep  $\Delta C_m$  is shown (**D**, **J**).  $Q_{Ca}$  was compared for the total  $Q_{Ca}$  and  $\Delta Q_{(1-50)}$  (**E**, **K**).  $\Delta C_m/Q_{Ca}$  was compared for the total  $\Delta C_m/Q_{Ca}$  (**F**, **L**). Data in **C-F** and **I-L**, given as mean  $\pm$  S.D., were compared using K-W test followed by analysis of homogeneous subsets. \*: significantly different, i.e. belonging to different subsets; n.s.: not significant, i.e. same subset. No. of cells (animals): pre-mature, BT = 15 (10); pre-mature, dyngo-4a = 19 (16); mature, BT = 14 (12); mature, dyngo-4a = 14 (12).

*Sustained release upon excessive repetitive stimulation is altered in inner hair cells in presence of dyngo-4a*

According to the previous section, sustained release from the RRP and thus potentially its replenishment was attenuated in mature but not pre-mature IHCs when blocking dynamin-1. To test how release upon excessive stimulation is affected, which has been proposed to trigger the SRP (Duncker et al., 2013; Johnson et al., 2005), IHCs were stimulated by long-lasting repetitive voltage steps (0 mV for 1 s; **Fig. 42**).

In pre-mature IHCs, while the cumulative  $\Delta C_m$  showed an initial steep increase followed by a subsequently linear course in both groups, the initial rise appeared steeper in presence of dyngo-4a (**Fig. 42C**), as indicated by a typical trace from a P5 IHC (**Fig. 42A**), and was followed by a steeper linear decline (**Fig. 42C**). The parameter of the exponential-linear fit did, however, not reach significance in exponential amplitude (control,  $1639 \pm 738$  fF,  $n = 7$ ; dyngo-4a,  $2147 \pm 372$  fF,  $n = 8$ ; K-W Test, belonging to the same homogeneous subset,  $p = 0.43$ ; **Suppl. Table 12**), time constant (control,  $3.9 \pm 2.9$  s,  $n = 7$ ; dyngo-4a,  $2.5 \pm 1.5$  s,  $n = 8$ ; K-W Test, belonging to the same homogeneous subset,  $p = 0.57$ ; **Suppl. Table 13**) and linear slope (control,  $-2.8 \pm 17.3$  fF/s,  $n = 7$ ; dyngo-4a,  $-17.9 \pm 11.2$  fF/s,  $n = 8$ ; K-W Test, belonging to the same homogeneous subset,  $p = 0.32$ ; **Suppl. Table 14**), probably due to the large variance of data. The resulting interstep  $\Delta C_m$  was also similar to the control (**Fig. 42D**). Notably, the difference between the maximum  $\Delta C_m$  and the  $\Delta C_m$  at the last, 50<sup>th</sup> stimulus ( $\Delta C_{(max-50)}$ ) in the dyngo-4a group ( $831.3 \pm 442.4$  fF,  $n = 8$ ) was almost ten times as high as in the control ( $85.7 \pm 494.0$  fF,  $n = 7$ ; Mann-Whitney  $U$  test,  $p = 0.04$ ), reflecting the plateau phase in controls compared to the prominent declining course in the dyngo-4a group (**Fig. 42 C**). The decline of  $\Delta C_m$  indicates that at least part of endocytosis was still functional and exceeded exocytosis in presence of dyngo-4a, suggesting depletion the SRP in pre-mature IHCs. Similar to moderate stimulation, the inactivation of  $I_{Ca}$  was slower in presence of dyngo-4a (**Fig. 42B**; analysis conducted by Stephanie Eckrich, data not shown), and the dyngo-4a group ( $-5518 \pm 942$  pC,  $n = 8$ ) had a total  $Q_{Ca}$  twice as large as the control group ( $-2838 \pm 1454$  pC,  $n = 7$ ; K-W Test, belonging to different homogeneous subsets; **Fig. 42E**; **Suppl. Table 15**), and a similar increase in  $\Delta Q_{(1-50)}$  (control,  $100.2 \pm 45.1$  pC,  $n = 7$ ; dyngo-4a,  $204.2 \pm 49.1$  pC,  $n = 8$ ; K-W Test, belonging to different homogeneous subsets; **Suppl. Table 16**). Although the initial value seemed larger (no statistical analysis conducted), the total efficiency in the dyngo-4a group ( $2.7 \pm 5.1$  fF/pC,  $n = 8$ ) was 85% smaller than the control group ( $20.2 \pm 12.6$  fF/pC,  $n = 7$ ; K-W Test, belonging to different homogeneous subsets; **Fig. 42F**; **Suppl. Table 17**).

For mature IHCs, no statistical analysis was performed for dyngo-4a group due to its low sample number ( $n = 4$ ). In presence of dyngo-4a, the average cumulative  $\Delta C_m$  probably had a

larger initial increase and required less time to reach the plateau phase (**Fig. 42I, J, L**) than in controls, indicating a predominance of exocytosis during initial stimuli, possibly due to dyngo-4a-dependent inhibition of endocytosis. The  $Q_{Ca}$  course was unchanged by dyngo-4a (**Fig. 42K**) compared to the control. More data are, however, required to confirm whether the changes in  $\Delta C_m$  were indeed an effect of the dyngo-4a treatment.

In summary, the decline in  $\Delta C_m$  upon excessive repetitive stimulation in presence of dyngo-4a suggests that sustained release led to depletion of the SRP in pre-mature IHCs. Since  $Ca^{2+}$  influx was increased by dyngo-4a in pre-mature IHCs, this effect might be due to an increase of  $Ca^{2+}$ -triggered exocytosis rather than a dyngo-4a related reduction of endocytosis, thereby causing faster exhaustion of the vesicle pool. The putatively faster and larger increase in  $\Delta C_m$  in the preliminary recordings of mature IHCs again suggest dynamin-dependence of endocytosis and possibly SRP replenishment at this age.

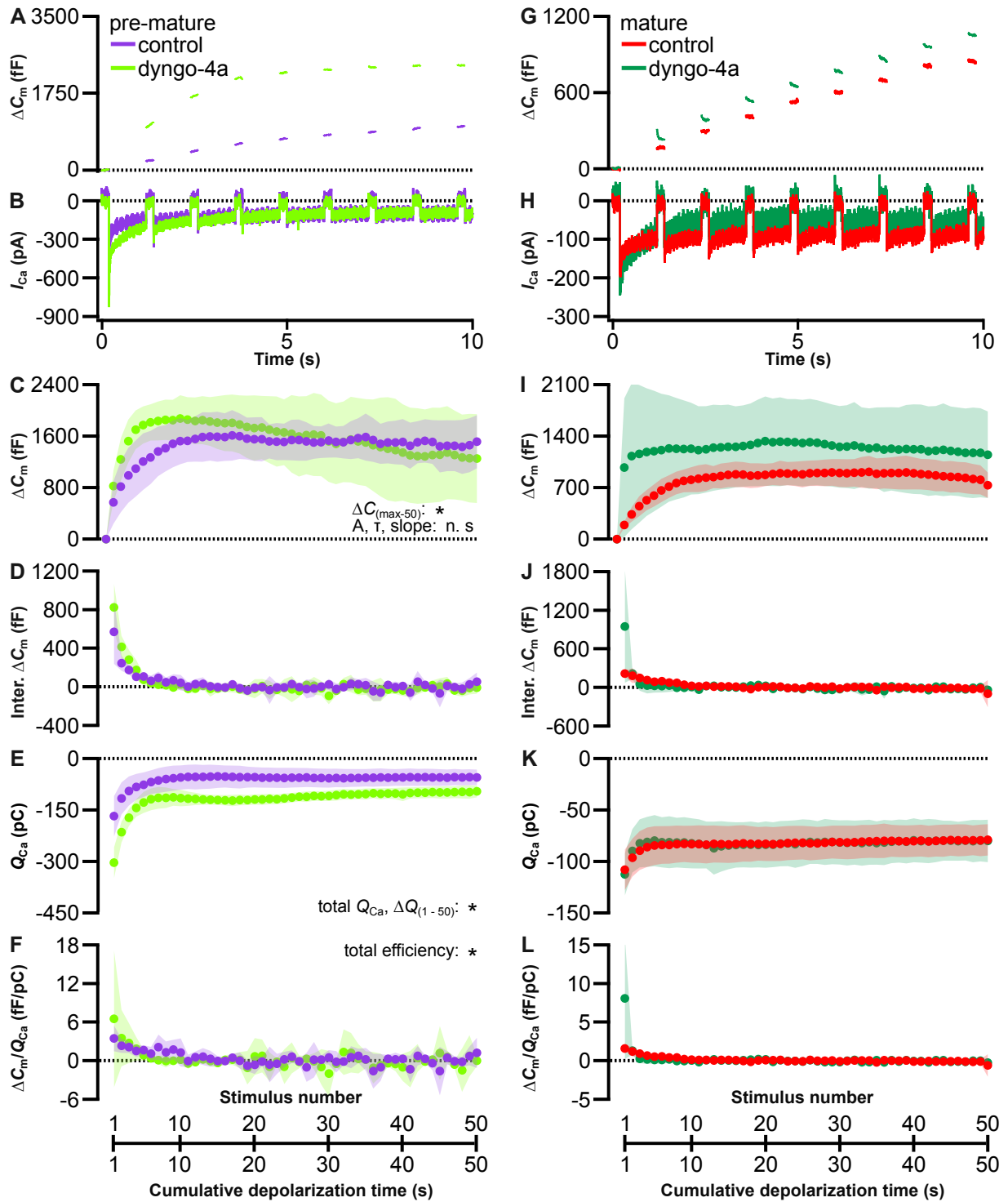


**Figure 42 Effect of dyngo-4a on sustained excessive release of inner hair cells.** The effect of dyngo-4a on sustained release upon excessive repetitive stimulation of the SRP was studied in pre-mature and mature IHCs by application of 1-s repetitive voltage steps to 0 mV (200-ms interstimulus interval) at BT in presence of 30  $\mu$ M dyngo-4a compared with BT controls. Typical traces of the resulting  $\Delta C_m$  (A, G) and corresponding  $I_{Ca}$  (B, H) in response to the first eight stimuli are shown. Averaged cumulative  $\Delta C_m$  were compared for the exponential A,  $\tau$ , and linear slope resulting from fitting with an exponential-linear function, and the difference between the maximum  $\Delta C_m$  and the  $\Delta C_m$  at the 50<sup>th</sup> step ( $\Delta C_{(max-50)}$ ) (C, I). Interstep  $\Delta C_m$  are shown (D, J).  $Q_{Ca}$  was compared for the total  $Q_{Ca}$  and  $\Delta Q_{(1-50)}$  (E, K).  $\Delta C_m/Q_{Ca}$  was compared for the total  $\Delta C_m/Q_{Ca}$  (F, L). Data in C-F and I-L are given as mean  $\pm$  S.D.. No statistic was performed for mature IHCs. Data of  $\Delta C_{(max-50)}$  were compared using Mann-Whitney  $U$  test, and the remaining data were compared using K-W test followed by analysis of homogeneous subsets. \*: significantly different (all data), i.e. belonging to different subsets (only Kruskal-Wallis test); n.s.: not significant, i.e. same subset. No. of cells (animals): pre-mature, BT = 7 (6); pre-mature, dyngo-4a = 8 (6); mature, BT = 9 (9); mature, dyngo-4a = 4 (3).

### 3.5.4 Low concentrated DMSO in inner hair cells does not affect the calcium current

The previous sections showed an increase of  $I_{Ca}$  in dyngo-4a-treated pre-mature IHCs due to reduced inactivation (Fig. 41B, E; 42B, E). Experiments with dyngo-4a were carried out in presence of 0.1% DMSO, whereas DMSO was absent from controls. This raises the question of whether DMSO, rather than dyngo-4a, increased  $I_{Ca}$  in pre-mature IHCs, despite being reported to have no effect on IHCs at such a low concentration (Qi et al., 2008). To rule out this possibility,  $I_{Ca}$  was recorded at BT in pre-mature IHCs with and without addition of 0.1% DMSO to the intracellular solution (Fig. 43). No difference was observed in  $Q_{Ca}$  in response to single depolarizing steps lasting 50 ms (control,  $-17.4 \pm 4.6$  pC,  $n = 9$ ; DMSO,  $-14.8 \pm 4.7$  pC,  $n = 8$ ; Mann-Whitney  $U$  test,  $U = 36$ ,  $p = 1.00$ ; Fig. 43A-B), 100 ms (control,  $-29.8 \pm 7.6$  pC,  $n = 9$ ; DMSO,  $-25.3 \pm 7.9$  pC,  $n = 8$ ; Mann-Whitney  $U$  test,  $U = 32$ ,  $p = 0.74$ ; Fig. 43B), and 1 s (control,  $-145.8 \pm 68.4$  pC,  $n = 9$ ; DMSO,  $-133.5 \pm 62.8$  pC,  $n = 8$ ; Mann-Whitney  $U$  test,  $U = 35$ ,  $p = 0.96$ ; Fig. 43B). This shows that the change in  $I_{Ca}$  observed in dyngo-4a-treated pre-mature IHCs was not caused by 0.1% DMSO, but attributable to a so far unknown effect of intracellular dyngo-4a.

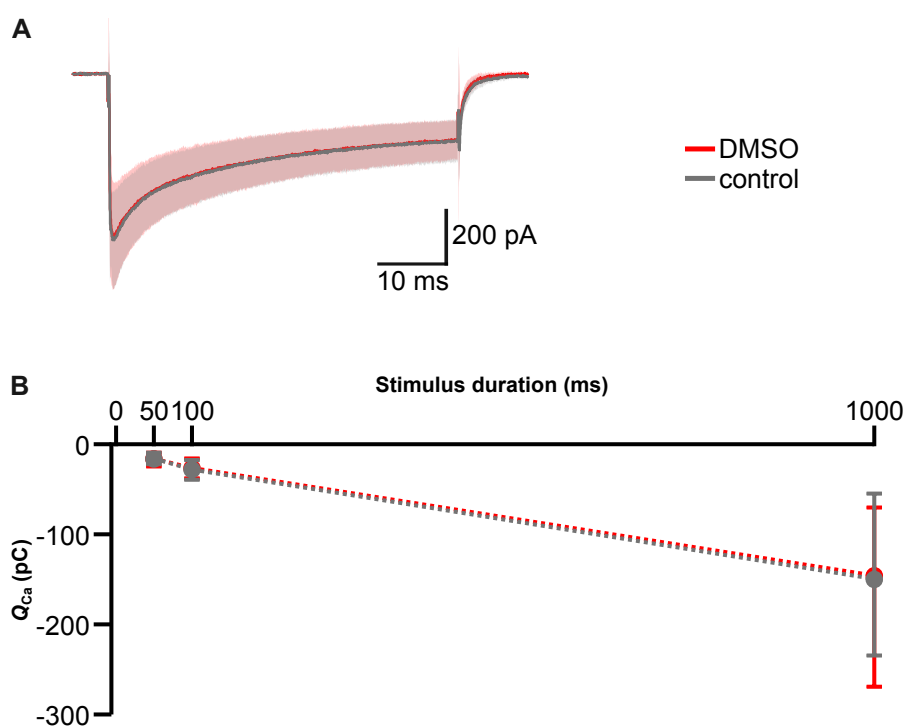


**Figure 43 Effect of DMSO on inner hair cells.**  $I_{Ca}$  traces (mean  $\pm$  S.D.) of pre-mature IHCs in response to a 50-ms voltage step to 0 mV at BT with and without 0.1% DMSO in the intracellular solution (A). Average  $Q_{Ca}$  was not affected by 0.1% DMSO for different stimulus durations (50 ms, 100 ms and 1 s; B). Data were compared using Mann-Whitney  $U$  test. No. of cells (animals): control = 9 (6); DMSO = 8 (6).

## 4 Discussion

This study is the first to systematically analyze the functional development of the endocytic machinery of mouse IHCs and the accompanying regulation of several endocytic proteins. Membrane capacitance recordings revealed an increased rate of endocytosis after the maturation of IHCs, which presumably led to more efficient replenishment of synaptic vesicle pools. The recordings also showed that the temperature-sensitivity of endocytosis increased during maturation, suggesting the developmental upregulation of temperature-sensitive proteins or mechanisms in the endocytic machinery of IHCs. Electrophysiological data were corroborated by *FISH* and immunohistochemistry revealing that mRNA transcription and protein expression of the endocytic protein dynamin-1 were developmentally upregulated in IHCs. Accordingly, inhibition of dynamin-1 by dyngo-4a impaired the endocytosis rate and the associated vesicle pool replenishment in mature IHCs to a greater extent than in pre-mature IHCs. Moreover, dyngo-4a caused an unexpected increase of  $\text{Ca}^{2+}$  influx that might partly or even largely account for the effect of dyngo-4a on endocytosis of pre-mature IHCs. In addition, dynamin-3 was predominantly expressed in OHCs before and after the onset of hearing. Due to its localization at the cuticular plate, dynamin-3 might serve a different purpose in OHCs, possibly for activity-independent endocytosis.

### 4.1 Endocytosis is enhanced after inner hair cell maturation

Terminal differentiation of IHCs comprises changes in various functions to assure highly efficient and indefatigable vesicle release after the onset of hearing. Whether compensatory endocytosis undergoes similar developmental changes is largely unknown. To this end, I used membrane capacitance recordings of pre-mature and mature IHCs at near-physiological temperature, i.e. BT, to measure endocytosis and the associated replenishment of the synaptic vesicle pool.

Endocytosis rates following stimulus-evoked exocytosis increased with IHC maturation. A linear decline of  $\Delta C_m$  following short stimuli (20 – 100 ms) – observed here at both ages – has previously been described in mature IHCs and was attributed to clathrin-mediated endocytosis (Jung et al., 2015; Kroll et al., 2019, 2020; Martelletti et al., 2020; Neef et al., 2014). Despite less exocytosis, the time to 0 in Jung et al. (2015), Kroll et al. (2019, 2020) and Neef et al. (2014) was significantly longer than that in the present study (~20 – 40 s vs. ~5 s). This is most likely due to different experimental conditions, as they performed perforated patch clamp at RT instead of whole-cell patch clamp at BT used here. Similarly, Martelletti et al. (2020) showed less exocytosis but a slightly longer time to 0 at near-physiological temperature compared to the result here, as they used 1.3 mM instead of 5 mM extracellular  $[\text{Ca}^{2+}]$  and IHCs from the basal cochlear coil rather than apical IHCs, which could have different endocytic

properties (Beutner et al., 2001; Johnson et al., 2008). In addition, in these studies, longer stimuli (200 ms – 1 s) added a rapid exponential decline, likely reflecting activity-dependent bulk retrieval, which could not be analyzed here for reasons of time. It would be worthwhile to conduct further experiments with long single stimuli to assess how bulk retrieval differs between pre-mature and mature IHCs.

The  $\text{Ca}^{2+}$  content in IHCs is a critical determinant of exocytosis and endocytosis. Here, stronger exocytosis after maturation of IHCs despite a smaller  $\text{Ca}^{2+}$  influx confirmed the increased  $\text{Ca}^{2+}$  sensitivity of exocytosis that allows precisely timed responses to an auditory stimulus (Beutner and Moser, 2001; Johnson et al., 2009, 2005; Wong et al., 2014; Zampini et al., 2010). Notably, endocytosis also became more  $\text{Ca}^{2+}$  sensitive after the onset of hearing, i.e. the rate of endocytosis was increased despite the smaller  $\text{Ca}^{2+}$  influx in mature IHCs.  $\text{Ca}^{2+}$  influx alone is not sufficient to trigger endocytosis without prior exocytosis (Wu et al., 2005; Yamashita et al., 2005). Moreover, exocytic proteins have been proposed to recruit endocytic proteins to the retrieval site, thereby initiating endocytosis (Pangrsic and Vogl, 2018). Thus, the increased  $\text{Ca}^{2+}$  sensitivity of endocytosis might be a secondary effect of the increased  $\text{Ca}^{2+}$  sensitivity of exocytosis in mature IHCs by strengthening the recruitment of endocytic proteins.

Despite the initial steep rise of  $\Delta C_m$  due to strong exocytosis, mature IHCs showed sustained release upon moderate repetitive stimulation, as evidenced by the continuing linear increase of  $\Delta C_m$  during the remaining recording. This suggests that mature IHCs are capable of maintaining enhanced rates of endocytosis resulting in an increased refilling of their constantly discharged RRP, thereby preventing depletion better than the low-rate endocytosis of pre-mature IHCs. A similar linear  $\Delta C_m$  course was found in previous studies using repetitive stimuli, whereas the initial rapid rise in  $\Delta C_m$  of mature IHCs was not observed (Duncker et al., 2013; Jeng et al., 2020; Johnson et al., 2008; Martelletti et al., 2020). The reason for this difference could be the different calcium concentrations: While these previous studies used an extracellular solution with 1.3 mM  $[\text{Ca}^{2+}]$  for patch clamp recording, here, 5 mM  $[\text{Ca}^{2+}]$  were used, affecting both exocytosis and endocytosis (Beutner et al., 2001; Johnson et al., 2005) and hence leading to different courses of  $\Delta C_m$ . In pre-mature IHCs, the saturating  $\Delta C_m$  course indicates RRP depletion, i.e. a reduction of exocytosis over time. This might be a result of slow endocytosis and, thus, insufficient RRP replenishment, when the RRP is stimulated repetitively. Alternatively, rather than being a direct result of slow endocytosis from the release site, it might be due to an insufficient vesicle reformation from another pool, such as the reserve pool or from endosomes (Chakrabarti and Wichmann, 2019). Moreover, the RRP of pre-mature IHCs might be smaller and therefore more likely to deplete than that of mature IHCs, which is supported by Johnson et al. (2009), who described a larger RRP size in mature than in pre-

mature gerbil IHCs. However, in another study the same authors found similar RRP sizes in mouse IHCs at both ages (Johnson et al., 2005). Notably, the course of pre-mature IHCs on pre-mature gerbil IHCs shown by Johnson et al. (2009) was linear instead of saturating, which again might be due to a lower  $\text{Ca}^{2+}$  concentration and thus less exocytosis requiring less endocytosis.

Upon excessive stimulation that challenged the SRP, the overall increase in  $\Delta C_m$  was smaller in mature IHCs compared to pre-mature IHCs, supporting that enhanced endocytosis in mature IHCs might replenish the SRP more efficiently and therefore prevent depletion of the vesicle pool and swelling of the IHC better than the slow endocytosis of pre-mature IHCs. Endocytosis in mature IHCs might further be accelerated by bulk retrieval recruited upon strong activity, thus restricting the total membrane enlargement induced by exocytosis (Neef et al., 2014). However, in previous studies using 1.3 mM  $[\text{Ca}^{2+}]$ , the overall increase of mature IHCs was comparable with or slightly exceeded that of pre-mature IHCs (Duncker et al., 2013; Johnson et al., 2009, 2008). The higher  $[\text{Ca}^{2+}]$  used in the present study might increase endocytosis of mature IHCs more than exocytosis, thereby resulting in this different course.

Excessive repetitive stimulation of mature IHCs eventually caused a slight decline in  $\Delta C_m$  (which was in the same range as the activity-independent  $\Delta C_m$  decline observed here in all groups), suggesting that during long-term activation endocytosis caught up with or even exceeded exocytosis. Again, this could be caused by activation of bulk retrieval initiating efficient retrieval of large membrane areas at once (Neef et al., 2014). Alternatively, excessive repetitive exocytosis might eventually deplete the SRP. This, however, is less likely since the maximum cumulative increase in  $\Delta C_m$  in mature IHCs at RT exceeded that at BT and still increased over time, implying that the SRP content was not yet exhausted at the end of the recording (cf. **Fig. 39**). Importantly, the decline in  $\Delta C_m$  was not caused by a reduced  $\text{Ca}^{2+}$  influx: Mature IHCs were able to maintain  $I_{\text{Ca}}$  during long-lasting repetitive stimuli, as previously described in gerbils (Johnson and Marcotti, 2008), supporting the continuous discharge of vesicles from the RRP and SRP (Duncker et al., 2013; Johnson et al., 2008; Neef et al., 2014).  $\Delta C_m$  also declined in pre-mature IHCs during later steps upon excessive stimulation, most likely due to SRP depletion caused by insufficient endocytosis from the release site or insufficient reformation of vesicles. Moreover, it cannot be excluded that the decline of  $\Delta C_m$  over time was related to the intracellular  $\text{Ca}^{2+}$  concentration of pre-mature IHCs:  $I_{\text{Ca}}$  declined over time upon intense repetitive stimulation as previously shown in pre-mature gerbil IHCs (Johnson and Marcotti, 2008). The accompanying decline in  $\text{Ca}^{2+}$  influx could reduce both exo- and endocytosis. Alternatively, while some  $\text{Ca}^{2+}$  buffering proteins such as calbindin-D28k are less expressed in mature IHCs than pre-mature IHCs, other  $\text{Ca}^{2+}$  buffering proteins such as

parvalbumin- $\alpha$  undergo up-regulation in mature IHCs (Hackney et al., 2005). Furthermore, mitochondria, which are critical for  $\text{Ca}^{2+}$  homeostasis in IHCs (Liu et al., 2022; O'Sullivan et al., 2023), are potentially upregulated in their amount during development of IHCs, since mature IHCs have more activity and therefore require more energy than pre-mature IHCs. In other words, pre-mature IHCs might have less  $\text{Ca}^{2+}$  buffering capacity than mature IHCs, causing  $\text{Ca}^{2+}$  accumulation in pre-mature IHCs during excessive repetitive stimulation and thus suppression of endocytosis as was found in retinal bipolar neurons and hippocampal neurons (Leitz and Kavalali, 2011; von Gersdorff and Matthews, 1994). The resulting reduced vesicle replenishment could ultimately cause vesicle pool depletion, thereby reducing exocytosis. In order to verify this assumption, further experiments should address the  $\text{Ca}^{2+}$  concentration in IHCs during excessive repetitive stimulation, e.g. by  $\text{Ca}^{2+}$  imaging. Notably, the late-onset decline of  $\Delta C_m$  was not observed during intense stimulation in previous studies on IHCs at both ages, where less  $\text{Ca}^{2+}$  was used and IHCs were stimulated only 35 instead of 50 times, which was most likely not intensive enough to trigger this phenomenon (Duncker et al., 2013; Johnson et al., 2008).

In summary, faster compensatory endocytosis in mature IHCs presumably allows them to maintain the release of neurotransmitters better than pre-mature IHCs, and thus to fulfill their function of continuously transmitting acoustic information, even at high intensity, in hearing mice (Neef et al., 2014). Although pre-mature IHCs have slower endocytosis, this is likely sufficient to ensure the release of neurotransmitter during the generation of action potentials required for terminal differentiation of the auditory system (Johnson et al., 2013, 2007).

#### **4.2 Endocytosis in inner hair cells at different ages is differently affected by temperature**

Despite being highly temperature-sensitive (Delvendahl et al., 2016; Nouvian, 2007), the synaptic function of IHCs has often been studied at RT due to the challenging recording conditions at BT (Jung et al., 2015; Kroll et al., 2019, 2020; Neef et al., 2014). This study provides the first direct comparison of endocytosis and sustained release at BT versus RT in pre-mature and mature IHCs.

The temperature-dependent enhancement of exocytosis following a single stimulus in both mature and pre-mature IHCs is in agreement with previous studies on mature IHCs and other cells (Feng et al., 2022; Nouvian, 2007; Renström et al., 1996). In contrast, compensatory endocytosis was enhanced with temperature solely after the onset of hearing, but was temperature-insensitive in pre-mature IHCs. Similarly, in the Calyx of Held, a faster endocytic component only present at BT was augmented with maturation (Renden and von Gersdorff,

2007). The temperature dependence of exocytosis and endocytosis could be (at least partly) due to the changes of  $I_{Ca}$  at different temperatures. Indeed,  $Ca^{2+}$  influx was largely reduced at RT in pre-mature IHCs, whereas that of mature IHCs was barely affected, as previously shown in gerbils (Johnson and Marcotti, 2008). The strong reduction in  $I_{Ca}$  found here could thus explain the temperature-sensitivity of exocytosis in pre-mature IHCs, whereas the finding that endocytosis was not reduced suggests that the endocytic rate of pre-mature IHCs is less affected by  $Ca^{2+}$ . In mature IHCs, the largely unaffected  $I_{Ca}$  suggests that the temperature-sensitivity of exocytosis and endocytosis is independent from  $Ca^{2+}$  influx. Similarly, Nouvian (2007) demonstrated in mature IHCs, that the small increase of  $I_{Ca}$  could only partially explain the large increase in exocytosis when changing from ambient to physiological temperature. Delvendahl et al. (2016) suggested that the temperature-sensitivity of endocytosis might be partly caused by the highly temperature-dependent GTPase activity of dynamin. Thus, the higher expression of dynamin-1 upon maturation shown here might explain the stronger temperature dependence of endocytosis of mature IHCs compared to pre-mature IHCs. Moreover, the temperature-dependence of endocytosis is also mediated by an increased fluidity of the lipid membrane (Faghihi Shirazi et al., 1982). Given that cholesterol, which reduces the fluidity of membranes (Yang et al., 2016), is present in the membrane of mature IHCs (Forge, 1987; Kimitsuki, 2017), it would be interesting to analyze whether pre-mature and mature IHCs have a different cholesterol content in their cell membrane, thereby contributing to the different temperature dependence of endocytosis.

Since exocytosis governs RRP release, and endocytosis potentially controls RRP replenishment, sustained release upon moderate repetitive stimulation should be affected by temperature as well. Indeed, when triggering the RRP at RT, the increase of  $\Delta C_m$  at both ages was slowed down to a mainly linear course. This was most likely due to the strong reduction of exocytosis, suggesting that endocytosis (despite being reduced in mature IHCs) was able to compensate for the rate of exocytosis already during the initial stimuli. Previous studies on mature IHCs showed an rapid non-linear increase of  $\Delta C_m$  during RRP stimulation at RT (Jean et al., 2018; Kroll et al., 2020). This contrast to our results could be due the use of perforated patch clamp recordings, which maintain the integrity of cytoplasmic components better than whole-cell recordings including the exocytic and endocytic machinery (Lippiat, 2009). Consequently, exocytosis and endocytosis functioned potentially better, causing a different course of  $\Delta C_m$  compared to the present study. Similar to IHCs, RRP replenishment of mature chromaffin cells and hippocampal neurons is accelerated with rising temperature (Dinkelacker et al., 2000; Pyott and Rosenmund, 2002). In pre-mature IHCs, the absence of the fast initial rise of  $\Delta C_m$  at RT, as opposite to its presence at BT, could be partly explained by the reduction of  $I_{Ca}$  during the first stimuli. Compared to that at BT,  $I_{Ca}$  at RT exhibited moreover reduced

inactivation. Similarly, slower inactivation kinetics of L-type  $\text{Ca}^{2+}$  channels at lower temperatures have been shown in rat IHCs, rat smooth muscle cells and rainbow trout atrial myocytes (Grant and Fuchs, 2008; Shiels et al., 2000; Wang et al., 1991). In addition, since  $\text{Ca}^{2+}$  influx was not reduced in mature IHCs, it cannot account for the effect of temperature on the  $\Delta C_m$  course at this age.

When excessive repetitive stimulation was applied, potentially triggering the SRP in pre-mature IHCs, the reduced  $\Delta C_m$  increase again reflected smaller exocytosis at RT and thus low, temperature-insensitive endocytosis was likely still able to sufficiently replenish the SRP even upon long-term excessive stimulation, similar to the RRP. In mature IHCs, the reduction of both exocytosis and endocytosis resulted in a similar initial course of  $\Delta C_m$  at RT compared to BT. However, the subsequent constant increase at RT suggests that upon several repetitions of stimulation, endocytosis was impaired so that exocytosis greatly exceeded endocytosis. This could be attributed to lack of bulk retrieval, which previously has been suggested to be reduced or even completely abolished at RT in the calyx of Held (Renden and von Gersdorff, 2007). Furthermore, bulk endocytosis could involve ultrafast endocytosis mechanisms that appear exclusively at BT (Delvendahl et al., 2016; Watanabe et al., 2013), although another study suggested that ultrafast endocytosis is almost unaffected by temperature (Chanaday and Kavalali, 2018). Different to the non-saturating course observed here, a saturating increasing course of  $\Delta C_m$  of mature IHCs at RT was observed in a previous study (Neef et al., 2014). This could be caused by the interstep interval, which was twice as long as in the present study, thus allowing a longer time for endocytosis between each exocytosis event and diminishing the increase in  $\Delta C_m$ . Notably, upon excessive stimulation,  $\text{Ca}^{2+}$  influx of pre-mature IHCs was no longer temperature-sensitive, whereas in mature IHCs it strongly declined over time at RT, both contrasting the behavior of  $I_{\text{Ca}}$  upon single or short-term repetitive stimulation (see above). In pre-mature IHCs, this effect might be due to a failure of  $\text{Ca}_v1.3$  channels to recover from inactivation after the first stimulus at ambient temperature. Accordingly, a previous study on  $\text{Ca}_v3.3$  showed that its recovery from inactivation is significantly decelerated when reducing temperature (Iftinca et al., 2006). Despite weaker inactivation, the  $\text{Ca}^{2+}$  influx upon excessive stimulation declined more prominent in mature IHCs at RT compared with BT, the cause of which remains to be elucidated.

In conclusion, different temperature-sensitivities of exocytosis and endocytosis at different developmental stages fundamentally affected sustained release upon moderate and excessive stimulation in IHCs, thus highlighting the necessity to conduct patch clamp experiments at near-physiological temperature despite technical challenges.

### 4.3 Expression of endocytic proteins is developmentally regulated in inner hair cells

The process of endocytosis depends on the collaboration of various endocytic proteins. Therefore, the functional differences in endocytosis found between pre-mature and mature IHCs potentially reflect the differential regulation of endocytic proteins. Indeed, the abundance and spatial distribution of mRNA transcripts of *dnm1*, *dnm3*, and *sh3gl2* in IHCs differed at single-cell level between developmental stages, as shown by quantitative *FISH* on whole-mount tissue. These findings confirm and add spatial information to previous RNA-sequencing and DNA-microarray studies on pooled cells isolated from the OC (Li et al., 2018; Liu et al., 2014; Wiwatpanit et al., 2018). Furthermore, immunohistochemistry confirmed a difference in the abundance and localization of dynamin-1 and dynamin-3 proteins in pre-mature and mature IHCs.

In early postnatal pre-mature IHCs, dynamin-1 protein was weakly expressed in IHCs despite the relatively high transcription of *dnm1* mRNA, whereas in mature IHCs, the high expression of dynamin-1 was in line with the developmentally increased transcription rate of *dnm1*. This indicates that dynamin-1 abundance builds up slowly during progression of terminal differentiation. Similarly, increased mRNA transcription preceded increased translation of dynamin-1 during maturation of spinal neurons (Noakes et al., 1999). The exact correlation between transcription and translation of dynamin-1 at different time points remains to be determined, for example by closely examining the transcription and translation profiles of OCs at several time points of terminal differentiation. Given that RNAscope™ allows immunolabeling after *FISH*, both profiles could be examined within the same specimen at a given time point. The developmental upregulation of dynamin-1 is also present in the rat brain and in the calyx of Held (Faire et al., 1992; Fan et al., 2016). This has been proposed to contribute to an increase in the vesicle retrieval capacity, resulting in more efficient and less saturable endocytosis, thereby ensuring intensive neurotransmitter release (Renden and von Gersdorff, 2007). Thus, the increase in dynamin-1 expression found here might ensure the ability of IHCs to retrieve the large amounts of vesicle membrane arising after maturation.

Dynamin-3 was weakly expressed on mRNA and protein levels in IHCs at both ages, which is consistent with a previous study that observed sparse dynamin-3 content in mature IHCs (Ting Cai et al., 2015). In contrast, Neef et al. (2014) found relatively strong expression of dynamin-3 in mature IHCs using the same antibody used in the present study. Here, dynamin-3 signals were detected in IHCs in only seven out of 32 experiments, regardless of developmental state and fixative (EtOH or Zamboni's fixative). Notably, IHCs never contained dynamin-3 labeling when the primary antibody was incubated for 90 min at RT (ten experiments) instead of overnight at 4 °C. A possible explanation for the discrepancy to Neef et al. (2014) could thus

be that they incubated the primary antibody overnight, which was moreover less diluted (1:1000) than in the present study (1:2000). Alternatively, the different mouse strains used in both studies (C57BL/6 in Neef et al. (2014) vs. NMRI used here) might express different levels of dynamin-3 in IHCs. Together with the low *dmn3* mRNA abundance, this heterogeneous labeling pattern likely reflects a generally low expression of dynamin-3 in IHCs, suggesting that dynamin-3 contributes little to activity-dependent endocytosis in IHCs.

IHCs at both ages contained *sh3gl2* mRNA, but the localization and abundance of endophilin-A1 was not studied here due to the lack of a commercially available antibody suitable for immunolabeling (this study and Kroll et al. (2019)). Kroll et al. (2019) showed the expression of endophilin-A1 in lysates of mature cochleae and, using knock-out (KO) mice, demonstrated its essential role in endocytosis of mature IHCs. The subcellular localization and function of endophilin-A1 in pre-mature IHCs remains, however, to be determined.

Like dynamin-1, another endocytic protein, ap-180, was increasingly expressed with maturation of IHCs in the present study. Mature IHCs from ap-180-KO mice showed impaired endocytosis and vesicle reformation (Kroll et al., 2020), emphasizing its crucial role in mature IHCs. The developmentally increased abundance of dynamin-1 and ap-180 found in this study supports previous studies showing upregulation of several endocytic proteins in mature IHCs (Beurg et al., 2010; Duncker et al., 2013; Jean et al., 2023; Roux et al., 2006).

The strong expression of dynamin-1 and dynamin-3 in NFs below IHCs at both ages confirms the findings of Neef et al. (2014) in mature OCs. *Dnm1* and *dnm3* mRNA was absent from these NFs but enriched in the somata of SGNs, suggesting that dynamin-1 and dynamin-3 found in NFs originate in the SGN soma, where they are synthesized before being transported to the afferent terminal.

In conclusion, the developmentally increased abundance of endocytic proteins observed here could contribute to the strengthened efficiency of endocytosis found upon maturation of IHCs (Renden and von Gersdorff, 2007).

#### **4.4 Blocking dynamin differentially affects endocytosis of pre-mature and mature inner hair cells**

The impact of developmental upregulation of dynamin-1 on the endocytosis function of IHCs at different ages was analyzed using dyngo-4a that blocks dynamin-1/2 (McCluskey et al., 2013). In pre-mature IHCs, inhibition of dynamin caused no difference in endocytosis following single-stimulus induced exocytosis, or in sustained release upon moderate repetitive

stimulation, which has previously been proposed to trigger RRP release and replenishment (Duncker et al., 2013; Johnson et al., 2009, 2005). This supports the weak expression of dynamin-1 in pre-mature IHCs (cf. **Fig. 23A, 25**) and suggests that endocytosis of pre-mature IHCs might largely operate in a dynamin-independent manner (Wu et al., 2014; Xu et al., 2008). Possible dynamin-independent mechanisms include kiss-and-run endocytosis (Chakrabarti et al., 2022; Graham et al., 2002) or expression of an alternative GTPase in IHCs such as Rab5 despite its low abundance in the basal pole (Shi and Nuttall, 2006), which has been shown to regulate dynamin-independent endocytosis in cortical astrocytes (Jiang and Chen, 2009). Despite its presence in pre-mature IHCs (Kolla et al., 2020), dynamin-2 is unlikely to replace dynamin-1 function, because its function is also blocked by dyngo-4a (McCluskey et al., 2013).

In contrast to moderate stimulation, the  $\Delta C_m$  course upon excessive repetitive stimulation was affected by dynamin-block in pre-mature IHCs, causing a stronger decline of  $\Delta C_m$  over time. This is unlikely to be an effect directly related to dynamin function in endocytosis due to its low expression in pre-mature IHCs (see above). The effect can, however, be explained by the off-target increase of  $Ca^{2+}$  currents by dyngo-4a firstly found in this study (cf. **Fig. 42B, E**), thereby boosting exocytosis (Johnson et al., 2005). If pre-mature endocytosis is functional but insufficient to retrieve the additionally released vesicle membrane, this would cause an initially overshooting increase in  $\Delta C_m$  followed by emptying of the SRP and thus a decline in  $\Delta C_m$ . A similar effect was observed in a previous study using dynasore, an analog of dyngo-4a that also blocks dynamin (Duncker et al., 2013). The underlying mechanism of the increased calcium charge due to a weakened inactivation of  $Ca_v1.3$  channels by dyngo-4a is still unclear.

In mature IHCs, the rate of endocytosis was reduced by dynamin block. Similarly, a deceleration of endocytosis by dyngo-4a and dynasore was previously shown in mature IHCs and central synapses, respectively (Delvendahl et al., 2016; Neef et al., 2014). The reduced endocytosis was reflected in the  $\Delta C_m$  course of sustained release upon moderate repetitive stimulation of the RRP: The continuing non-linear rise in  $\Delta C_m$  in presence of dyngo-4a (as opposed to the linear increase following an initial short non-linear rise found in controls) suggested that the presumably unchanged exocytosis was higher than the reduced endocytosis. In contrast, blocking dynamin using dynasore did not alter the course of  $\Delta C_m$  in the study of Duncker et al. (2013), when triggering the RRP. This discrepancy could be due to their use of a lower extracellular  $[Ca^{2+}]$  or a different mouse strain.

Sustained release following excessive stimulation in mature IHCs was presumably affected more severe by dynamin block. Although the amount of data upon excessive repetitive stimulation under dyngo-4a in mature IHCs was insufficient for statistical analysis, it showed

that the initial increase of  $\Delta C_m$  was substantially larger than in controls, possibly as a result of impaired compensatory endocytosis. Similarly, Neef et al. (2014) showed that IHCs treated with dyngo-4a had higher (not statically significant) cumulative  $\Delta C_m$  than control IHCs treated with dyngo-8a, an inactive dyngo-4a analog. In contrast, according to Duncker et al. (2013), the increase of  $\Delta C_m$  using dynasore was significantly smaller than in controls, which might be due to the off-target effects (e.g. disruption of lipid rafts) and higher cytotoxicity of dynasore compared to dyngo-4a (McCluskey et al., 2013; Park et al., 2013; Preta et al., 2015a, 2015b). Moreover, the higher concentration of dynasore and its application in the extracellular solution used by Duncker et al. (2013) potentially affected the cell and the surrounding tissue more severely.

In summary, reduced endocytosis and a possibly related delay in vesicle pool replenishment in presence of dyngo-4a, together with increased expression of dynamin-1, demonstrates a greater participation of dynamin in endocytosis in mature than in pre-mature IHCs.

#### **4.5 Endocytic proteins in outer hair cells**

In contrast to the sound-encoding IHCs, the sound-amplifying OHCs have fewer ribbon synapses, and smaller  $Ca^{2+}$  currents, implying less exocytosis (Knirsch et al., 2007). Reflecting the differences in their functions and the need for endocytosis balancing exocytosis, this study shows that OHCs had different expression and developmental regulation of endocytic proteins compared to IHCs: Expression of *dnm1*/dynamin-1 and *sh3gl2* was lower in OHCs than in IHCs, and that of *dnm1*/dynamin-1 was further reduced upon maturation, whereas expression of *dnm3*/dynamin3 was higher in OHCs than in IHCs regardless of age. The expression of dynamin-3 in both the soma and at the edge of the cuticular plate of OHCs contradicts a previous study, where dynamin-3 expression was confined to the stereocilia (Li et al., 2018). This discrepancy might be caused by the use of different antibodies generated from different immunogens (rat dynamin-3 amino acid 623-639 in Li et al., 2018; mouse dynamin-3 amino acid 773-794 in the present study), which might bind to different splice variants of *dnm3* (Cao et al., 1998). However, its presence, location and function in OHCs demand further study, e.g. by immunohistochemistry using antibodies generated against specific variants and by analyzing the impact of dynamin-3 loss. The differential regulation of endocytic proteins between IHCs and OHCs is a consequence of their functional differentiation from physiologically similar precursor cells (Kuhn et al., 2011), which is driven by the synergy of several regulators: Some of them are shared by both HC types, such as the transcription factor *atoh1* (Bermingham et al., 1999) and microRNA-96 (Kuhn et al., 2011); others are involved in only one of the two HC types, such as *tbx2* in IHCs suppressing the expression of OHC-specific genes (García-Añoveros et al., 2022), and *insm1* and *ikzf2* in OHCs, both of which induce

OHC-specific genes and simultaneously suppress IHC-specific genes (Chessum et al., 2018; Wiwatpanit et al., 2018).

One site of endocytosis in OHCs is their apical pole, where activity-independent endocytosis has been proposed to recycle proteins from the stereocilia, such as plasma-membrane  $\text{Ca}^{2+}$  ATPase (Grati et al., 2006; Griesinger et al., 2004; Kaneko et al., 2006), or might mediate otoprotective uptake of heat shock protein similar to utricle hair cells (Breglio et al., 2020). Moreover, vesicle transport, implying exocytosis and endocytosis, has been observed beneath the cuticula plate of bullfrog vestibular hair cells, and vesicles of various sizes are found circumscribing the cuticular plate (Kachar et al., 1997). The expression of dynamin-3 at the edge of the cuticular plate of OHCs at both ages found in the present study suggests its function in apical endocytosis.

Another location of endocytosis is the basal pole of OHCs, where endocytosis is stronger than at the apical pole (Harasztosi et al., 2021; Harasztosi and Gummer, 2019), possibly requiring not only dynamin-3, but also dynamin-1 and endophilin-A1. Notably, the transcription of all endocytic protein genes examined in this study (not reaching significance for *sh3gl2*) was developmentally downregulated in OHCs. This reflects that OHCs are synaptically more active before than after the onset of hearing: In pre-mature OHCs spontaneous action potential activity and accompanying exocytosis induce refinement of their afferent pathway (Beurg et al., 2008; Ceriani et al., 2019); in contrast, mature OHCs are less active and have been proposed to mediate noise-induced trauma via type II afferent neurons (Liu et al., 2015). Since trauma reporting requires infrequent activity and type II SGNs are slower and less abundant than type I SGNs, synapses become smaller and fewer along with reduced  $\text{Ca}^{2+}$  currents in mature OHCs (Ceriani et al., 2019; Reid et al., 2004). This suggests that compared to pre-mature OHCs, mature OHCs have less exocytosis, requiring less compensatory endocytosis and thus smaller amounts of endocytic proteins, which is consistent with the findings in the present study. Notably, reduced dynamin-1 activity due to a point mutation in mature OHCs did not impact distortion product otoacoustic emissions, reflecting an unaffected OHC amplifier function (Boumil et al., 2010). This demonstrates that dynamin-1 is not a critical factor for OHC amplifying function.

## 5 References

1. Abe, T., Kakehata, S., Kitani, R., Maruya, S., Navaratnam, D., Santos-Sacchi, J., & Shinkawa, H. (2007). Developmental Expression of the Outer Hair Cell Motor Prestin in the Mouse. *The Journal of Membrane Biology*, 215(1), 49–56. <https://doi.org/10.1007/s00232-007-9004-5>
2. Anthwal, N., & Thompson, H. (2016). The development of the mammalian outer and middle ear. *Journal of Anatomy*, 228(2), 217–232. <https://doi.org/10.1111/joa.12344>
3. Ashmore, J. (2008). Cochlear Outer Hair Cell Motility. *Physiological Reviews*, 88(1), 173–210. <https://doi.org/10.1152/physrev.00044.2006>
4. Basch, M. L., Brown, R. M., Jen, H.-I., & Groves, A. K. (2016). Where hearing starts: The development of the mammalian cochlea. *Journal of Anatomy*, 228(2), 233–254. <https://doi.org/10.1111/joa.12314>
5. Bermingham, N. A., Hassan, B. A., Price, S. D., Vollrath, M. A., Ben-Arie, N., Eatock, R. A., Bellen, H. J., Lysakowski, A., & Zoghbi, H. Y. (1999). Math1: An Essential Gene for the Generation of Inner Ear Hair Cells. *Science*, 284(5421), 1837–1841. <https://doi.org/10.1126/science.284.5421.1837>
6. Berod, A., Hartman, B. K., & Pujol, J. F. (1981). Importance of fixation in immunohistochemistry: Use of formaldehyde solutions at variable pH for the localization of tyrosine hydroxylase. *Journal of Histochemistry & Cytochemistry*, 29(7), 844–850. <https://doi.org/10.1177/29.7.6167611>
7. Beurg, M., Michalski, N., Safieddine, S., Bouleau, Y., Schneggenburger, R., Chapman, E. R., Petit, C., & Dulon, D. (2010). Control of exocytosis by synaptotagmins and otoferlin in auditory hair cells. *The Journal of Neuroscience: The Official Journal of the Society for Neuroscience*, 30(40), 13281–13290. <https://doi.org/10.1523/JNEUROSCI.2528-10.2010>
8. Beurg, M., Safieddine, S., Roux, I., Bouleau, Y., Petit, C., & Dulon, D. (2008). Calcium- and Otoferlin-Dependent Exocytosis by Immature Outer Hair Cells. *Journal of Neuroscience*, 28(8), 1798–1803. <https://doi.org/10.1523/JNEUROSCI.4653-07.2008>
9. Beutner, D., & Moser, T. (2001). The presynaptic function of mouse cochlear inner hair cells during development of hearing. *The Journal of Neuroscience: The Official Journal of the Society for Neuroscience*, 21(13), 4593–4599.
10. Beutner, D., Voets, T., Neher, E., & Moser, T. (2001). Calcium dependence of exocytosis and endocytosis at the cochlear inner hair cell afferent synapse. *Neuron*, 29(3), 681–690.
11. Boumil, R. M., Letts, V. A., Roberts, M. C., Lenz, C., Mahaffey, C. L., Zhang, Z.-W., Moser, T., & Frankel, W. N. (2010). A missense mutation in a highly conserved alternate exon of dynamin-1 causes epilepsy in fitful mice. *PLoS Genetics*, 6(8). <https://doi.org/10.1371/journal.pgen.1001046>
12. Brandt, A., Khimich, D., & Moser, T. (2005). Few CaV1.3 Channels Regulate the Exocytosis of a Synaptic Vesicle at the Hair Cell Ribbon Synapse. *Journal of Neuroscience*, 25(50), 11577–11585. <https://doi.org/10.1523/JNEUROSCI.3411-05.2005>
13. Brandt, A., Striessnig, J., & Moser, T. (2003). CaV1.3 channels are essential for development and presynaptic activity of cochlear inner hair cells. *The Journal of Neuroscience: The Official Journal of the Society for Neuroscience*, 23(34), 10832–10840.
14. Breglio, A. M., May, L. A., Barzik, M., Welsh, N. C., Francis, S. P., Costain, T. Q., Wang, L., Anderson, D. E., Petralia, R. S., Wang, Y.-X., Friedman, T. B., Wood, M. J. A., & Cunningham, L. L. (2020). Exosomes mediate sensory hair cell protection in the inner

- ear. *The Journal of Clinical Investigation*, 130(5), 2657–2672.  
<https://doi.org/10.1172/JCI128867>
15. Brown, M. C., & Santos-Sacchi, J. (2013). Chapter 25—Audition. In L. R. Squire, D. Berg, F. E. Bloom, S. du Lac, A. Ghosh, & N. C. Spitzer (Eds.), *Fundamental Neuroscience (Fourth Edition)* (pp. 553–576). Academic Press. <https://doi.org/10.1016/B978-0-12-385870-2.00025-1>
  16. Cai, T., Chen, Z., Gu, X., Zhang, X., & Yuan, W. (2015). [Expression of Dynamin in the cochlea of mice of different ages]. *Zhonghua Er Bi Yan Hou Tou Jing Wai Ke Za Zhi = Chinese Journal of Otorhinolaryngology Head and Neck Surgery*, 50(7), 583–586.
  17. Cai, T., Jen, H.-I., Kang, H., Klisch, T. J., Zoghbi, H. Y., & Groves, A. K. (2015). Characterization of the Transcriptome of Nascent Hair Cells and Identification of Direct Targets of the Atoh1 Transcription Factor. *Journal of Neuroscience*, 35(14), 5870–5883. <https://doi.org/10.1523/JNEUROSCI.5083-14.2015>
  18. Campbell, G., & Skillings, J. H. (1985). Nonparametric Stepwise Multiple Comparison Procedures. *Journal of the American Statistical Association*, 80(392), 998–1003. <https://doi.org/10.1080/01621459.1985.10478216>
  19. Cao, H., Garcia, F., & McNiven, M. A. (1998). Differential Distribution of Dynamin Isoforms in Mammalian Cells. *Molecular Biology of the Cell*, 9(9), 2595–2609. <https://doi.org/10.1091/mbc.9.9.2595>
  20. Ceriani, F., Hendry, A., Jeng, J.-Y., Johnson, S. L., Stephani, F., Olt, J., Holley, M. C., Mammano, F., Engel, J., Kros, C. J., Simmons, D. D., & Marcotti, W. (2019). Coordinated calcium signalling in cochlear sensory and non-sensory cells refines afferent innervation of outer hair cells. *The EMBO Journal*, 38(9), e99839. <https://doi.org/10.15252/embj.201899839>
  21. Chakrabarti, R., Jaime Tobón, L. M., Slitin, L., Redondo Canales, M., Hoch, G., Slashcheva, M., Fritsch, E., Bodensiek, K., Özçete, Ö. D., Gültas, M., Michanski, S., Opazo, F., Neef, J., Pangrsic, T., Moser, T., & Wichmann, C. (2022). Optogenetics and electron tomography for structure-function analysis of cochlear ribbon synapses. *eLife*, 11, e79494. <https://doi.org/10.7554/eLife.79494>
  22. Chakrabarti, R., & Wichmann, C. (2019). Nanomachinery Organizing Release at Neuronal and Ribbon Synapses. *International Journal of Molecular Sciences*, 20(9), Article 9. <https://doi.org/10.3390/ijms20092147>
  23. Chanaday, N. L., & Kavalali, E. T. (2018). Time course and temperature dependence of synaptic vesicle endocytosis. *FEBS Letters*, 592(21), 3606–3614. <https://doi.org/10.1002/1873-3468.13268>
  24. Chen, P., Johnson, J. E., Zoghbi, H. Y., & Segil, N. (2002). The role of Math1 in inner ear development: Uncoupling the establishment of the sensory primordium from hair cell fate determination. *Development (Cambridge, England)*, 129(10), 2495–2505.
  25. Chen, Z., & Wiens, J. J. (2020). The origins of acoustic communication in vertebrates. *Nature Communications*, 11(1), Article 1. <https://doi.org/10.1038/s41467-020-14356-3>
  26. Chessum, L., Matern, M. S., Kelly, M. C., Johnson, S. L., Ogawa, Y., Milon, B., McMurray, M., Driver, E. C., Parker, A., Song, Y., Codner, G., Esapa, C. T., Prescott, J., Trent, G., Wells, S., Dragich, A. K., Frolenkov, G. I., Kelley, M. W., Marcotti, W., ... Hertzano, R. (2018). Helios is a key transcriptional regulator of outer hair cell maturation. *Nature*, 563(7733), Article 7733. <https://doi.org/10.1038/s41586-018-0728-4>
  27. Clayton, E. L., & Cousin, M. A. (2009). The molecular physiology of activity-dependent bulk endocytosis of synaptic vesicles. *Journal of Neurochemistry*, 111(4), 901–914. <https://doi.org/10.1111/j.1471-4159.2009.06384.x>

28. Coons, A. H., & Kaplan, M. H. (1950). Localization of antigen in tissue cells; improvements in a method for the detection of antigen by means of fluorescent antibody. *The Journal of Experimental Medicine*, 91(1), 1–13. <https://doi.org/10.1084/jem.91.1.1>
29. Dallos, P. (1992). The active cochlea. *Journal of Neuroscience*, 12(12), 4575–4585. <https://doi.org/10.1523/JNEUROSCI.12-12-04575.1992>
30. Dallos, P. (1996). Overview: Cochlear Neurobiology. In P. Dallos, A. N. Popper, & R. R. Fay (Eds.), *The Cochlea* (pp. 1–43). Springer. [https://doi.org/10.1007/978-1-4612-0757-3\\_1](https://doi.org/10.1007/978-1-4612-0757-3_1)
31. Dannhof, B. J., & Bruns, V. (1993). The innervation of the organ of Corti in the rat. *Hearing Research*, 66(1), 8–22. [https://doi.org/10.1016/0378-5955\(93\)90255-y](https://doi.org/10.1016/0378-5955(93)90255-y)
32. Delacroix, L., & Malgrange, B. (2015). Cochlear afferent innervation development. *Hearing Research*, 330, 157–169. <https://doi.org/10.1016/j.heares.2015.07.015>
33. Delvendahl, I., Vyleta, N. P., von Gersdorff, H., & Hallermann, S. (2016). Fast, Temperature-Sensitive and Clathrin-Independent Endocytosis at Central Synapses. *Neuron*, 90(3), 492–498. <https://doi.org/10.1016/j.neuron.2016.03.013>
34. Dierich, M., Altoè, A., Koppelman, J., Evers, S., Renigunta, V., Schäfer, M. K., Naumann, R., Verhulst, S., Oliver, D., & Leitner, M. G. (2020). Optimized Tuning of Auditory Inner Hair Cells to Encode Complex Sound through Synergistic Activity of Six Independent K<sup>+</sup> Current Entities. *Cell Reports*, 32(1), 107869. <https://doi.org/10.1016/j.celrep.2020.107869>
35. Dietrich, M., Hartung, H.-P., & Albrecht, P. (2021). Neuroprotective Properties of 4-Aminopyridine. *Neurology - Neuroimmunology Neuroinflammation*, 8(3). <https://doi.org/10.1212/NXI.0000000000000976>
36. Dinkelacker, V., Voets, T., Neher, E., & Moser, T. (2000). The Readily Releasable Pool of Vesicles in Chromaffin Cells Is Replenished in a Temperature-Dependent Manner and Transiently Overfills at 37°C. *The Journal of Neuroscience*, 20(22), 8377–8383. <https://doi.org/10.1523/JNEUROSCI.20-22-08377.2000>
37. Duncker, S. V., Franz, C., Kuhn, S., Schulte, U., Campanelli, D., Brandt, N., Hirt, B., Fakler, B., Blin, N., Ruth, P., Engel, J., Marcotti, W., Zimmermann, U., & Knipper, M. (2013). Otoferlin couples to clathrin-mediated endocytosis in mature cochlear inner hair cells. *The Journal of Neuroscience: The Official Journal of the Society for Neuroscience*, 33(22), 9508–9519. <https://doi.org/10.1523/JNEUROSCI.5689-12.2013>
38. Dunlap, K., Luebke, J. I., & Turner, T. J. (1995). Exocytotic Ca<sup>2+</sup> channels in mammalian central neurons. *Trends in Neurosciences*, 18(2), 89–98. [https://doi.org/10.1016/0166-2236\(95\)80030-6](https://doi.org/10.1016/0166-2236(95)80030-6)
39. Ehret, G. (1983). 7 - Development of Hearing and Response Behavior to Sound Stimuli: Behavioral Studies  
Research in this chapter was supported by the Deutsche Forschungsgemeinschaft (Eh 53/1–5 and Ma 374/2.4). In R. Romand (Ed.), *Development of Auditory and Vestibular Systems* (pp. 211–237). Academic Press. <https://doi.org/10.1016/B978-0-12-594450-2.50012-5>
40. Ekdale, E. G. (2016). Form and function of the mammalian inner ear. *Journal of Anatomy*, 228(2), 324–337. <https://doi.org/10.1111/joa.12308>
41. Engel, J., Braig, C., Rüttiger, L., Kuhn, S., Zimmermann, U., Blin, N., Sausbier, M., Kalbacher, H., Münkner, S., Rohbock, K., Ruth, P., Winter, H., & Knipper, M. (2006). Two classes of outer hair cells along the tonotopic axis of the cochlea. *Neuroscience*, 143(3), 837–849. <https://doi.org/10.1016/j.neuroscience.2006.08.060>
42. Eybalin, M. (1993). Neurotransmitters and neuromodulators of the mammalian cochlea. *Physiological Reviews*, 73(2), 309–373. <https://doi.org/10.1152/physrev.1993.73.2.309>
43. Eybalin, M., Renard, N., Aure, F., & Safieddine, S. (2002). Cysteine-string protein in inner hair cells of the organ of Corti: Synaptic expression and upregulation at the onset of

- hearing. *European Journal of Neuroscience*, 15(9), 1409–1420. <https://doi.org/10.1046/j.1460-9568.2002.01978.x>
44. Faghihi Shirazi, M., Aronson, N. N., & Dean, R. T. (1982). Temperature dependence of certain integrated membrane functions in macrophages. *Journal of Cell Science*, 57, 115–127. <https://doi.org/10.1242/jcs.57.1.115>
  45. Faire, K., Trent, F., Tepper, J. M., & Bonder, E. M. (1992). Analysis of dynamin isoforms in mammalian brain: Dynamin-1 expression is spatially and temporally regulated during postnatal development. *Proceedings of the National Academy of Sciences of the United States of America*, 89(17), 8376–8380. <https://doi.org/10.1073/pnas.89.17.8376>
  46. Fan, F., Funk, L., & Lou, X. (2016). Dynamin 1- and 3-Mediated Endocytosis Is Essential for the Development of a Large Central Synapse In Vivo. *Journal of Neuroscience*, 36(22), 6097–6115. <https://doi.org/10.1523/JNEUROSCI.3804-15.2016>
  47. Feng, Z., Saha, L., Dritsa, C., Wan, Q., & Glebov, O. O. (2022). Temperature-dependent structural plasticity of hippocampal synapses. *Frontiers in Cellular Neuroscience*, 16, 1009970. <https://doi.org/10.3389/fncel.2022.1009970>
  48. Fettiplace, R. (2017). Hair Cell Transduction, Tuning, and Synaptic Transmission in the Mammalian Cochlea. *Comprehensive Physiology*, 7(4), 1197–1227. <https://doi.org/10.1002/cphy.c160049>
  49. Fettiplace, R., & Kim, K. X. (2014). The physiology of mechano-electrical transduction channels in hearing. *Physiological Reviews*, 94(3), 951–986. <https://doi.org/10.1152/physrev.00038.2013>
  50. Forge, A. (1987). Specialisations of the lateral membrane of inner hair cells. *Hearing Research*, 31(1), 99–109. [https://doi.org/10.1016/0378-5955\(87\)90217-6](https://doi.org/10.1016/0378-5955(87)90217-6)
  51. Frank, T., Rutherford, M. A., Strenzke, N., Neef, A., Pangršič, T., Khimich, D., Fejtova, A., Fetjova, A., Gundelfinger, E. D., Liberman, M. C., Harke, B., Bryan, K. E., Lee, A., Egner, A., Riedel, D., & Moser, T. (2010). Bassoon and the synaptic ribbon organize Ca<sup>2+</sup> channels and vesicles to add release sites and promote refilling. *Neuron*, 68(4), 724–738. <https://doi.org/10.1016/j.neuron.2010.10.027>
  52. Fuchs, P. A., Glowatzki, E., & Moser, T. (2003). The afferent synapse of cochlear hair cells. *Current Opinion in Neurobiology*, 13(4), 452–458. [https://doi.org/10.1016/S0959-4388\(03\)00098-9](https://doi.org/10.1016/S0959-4388(03)00098-9)
  53. García-Añoveros, J., Clancy, J. C., Foo, C. Z., García-Gómez, I., Zhou, Y., Homma, K., Cheatham, M. A., & Duggan, A. (2022). Tbx2 is a master regulator of inner versus outer hair cell differentiation. *Nature*, 605(7909), 298–303. <https://doi.org/10.1038/s41586-022-04668-3>
  54. Gentet, L. J., Stuart, G. J., & Clements, J. D. (2000). Direct measurement of specific membrane capacitance in neurons. *Biophysical Journal*, 79(1), 314–320.
  55. Gillis, K. D. (1995). Techniques for Membrane Capacitance Measurements. In B. Sakmann & E. Neher (Eds.), *Single-Channel Recording* (pp. 155–198). Springer US. [https://doi.org/10.1007/978-1-4419-1229-9\\_7](https://doi.org/10.1007/978-1-4419-1229-9_7)
  56. Graham, M. E., O’Callaghan, D. W., McMahon, H. T., & Burgoyne, R. D. (2002). Dynamin-dependent and dynamin-independent processes contribute to the regulation of single vesicle release kinetics and quantal size. *Proceedings of the National Academy of Sciences of the United States of America*, 99(10), 7124–7129. <https://doi.org/10.1073/pnas.102645099>
  57. Grant, L., & Fuchs, P. (2008). Calcium- and Calmodulin-Dependent Inactivation of Calcium Channels in Inner Hair Cells of the Rat Cochlea. *Journal of Neurophysiology*, 99(5), 2183–2193. <https://doi.org/10.1152/jn.01174.2007>

58. Grati, M., Schneider, M. E., Lipkow, K., Strehler, E. E., Wenthold, R. J., & Kachar, B. (2006). Rapid turnover of stereocilia membrane proteins: Evidence from the trafficking and mobility of plasma membrane Ca<sup>2+</sup>-ATPase 2. *The Journal of Neuroscience: The Official Journal of the Society for Neuroscience*, 26(23), 6386–6395. <https://doi.org/10.1523/JNEUROSCI.1215-06.2006>
59. Griesinger, C. B., Richards, C. D., & Ashmore, J. F. (2004). Apical endocytosis in outer hair cells of the mammalian cochlea. *European Journal of Neuroscience*, 20(1), 41–50. <https://doi.org/10.1111/j.0953-816X.2004.03452.x>
60. Gu, C., Yaddanapudi, S., Weins, A., Osborn, T., Reiser, J., Pollak, M., Hartwig, J., & Sever, S. (2010). Direct dynamin–actin interactions regulate the actin cytoskeleton. *The EMBO Journal*, 29(21), 3593–3606. <https://doi.org/10.1038/emboj.2010.249>
61. Hackney, C. M., Mahendrasingam, S., Penn, A., & Fettiplace, R. (2005). The Concentrations of Calcium Buffering Proteins in Mammalian Cochlear Hair Cells. *Journal of Neuroscience*, 25(34), 7867–7875. <https://doi.org/10.1523/JNEUROSCI.1196-05.2005>
62. Harasztosi, C., & Gummer, A. W. (2019). Different rates of endocytic activity and vesicle transport from the apical and synaptic poles of the outer hair cell. *HNO*, 67(6), 449–457. <https://doi.org/10.1007/s00106-019-0674-y>
63. Harasztosi, C., Klenske, E., & Gummer, A. W. (2021). Vesicle traffic in the outer hair cell. *European Journal of Neuroscience*, 54(3), 4755–4767. <https://doi.org/10.1111/ejn.15331>
64. Heidrych, P., Zimmermann, U., Kuhn, S., Franz, C., Engel, J., Duncker, S. V., Hirt, B., Pusch, C. M., Ruth, P., Pfister, M., Marcotti, W., Blin, N., & Knipper, M. (2009). Otoferlin interacts with myosin VI: Implications for maintenance of the basolateral synaptic structure of the inner hair cell. *Human Molecular Genetics*, 18(15), 2779–2790. <https://doi.org/10.1093/hmg/ddp213>
65. Howat, W. J., & Wilson, B. A. (2014). Tissue fixation and the effect of molecular fixatives on downstream staining procedures. *Methods (San Diego, Calif.)*, 70(1), 12–19. <https://doi.org/10.1016/j.ymeth.2014.01.022>
66. Huang, G., & Eckrich, S. (2021). Quantitative Fluorescent in situ Hybridization Reveals Differential Transcription Profile Sharpening of Endocytic Proteins in Cochlear Hair Cells Upon Maturation. *Frontiers in Cellular Neuroscience*, 15. <https://www.frontiersin.org/article/10.3389/fncel.2021.643517>
67. Huang, G., & Santos-Sacchi, J. (1993). Mapping the distribution of the outer hair cell motility voltage sensor by electrical amputation. *Biophysical Journal*, 65(5), 2228–2236. [https://doi.org/10.1016/S0006-3495\(93\)81248-7](https://doi.org/10.1016/S0006-3495(93)81248-7)
68. Huang, L.-C., Barclay, M., Lee, K., Peter, S., Housley, G. D., Thorne, P. R., & Montgomery, J. M. (2012). Synaptic profiles during neurite extension, refinement and retraction in the developing cochlea. *Neural Development*, 7(1), 38. <https://doi.org/10.1186/1749-8104-7-38>
69. Huang, L.-C., Thorne, P. R., Housley, G. D., & Montgomery, J. M. (2007). Spatiotemporal definition of neurite outgrowth, refinement and retraction in the developing mouse cochlea. *Development*, 134(16), 2925–2933. <https://doi.org/10.1242/dev.001925>
70. Hudspeth, A. J. (1989). How the ear's works work. *Nature*, 341(6241), Article 6241. <https://doi.org/10.1038/341397a0>
71. Iftinca, M., McKay, B. E., Snutch, T. P., McRory, J. E., Turner, R. W., & Zamponi, G. W. (2006). Temperature dependence of T-type calcium channel gating. *Neuroscience*, 142(4), 1031–1042. <https://doi.org/10.1016/j.neuroscience.2006.07.010>

72. Jamur, M. C., & Oliver, C. (2010). Permeabilization of Cell Membranes. In C. Oliver & M. C. Jamur (Eds.), *Immunocytochemical Methods and Protocols* (pp. 63–66). Humana Press. [https://doi.org/10.1007/978-1-59745-324-0\\_9](https://doi.org/10.1007/978-1-59745-324-0_9)
73. Jean, P., Morena, D. L. de la, Michanski, S., Tobón, L. M. J., Chakrabarti, R., Picher, M. M., Neef, J., Jung, S., Gültas, M., Maxeiner, S., Neef, A., Wichmann, C., Strenzke, N., Grabner, C., & Moser, T. (2018). The synaptic ribbon is critical for sound encoding at high rates and with temporal precision. *eLife*, 7, e29275. <https://doi.org/10.7554/eLife.29275>
74. Jean, P., Wong Jun Tai, F., Singh-Estivalet, A., Lelli, A., Scandola, C., Megharba, S., Schmutz, S., Roux, S., Mechaussier, S., Sudres, M., Mouly, E., Heritier, A.-V., Bonnet, C., Mallet, A., Novault, S., Libri, V., Petit, C., & Michalski, N. (2023). Single-cell transcriptomic profiling of the mouse cochlea: An atlas for targeted therapies. *Proceedings of the National Academy of Sciences of the United States of America*, 120(26), e2221744120. <https://doi.org/10.1073/pnas.2221744120>
75. Jeng, J.-Y., Ceriani, F., Hendry, A., Johnson, S. L., Yen, P., Simmons, D. D., Kros, C. J., & Marcotti, W. (2020). Hair cell maturation is differentially regulated along the tonotopic axis of the mammalian cochlea. *The Journal of Physiology*, 598(1), 151–170. <https://doi.org/10.1113/JP279012>
76. Jiang, M., & Chen, G. (2009). Ca<sup>2+</sup> Regulation of Dynamin-Independent Endocytosis in Cortical Astrocytes. *Journal of Neuroscience*, 29(25), 8063–8074. <https://doi.org/10.1523/JNEUROSCI.6139-08.2009>
77. Johnson, S. L., Adelman, J. P., & Marcotti, W. (2007). Genetic deletion of SK2 channels in mouse inner hair cells prevents the developmental linearization in the Ca<sup>2+</sup> dependence of exocytosis. *The Journal of Physiology*, 583(Pt 2), 631–646. <https://doi.org/10.1113/jphysiol.2007.136630>
78. Johnson, S. L., Beurg, M., Marcotti, W., & Fettiplace, R. (2011). Prestin-Driven Cochlear Amplification Is Not Limited by the Outer Hair Cell Membrane Time Constant. *Neuron*, 70(6), 1143–1154. <https://doi.org/10.1016/j.neuron.2011.04.024>
79. Johnson, S. L., Forge, A., Knipper, M., Münkner, S., & Marcotti, W. (2008). Tonotopic variation in the calcium dependence of neurotransmitter release and vesicle pool replenishment at mammalian auditory ribbon synapses. *The Journal of Neuroscience: The Official Journal of the Society for Neuroscience*, 28(30), 7670–7678. <https://doi.org/10.1523/JNEUROSCI.0785-08.2008>
80. Johnson, S. L., Franz, C., Knipper, M., & Marcotti, W. (2009). Functional maturation of the exocytotic machinery at gerbil hair cell ribbon synapses. *The Journal of Physiology*, 587(Pt 8), 1715–1726. <https://doi.org/10.1113/jphysiol.2009.168542>
81. Johnson, S. L., Kuhn, S., Franz, C., Ingham, N., Furness, D. N., Knipper, M., Steel, K. P., Adelman, J. P., Holley, M. C., & Marcotti, W. (2013). Presynaptic maturation in auditory hair cells requires a critical period of sensory-independent spiking activity. *Proceedings of the National Academy of Sciences of the United States of America*, 110(21), 8720–8725. <https://doi.org/10.1073/pnas.1219578110>
82. Johnson, S. L., & Marcotti, W. (2008a). Biophysical properties of Ca<sub>v</sub>1.3 calcium channels in gerbil inner hair cells. *The Journal of Physiology*, 586(4), 1029–1042. <https://doi.org/10.1113/jphysiol.2007.145219>
83. Johnson, S. L., Marcotti, W., & Kros, C. J. (2005). Increase in efficiency and reduction in Ca<sup>2+</sup> dependence of exocytosis during development of mouse inner hair cells. *The Journal of Physiology*, 563(Pt 1), 177–191. <https://doi.org/10.1113/jphysiol.2004.074740>

84. Johnson, S. L., Safieddine, S., Mustapha, M., & Marcotti, W. (2019). Hair Cell Afferent Synapses: Function and Dysfunction. *Cold Spring Harbor Perspectives in Medicine*, 9(12), a033175. <https://doi.org/10.1101/cshperspect.a033175>
85. Johnson, S. L., Thomas, M. V., & Kros, C. J. (2002). Membrane capacitance measurement using patch clamp with integrated self-balancing lock-in amplifier. *Pflügers Archiv - European Journal of Physiology*, 443(4), 653–663. <https://doi.org/10.1007/s00424-001-0763-z>
86. Jung, S., Maritzen, T., Wichmann, C., Jing, Z., Neef, A., Revelo, N. H., Al-Moyed, H., Meese, S., Wojcik, S. M., Panou, I., Bulut, H., Schu, P., Ficner, R., Reisinger, E., Rizzoli, S. O., Neef, J., Strenzke, N., Haucke, V., & Moser, T. (2015). Disruption of adaptor protein 2 $\mu$  (AP-2 $\mu$ ) in cochlear hair cells impairs vesicle reloading of synaptic release sites and hearing. *The EMBO Journal*, 34(21), 2686–2702. <https://doi.org/10.15252/embj.201591885>
87. Kachar, B., Battaglia, A., & Fex, J. (1997). Compartmentalized vesicular traffic around the hair cell cuticular plate. *Hearing Research*, 107(1), 102–112. [https://doi.org/10.1016/S0378-5955\(97\)00027-0](https://doi.org/10.1016/S0378-5955(97)00027-0)
88. Kaltenbach, J. A., Falzarano, P. R., & Simpson, T. H. (1994). Postnatal development of the hamster cochlea. II. Growth and differentiation of stereocilia bundles. *The Journal of Comparative Neurology*, 350(2), 187–198. <https://doi.org/10.1002/cne.903500204>
89. Kaneko, T., Harasztosi, C., Mack, A. F., & Gummer, A. W. (2006). Membrane traffic in outer hair cells of the adult mammalian cochlea. *European Journal of Neuroscience*, 23(10), 2712–2722. <https://doi.org/10.1111/j.1460-9568.2006.04796.x>
90. Kersigo, J., Pan, N., Lederman, J. D., Chatterjee, S., Abel, T., Pavlinkova, G., Silos-Santiago, I., & Fritzsche, B. (2018). A RNAscope whole mount approach that can be combined with immunofluorescence to quantify differential distribution of mRNA. *Cell and Tissue Research*, 374(2), 251–262. <https://doi.org/10.1007/s00441-018-2864-4>
91. Khodakhah, K., Melishchuk, A., & Armstrong, C. M. (1997). Killing K Channels with TEA+. *Proceedings of the National Academy of Sciences*, 94(24), 13335–13338. <https://doi.org/10.1073/pnas.94.24.13335>
92. Kim, S.-W., Roh, J., & Park, C.-S. (2016). Immunohistochemistry for Pathologists: Protocols, Pitfalls, and Tips. *Journal of Pathology and Translational Medicine*, 50(6), 411–418. <https://doi.org/10.4132/jptm.2016.08.08>
93. Kimitsuki, T. (2017). Cholesterol influences potassium currents in inner hair cells isolated from guinea pig cochlea. *Auris Nasus Larynx*, 44(1), 46–51. <https://doi.org/10.1016/j.anl.2016.04.010>
94. Knirsch, M., Brandt, N., Braig, C., Kuhn, S., Hirt, B., Münkner, S., Knipper, M., & Engel, J. (2007). Persistence of Cav1.3 Ca<sup>2+</sup> Channels in Mature Outer Hair Cells Supports Outer Hair Cell Afferent Signaling. *Journal of Neuroscience*, 27(24), 6442–6451. <https://doi.org/10.1523/JNEUROSCI.5364-06.2007>
95. Kolla, L., Kelly, M. C., Mann, Z. F., Anaya-Rocha, A., Ellis, K., Lemons, A., Palermo, A. T., So, K. S., Mays, J. C., Orvis, J., Burns, J. C., Hertzano, R., Driver, E. C., & Kelley, M. W. (2020). Characterization of the development of the mouse cochlear epithelium at the single cell level. *Nature Communications*, 11(1), 2389. <https://doi.org/10.1038/s41467-020-16113-y>
96. Kroll, J., Özçete, Ö. D., Jung, S., Maritzen, T., Milosevic, I., Wichmann, C., & Moser, T. (2020). AP180 promotes release site clearance and clathrin-dependent vesicle reformation in mouse cochlear inner hair cells. *Journal of Cell Science*, 133(2), jcs236737. <https://doi.org/10.1242/jcs.236737>
97. Kroll, J., Tobón, L. M. J., Vogl, C., Neef, J., Kondratiuk, I., König, M., Strenzke, N., Wichmann, C., Milosevic, I., & Moser, T. (2019). Endophilin-A regulates presynaptic

- Ca<sup>2+</sup> influx and synaptic vesicle recycling in auditory hair cells. *The EMBO Journal*, e100116. <https://doi.org/10.15252/embj.2018100116>
98. Kros, C. J., Ruppersberg, J. P., & Rüscher, A. (1998). Expression of a potassium current in inner hair cells during development of hearing in mice. *Nature*, 394(6690), 281–284. <https://doi.org/10.1038/28401>
  99. Kuhn, S., Johnson, S. L., Furness, D. N., Chen, J., Ingham, N., Hilton, J. M., Steffes, G., Lewis, M. A., Zampini, V., Hackney, C. M., Masetto, S., Holley, M. C., Steel, K. P., & Marcotti, W. (2011). miR-96 regulates the progression of differentiation in mammalian cochlear inner and outer hair cells. *Proceedings of the National Academy of Sciences of the United States of America*, 108(6), 2355–2360. <https://doi.org/10.1073/pnas.1016646108>
  100. Leitz, J., & Kavalali, E. T. (2011). Ca<sup>2+</sup> Influx Slows Single Synaptic Vesicle Endocytosis. *Journal of Neuroscience*, 31(45), 16318–16326. <https://doi.org/10.1523/JNEUROSCI.3358-11.2011>
  101. Lenzi, D., Runyeon, J. W., Crum, J., Ellisman, M. H., & Roberts, W. M. (1999). Synaptic vesicle populations in saccular hair cells reconstructed by electron tomography. *The Journal of Neuroscience: The Official Journal of the Society for Neuroscience*, 19(1), 119–132.
  102. Li, S., Mecca, A., Kim, J., Caprara, G. A., Wagner, E. L., Du, T.-T., Petrov, L., Xu, W., Cui, R., Rebutini, I. T., Kachar, B., Peng, A. W., & Shin, J.-B. (2020). Myosin-VIIa is expressed in multiple isoforms and essential for tensioning the hair cell mechanotransduction complex. *Nature Communications*, 11(1), Article 1. <https://doi.org/10.1038/s41467-020-15936-z>
  103. Li, Y., Liu, H., Giffen, K. P., Chen, L., Beisel, K. W., & He, D. Z. Z. (2018). Transcriptomes of cochlear inner and outer hair cells from adult mice. *Scientific Data*, 5(1), Article 1. <https://doi.org/10.1038/sdata.2018.199>
  104. Liberman, L. D., & Liberman, M. C. (2016). Postnatal maturation of auditory-nerve heterogeneity, as seen in spatial gradients of synapse morphology in the inner hair cell area. *Hearing Research*, 339, 12–22. <https://doi.org/10.1016/j.heares.2016.06.002>
  105. Liberman, M. C., Dodds, L. W., & Pierce, S. (1990). Afferent and efferent innervation of the cat cochlea: Quantitative analysis with light and electron microscopy. *Journal of Comparative Neurology*, 301(3), 443–460. <https://doi.org/10.1002/cne.903010309>
  106. Liberman, M. C., Gao, J., He, D. Z. Z., Wu, X., Jia, S., & Zuo, J. (2002). Prestin is required for electromotility of the outer hair cell and for the cochlear amplifier. *Nature*, 419(6904), Article 6904. <https://doi.org/10.1038/nature01059>
  107. Lindsay, P. H., & Norman, D. A. (1977). 4—The auditory system. In P. H. Lindsay & D. A. Norman (Eds.), *Human Information Processing (Second Edition)* (pp. 122–145). Academic Press. <https://doi.org/10.1016/B978-0-12-450960-3.50008-7>
  108. Lippiat, J. D. (2009). Whole-Cell Recording Using the Perforated Patch Clamp Technique. In J. D. Lippiat (Ed.), *Potassium Channels: Methods and Protocols* (pp. 141–149). Humana Press. [https://doi.org/10.1007/978-1-59745-526-8\\_11](https://doi.org/10.1007/978-1-59745-526-8_11)
  109. Liu, C., Glowatzki, E., & Fuchs, P. A. (2015). Unmyelinated type II afferent neurons report cochlear damage. *Proceedings of the National Academy of Sciences of the United States of America*, 112(47), 14723–14727. <https://doi.org/10.1073/pnas.1515228112>
  110. Liu, H., Pecka, J. L., Zhang, Q., Soukup, G. A., Beisel, K. W., & He, D. Z. Z. (2014). Characterization of Transcriptomes of Cochlear Inner and Outer Hair Cells. *Journal of Neuroscience*, 34(33), 11085–11095. <https://doi.org/10.1523/JNEUROSCI.1690-14.2014>

111. Liu, J., Wang, S., Lu, Y., Wang, H., Wang, F., Qiu, M., Xie, Q., Han, H., & Hua, Y. (2022). Aligned Organization of Synapses and Mitochondria in Auditory Hair Cells. *Neuroscience Bulletin*, 38(3), 235–248. <https://doi.org/10.1007/s12264-021-00801-w>
112. Mann, Z. F., & Kelley, M. W. (2011). Development of tonotopy in the auditory periphery. *Hearing Research*, 276(1–2), 2–15. <https://doi.org/10.1016/j.heares.2011.01.011>
113. Marcotti, W., Johnson, S. L., Holley, M. C., & Kros, C. J. (2003). Developmental changes in the expression of potassium currents of embryonic, neonatal and mature mouse inner hair cells. *The Journal of Physiology*, 548(Pt 2), 383–400. <https://doi.org/10.1113/jphysiol.2002.034801>
114. Marcotti, W., Johnson, S. L., & Kros, C. J. (2004a). A transiently expressed SK current sustains and modulates action potential activity in immature mouse inner hair cells. *The Journal of Physiology*, 560(Pt 3), 691–708. <https://doi.org/10.1113/jphysiol.2004.072868>
115. Marcotti, W., Johnson, S. L., & Kros, C. J. (2004b). Effects of intracellular stores and extracellular Ca<sup>2+</sup> on Ca<sup>2+</sup>-activated K<sup>+</sup> currents in mature mouse inner hair cells. *The Journal of Physiology*, 557(Pt 2), 613–633. <https://doi.org/10.1113/jphysiol.2003.060137>
116. Marcotti, W., Johnson, S. L., Rusch, A., & Kros, C. J. (2003). Sodium and calcium currents shape action potentials in immature mouse inner hair cells. *The Journal of Physiology*, 552(Pt 3), 743–761. <https://doi.org/10.1113/jphysiol.2003.043612>
117. Marcotti, W., & Kros, C. J. (1999). Developmental expression of the potassium current I<sub>K,n</sub> contributes to maturation of mouse outer hair cells. *The Journal of Physiology*, 520(3), 653–660. <https://doi.org/10.1111/j.1469-7793.1999.00653.x>
118. Martelletti, E., Ingham, N. J., Houston, O., Pass, J. C., Chen, J., Marcotti, W., & Steel, K. P. (2020). Synaptojanin2 Mutation Causes Progressive High-frequency Hearing Loss in Mice. *Frontiers in Cellular Neuroscience*, 14, 561857. <https://doi.org/10.3389/fncel.2020.561857>
119. Matsuda, Y., Fujii, T., Suzuki, T., Yamahatsu, K., Kawahara, K., Teduka, K., Kawamoto, Y., Yamamoto, T., Ishiwata, T., & Naito, Z. (2011). Comparison of Fixation Methods for Preservation of Morphology, RNAs, and Proteins From Paraffin-Embedded Human Cancer Cell-Implanted Mouse Models. *Journal of Histochemistry and Cytochemistry*, 59(1), 68–75. <https://doi.org/10.1369/jhc.2010.957217>
120. McCluskey, A., Daniel, J. A., Hadzic, G., Chau, N., Clayton, E. L., Mariana, A., Whiting, A., Gorgani, N. N., Lloyd, J., Quan, A., Moshkanbaryans, L., Krishnan, S., Perera, S., Chircop, M., von Kleist, L., McGeachie, A. B., Howes, M. T., Parton, R. G., Campbell, M., ... Robinson, P. J. (2013). Building a better dynasore: The dyngo compounds potently inhibit dynamin and endocytosis. *Traffic (Copenhagen, Denmark)*, 14(12), 1272–1289. <https://doi.org/10.1111/tra.12119>
121. McMahan, H. T., & Boucrot, E. (2011). Molecular mechanism and physiological functions of clathrin-mediated endocytosis. *Nature Reviews Molecular Cell Biology*, 12(8), Article 8. <https://doi.org/10.1038/nrm3151>
122. Michalski, N., Goutman, J. D., Auclair, S. M., Monvel, J. B. de, Tertrais, M., Emptoz, A., Parrin, A., Nouaille, S., Guillon, M., Sachse, M., Ciric, D., Bahloul, A., Hardelin, J.-P., Sutton, R. B., Avan, P., Krishnakumar, S. S., Rothman, J. E., Dulon, D., Safieddine, S., & Petit, C. (2017). Otoferlin acts as a Ca<sup>2+</sup> sensor for vesicle fusion and vesicle pool replenishment at auditory hair cell ribbon synapses. *eLife*, 6, e31013. <https://doi.org/10.7554/eLife.31013>
123. Michanski, S., Smaluch, K., Steyer, A. M., Chakrabarti, R., Setz, C., Oestreicher, D., Fischer, C., Möbius, W., Moser, T., Vogl, C., & Wichmann, C. (2019). Mapping developmental maturation of inner hair cell ribbon synapses in the apical mouse

cochlea. *Proceedings of the National Academy of Sciences*, 116(13), 6415–6424. <https://doi.org/10.1073/pnas.1812029116>

124. Michna, M., Knirsch, M., Hoda, J.-C., Muenkner, S., Langer, P., Platzner, J., Striessnig, J., & Engel, J. (2003). Cav1.3 ( $\alpha 1D$ )  $Ca^{2+}$  Currents in Neonatal Outer Hair Cells of Mice. *The Journal of Physiology*, 553(3), 747–758. <https://doi.org/10.1113/jphysiol.2003.053256>
125. Midorikawa, M., Okamoto, Y., & Sakaba, T. (2014). Developmental changes in  $Ca^{2+}$  channel subtypes regulating endocytosis at the calyx of Held. *The Journal of Physiology*, 592(16), 3495–3510. <https://doi.org/10.1113/jphysiol.2014.273243>
126. Mintz, I. M., Sabatini, B. L., & Regehr, W. G. (1995). Calcium control of transmitter release at a cerebellar synapse. *Neuron*, 15(3), 675–688. [https://doi.org/10.1016/0896-6273\(95\)90155-8](https://doi.org/10.1016/0896-6273(95)90155-8)
127. Molleman, A. (2003). *Patch Clamping: An Introductory Guide to Patch Clamp Electrophysiology*. Wiley.
128. Moss, C. F., & Surlykke, A. (2010). Probing the Natural Scene by Echolocation in Bats. *Frontiers in Behavioral Neuroscience*, 4. <https://doi.org/10.3389/fnbeh.2010.00033>
129. Neef, A., Khimich, D., Pirih, P., Riedel, D., Wolf, F., & Moser, T. (2007). Probing the Mechanism of Exocytosis at the Hair Cell Ribbon Synapse. *Journal of Neuroscience*, 27(47), 12933–12944. <https://doi.org/10.1523/JNEUROSCI.1996-07.2007>
130. Neef, J., Jung, S., Wong, A. B., Reuter, K., Pangrsic, T., Chakrabarti, R., Kügler, S., Lenz, C., Nouvian, R., Boumil, R. M., Frankel, W. N., Wichmann, C., & Moser, T. (2014). Modes and regulation of endocytic membrane retrieval in mouse auditory hair cells. *The Journal of Neuroscience: The Official Journal of the Society for Neuroscience*, 34(3), 705–716. <https://doi.org/10.1523/JNEUROSCI.3313-13.2014>
131. Neuweiler, G., & Heldmaier, G. (2003). Das Hören. In G. Neuweiler & G. Heldmaier (Eds.), *Vergleichende Tierphysiologie: Neuro- und Sinnesphysiologie* (pp. 233–332). Springer. [https://doi.org/10.1007/978-3-642-55699-9\\_8](https://doi.org/10.1007/978-3-642-55699-9_8)
132. Noakes, P. g., Chin, D., Kim, S. s., Liang, S., & Phillips, W. d. (1999). Expression and localisation of dynamin and syntaxin during neural development and neuromuscular synapse formation. *Journal of Comparative Neurology*, 410(4), 531–540. [https://doi.org/10.1002/\(SICI\)1096-9861\(19990809\)410:4<531::AID-CNE2>3.0.CO;2-C](https://doi.org/10.1002/(SICI)1096-9861(19990809)410:4<531::AID-CNE2>3.0.CO;2-C)
133. Nouvian, R. (2007). Temperature enhances exocytosis efficiency at the mouse inner hair cell ribbon synapse. *The Journal of Physiology*, 584(Pt 2), 535–542. <https://doi.org/10.1113/jphysiol.2007.139675>
134. Nouvian, R., Neef, J., Bulankina, A. V., Reisinger, E., Pangršič, T., Frank, T., Sikorra, S., Brose, N., Binz, T., & Moser, T. (2011). Exocytosis at the hair cell ribbon synapse apparently operates without neuronal SNARE proteins. *Nature Neuroscience*, 14(4), 411–413. <https://doi.org/10.1038/nn.2774>
135. Oliver, D., & Fakler, B. (1999). Expression density and functional characteristics of the outer hair cell motor protein are regulated during postnatal development in rat. *The Journal of Physiology*, 519(3), 791–800. <https://doi.org/10.1111/j.1469-7793.1999.0791n.x>
136. Oliver, D., Knipper, M., Derst, C., & Fakler, B. (2003). Resting potential and submembrane calcium concentration of inner hair cells in the isolated mouse cochlea are set by KCNQ-type potassium channels. *The Journal of Neuroscience: The Official Journal of the Society for Neuroscience*, 23(6), 2141–2149.
137. O'Sullivan, J. D. B., Bullen, A., & Mann, Z. F. (2023). Mitochondrial form and function in hair cells. *Hearing Research*, 428, 108660. <https://doi.org/10.1016/j.heares.2022.108660>

138. Paavilainen, L., Edvinsson, Å., Asplund, A., Hober, S., Kampf, C., Pontén, F., & Wester, K. (2010). The Impact of Tissue Fixatives on Morphology and Antibody-based Protein Profiling in Tissues and Cells. *Journal of Histochemistry and Cytochemistry*, 58(3), 237–246. <https://doi.org/10.1369/jhc.2009.954321>
139. Pangrsic, T., Lasarow, L., Reuter, K., Takago, H., Schwander, M., Riedel, D., Frank, T., Tarantino, L. M., Bailey, J. S., Strenzke, N., Brose, N., Müller, U., Reisinger, E., & Moser, T. (2010). Hearing requires otoferlin-dependent efficient replenishment of synaptic vesicles in hair cells. *Nature Neuroscience*, 13(7), 869–876. <https://doi.org/10.1038/nn.2578>
140. Pangrsic, T., & Vogl, C. (2018). Balancing presynaptic release and endocytic membrane retrieval at hair cell ribbon synapses. *FEBS Letters*, 592(21), 3633–3650. <https://doi.org/10.1002/1873-3468.13258>
141. Park, R. J., Shen, H., Liu, L., Liu, X., Ferguson, S. M., & De Camilli, P. (2013). Dynamin triple knockout cells reveal off target effects of commonly used dynamin inhibitors. *Journal of Cell Science*, 126(22), 5305–5312. <https://doi.org/10.1242/jcs.138578>
142. Platzer, J., Engel, J., Schrott-Fischer, A., Stephan, K., Bova, S., Chen, H., Zheng, H., & Striessnig, J. (2000). Congenital deafness and sinoatrial node dysfunction in mice lacking class D L-type Ca<sup>2+</sup> channels. *Cell*, 102(1), 89–97.
143. Polak, J. M., & Van Noorden, S. (2003). *Introduction to Immunocytochemistry*. BIOS Scientific Publishers. <https://books.google.de/books?id=JwRjQgAACAAJ>
144. Preta, G., Cronin, J. G., & Sheldon, I. M. (2015). Dynasore—Not just a dynamin inhibitor. *Cell Communication and Signaling : CCS*, 13, 24. <https://doi.org/10.1186/s12964-015-0102-1>
145. Preta, G., Lotti, V., Cronin, J. G., & Sheldon, I. M. (2015). Protective role of the dynamin inhibitor Dynasore against the cholesterol-dependent cytolysin of *Trueperella pyogenes*. *The FASEB Journal*, 29(4), 1516–1528. <https://doi.org/10.1096/fj.14-265207>
146. Pyott, S. J., & Rosenmund, C. (2002). The effects of temperature on vesicular supply and release in autaptic cultures of rat and mouse hippocampal neurons. *The Journal of Physiology*, 539(Pt 2), 523–535. <https://doi.org/10.1113/jphysiol.2001.013277>
147. Qi, W., Ding, D., & Salvi, R. J. (2008). Cytotoxic effects of dimethyl sulphoxide (DMSO) on cochlear organotypic cultures. *Hearing Research*, 236(1–2), 52–60. <https://doi.org/10.1016/j.heares.2007.12.002>
148. Ramos-Vara, J. A. (2005). Technical Aspects of Immunohistochemistry. *Veterinary Pathology*, 42(4), 405–426. <https://doi.org/10.1354/vp.42-4-405>
149. Ramos-Vara, J. A., & Miller, M. A. (2014). When tissue antigens and antibodies get along: Revisiting the technical aspects of immunohistochemistry--the red, brown, and blue technique. *Veterinary Pathology*, 51(1), 42–87. <https://doi.org/10.1177/0300985813505879>
150. Reid, C. A., Bekkers, J. M., & Clements, J. D. (2003). Presynaptic Ca<sup>2+</sup> channels: A functional patchwork. *Trends in Neurosciences*, 26(12), 683–687. <https://doi.org/10.1016/j.tins.2003.10.003>
151. Reid, M. A., Flores-Otero, J., & Davis, R. L. (2004). Firing patterns of type II spiral ganglion neurons in vitro. *The Journal of Neuroscience: The Official Journal of the Society for Neuroscience*, 24(3), 733–742. <https://doi.org/10.1523/JNEUROSCI.3923-03.2004>
152. Renden, R., & von Gersdorff, H. (2007). Synaptic Vesicle Endocytosis at a CNS Nerve Terminal: Faster Kinetics at Physiological Temperatures and Increased Endocytotic Capacity During Maturation. *Journal of Neurophysiology*, 98(6), 3349–3359. <https://doi.org/10.1152/jn.00898.2007>

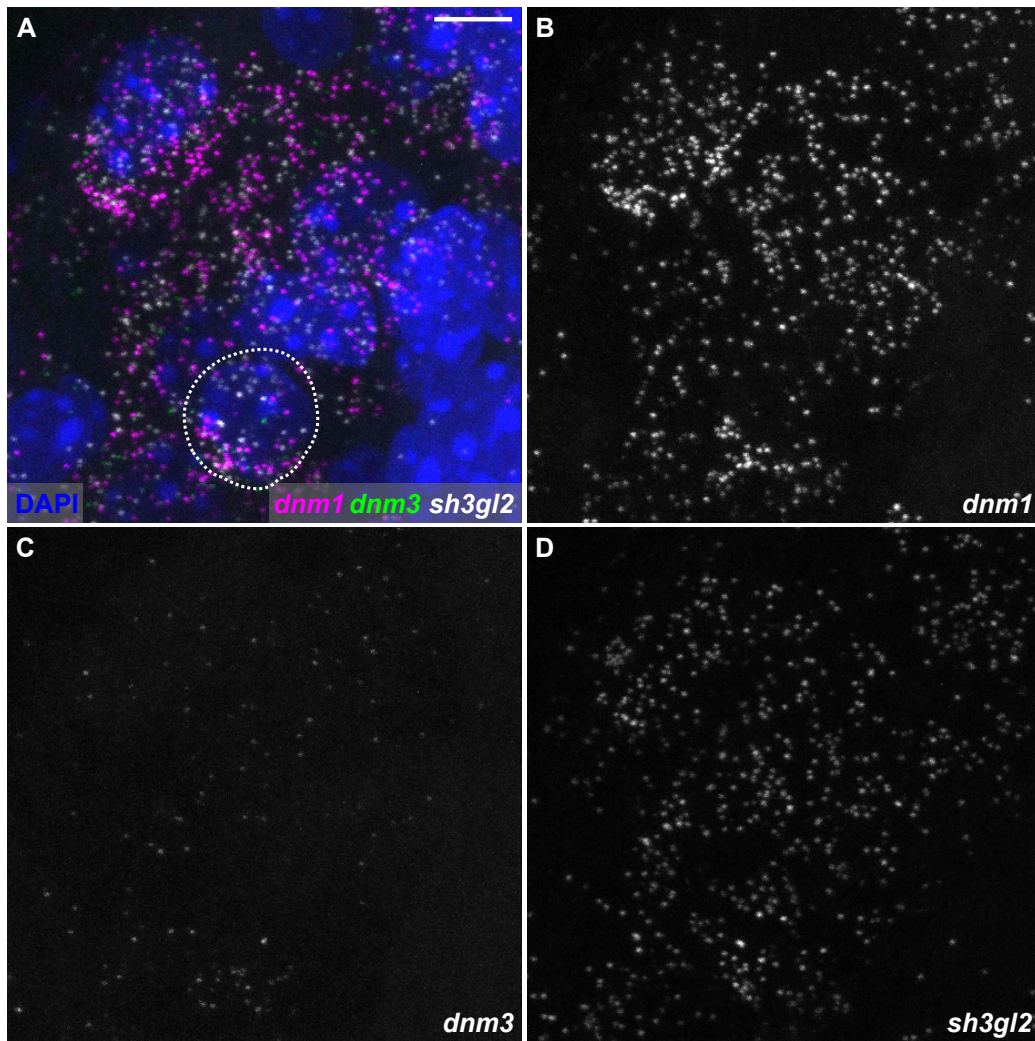
153. Renström, E., Eliasson, L., Bokvist, K., & Rorsman, P. (1996). Cooling inhibits exocytosis in single mouse pancreatic B-cells by suppression of granule mobilization. *The Journal of Physiology*, 494(Pt 1), 41–52.
154. Richardson, G., Lukashkin, A., & Russell, I. (2008). The tectorial membrane: One slice of a complex cochlear sandwich. *Current Opinion in Otolaryngology & Head and Neck Surgery*, 16(5), 458–464. <https://doi.org/10.1097/MOO.0b013e32830e20c4>
155. Roux, I., Safieddine, S., Nouvian, R., Grati, M., Simmler, M.-C., Bahloul, A., Perfettini, I., Le Gall, M., Rostaing, P., Hamard, G., Triller, A., Avan, P., Moser, T., & Petit, C. (2006). Otoferlin, defective in a human deafness form, is essential for exocytosis at the auditory ribbon synapse. *Cell*, 127(2), 277–289. <https://doi.org/10.1016/j.cell.2006.08.040>
156. Rutherford, M. A., von Gersdorff, H., & Goutman, J. D. (2021). Encoding sound in the cochlea: From receptor potential to afferent discharge. *The Journal of Physiology*, 599(10), 2527–2557. <https://doi.org/10.1113/JP279189>
157. Safieddine, S., El-Amraoui, A., & Petit, C. (2012). The auditory hair cell ribbon synapse: From assembly to function. *Annual Review of Neuroscience*, 35, 509–528. <https://doi.org/10.1146/annurev-neuro-061010-113705>
158. Safieddine, S., & Wenthold, R. J. (1999). SNARE complex at the ribbon synapses of cochlear hair cells: Analysis of synaptic vesicle- and synaptic membrane-associated proteins. *European Journal of Neuroscience*, 11(3), 803–812. <https://doi.org/10.1046/j.1460-9568.1999.00487.x>
159. Sakmann, B., & Neher, E. (1984). Patch clamp techniques for studying ionic channels in excitable membranes. *Annual Review of Physiology*, 46, 455–472. <https://doi.org/10.1146/annurev.ph.46.030184.002323>
160. Schindelin, J., Arganda-Carreras, I., Frise, E., Kaynig, V., Longair, M., Pietzsch, T., Preibisch, S., Rueden, C., Saalfeld, S., Schmid, B., Tinevez, J.-Y., White, D. J., Hartenstein, V., Eliceiri, K., Tomancak, P., & Cardona, A. (2012). Fiji: An open-source platform for biological-image analysis. *Nature Methods*, 9(7), 676–682. <https://doi.org/10.1038/nmeth.2019>
161. Schmitz, F., Königstorfer, A., & Südhof, T. C. (2000). RIBEYE, a component of synaptic ribbons: A protein's journey through evolution provides insight into synaptic ribbon function. *Neuron*, 28(3), 857–872. [https://doi.org/10.1016/s0896-6273\(00\)00159-8](https://doi.org/10.1016/s0896-6273(00)00159-8)
162. Sheets, L., Trapani, J. G., Mo, W., Obholzer, N., & Nicolson, T. (2011). Ribeye is required for presynaptic Ca(V)1.3a channel localization and afferent innervation of sensory hair cells. *Development (Cambridge, England)*, 138(7), 1309–1319. <https://doi.org/10.1242/dev.059451>
163. Shi, X.-R., & Nuttall, A. L. (2006). Early Endocytic Small GTPase Rab5 Expression at the Apical Domain of Cochlear Hair Cells. *The FASEB Journal*, 20(5), A1295–A1295. <https://doi.org/10.1096/fasebj.20.5.A1295-c>
164. Shiels, H. A., Vornanen, M., & Farrell, A. P. (2000). Temperature-Dependence of L-Type Ca<sup>2+</sup> Channel Current in Atrial Myocytes From Rainbow Trout. *Journal of Experimental Biology*, 203(18), 2771–2780. <https://doi.org/10.1242/jeb.203.18.2771>
165. Shrestha, B. R., Chia, C., Wu, L., Kujawa, S. G., Liberman, M. C., & Goodrich, L. V. (2018). Sensory Neuron Diversity in the Inner Ear Is Shaped by Activity. *Cell*, 174(5), 1229–1246.e17. <https://doi.org/10.1016/j.cell.2018.07.007>
166. Siegel, J., Sikka, R., Zeddies, D., & Dong, Q. (2001). Intact explanted adult gerbil cochleae maintained at body temperature. *Assoc Res Otolaryngol Abstr*, 24, 858.
167. Simmons, D. D., & Liberman, M. C. (1988). Afferent innervation of outer hair cells in adult cats: I. Light microscopic analysis of fibers labeled with horseradish peroxidase. *The*

168. Smith, C. A., & Sjöstrand, F. S. (1961). A synaptic structure in the hair cells of the guinea pig cochlea. *Journal of Ultrastructure Research*, 5(2), 184–192. [https://doi.org/10.1016/S0022-5320\(61\)90013-2](https://doi.org/10.1016/S0022-5320(61)90013-2)
169. Smith, C., Kongsamut, S., Wang, H., Ji, J., Kang, J., & Rampe, D. (2009). In Vitro electrophysiological activity of nerispiridine, a novel 4-aminopyridine derivative. *Clinical and Experimental Pharmacology and Physiology*, 36(11), 1104–1109. <https://doi.org/10.1111/j.1440-1681.2009.05200.x>
170. Sobkowicz, H. M., Rose, J. E., Scott, G. E., & Slapnick, S. M. (1982). Ribbon synapses in the developing intact and cultured organ of Corti in the mouse. *The Journal of Neuroscience: The Official Journal of the Society for Neuroscience*, 2(7), 942–957.
171. Solntseva, G. (2007). Morphology of the Auditory and Vestibular Organs in Mammals, with Emphasis on Marine Species. In *Morphology of the Auditory and Vestibular Organs in Mammals, with Emphasis on Marine Species*. Brill. <https://brill.com/view/title/14518>
172. Spoendlin, H. (1985). Anatomy of Cochlear Innervation. *American Journal of Otolaryngology*, 6(6), 453–467. [https://doi.org/10.1016/S0196-0709\(85\)80026-0](https://doi.org/10.1016/S0196-0709(85)80026-0)
173. Strenzke, N., Chanda, S., Kopp-Scheinflug, C., Khimich, D., Reim, K., Bulankina, A. V., Neef, A., Wolf, F., Brose, N., Xu-Friedman, M. A., & Moser, T. (2009). Complexin-I is required for high-fidelity transmission at the endbulb of Held auditory synapse. *The Journal of Neuroscience: The Official Journal of the Society for Neuroscience*, 29(25), 7991–8004. <https://doi.org/10.1523/JNEUROSCI.0632-09.2009>
174. Sundborger, A. C., & Hinshaw, J. E. (2014). Regulating dynamin dynamics during endocytosis. *F1000Prime Rep*, 6(85). <https://doi.org/10.12703/P6-85>
175. Trapani, J. G., Obholzer, N., Mo, W., Brockerhoff, S. E., & Nicolson, T. (2009). Synaptojanin1 is required for temporal fidelity of synaptic transmission in hair cells. *PLoS Genetics*, 5(5), e1000480. <https://doi.org/10.1371/journal.pgen.1000480>
176. Vogl, C., Cooper, B. H., Neef, J., Wojcik, S. M., Reim, K., Reisinger, E., Brose, N., Rhee, J.-S., Moser, T., & Wichmann, C. (2015). Unconventional molecular regulation of synaptic vesicle replenishment in cochlear inner hair cells. *Journal of Cell Science*, 128(4), 638–644. <https://doi.org/10.1242/jcs.162099>
177. von Gersdorff, H., & Matthews, G. (1994). Inhibition of endocytosis by elevated internal calcium in a synaptic terminal. *Nature*, 370(6491), Article 6491. <https://doi.org/10.1038/370652a0>
178. Wan, G., Corfas, G., & Stone, J. S. (2013). Inner ear supporting cells: Rethinking the silent majority. *Seminars in Cell & Developmental Biology*, 24(5), 448–459. <https://doi.org/10.1016/j.semcdb.2013.03.009>
179. Wang, F., Flanagan, J., Su, N., Wang, L.-C., Bui, S., Nielson, A., Wu, X., Vo, H.-T., Ma, X.-J., & Luo, Y. (2012). RNAscope. *The Journal of Molecular Diagnostics: JMD*, 14(1), 22–29. <https://doi.org/10.1016/j.jmoldx.2011.08.002>
180. Wang, R., Karpinski, E., & Pang, P. K. T. (1991). Temperature dependence of L-type calcium channel currents in isolated smooth muscle cells from the rat tail artery. *Journal of Thermal Biology*, 16(2), 83–87. [https://doi.org/10.1016/0306-4565\(91\)90003-K](https://doi.org/10.1016/0306-4565(91)90003-K)
181. Wangemann, P. (2006). Supporting sensory transduction: Cochlear fluid homeostasis and the endocochlear potential. *The Journal of Physiology*, 576(Pt 1), 11–21. <https://doi.org/10.1113/jphysiol.2006.112888>
182. Watanabe, S., Rost, B. R., Camacho-Pérez, M., Davis, M. W., Söhl-Kielczynski, B., Rosenmund, C., & Jorgensen, E. M. (2013). Ultrafast endocytosis at mouse

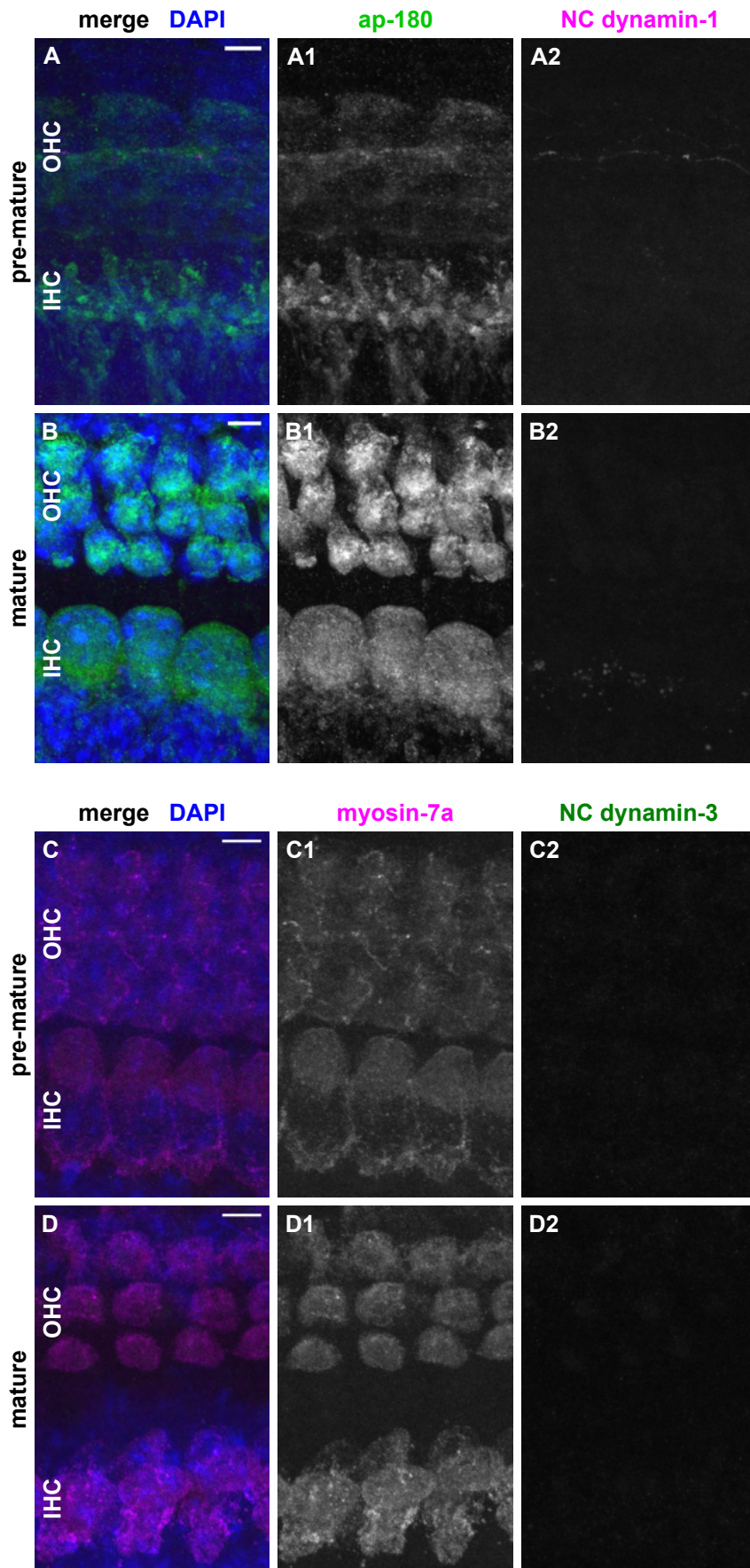
hippocampal synapses. *Nature*, 504(7479), 242–247.  
<https://doi.org/10.1038/nature12809>

183. Werner, M., Chott, A., Fabiano, A., & Battifora, H. (2000). Effect of Formalin Tissue Fixation and Processing on Immunohistochemistry. *The American Journal of Surgical Pathology*, 24(7), 1016–1019.
184. Wiwatpanit, T., Lorenzen, S. M., Cantú, J. A., Foo, C. Z., Hogan, A. K., Márquez, F., Clancy, J. C., Schipma, M. J., Cheatham, M. A., Duggan, A., & García-Añoveros, J. (2018). Trans-differentiation of outer hair cells into inner hair cells in the absence of INSM1. *Nature*, 563(7733), Article 7733. <https://doi.org/10.1038/s41586-018-0570-8>
185. Wong, A. B., Rutherford, M. A., Gabrielaitis, M., Pangrsic, T., Göttfert, F., Frank, T., Michanski, S., Hell, S., Wolf, F., Wichmann, C., & Moser, T. (2014). Developmental refinement of hair cell synapses tightens the coupling of Ca<sup>2+</sup> influx to exocytosis. *The EMBO Journal*, 33(3), 247–264. <https://doi.org/10.1002/embj.201387110>
186. Wong, M. L., & Medrano, J. F. (2005). Real-time PCR for mRNA quantitation. *BioTechniques*, 39(1), 75–85. <https://doi.org/10.2144/05391RV01>
187. Wright, A. (1984). Dimensions of the cochlear stereocilia in man and the guinea pig. *Hearing Research*, 13(1), 89–98. [https://doi.org/10.1016/0378-5955\(84\)90099-6](https://doi.org/10.1016/0378-5955(84)90099-6)
188. Wu, W., Xu, J., Wu, X.-S., & Wu, L.-G. (2005). Activity-Dependent Acceleration of Endocytosis at a Central Synapse. *Journal of Neuroscience*, 25(50), 11676–11683. <https://doi.org/10.1523/JNEUROSCI.2972-05.2005>
189. Wu, Y., O'Toole, E. T., Girard, M., Ritter, B., Messa, M., Liu, X., McPherson, P. S., Ferguson, S. M., & Camilli, P. D. (2014). A dynamin 1-, dynamin 3- and clathrin-independent pathway of synaptic vesicle recycling mediated by bulk endocytosis. *eLife*, 3, e01621. <https://doi.org/10.7554/eLife.01621>
190. Xu, J., McNeil, B., Wu, W., Nees, D., Bai, L., & Wu, L.-G. (2008). GTP-independent rapid and slow endocytosis at a central synapse. *Nature Neuroscience*, 11(1), Article 1. <https://doi.org/10.1038/nn2021>
191. Yamashita, T., Hige, T., & Takahashi, T. (2005). Vesicle Endocytosis Requires Dynamin-Dependent GTP Hydrolysis at a Fast CNS Synapse. *Science*, 307(5706), 124–127. <https://doi.org/10.1126/science.1103631>
192. Yang, S.-T., Kreutzberger, A. J. B., Lee, J., Kiessling, V., & Tamm, L. K. (2016). The Role of Cholesterol in Membrane Fusion. *Chemistry and Physics of Lipids*, 199, 136–143. <https://doi.org/10.1016/j.chemphyslip.2016.05.003>
193. Zampini, V., Johnson, S. L., Franz, C., Lawrence, N. D., Münkner, S., Engel, J., Knipper, M., Magistretti, J., Masetto, S., & Marcotti, W. (2010). Elementary properties of CaV1.3 Ca(2+) channels expressed in mouse cochlear inner hair cells. *The Journal of Physiology*, 588(Pt 1), 187–199. <https://doi.org/10.1113/jphysiol.2009.181917>
194. Zhang, L., Wang, Y., Dong, Y., Pant, A., Liu, Y., Masserman, L., Xu, Y., McLaughlin, R. N., & Bai, J. (2022). The endophilin curvature-sensitive motif requires electrostatic guidance to recycle synaptic vesicles in vivo. *Developmental Cell*, 57(6), 750-766.e5. <https://doi.org/10.1016/j.devcel.2022.02.021>

## 6 Supplement

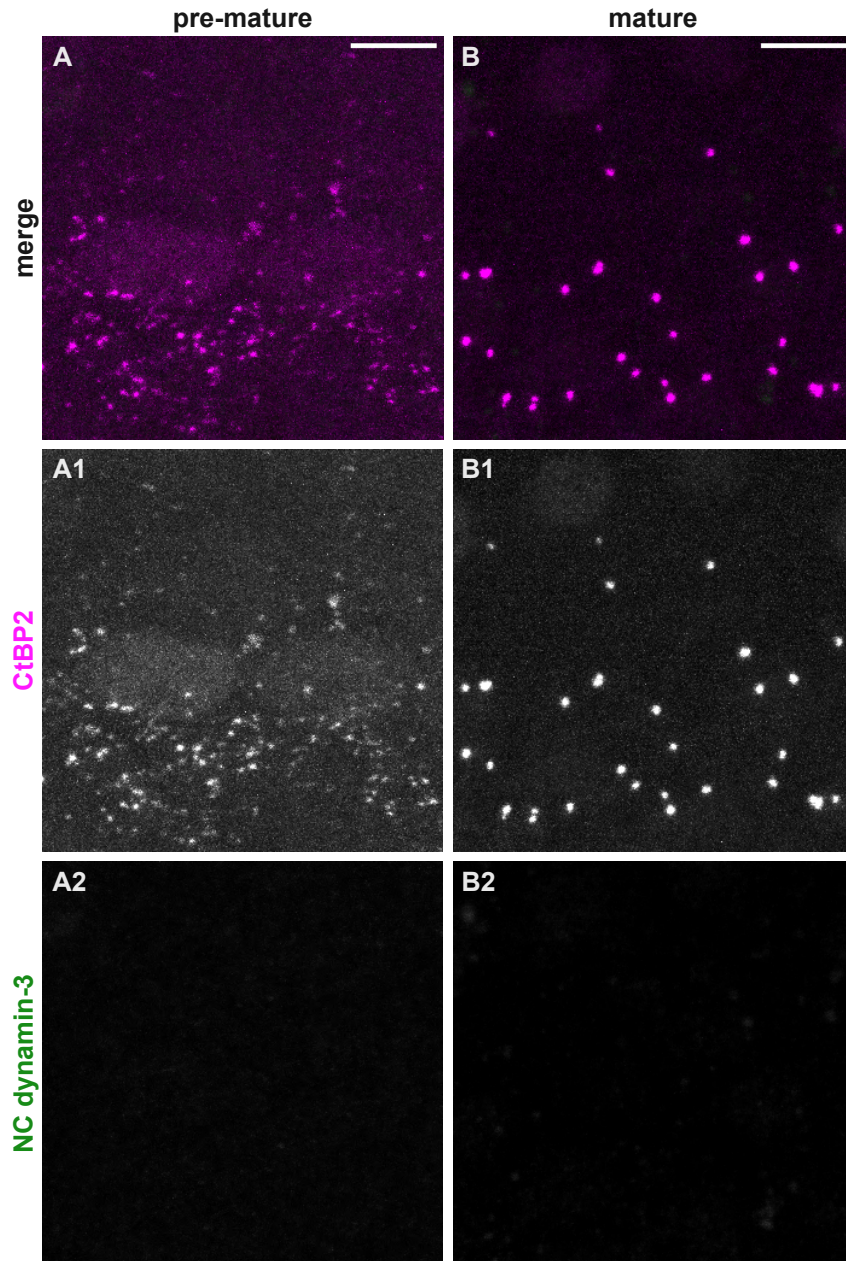


**Supplement Figure 1 Transcription of *dnm1*, *dnm3* and *sh3gl2* in spiral ganglion neurons of the mature organ of Corti.** MIZP of FISH of SGNs in the whole-mount apical cochlear turn of the mature OC from a P20 mouse using probes targeting *dnm1* (magenta), *dnm3* (green) and *sh3gl2* (greyscale). Transcripts of all three genes were detected in SGNs as evident from the merged image (A) and images separated by target probe (B-D). Nuclei were labeled with DAPI (blue, A). Scale bar: 5  $\mu$ m.



**Supplement Figure 2  
Negative controls of immunolabeling.**

Immunolabeling performed on the apical turn of whole-mount OCs from pre-hearing and hearing mice for ap-180 (green in **A, B**; grayscale in **A1, B1**) in absence of the dynamin-1 antibody, and for myosin-7a (magenta in **C, D**; grayscale in **C1, D1**) in absence of the dynamin-3 antibody, respectively. No non-specific staining was found in IHCs or OHCs for secondary antibodies without primary antibodies (magenta for dynamin-1 in **A, B**; green for dynamin-3 in **C, D**; grey scale for both in **A2-D2**). Scale bars: 5  $\mu$ m.



**Supplement Figure 3 Negative controls of immunolabeling in organs of Corti fixed with Zamboni's fixative.** Immunolabeling for CtBP2 (magenta in **A, B**; grayscale in **A1, B1**) in apical-turn IHCs from a pre-hearing and a hearing mouse using Zamboni's fixative in absence of the dynamin-3 antibody. No non-specific staining was found for the secondary antibody in absence of the dynamin-3 antibody (green in **A, B**; grey scale in **A2, B2**). Scale bars: 5  $\mu$ m.

**Supplement Table 1 Slope of the linear function fitted to the change of membrane capacitance ( $\Delta C_m$ ) of the reference recordings and to the last 8 s of the  $\Delta C_m$  following a 100-ms stimulus.** The slope of pre-mature and mature IHCs at room temperature (RT), near body temperature (BT), and during application of dyngo-4a at BT was compared using Kruskal-Wallis (K-W) test ( $H = 16.826$ ,  $p = 0.113$ ). n (N): number of cells (animals).

			Median $\pm$ S.D. (fF/s)	n (N)
pre-mature	reference	RT	-3.5 $\pm$ 2.0	8 (5)
		BT	-3.1 $\pm$ 1.8	9 (7)
		dyngo-4a	-1.7 $\pm$ 2.0	10 (8)
	stimulus	RT	-4.8 $\pm$ 3.2	9 (8)
		BT	-2.1 $\pm$ 2.7	12 (9)
		dyngo-4a	-1.1 $\pm$ 3.0	12 (11)
mature	reference	RT	-4.5 $\pm$ 2.1	7 (5)
		BT	-4.4 $\pm$ 1.9	8 (6)
		dyngo-4a	-2.9 $\pm$ 2.0	7 (6)
	stimulus	RT	-3.5 $\pm$ 1.2	10 (9)
		BT	-4.5 $\pm$ 3.1	15 (11)
		dyngo-4a	-4.0 $\pm$ 1.9	11 (10)
$p = 0.113$				

**Supplement Table 2 Peak  $\Delta C_m$  reflecting exocytosis induced by a 100-ms depolarization.** The peak  $\Delta C_m$  of pre-mature and mature IHCs at RT, BT and during application of dyngo-4a at BT was compared using K-W test ( $H = 41.040$ ,  $p < 0.001$ ) followed by sorting the groups into homogeneous subsets (represented by “+”). Groups belonging to different subsets (columns 1-4) were significantly different; groups within the same subset were not different with  $p > 0.05$  (“ $p$  within subset”). n (N): number of cells (animals).

		Median $\pm$ S.D. (fF)	n (N)	Homogeneous subset			
				1	2	3	4
pre-mature	RT	6.7 $\pm$ 5.6	9 (8)	+			
	BT	35.8 $\pm$ 18.9	12 (9)			+	
	dyngo-4a	24.6 $\pm$ 14.8	12 (11)		+	+	
mature	RT	18.2 $\pm$ 6.2	10 (9)		+		
	BT	50.0 $\pm$ 13.2	15 (11)				+
	dyngo-4a	42.8 $\pm$ 9.7	11 (10)			+	
$p$ within subset					0.60	0.18	

**Supplement Table 3 Time required for  $\Delta C_m$  to return to the baseline at 0 fF (time to 0) following exocytosis induced by a 100-ms depolarization.** The time to 0 of pre-mature and mature IHCs at RT, BT and during application of dyngo-4a at BT was compared using K-W test ( $H = 17.014$ ,  $p = 0.004$ ) followed by sorting the groups into homogeneous subsets (represented by "+"). Groups belonging to different subsets (columns 1-2) were significantly different; groups within the same subset were not different with  $p > 0.05$  ("p within subset"). n (N): number of cells (animals).

		Median $\pm$ S.D. (s)	n (N)	Homogeneous subset	
				1	2
pre-mature	RT	1.1 $\pm$ 1.1	9 (8)	+	
	BT	4.4 $\pm$ 3.7	12 (9)		+
	dyngo-4a	4.0 $\pm$ 3.6	12 (11)		+
mature	RT	4.2 $\pm$ 1.6	10 (9)		+
	BT	4.0 $\pm$ 1.3	15 (11)		+
	dyngo-4a	6.2 $\pm$ 1.9	11 (10)		+
<i>p</i> within subset				0.55	

**Supplement Table 4 Endocytosis (decline) rate of  $\Delta C_m$  (calculated as peak  $\Delta C_m$  divided by time to 0) following exocytosis induced by a 100-ms depolarization.** The decline rate of pre-mature and mature IHCs at RT, BT and during application of dyngo-4a at BT was compared using K-W test ( $H = 28.567$ ,  $p < 0.001$ ) followed by sorting the groups into homogeneous subsets (represented by "+"). Groups belonging to different subsets (columns 1-3) were significantly different; groups within the same subset were not different with  $p > 0.05$  ("p within subset"). n (N): number of cells (animals).

		Median $\pm$ S.D. (fF/s)	n (N)	Homogeneous subset		
				1	2	3
pre-mature	RT	5.7 $\pm$ 2.7	9 (8)	+	+	
	BT	10.0 $\pm$ 3.9	12 (9)		+	
	dyngo-4a	4.8 $\pm$ 4.7	12 (11)	+	+	
mature	RT	4.3 $\pm$ 2.3	10 (9)	+		
	BT	13.4 $\pm$ 6.2	15 (11)			+
	dyngo-4a	7.1 $\pm$ 1.5	11 (10)	+	+	
<i>p</i> within subset				0.10	0.17	

**Supplement Table 5 Ca<sup>2+</sup> charge (Q<sub>Ca</sub>) calculated from the Ca<sup>2+</sup> current (I<sub>Ca</sub>) elicited by a 100-ms depolarization.** Q<sub>Ca</sub> of pre-mature and mature IHCs at RT, BT and during application of dyngo-4a at BT was compared using K-W test ( $H = 46.436$ ,  $p < 0.001$ ) followed by sorting the groups into homogeneous subsets (represented by "+"). Groups belonging to different subsets (columns 1-2) were significantly different; groups within the same subset were not different with  $p > 0.05$  ("p within subset"). n (N): number of cells (animals).

		Median ± S.D. (pC)	n (N)	Homogeneous subset	
				1	2
pre-mature	RT	-15.1 ± 4.0	9 (8)		+
	BT	-29.7 ± 6.0	12 (9)	+	
	dyngo-4a	-28.4 ± 7.6	12 (11)	+	
mature	RT	-11.7 ± 1.7	10 (9)		+
	BT	-15.0 ± 3.3	15 (11)		+
	dyngo-4a	-15.1 ± 3.4	11 (10)		+
<i>p</i> within subset				0.95	0.44

**Supplement Table 6 Exponential amplitude (A) of the exponential-linear function fitted to cumulative  $\Delta C_m$  traces following repetitive 50-ms depolarizations.** The exponential A of pre-mature and mature IHCs at RT, BT and during application of dyngo-4a at BT was compared using K-W test ( $H = 51.209$ ,  $p < 0.001$ ) followed by sorting the groups into homogeneous subsets (represented by "+"). Groups belonging to different subsets (columns 1-4) were significantly different; groups within the same subset were not different with  $p > 0.05$  ("p within subset"). n (N): number of cells (animals). Fit: number of cells that could be fitted with an exponential-linear function.

		Median ± S.D. (fF)	n (N)	Fit	Homogeneous subset			
					1	2	3	4
pre-mature	RT	510.6 ± 243.0	17 (13)	4			+	+
	BT	825.1 ± 232.9	15 (10)	10				+
	dyngo-4a	627.5 ± 428.3	19 (16)	all				+
mature	RT	25.0 ± 24.1	15 (11)	10	+			
	BT	150.5 ± 78.1	14 (12)	all		+		
	dyngo-4a	240.0 ± 145.3	14 (12)	all			+	
<i>p</i> within subset							0.20	0.29

**Supplement Table 7 Exponential time constant ( $\tau$ ) of the exponential-linear function fitted to cumulative  $\Delta C_m$  traces following repetitive 50-ms depolarizations.** The exponential  $\tau$  of pre-mature and mature IHCs at RT, BT and during application of dyngo-4a at BT was compared using K-W test ( $H = 45.035$ ,  $p < 0.001$ ) followed by sorting the groups into homogeneous subsets (represented by "+"). Groups belonging to different subsets (columns 1-3) were significantly different; groups within the same subset were not different with  $p > 0.05$  ("p within subset"). n (N): number of cells (animals). Fit: number of cells that could be fitted with an exponential-linear function.

		Median $\pm$ S.D. (s)	n (N)	Fit	Homogeneous subset		
					1	2	3
pre-mature	RT	5.1 $\pm$ 1.0	17 (13)	4			+
	BT	5.7 $\pm$ 1.8	15 (10)	10			+
	dyngo-4a	5.6 $\pm$ 1.7	19 (16)	all			+
mature	RT	0.8 $\pm$ 0.7	15 (11)	10	+		
	BT	0.9 $\pm$ 1.3	14 (12)	all	+		
	dyngo-4a	2.1 $\pm$ 1.6	14 (12)	all		+	
				<i>p</i> within subset	0.91		1.00

**Supplement Table 8 Slope of the linear function and the linear part of the exponential-linear function fitted to cumulative  $\Delta C_m$  traces following repetitive 50-ms depolarizations.** The slope of pre-mature and mature IHCs at RT, BT and during application of dyngo-4a at BT was compared using K-W test ( $H = 36.642$ ,  $p < 0.001$ ) followed by sorting the groups into homogeneous subsets (represented by "+"). Groups belonging to different subsets (columns 1-2) were significantly different; groups within the same subset were not different with  $p > 0.05$  ("p within subset"). n (N): number of cells (animals).

		Median $\pm$ S.D. (fF/s)	n (N)	Homogeneous subset	
				1	2
pre-mature	RT	24.0 $\pm$ 23.1	17 (13)		+
	BT	-6.9 $\pm$ 40.4	15 (10)	+	
	dyngo-4a	-12.2 $\pm$ 31.4	19 (16)	+	
mature	RT	35.8 $\pm$ 13.9	15 (11)		+
	BT	23.5 $\pm$ 7.8	14 (12)		+
	dyngo-4a	27.8 $\pm$ 20.5	14 (12)		+
				<i>p</i> within subset	0.76 0.49

**Supplement Table 9 Total  $Q_{Ca}$  summarized from all stimuli during repetitive 50-ms depolarizations.** The total  $Q_{Ca}$  of pre-mature and mature IHCs at RT, BT and during application of dyngo-4a at BT was compared using K-W test ( $H = 32.384$ ,  $p < 0.001$ ) followed by sorting the groups into homogeneous subsets (represented by "+"). Groups belonging to different subsets (columns 1-3) were significantly different; groups within the same subset were not different with  $p > 0.05$  ("p within subset"). n (N): number of cells (animals).

		Median $\pm$ S.D. (pC)	n (N)	Homogeneous subset		
				1	2	3
pre-mature	RT	-359.1 $\pm$ 75.0	17 (13)		+	+
	BT	-461.1 $\pm$ 196.7	15 (10)		+	
	dyngo-4a	-573.9 $\pm$ 190.9	19 (16)	+		
mature	RT	-307.2 $\pm$ 66.7	15 (11)			+
	BT	-348.4 $\pm$ 74.5	14 (12)		+	+
	dyngo-4a	-345.3 $\pm$ 69.4	14 (12)		+	+
$p$ within subset					0.43	0.09

**Supplement Table 10 Difference between  $Q_{Ca}$  at the first and last, 50<sup>th</sup> stimulus ( $\Delta Q_{(1-50)}$ ) during repetitive 50-ms depolarizations.**  $\Delta Q_{(1-50)}$  of pre-mature and mature IHCs at RT, BT and during application of dyngo-4a at BT was compared using K-W test ( $H = 73.613$ ,  $p < 0.001$ ) followed by sorting the groups into homogeneous subsets (represented by "+"). Groups belonging to different subsets (columns 1-3) were significantly different; groups within the same subset were not different with  $p > 0.05$  ("p within subset"). n (N): number of cells (animals).

		Median $\pm$ S.D. (pC)	n (N)	Homogeneous subset		
				1	2	3
pre-mature	RT	3.5 $\pm$ 0.9	17 (13)		+	
	BT	10.0 $\pm$ 2.1	15 (10)			+
	dyngo-4a	7.4 $\pm$ 4.9	19 (16)			+
mature	RT	1.3 $\pm$ 0.5	15 (11)	+		
	BT	1.2 $\pm$ 0.5	14 (12)	+		
	dyngo-4a	1.1 $\pm$ 0.6	14 (12)	+		
$p$ within subset				0.87		0.55

**Supplement Table 11 Total efficiency ( $\Delta C_m/Q_{Ca}$ , calculated from interstep  $\Delta C_m$  normalized to  $Q_{Ca}$ ) summarized from all stimuli during repetitive 50-ms depolarizations.** The total efficiency of pre-mature and mature IHCs at RT, BT and during application of dyngo-4a at BT was compared using K-W test ( $H = 34.340$ ,  $p < 0.001$ ) followed by sorting the groups into homogeneous subsets (represented by “+”). Groups belonging to different subsets (columns 1-3) were significantly different; groups within the same subset were not different with  $p > 0.05$  (“ $p$  within subset”). n (N): number of cells (animals).

		Median $\pm$ S.D. (fF/pC)	n (N)	Homogeneous subset		
				1	2	3
pre-mature	RT	34.9 $\pm$ 18.7	17 (13)	+	+	
	BT	54.3 $\pm$ 18.1	15 (10)		+	+
	dyngo-4a	29.1 $\pm$ 11.0	19 (16)	+		
mature	RT	48.1 $\pm$ 14.4	15 (11)		+	
	BT	41.6 $\pm$ 12.7	14 (12)		+	
	dyngo-4a	65.2 $\pm$ 11.3	14 (12)			+
$p$ within subset				1.00	0.08	0.16

**Supplement Table 12 Exponential A of the exponential-linear function fitted to cumulative  $\Delta C_m$  traces following repetitive 1-s depolarizations.** The exponential A of pre-mature and mature IHCs at RT, BT and during application of dyngo-4a at BT was compared using K-W test ( $H = 23.142$ ,  $p < 0.001$ ) followed by sorting the groups into homogeneous subsets (represented by “+”). Groups belonging to different subsets (columns 1-3) were significantly different; groups within the same subset were not different with  $p > 0.05$  (“ $p$  within subset”). n (N): number of cells (animals). Fit: number of cells fitted with an exponential-linear function.

		Median $\pm$ S.D. (fF)	n (N)	Homogeneous subset		
				1	2	3
pre-mature	RT	653 $\pm$ 323	11 (9)	+		
	BT	1639 $\pm$ 738	7 (6)			+
	dyngo-4a	2147 $\pm$ 372	8 (6)			+
mature	RT	1626 $\pm$ 995	13 (9)		+	+
	BT	1048 $\pm$ 249	9 (9)		+	
$p$ within subset					0.16	0.43

**Supplement Table 13 Exponential  $\tau$  of the exponential-linear function fitted to cumulative  $\Delta C_m$  traces following repetitive 1-s depolarizations.** The exponential  $\tau$  of pre-mature and mature IHCs at RT, BT and during application of dyngo-4a at BT was compared using K-W test ( $H = 26.244$ ,  $p < 0.001$ ) followed by sorting the groups into homogeneous subsets (represented by "+"). Groups belonging to different subsets (columns 1-3) were significantly different; groups within the same subset were not different with  $p > 0.05$  ("p within subset"). n (N): number of cells (animals). Fit: number of cells fitted with an exponential-linear function.

		Median $\pm$ S.D. (s)	n (N)	Homogeneous subset		
				1	2	3
pre-mature	RT	6.2 $\pm$ 2.3	11 (9)		+	
	BT	3.9 $\pm$ 2.9	7 (6)	+	+	
	dyngo-4a	2.5 $\pm$ 1.5	8 (6)	+		
mature	RT	10.3 $\pm$ 11.2	13 (9)			+
	BT	6.9 $\pm$ 3.6	9 (9)		+	
$p$ within subset				0.57	0.34	

**Supplement Table 14 Slope of the linear function and the linear part of the exponential-linear function fitted to cumulative  $\Delta C_m$  traces following repetitive 1-s depolarizations.** The slope of pre-mature and mature IHCs at RT, BT and during application of dyngo-4a at BT was compared using K-W test ( $H = 20.013$ ,  $p < 0.001$ ) followed by sorting the groups into homogeneous subsets (represented by "+"). Groups belonging to different subsets (columns 1-2) were significantly different; groups within the same subset were not different with  $p > 0.05$  ("p within subset"). n (N): number of cells (animals).

		Median $\pm$ S.D. (fF/s)	n (N)	Homogeneous subset	
				1	2
pre-mature	RT	3.2 $\pm$ 4.3	11 (9)		+
	BT	-2.8 $\pm$ 17.3	7 (6)	+	+
	dyngo-4a	-17.9 $\pm$ 11.2	8 (6)	+	
mature	RT	7.1 $\pm$ 13.5	13 (9)		+
	BT	-2.7 $\pm$ 3.2	9 (9)	+	
$p$ within subset				0.32	0.14

**Supplement Table 15 Total  $Q_{Ca}$  summarized from all stimuli during repetitive 1-s depolarizations.** The total  $Q_{Ca}$  of pre-mature and mature IHCs at RT, BT and during application of dyngo-4a at BT was compared using K-W test ( $H = 27.839$ ,  $p < 0.001$ ) followed by sorting the groups into homogeneous subsets (represented by “+”). Groups belonging to different subsets (columns 1-3) were significantly different; groups within the same subset were not different with  $p > 0.05$  (“ $p$  within subset”). n (N): number of cells (animals).

		Median $\pm$ S.D. (pC)	n (N)	Homogeneous subset		
				1	2	3
pre-mature	RT	-2384 $\pm$ 716	11 (9)			+
	BT	-2838 $\pm$ 1454	7 (6)		+	+
	dyngo-4a	-5518 $\pm$ 942	8 (6)	+		
mature	RT	-2242 $\pm$ 828	13 (9)			+
	BT	-3911 $\pm$ 775	9 (9)		+	
$p$ within subset					0.22	0.86

**Supplement Table 16  $\Delta Q_{(1-50)}$  during repetitive 1-s depolarizations.**  $\Delta Q_{(1-50)}$  of pre-mature and mature IHCs at RT, BT and during application of dyngo-4a at BT was compared using K-W test ( $H = 38.475$ ,  $p < 0.001$ ) followed by sorting the groups into homogeneous subsets (represented by “+”). Groups belonging to different subsets (columns 1-4) were significantly different; groups within the same subset were not different with  $p > 0.05$  (“ $p$  within subset”). n (N): number of cells (animals).

		Median $\pm$ S.D. (pC)	n (N)	Homogeneous subset			
				1	2	3	4
pre-mature	RT	103.9 $\pm$ 24.6	11 (9)			+	
	BT	100.2 $\pm$ 45.1	7 (6)			+	
	dyngo-4a	204.2 $\pm$ 49.1	8 (6)				+
mature	RT	61.8 $\pm$ 21.4	13 (9)		+		
	BT	32.0 $\pm$ 9.5	9 (9)	+			
$p$ within subset						1.00	

**Supplement Table 17 Total efficiency summarized from all stimuli during repetitive 1-s depolarizations.** The total efficiency of pre-mature and mature IHCs at RT, BT and during application of dyngo-4a at BT was compared using K-W test ( $H = 32.260$ ,  $p < 0.001$ ) followed by sorting the groups into homogeneous subsets (represented by “+”). Groups belonging to different subsets (columns 1-3) were significantly different; groups within the same subset were not different with  $p > 0.05$  (“ $p$  within subset”). n (N): number of cells (animals).

		Median $\pm$ S.D. (fF/pC)	n (N)	Homogeneous subset		
				1	2	3
pre-mature	RT	12.1 $\pm$ 3.6	11 (9)		+	
	BT	20.2 $\pm$ 12.6	7 (6)		+	
	dyngo-4a	2.7 $\pm$ 5.1	8 (6)	+		
mature	RT	46.1 $\pm$ 13.0	13 (9)			+
	BT	9.3 $\pm$ 2.8	9 (9)	+	+	
$p$ within subset				0.18	0.12	

**Supplement Table 18 List of equipment.**

Equipment	Company
Axioskop microscope	Carl Zeiss AG, Germany
B FWCAM X M camera	The Imaging Source Europe GmbH, Germany
C-MAG HS 7 magnetic stirrer	IKA-Werke GmbH & CO. KG, Germany
DMZ-universal puller	Zeitz-Instrumente Vertriebs GmbH, Germany
HI 221 pH meter	Hanna Instruments Deutschland GmbH, Germany
HM507 oscilloscope	HAMEG Instruments GmbH, Germany
INCU-Line IL23 digital incubator	VWR International GmbH, Germany
ISM940E tubing pump	Cole-Parmer GmbH, Germany
ITC-1600 data acquisition system	HEKA Elektronik GmbH, Germany
KS 260 basic shaker	IKA-Werke GmbH & CO. KG, Germany
LPBF-01GX amplifier / filter module	npi electronic GmbH, Germany
LPBF-48DG 8-pole Bessel low-pass filter	npi electronic GmbH, Germany
LSM 710 confocal laser scanning microscope	Carl Zeiss AG, Germany
MCL-3 electronic micromanipulator	Bachofer GmbH & Co. KG, Germany
MP85-1120 manual micromanipulator	Sutter Instrument Co., USA
Optopatch patch clamp amplifier	Cairn Research Ltd., UK
OSMOMAT 030 osmometer	Gonotec Meß- und Regeltechnik GmbH, Germany
P-2000 micropipette puller	Sutter Instrument, USA
PatchStar micromanipulator	Scientifica Ltd, UK
PLP 330 peristaltic pump	behr Labor-Technik GmbH, Germany
Q-Series with BNC connector pipette holder	Warner Instruments, LLC, USA
Sonorex RK 31 ultrasonic bath	BANDELIN electronic GmbH & Co. KG, Germany
SZX16 stereo microscope	Olympus Europa SE & Co. KG, Germany
TC-20 temperature controller	npi electronic GmbH, Germany
VH-3036-OPT anti-vibration table	Newport Spectra-Physics GmbH, Germany

**Supplement Table 19 List of software.**

Software	Company/Developer
Fiji 2.11.0	Schindelin et al., 2012; <a href="https://imagej.net/software/">https://imagej.net/software/</a>
IC Capture 2.4.633.2555	The Imaging Source Europe GmbH, Germany
Igor Pro 8.04	WaveMetrics, Inc., USA
Inkscape 1.2.1	The Inkscape Project; <a href="https://inkscape.org/">https://inkscape.org/</a>
PatchMaster 2x90.6 beta	HEKA Elektronik GmbH, Germany
SPSS 28.0.0.0	IBM Corp., USA
ZEN 8.1.10.484	Carl Zeiss AG, Germany

**Supplement Table 20 List of chemicals.**

Chemical	Catalog No.	Company
300 mOsmol/kg NaCl/H <sub>2</sub> O	30.9.0020	Gonotec Meß- und Regeltechnik GmbH, Germany
4-AP	A78403-25G	Sigma-Aldrich Chemie GmbH, Germany
Apamin	178270	Merck KGaA, Germany
Bovine serum albumin	A3912-10G	Sigma-Aldrich Chemie GmbH, Germany
CaCl <sub>2</sub>	223506-500G	Honeywell Riedel-de Haën AG, Germany
CsCl	289329-25G	Honeywell Riedel-de Haën AG, Germany
CsOH	16505	Thermo Fisher (Kandel) GmbH, Germany
DAPI	D9542	Sigma-Aldrich Chemie GmbH, Germany
DMSO	327182500	Acros Organics Bvba, Belgium
Dyngo-4a	5364	Tocris Bioscience, UK
EGTA acid	3779	Honeywell Riedel-de Haën AG, Germany
Ethanol	32205-2.5L	Sigma-Aldrich Chemie GmbH, Germany
FluorSave	345789	Millipore Corp., USA
Glucose•H <sub>2</sub> O	143140.1211	AppliChem GmbH, Germany
GTP	151216	MP Biomedicals, LLC, France
HEPES	172572500	Acros Organics Bvba, Belgium
HCl	1.09057.1000	Merck KGaA, Germany
KCl	26764.298	VWR International GmbH, Germany
Lactobionic acid	J66368	Thermo Fisher (Kandel) GmbH, Germany
L-glutamic acid	156211000	Acros Organics Bvba, Belgium
Linopirdine	L134-10MG	Sigma-Aldrich Chemie GmbH, Germany
Methanol	20847.32	VWR International GmbH, Germany
MgCl <sub>2</sub>	M9272-100G	Honeywell Riedel-de Haën AG, Germany
NaCl	S/3160/60	Fisher Scientific GmbH, Germany
NaH <sub>2</sub> PO <sub>4</sub> •H <sub>2</sub> O	71504-250G	Honeywell Riedel-de Haën AG, Germany
NaOH	71463-1L	Honeywell Riedel-de Haën AG, Germany
NaOH	28244.295	VWR International GmbH, Germany
Na <sub>2</sub> Phosphocreatine	P7936-5G	Sigma-Aldrich Chemie GmbH, Germany
Na <sub>2</sub> ATP	L14522	Thermo Fisher (Kandel) GmbH, Germany
Normal goat serum	G9023	Sigma-Aldrich Chemie GmbH, Germany
PBS tablets	18912-014	Life Technologies Limited, UK
PFA	28908	Thermo Fisher (Kandel) GmbH, Germany
pH 7.01 standard solutions	HI70007	Hanna Instruments Deutschland GmbH, Germany
pH 10.01 standard solutions	HI70010	Hanna Instruments Deutschland GmbH, Germany
ProLong	P36982	Thermo Fisher (Kandel) GmbH, Germany
RNAscope™ 3-plex Positive Control Probe Mr	320881	Advanced Cell Diagnostics, Inc., USA
RNAscope™ 3-plex Negative Control Probe	320871	Advanced Cell Diagnostics, Inc., USA
RNAscope™ FL AMP 1	320852	Advanced Cell Diagnostics, Inc., USA
RNAscope™ FL AMP 2	320853	Advanced Cell Diagnostics, Inc., USA
RNAscope™ FL AMP 3	320854	Advanced Cell Diagnostics, Inc., USA
RNAscope™ FL AMP 4 ALT B	320856	Advanced Cell Diagnostics, Inc., USA
RNAscope™ Protease III	322337	Advanced Cell Diagnostics, Inc., USA
RNAscope™ Probe- Mm-Dnm1	446931	Advanced Cell Diagnostics, Inc., USA
RNAscope™ Probe- Mm-Dnm3-C2	451841-C2	Advanced Cell Diagnostics, Inc., USA
RNAscope™ Probe- Mm-Sh3gl2-C3	492641-C3	Advanced Cell Diagnostics, Inc., USA
RNAscope™ wash buffer	310091	Advanced Cell Diagnostics, Inc., USA
TEA chloride	150900250	Acros Organics Bvba, Belgium
Triton X-100	T8787-50ML	Sigma-Aldrich Chemie GmbH, Germany
Tween 20	P1379-25ML	Sigma-Aldrich Chemie GmbH, Germany
Vectashield	H-1000	Vector Laboratories, Inc., USA
Zamboni's fixative	12773.025	Morphisto GmbH, Germany

**Supplement Table 21 List of primary antibodies.**

Target	Clonality	Host	Catalog No.	Company/Organization
Alix	monoclonal	mouse	sc-53540	Santa Cruz Biotechnology, Inc., USA
Ap-180	polyclonal	rabbit	155003	Synaptic Systems GmbH, Germany
Calbindin	monoclonal	mouse	Sc-365360	Santa Cruz Biotechnology, Inc., USA
Calcineurin-a	polyclonal	rabbit	387003	Synaptic Systems GmbH, Germany
CtBP2	monoclonal	mouse	612044	Becton Dickinson GmbH, Germany
CtBP2	polyclonal	rabbit	10-P1554	American Research Products, Inc., USA
Dynamin-1	monoclonal	mouse	610245	Becton Dickinson GmbH, Germany
Dynamin-3	polyclonal	rabbit	115302	Synaptic Systems GmbH, Germany
Endophilin-a1	polyclonal	rabbit	159002	Synaptic Systems GmbH, Germany
Myosin-6	monoclonal	mouse	sc-393558	Santa Cruz Biotechnology, Inc., USA
Myosin-7a	monoclonal	mouse	sc-74516	Santa Cruz Biotechnology, Inc., USA
Otoferlin	monoclonal	mouse	ab53233	Abcam plc., UK
Otoferlin	polyclonal	rabbit	-	AG Knipper, University of Tübingen, Germany
Pacsin1	polyclonal	rabbit	196003	Synaptic Systems GmbH, Germany
Pacsin1	polyclonal	rabbit	196002	Synaptic Systems GmbH, Germany
PSD95	monoclonal	mouse	75-028	NeuroMab, USA
Hsc70	monoclonal	mouse	149011	Synaptic Systems GmbH, Germany

**Supplement Table 22 List of secondary antibodies.**

Conjugate	Clonality	Reactivity	Host	Catalog No.	Company
AlexaFluor568	polyclonal	mouse	goat	A-11019	Thermo Fisher (Kandel) GmbH, Germany
AlexaFluor488	polyclonal	rabbit	donkey	ab150073	Abcam plc., UK
AlexaFluor405	polyclonal	mouse	donkey	ab175659	Abcam plc., UK
AlexaFluor488	polyclonal	mouse	donkey	A-21202	Thermo Fisher (Kandel) GmbH, Germany
AlexaFluor488	polyclonal	mouse	goat	A-11001	Thermo Fisher (Kandel) GmbH, Germany
Cy3	polyclonal	rabbit	goat	111-166-046	Jackson ImmunoResearch Europe Ltd., UK
Cy3	polyclonal	rabbit	donkey	711-166-152	Jackson ImmunoResearch Europe Ltd., UK
DyLight405	polyclonal	rabbit	donkey	711-475-152	Jackson ImmunoResearch Europe Ltd., UK



EtOH, 20 min, -20 °C	1% BSA, 30 min	Dynammin-3	1:2000	overnight, 4 °C	Cy3 GAR	1:1500	70 min, RT	FluorSave	Yes
<b>EtOH, 20 min, -20 °C</b>	<b>1% BSA, 30 min</b>	<b>Dynammin-3</b>	<b>1:2000</b>	<b>overnight, 4 °C</b>	<b>AlexaFluor488 DAR</b>	<b>1:500</b>	<b>70 min, RT</b>	<b>FluorSave</b>	<b>Yes</b>
Zamboni's fixative, 5 min, ice-cold	1% BSA, 30 min	Dynammin-3	1:500	90 min, RT	AlexaFluor488 DAR	1:1500	overnight, 4 °C	Vectashield	Only for dynammin-3
Zamboni's fixative, 5 min, ice-cold	1% BSA, 30 min	Dynammin-3	1:2000	RT	Cy3 GAR	1:1500	overnight, 4 °C	Vectashield	Only for dynammin-3
Zamboni's fixative, 5 min, ice-cold	1% BSA, 30 min	Dynammin-3	1:1000	90 min, RT	AlexaFluor488 DAR	1:1500	overnight, 4 °C	Vectashield	Only for dynammin-3
Zamboni's fixative, 5 min, ice-cold	1% BSA, 30 min	Dynammin-3	1:2000	RT	Cy3 GAR	1:1500	overnight, 4 °C	Vectashield	Only for dynammin-3
Zamboni's fixative, 5 min, ice-cold	1% BSA, 30 min	Dynammin-3	1:2000	RT	AlexaFluor488 DAR	1:1500	overnight, 4 °C	Vectashield	Only for dynammin-3
Zamboni's fixative, 5 min, ice-cold	1% BSA, 30 min	Dynammin-3	1:5000	90 min, RT	AlexaFluor488 DAR	1:1500	overnight, 4 °C	Vectashield	Only for dynammin-3
EtOH, 20 min, -20 °C	1% BSA, 30 min	Dynammin-3	1:2000	overnight, 4 °C	Cy3 GAR	1:1500	70 min, RT	Vectashield	Yes
EtOH, 20 min, -20 °C	1% BSA, 30 min	Dynammin-3	1:2000	overnight, 4 °C	Cy3 GAR	1:1500	70 min, RT	Vectashield	Yes
EtOH, 20 min, -20 °C	4% BSA, 65 min	Dynammin-3	1:2000	4 °C	AlexaFluor488 DAR	1:1500	70 min, RT	Vectashield	Yes
EtOH, 20 min, -20 °C	4% BSA, 75 min	Otofertin (r)	1:8000	overnight, 4 °C	Cy3 GAR	1:1500	70 min, RT	Vectashield	Yes
EtOH, 20 min, -20 °C	4% BSA, 1 h	Dynammin-1	1:200	overnight, 4 °C	AlexaFluor488 DAR	1:1500	70 min, RT	Vectashield	Yes
EtOH, 20 min, -20 °C	4% BSA, 1 h	Otofertin (r)	1:8000	overnight, 4 °C	Cy3 GAR	1:1500	70 min, RT	FluorSave	Yes
EtOH, 20 min, -20 °C	4% BSA, 1 h	Dynammin-1	1:200	overnight, 4 °C	AlexaFluor488 DAR	1:1500	70 min, RT	FluorSave	Yes
EtOH, 20 min, -20 °C	4% BSA, 1 h	Otofertin (r)	1:8000	overnight, 4 °C	Cy3 GAR	1:1500	70 min, RT	FluorSave	Yes
EtOH, 20 min, -20 °C	4% BSA, 1 h	Dynammin-1	1:200	overnight, 4 °C	AlexaFluor568 DAR	1:1500	70 min, RT	FluorSave	Yes
EtOH, 20 min, -20 °C	4% BSA, 1 h	Otofertin (r)	1:8000	overnight, 4 °C	DyLight405 DAR	1:500	2 h, RT	FluorSave	No
EtOH, 20 min, -20 °C	4% BSA, 1 h	Dynammin-1	1:200	overnight, 4 °C	AlexaFluor568 DAR	1:1500	70 min, RT	FluorSave	Yes
EtOH, 20 min, -20 °C	4% BSA, 1 h	Otofertin (r)	1:8000	overnight, 4 °C	Cy3 GAR	1:1500	70 min, RT	FluorSave	Yes
EtOH, 20 min, -20 °C	4% BSA, 1 h	Dynammin-1	1:200	overnight, 4 °C	AlexaFluor568 DAR	1:1500	70 min, RT	Vectashield	Yes
EtOH, 20 min, -20 °C	4% BSA, 1 h	CtBP2 (r)	1:250	overnight, 4 °C	Cy3 GAR	1:1500	70 min, RT	Vectashield	Yes
EtOH, 20 min, -20 °C	4% BSA, 1 h	Dynammin-1	1:200	overnight, 4 °C	AlexaFluor488 DAR	1:1500	70 min, RT	FluorSave	Only for CtBP2
EtOH, 20 min, -20 °C	4% BSA, 1 h	CtBP2 (r)	1:250	overnight, 4 °C	Cy3 GAR	1:1500	70 min, RT	FluorSave	Yes
EtOH, 20 min, -20 °C	4% BSA, 1 h	Dynammin-1	1:200	overnight, 4 °C	AlexaFluor488 DAR	1:1500	70 min, RT	FluorSave	Yes
EtOH, 20 min, -20 °C	4% BSA, 1 h	CtBP2 (r)	1:250	overnight, 4 °C	AlexaFluor488 DAR	1:1500	70 min, RT	FluorSave	Only for dynammin-1
EtOH, 20 min, -20 °C	4% BSA, 1 h	Dynammin-1	1:200	overnight, 4 °C	DyLight405 DAR	1:1500	2 h, RT	FluorSave	No
EtOH, 20 min, -20 °C	4% BSA, 1 h	CtBP2 (r)	1:250	overnight, 4 °C	DyLight405 DAR	1:1500	2 h, RT	FluorSave	No
EtOH, 20 min, -20 °C	1% BSA, 30 min	Dynammin-1	1:200	overnight, 4 °C	AlexaFluor568 DAR	1:1500	70 min, RT	FluorSave	Yes
EtOH, 20 min, -20 °C	1% BSA, 30 min	CtBP2 (r)	1:250	overnight, 4 °C	AlexaFluor568 DAR	1:1500	70 min, RT	FluorSave	Yes
<b>EtOH, 20 min, -20 °C</b>	<b>1% BSA, 30 min</b>	<b>Dynammin-1</b>	<b>1:200</b>	<b>overnight, 4 °C</b>	<b>AlexaFluor568 DAR</b>	<b>1:500</b>	<b>70 min, RT</b>	<b>FluorSave</b>	<b>Yes</b>
EtOH, 20 min, -20 °C	1% BSA, 30 min	Pacsin-1	1:200	overnight, 4 °C	Cy3 GAR	1:1500	70 min, RT	Vectashield	Only for CtBP2
EtOH, 20 min, -20 °C	1% BSA, 30 min	CtBP2 (m)	1:250	overnight, 4 °C	AlexaFluor488 DAR	1:1500	70 min, RT	Vectashield	Only for CtBP2

EtOH, 20 min, -20 °C	1% BSA, 30 min	Pacsin-1 CtBP2 (m)	1:500	overnight, 4 °C	Cy3 GAR AlexaFluor488 DAM	1:1500	70 min, RT	Vectashield	Only for CtBP2
Zamboni's fixative, 8 min, ice-cold	1% BSA, 30 min	Pacsin-1 CtBP2 (m)	1:500	90 min, RT	Cy3 GAR AlexaFluor488 DAM	1:1500	70 min, RT	Vectashield	Only for CtBP2
EtOH, 20 min, -20 °C	1% BSA, 30 min	Pacsin-1 CtBP2 (m)	1:1000	90 min, RT	Cy3 GAR AlexaFluor488 DAM	1:1500	70 min, RT	Vectashield	Only for CtBP2
Zamboni's fixative, 8 min, ice-cold	1% BSA, 30 min	Pacsin-1 CtBP2 (m)	1:1000	90 min, RT	Cy3 GAR AlexaFluor488 DAM	1:1500	70 min, RT	Vectashield	Only for CtBP2
EtOH, 20 min, -20 °C	1% BSA, 30 min	Pacsin-1 CtBP2 (m)	1:2000	90 min, RT	Cy3 GAR AlexaFluor488 DAM	1:1500	70 min, RT	Vectashield	Only for CtBP2
Zamboni's fixative, 8 min, ice-cold	1% BSA, 30 min	Pacsin-1 CtBP2 (m)	1:2000	90 min, RT	Cy3 GAR AlexaFluor488 DAM	1:1500	70 min, RT	Vectashield	Only for CtBP2
Zamboni's fixative, 8 min, ice-cold	0.3% TX-100, 4% BSA, 1 h	Pacsin-1 Otoferrin (m)	1:1000	90 min, RT	Cy3 GAR AlexaFluor488 DAM	1:1500	70 min, RT	FluorSave	Only for otoferlin
EtOH, 20 min, -20 °C	0.3% TX-100, 4% BSA, 1 h	Pacsin-1 Otoferrin (m)	1:1000	90 min, RT	Cy3 GAR AlexaFluor488 DAM	1:1500	70 min, RT	FluorSave	Only for otoferlin
Zamboni's fixative, 8 min, ice-cold	1% BSA, 30 min	Pacsin-1 Otoferrin (m)	1:250	overnight, 4 °C	Cy3 GAR AlexaFluor488 DAM	1:1500	70 min, RT	ProLong	Only for otoferlin
2% PFA, 8 min, ice-cold	1% BSA, 30 min	Pacsin-1 Otoferrin (m)	1:250	overnight, 4 °C	Cy3 GAR AlexaFluor488 DAM	1:1500	70 min, RT	ProLong	Only for otoferlin
Zamboni's fixative, 8 min, ice-cold	1% BSA, 30 min	Pacsin-1 Otoferrin (m)	1:100	overnight, 4 °C	Cy3 GAR AlexaFluor488 DAM	1:1500	70 min, RT	ProLong	Only for otoferlin
Zamboni's fixative, 8 min, ice-cold	1% BSA, 30 min	Pacsin-1 Otoferrin (m)	1:500	overnight, 4 °C	Cy3 GAR AlexaFluor488 DAM	1:1500	70 min, RT	ProLong	Only for otoferlin
2% PFA, 8 min, ice-cold	1% BSA, 30 min	Pacsin-1 Otoferrin (m)	1:100	overnight, 4 °C	Cy3 GAR AlexaFluor488 DAM	1:1500	70 min, RT	ProLong	Only for otoferlin
Zamboni's fixative, 8 min, ice-cold	0.3% TX-100, 4% BSA, 1 h	Pacsin-1 Otoferrin (m)	1:250	overnight, 4 °C	Cy3 GAR AlexaFluor488 DAM	1:1500	70 min, RT	ProLong	Only for otoferlin
Zamboni's fixative, 8 min, ice-cold	0.3% TX-100, 4% BSA, 1 h	Pacsin-1 Otoferrin (m)	1:100	overnight, 4 °C	Cy3 GAR AlexaFluor488 DAM	1:1500	70 min, RT	ProLong	Only for otoferlin
EtOH, 20 min, -20 °C	1% BSA, 1 h	Pacsin-1 Otoferrin (m)	1:250	overnight, 4 °C	Cy3 GAR AlexaFluor488 DAM	1:1500	70 min, RT	ProLong	Only for otoferlin
EtOH, 20 min, -20 °C	1% BSA, 1 h	Pacsin-1 Otoferrin (m)	1:500	overnight, 4 °C	Cy3 GAR AlexaFluor488 DAM	1:1500	70 min, RT	ProLong	Only for otoferlin
EtOH, 20 min, -20 °C	1% BSA, 1 h	Pacsin-1 Otoferrin (m)	1:100	overnight, 4 °C	Cy3 GAR AlexaFluor488 DAM	1:1500	70 min, RT	ProLong	Only for otoferlin
EtOH, 20 min, -20 °C	1% BSA, 1 h	Pacsin-1 Otoferrin (m)	1:1000	overnight, 4 °C	Cy3 GAR AlexaFluor488 DAM	1:1500	70 min, RT	ProLong	Only for otoferlin
EtOH, 20 min, -20 °C	1% BSA, 1 h	Pacsin-1 Otoferrin (m)	1:2000	overnight, 4 °C	Cy3 GAR AlexaFluor488 DAM	1:1500	70 min, RT	ProLong	Only for otoferlin
Zamboni's fixative, 8 min, ice-cold	1% BSA, 1 h	Pacsin-1 Otoferrin (m)	1:500	90 min, RT	Cy3 GAR AlexaFluor488 DAM	1:1500	70 min, RT	ProLong	Only for otoferlin
Zamboni's fixative, 8 min, ice-cold	1% BSA, 1 h	Pacsin-1 Otoferrin (m)	1:1000	90 min, RT	Cy3 GAR AlexaFluor488 DAM	1:1500	70 min, RT	ProLong	Only for otoferlin
Zamboni's fixative, 8 min, ice-cold	1% BSA, 1 h	Pacsin-1 Otoferrin (m)	1:2000	90 min, RT	Cy3 GAR AlexaFluor488 DAM	1:1500	70 min, RT	ProLong	Only for otoferlin
EtOH, 20 min, -20 °C	1% BSA, 30 min	Pacsin-1 Otoferrin (m)	1:100	overnight, 4 °C	Cy3 GAR AlexaFluor488 DAM	1:1500	70 min, RT	FluorSave	Only for otoferlin
EtOH, 20 min, -20 °C	1% BSA, 30 min	Endophilin-1 Otoferrin (m)	1:200	overnight, 4 °C	Cy3 GAR AlexaFluor488 DAM	1:1500	70 min, RT	FluorSave	Only for otoferlin

EtOH, 20 min, -20 °C	1% BSA, 30 min	Endophilin-1 Otofelin (m)	1:500	overnight, 4 °C	Cy3 GAR	1:1500	70 min, RT	FluorSave	Only for otoferlin
EtOH, 20 min, -20 °C	1% BSA, 30 min	Endophilin-1 Otofelin (m)	1:1000	overnight, 4 °C	AlexaFluor488 DAM	1:500	70 min, RT	FluorSave	Only for otoferlin
EtOH, 20 min, -20 °C	30% BSA, 1 h	Endophilin-1 Otofelin (m)	1:1000	overnight, 4 °C	AlexaFluor488 DAM	1:500	70 min, RT	FluorSave	Only for otoferlin
Zamboni's fixative, 8 min, ice-cold	30% BSA, 1 h	Endophilin-1 Otofelin (m)	1:1000	overnight, 4 °C	AlexaFluor488 DAM	1:500	70 min, RT	FluorSave	Only for otoferlin
EtOH, 20 min, -20 °C	1% BSA, 30 min	Ap-180 Otofelin (m)	1:100	overnight, 4 °C	Cy3 GAR	1:500	70 min, RT	FluorSave	Yes
EtOH, 20 min, -20 °C	1% BSA, 30 min	Ap-180 Otofelin (m)	1:500	overnight, 4 °C	AlexaFluor488 DAM	1:500	70 min, RT	FluorSave	Yes
EtOH, 20 min, -20 °C	1% BSA, 30 min	Ap-180 Otofelin (m)	1:100	overnight, 4 °C	AlexaFluor488 DAM	1:500	70 min, RT	FluorSave	Only for ap-180
EtOH, 20 min, -20 °C	1% BSA, 30 min	Ap-180 Otofelin (m)	1:500	overnight, 4 °C	AlexaFluor405 DAM	1:500	70 min, RT	FluorSave	Only for ap-180
EtOH, 20 min, -20 °C	1% BSA, 30 min	Ap-180 CtBP2 (m)	1:250	overnight, 4 °C	Cy3 GAR	1:500	70 min, RT	FluorSave	Yes
EtOH, 20 min, -20 °C	1% BSA, 30 min	Ap-180 CtBP2 (m)	1:250	overnight, 4 °C	AlexaFluor488 DAM	1:500	70 min, RT	FluorSave	Yes
EtOH, 20 min, -20 °C	1% BSA, 30 min	Ap-180 CtBP2 (m)	1:250	overnight, 4 °C	AlexaFluor488 DAM	1:500	70 min, RT	FluorSave	Yes
EtOH, 20 min, -20 °C	1% BSA, 30 min	Ap-180 Otofelin (m)	1:1000	overnight, 4 °C	Cy3 GAR	1:500	70 min, RT	FluorSave	Yes
EtOH, 20 min, -20 °C	1% BSA, 30 min	Ap-180 Otofelin (m)	1:2000	overnight, 4 °C	AlexaFluor488 DAM	1:500	70 min, RT	FluorSave	Yes
4% PFA, 8 min, ice-cold	1% BSA, 40 min	Hsc70 Ap-180	1:200	overnight, 4 °C	AlexaFluor488 DAM	1:500	70 min, RT	FluorSave	Only for ap-180
EtOH, 20 min, -20 °C	10% BSA, 1 h	Hsc70 Ap-180	1:200	overnight, 4 °C	Cy3 GAR	1:500	70 min, RT	FluorSave	Only for ap-180
EtOH, 20 min, -20 °C	10% NGS, 1 h	Hsc70 Ap-180	1:500	overnight, 4 °C	AlexaFluor488 DAM	1:500	70 min, RT	FluorSave	Only for ap-180
4% PFA, 8 min, ice-cold	1% BSA, 40 min	Hsc70 Ap-180	1:500	overnight, 4 °C	AlexaFluor488 DAM	1:500	70 min, RT	FluorSave	Only for ap-180
4% PFA, 8 min, ice-cold	1% BSA, 40 min	Hsc70 Ap-180	1:1000	overnight, 4 °C	Cy3 GAR	1:500	70 min, RT	FluorSave	Only for ap-180
4% PFA, 1 h, ice-cold	0.2% TX-100, 5% NGS, 2 h	Hsc70 CtBP2 (r)	1:100	overnight, 4 °C	AlexaFluor488 DAM	1:500	2 h, RT	FluorSave	Only for CtBP2
EtOH, 20 min, -20 °C	1% BSA, 30 min	Calcineurin-A Otofelin (m)	1:100	overnight, 4 °C	Cy3 GAR	1:500	70 min, RT	FluorSave	Only for otoferlin
EtOH, 20 min, -20 °C	1% BSA, 30 min	Calcineurin-A Otofelin (m)	1:1000	overnight, 4 °C	AlexaFluor488 DAM	1:500	70 min, RT	FluorSave	Only for otoferlin
EtOH, 20 min, -20 °C	10% BSA, 1 h	Calcineurin-A Otofelin (m)	1:500	overnight, 4 °C	Cy3 GAR	1:500	70 min, RT	FluorSave	Only for otoferlin
EtOH, 20 min, -20 °C	10% NGS, 1 h	Calcineurin-A Otofelin (m)	1:100	overnight, 4 °C	AlexaFluor488 DAM	1:500	70 min, RT	FluorSave	Only for otoferlin
4% PFA, 8 min, ice-cold	1% BSA, 30 min	Calcineurin-A Otofelin (m)	1:500	overnight, 4 °C	Cy3 GAR	1:500	70 min, RT	FluorSave	Only for otoferlin

4% PFA, 8 min, ice-cold	1% BSA, 30 min	Calceineurin-A Otoferlin (m)	1:1000	overnight, 4 °C	Cy3 GAR AlexaFluor488 DAM	1:1500 1:500	70 min, RT	FluorSave	Only for otoferlin
EtOH, 20 min, -20 °C	30% BSA, 1 h	Calceineurin-A Otoferlin (m)	1:500	overnight, 4 °C	Cy3 GAR AlexaFluor488 DAM	1:1500 1:500	70 min, RT	FluorSave	Only for otoferlin
EtOH, 20 min, -20 °C	30% BSA, 1 h	Calceineurin-A Otoferlin (m)	1:500	90 min, RT	Cy3 GAR AlexaFluor488 DAM	1:1500 1:500	70 min, RT	FluorSave	Only for otoferlin
EtOH, 20 min, -20 °C	1% BSA, 30 min	Myosin-7a Otoferlin (r)	1:50	overnight, 4 °C	AlexaFluor568 GAM AlexaFluor488 DAR	1:500 1:500	70 min, RT	FluorSave	Yes
Zamboni's fixative, 10 min, ice-cold	1% BSA, 30 min	Myosin-7a Otoferlin (r)	1:50	overnight, 4 °C	AlexaFluor568 GAM AlexaFluor488 DAR	1:500 1:500	70 min, RT	FluorSave	Yes
EtOH, 20 min, -20 °C	1% BSA, 30 min	Myosin-7a CtBP2 (r)	1:50	overnight, 4 °C	AlexaFluor488 DAM	1:500	70 min, RT	FluorSave	Yes
Zamboni's fixative, 8 min, ice-cold	1% BSA, 30 min	Myosin-7a CtBP2 (r)	1:50	overnight, 4 °C	AlexaFluor488 DAM Cy3 GAR	1:500 1:1500	70 min, RT	FluorSave	Only for CtBP2
EtOH, 20 min, -20 °C	1% BSA, 30 min	Myosin-7a Otoferlin (r)	1:200	overnight, 4 °C	AlexaFluor568 GAM AlexaFluor488 DAR	1:500 1:500	70 min, RT	FluorSave	Yes
Zamboni's fixative, 10 min, ice-cold	1% BSA, 30 min	Myosin-7a Otoferlin (r)	1:200	overnight, 4 °C	AlexaFluor568 GAM AlexaFluor488 DAR	1:500 1:500	70 min, RT	FluorSave	Yes
EtOH, 20 min, -20 °C	1% BSA, 30 min	Calbindin Otoferlin (r)	1:100	overnight, 4 °C	AlexaFluor568 GAM AlexaFluor488 DAR	1:500 1:500	70 min, RT	FluorSave	Yes
Zamboni's fixative, 15 min, ice-cold	1% BSA, 30 min	Calbindin Otoferlin (r)	1:100	overnight, 4 °C	AlexaFluor568 GAM AlexaFluor488 DAR	1:500 1:500	70 min, RT	FluorSave	Only for otoferlin
EtOH, 20 min, -20 °C	1% BSA, 30 min	Calbindin Otoferlin (r)	1:500	overnight, 4 °C	AlexaFluor568 GAM AlexaFluor488 DAR	1:500 1:500	70 min, RT	FluorSave	Yes
Zamboni's fixative, 15 min, ice-cold	1% BSA, 30 min	Calbindin Otoferlin (r)	1:500	overnight, 4 °C	AlexaFluor568 GAM AlexaFluor488 DAR	1:500 1:500	70 min, RT	FluorSave	Only for otoferlin
EtOH, 20 min, -20 °C	1% BSA, 30 min	Myosin-6 Otoferlin (r)	1:100	overnight, 4 °C	AlexaFluor568 GAM AlexaFluor488 DAR	1:500 1:500	70 min, RT	FluorSave	Only for otoferlin
EtOH, 20 min, -20 °C	1% BSA, 30 min	Myosin-6 Otoferlin (r)	1:100	overnight, 4 °C	AlexaFluor568 GAM AlexaFluor488 DAR	1:500 1:500	70 min, RT	FluorSave	Only for otoferlin
EtOH, 20 min, -20 °C	1% BSA, 30 min	Myosin-6 Otoferlin (r)	1:500	overnight, 4 °C	AlexaFluor568 GAM AlexaFluor488 DAR	1:500 1:500	70 min, RT	FluorSave	Only for otoferlin
EtOH, 20 min, -20 °C	1% BSA, 30 min	Myosin-6 Otoferlin (r)	1:500	overnight, 4 °C	AlexaFluor568 GAM AlexaFluor488 DAR	1:500 1:500	70 min, RT	FluorSave	Only for otoferlin
EtOH, 20 min, -20 °C	1% BSA, 30 min	Alix Otoferlin (r)	1:50	overnight, 4 °C	AlexaFluor568 GAM AlexaFluor488 DAR	1:500 1:500	70 min, RT	FluorSave	Yes
EtOH, 20 min, -20 °C	1% BSA, 30 min	Alix Otoferlin (r)	1:500	overnight, 4 °C	AlexaFluor568 GAM AlexaFluor488 DAR	1:500 1:500	70 min, RT	FluorSave	Yes
Zamboni's fixative, 10 min, ice-cold	1% BSA, 30 min	Alix Otoferlin (r)	1:50	overnight, 4 °C	AlexaFluor568 GAM AlexaFluor488 DAR	1:500 1:500	70 min, RT	FluorSave	Yes
Zamboni's fixative, 10 min, ice-cold	1% BSA, 30 min	Alix Otoferlin (r)	1:500	overnight, 4 °C	AlexaFluor568 GAM AlexaFluor488 DAR	1:500 1:500	70 min, RT	FluorSave	Yes

## **Acknowledgments**

I would like to express my gratitude to all those who have helped me in the preparation of this thesis. My foremost and deepest appreciation goes to Dr. Stephanie Eckrich, whose guidance and support realized my dissertation. My thanks also go to Prof. Dr. Jutta Engel for her invaluable opinions and for being the first reviewer, and to Prof. Dr. Dieter Bruns for being the second reviewer. Another appreciation goes to Dr. Stefan Münkner, who provided extensive help with patch clamp experiments and data analysis. Furthermore, I thank all other lab members, including Heike, Fische, Pauline, Kerstin and Simone, as well as the dedicated members of the animal facility. Last but not least, I thank my parents, my wife, and my friends for their unwavering support throughout this journey.

## **Publications and conferences**

Huang, G., Eckrich, S. (2021). Quantitative Fluorescent in situ Hybridization Reveals Differential Transcription Profile Sharpening of Endocytic Proteins in Cochlear Hair Cells Upon Maturation. *Frontiers in Cellular Neuroscience*, 15. <https://doi:10.3389/fncel.2021.643517>

Weigel, S., Kuenzel, T., Lischka, K., Huang, G., Luksch, H. (2022). Morphology and Dendrite-Specific Synaptic Properties of Midbrain Neurons Shape Multimodal Integration. *J. Neurosci.*, 42, 2614–2630. <https://doi.org/10.1523/JNEUROSCI.1695-21.2022>

03.2023            15th Göttingen Meeting of the German Neuroscience Society  
Poster: "Maturation of activity-dependent endocytosis during terminal differentiation of cochlear inner hair cells"

02.2021            Association for Research in Otolaryngology 2021 MidWinter Meeting  
Poster: "Transcriptional and Translational Cell-Level Profiling of Endocytic Proteins of the Differentiating and Mature Organ of Corti"

## **Curriculum Vitae**

The curriculum vitae was removed from the electronic version of the doctoral thesis for reasons of data protection.